AFRL-AFOSR-VA-TR-2023-0143

Chemistry and Dynamics of Pre-Ionization Controlled Laser Plasmas

Yalin, Azer
COLORADO STATE UNIVERSITY
601 S HOWES ST
FORT COLLINS, CO, 80521
USA

11/04/2022
Final Technical Report

Air Force Research Laboratory
Air Force Office of Scientific Research
Arlington, Virginia 22203
Air Force Materiel Command

REPORT DOCUMENTATION PAGE

PLEASE DO NOT RETURN YOUR FORM TO THE ABOVE ORGANIZATION.

1. REPORT DATE	2. REPORT TYPE	3. DATES COVERED	
20221104	Final	START DATE 20180425	END DATE 20220424

4. TITLE AND SUBTITLE
Chemistry and Dynamics of Pre-Ionization Controlled Laser Plasmas

5a. CONTRACT NUMBER	5b. GRANT NUMBER	5c. PROGRAM ELEMENT NUMBER
	FA9550-18-1-0239	61102F
5d. PROJECT NUMBER	**5e. TASK NUMBER**	**5f. WORK UNIT NUMBER**

6. AUTHOR(S)
Azer Yalin

7. PERFORMING ORGANIZATION NAME(S) AND ADDRESS(ES)
COLORADO STATE UNIVERSITY
601 S HOWES ST
FORT COLLINS, CO 80521
USA

8. PERFORMING ORGANIZATION REPORT NUMBER

9. SPONSORING/MONITORING AGENCY NAME(S) AND ADDRESS(ES)	10. SPONSOR/MONITOR'S ACRONYM(S)	11. SPONSOR/MONITOR'S REPORT NUMBER(S)
Air Force Office of Scientific Research 875 N. Randolph St. Room 3112 Arlington, VA 22203	AFRL/AFOSR RTB1	AFRL-AFOSR-VA-TR-2023-0143

12. DISTRIBUTION/AVAILABILITY STATEMENT
A Distribution Unlimited: PB Public Release

13. SUPPLEMENTARY NOTES

14. ABSTRACT
Executive Summary This research project has explored the physics of pre-ionization controlled laser induced plasmas in air. The pre-ionization plasma approach is based on the synergistic effect of combining multiple laser pulses where the first pulse provides periodization
(not full breakdown) thereby promoting controlled absorption and plasma formation in the presence of the second pulse. We have generally used ultraviolet (UV) pulses for periodization, owing to stronger multiphoton ionization (MPI), and near-infrared (NIR) pulses
for energy addition. The expanded window of conditions (size, temperature, active species etc.) achievable with the pre-ionization plasmas makes them potentially attractive for multiple Air Force applications including providing new sources for ignition of propulsion devices, for
atmospheric waveguides, and for novel diagnostics. We have followed a combined experimental and modeling approach to investigate the basic laser-induced plasma formation mechanisms, including detailed characterization of plasma properties and species, as well as
studies of ignition and combustion of air-fuel mixtures with the pre-ionization laser plasmas. Experimental measurements have included Rayleigh and Thomson scattering to determine gas temperature and electron density, optical emission spectroscopy and chemiluminescence, Schlieren imaging, as well as combustion studies in a fixed volume chamber (heat release from pressure rise). These measurements have been used to support the development and validation of a two-dimensional axisymmetric numeric model of the laser plasma system including a novel optical-solver (for beam-steering) based on the plasma chemistry. Some main results from the research include findings related to: the reduction in breakdown threshold due to preionization, the origin of vorticity and lobe generation due to plasmainduced gas dynamics and their impact on ignition, the possibility of efficient pre-ionization via resonance-enhanced MPI (REMPI) of oxygen, the potential to ignite leaner mixtures (in stationary, atmospheric-pressure air), and a database of ignition characteristics of fuel-air mixtures including hydrogen-air. Emerging directions from the research include the needs to further examine plasma-induced optical beam steering effects, possible non-equilibrium effects, and formation and properties of pre-ionization laser plasmas in moving gases and
multiphase flows.

15. SUBJECT TERMS

16. SECURITY CLASSIFICATION OF:			17. LIMITATION OF ABSTRACT	18. NUMBER OF PAGES
a. REPORT U	b. ABSTRACT U	c. THIS PAGE U	UU	137

19a. NAME OF RESPONSIBLE PERSON	19b. PHONE NUMBER *(Include area code)*
JOHN LUGINSLAND	000-0000

Executive Summary

This research project has explored the physics of pre-ionization controlled laser induced plasmas in air. The pre-ionization plasma approach is based on the synergistic effect of combining multiple laser pulses where the first pulse provides pre-ionization (not full breakdown) thereby promoting controlled absorption and plasma formation in the presence of the second pulse. We have generally used ultraviolet (UV) pulses for preionization, owing to stronger multiphoton ionization (MPI), and near-infrared (NIR) pulses for energy addition. The expanded window of conditions (size, temperature, active species etc.) achievable with the pre-ionization plasmas makes them potentially attractive for multiple Air Force applications including providing new sources for ignition of propulsion devices, for atmospheric waveguides, and for novel diagnostics. We have followed a combined experimental and modeling approach to investigate the basic laser-induced plasma formation mechanisms, including detailed characterization of plasma properties and species, as well as studies of ignition and combustion of air-fuel mixtures with the pre-ionization laser plasmas. Experimental measurements have included Rayleigh and Thomson scattering to determine gas temperature and electron density, optical emission spectroscopy and chemiluminescence, Schlieren imaging, as well as combustion studies in a fixed volume chamber (heat release from pressure rise). These measurements have been used to support the development and validation of a two-dimensional axisymmetric numeric model of the laser plasma system including a novel optical-solver (for beam-steering) based on the plasma chemistry. Some main results from the research include findings related to: the reduction in breakdown threshold due to pre-ionization, the origin of vorticity and lobe generation due to plasma-induced gas dynamics and their impact on ignition, the possibility of efficient pre-ionization via resonance-enhanced MPI (REMPI) of oxygen, the potential to ignite leaner mixtures (in stationary, atmospheric-pressure air), and a database of ignition characteristics of fuel-air mixtures including hydrogen-air. Emerging directions from the research include the needs to further examine plasma-induced optical beam steering effects, possible non-equilibrium effects, and formation and properties of pre-ionization laser plasmas in moving gases and multi-phase flows.

Journal and Conference Publications from the project:

1. R.Mahamud, A.A. Tropina, M. N. Shneider, R.B. Miles "Dual-Pulse Laser Ignition model", Phys. of Fluids 2018, Vol.30, p.106104
2. Tropina A.A., Mahamud R., Shneider M.N., Miles R.B. "Mathematical modeling of dual-pulse laser ignition in a turbulent flow" 2019 AIAA SciTech Forum, San-Diego, CA (AIAA-2019-0741)
3. Carter Butte, Ciprian Dumitrache, Azer Yalin "Properties of Dual-Pulse Laser Plasmas and Ignition Characteristics in Propane-Air and Methane-Air Mixtures", 2019 AIAA SciTech Forum, San Diego, CA (AIAA 2019-0464)
4. Carter Butte, Ciprian Dumitrache, Azer Yalin "Dual-Pulse Laser Ignition Using Oxygen REMPI Preionization", 2019 AIAA Aviation, Dallas, TX (AIAA 2019-3117)
5. A. Tropina, Matthew R. New-Tolley, M.N. Shneider, Modeling of laser ignition in hydrogen-air mixture, AIAA Scitech 2020 Forum, Orlando, FL (AIAA 2020-1892)
6. R. Mahamud, D. Hartman, A.A. Tropina. "Dynamics of dual-pulse laser energy deposition in a supersonic flow", Journal of Physics D: Appl. Physics 2020, Vol.53 , p. 265201
7. C. Dumitrache and A.P. Yalin "Gas Dynamics and Vorticity Generation in Laser-Induced Breakdown of Air" Optics Express 2020, 28 (4), 5835-5850
8. C. Dumitrache, C. Butte and A.P. Yalin 2020 "Resonant dual-pulse laser ignition technique based on oxygen REMPI pre-ionization" *Nature Scientific Reports*, 10: 19916.
9. C. Dumitrache and A.P. Yalin 2020 "Gas Dynamic Regimes Observed in Dual-Pulse Laser Ignition" *Int. J. Heat Mass Transfer*, 161 120302.
10. Carter Butte , Parneeth Lokini, Ciprian Dumitrache and Azer P. "Single and Dual-Pulse Laser Ignition of Methane-Air and Hydrogen-Air Mixtures", 2020 AIAA Scitech, Orlando FA (AIAA 2020-1893)
11. A. Tropina, S. Pokharel and M.N. Shneider 2021 "Effects of the Laser Intensity Profile on Ignition of Hydrogen-Air Mixture" AIAA 2021-1788, Scitech 2021 Forum, Virtual Event
12. M.R. New-Tolley, M.N. Shneider and R.B. Miles 2021 "Displacement of energy deposition during formation of nanosecond laser plasmas by self-defocusing" Laser Phys. Lett 18 036001
13. S.Pokharel, A.A. Tropina, M.N. Shneider, Vorticity Generation with Defocusing Effect for Dual-Pulse Laser Plasma in Air, 74th Annual Gaseous Electronics Conference, October 4-8, 2021, TF14.00003 – abstract only; not included in PDF attachment.
14. M.R. New-Tolley, Modeling laser-gas interactions for aerospace applications, PhD thesis, Department Mechanical & Aerospace Engineering, Princeton University, Princeton, NJ, 2021 – not included in PDF attachment.

Dual-pulse laser ignition model

Rajib Mahamud, Albina A. Tropina, Mikhail N. Shneider, and Richard B. Miles

Citation: Physics of Fluids **30**, 106104 (2018); doi: 10.1063/1.5043295
View online: https://doi.org/10.1063/1.5043295
View Table of Contents: http://aip.scitation.org/toc/phf/30/10
Published by the American Institute of Physics

Dual-pulse laser ignition model

Rajib Mahamud,[1,a)] Albina A. Tropina,[1] Mikhail N. Shneider,[2] and Richard B. Miles[1]
[1]*Aerospace Engineering Texas A&M University, College Station, Texas 77843, USA*
[2]*Mechanical and Aerospace Engineering, Princeton University, Princeton, New Jersey 08544, USA*

(Received 7 June 2018; accepted 12 September 2018; published online 4 October 2018)

A two-dimensional mathematical model of dual-pulse laser ignition that self-consistently integrates Navier-Stokes, translational and vibrational energy, and neutral and charged species equations has been presented. The results showed that the ignition kernel dynamics depends on the shape and initial energy distribution in the energy spot created by the first ultraviolet laser pulse. The results also suggest that the ignition delay time and the flame kernel development depend on the laser intensity, vibrational-nonequilibrium, and initial electron number density. For the high initial degree of ionization, we have obtained ignition of the lean methane–air mixture with the equivalence ratio of 0.6. Vibrational-nonequilibrium taken into account by the Landau-Teller model leads to the slower ignition kernel growth and the significant increase in the ignition delay time. For the case modeled, a change in the overlap of the second laser with the focal point of the first laser pulse leads to the early split up of the kernel and the flame extinguishment. *Published by AIP Publishing.* https://doi.org/10.1063/1.5043295

I. INTRODUCTION

Laser ignition presents many potential benefits over the conventional spark ignition system such as the decrease in the lean limit, absence of electrodes, and ability to locate the ignition kernel in any point inside the combustion chamber.[1–4] The main physical mechanisms of laser ignition were discussed by Ronney.[1] A recent comprehensive review of laser ignition systems in aerospace applications was performed by O'Briant *et al.*[3] The authors showed that an appropriate choice of the laser wavelength and repetition rate can result in a higher temperature, greater probability of the free radical formation, and subsequently greater ignition probability, especially for leaner mixtures. A review by Tropina *et al.*[4] summarized the main ignition concepts at high pressure conditions relevant to internal combustion engines. Dual pulse laser ignition can significantly enhance the capabilities of single pulse laser ignition. We present here a comprehensive 2D model that self-consistently integrates Navier-Stokes, energy, and species equations to understand the role of chemistry versus hydrodynamics for dual-pulse laser ignition and flame propagation enhancement.

According to Ronney,[1] the physical mechanisms of laser ignition include thermal ionization, photochemical dissociation of fuel molecules, non-resonant and resonant breakdown by multi-photon, and avalanche ionization. In the case of the thermal initiation, a laser discharge is used to heat a mixture or to excite vibrational and rotational degrees of freedom of molecules leading to subsequent heating. In the case of the non-resonant or resonant breakdown ignition, the focused laser beam causes the electrical breakdown of the gas similar to a thermal spark but with different breakdown mechanisms such as a multiphoton, tunnel, and avalanche ionization. Multiphoton and tunnel ionization were first described by Keldysh,[5] who identified two limiting regimes, depending on the value of the Keldysh parameter $\gamma = \frac{\omega_L \sqrt{2mI_i}}{eE_L}$, where ω_L is the oscillation frequency of the electric field, I_i is the ionization potential, e is the electric charge, E_L is the electric field amplitude, and m is the mass of the electron. At $\gamma \ll 1$, when the field oscillation frequency is much less than the electron period of motion, breakdown is in the tunneling limit. At $\gamma \gg 1$, when the field oscillation frequency is much higher than the electron period, breakdown is in the multiphoton ionization limit. Laser driven avalanche ionization depends on the electron-neutral collision frequency. The laser passes into the plasma, and the free electrons oscillate in the electric field of the laser. If there are no collisions, no energy is transferred, but with collisions, the oscillation phase of the electrons and the directions of their motion are changed, and if the laser intensity is high, the electrons can gain enough energy from the laser to ionize the neutral species. The avalanche ionization process leads to significant local heating and can ignite combustible gas mixtures. Laser breakdown mechanisms in different media are extensively studied in optics related to the development of high-sensitivity laser-induced breakdown spectroscopy (LIBS),[6] showing that high pressure conditions and presence of small particles reduce the laser breakdown threshold.[7]

The fluid dynamics phenomenon associated with the laser induced breakdown has been numerically investigated by Steiner *et al.*,[8] Jiang *et al.*,[9] and Ghosh and Mahesh.[10] It was shown that the strong pressure gradient after the laser breakdown produces a strong blast wave and the core of the plasma rolls up in time and forms a toroidal vortex region. The multiscale-multiphysics process comprises particle-wave interaction, chemical reaction, and fluid dynamics effect with time scales ranging from nanoseconds (plasma formation and decay) to microseconds (fluid dynamics).[10]

A main disadvantage of laser ignition is connected with the fact that a blast wave is likely to follow the optical

a)Author to whom correspondence should be addressed: mahamud@tamu.edu

breakdown and a significant amount of energy (around 90%) is consumed by the propagation wave.[11,12] It was also demonstrated that ignition near the lean limit is more difficult due to the high rate of the flame stretch, a phenomenon that is aggravated at low pressures.[13] Dual-pulse laser ignition has been recently proposed as an efficient alternative to single laser pulse ignition.[10] Decoupling of the initial ionization (without breakdown) from the subsequent energy deposition and heating using a dual-pulse laser technique allows tailoring the laser plasma parameters such as electron temperature, electron number density, and a size of the initial ignition kernel. For laser pulses with durations shorter than the avalanche buildup time, such as femtosecond and picosecond laser driven ionization, multiphoton ionization and tunnel ionization are the dominant mechanisms, which help generate well-controlled patterns of ionization. These patterns may be used to localize other energy addition processes for distributed ignition by the second laser pulse or by coupling of microwave energy.[14]

As the strength and the speed of the shock wave depend on the consumed energy, two successive laser pulses with a time interval between them reduce the energy loss by the propagating shock wave compared with a single pulse with the same total incident energy. Although a number of studies have been performed for single laser pulse ignition, the research studies of dual-pulse laser breakdown and ignition are relatively new. Matsuda *et al.*[15] performed experimental studies of dual-pulse laser induced breakdown in quiescent air and indicated that properties of plasmas induced by two successive laser pulses were independent of one another at the repetition frequency of less than 200 Hz. Based on the measurements of the laser energy absorption and flow field, Wermer *et al.*[16] recommended a pulse interval in the range of 250 ns–15 μs for efficient ignition. They have observed the lower energy losses on the shock wave propagation compared with the case of single pulse ignition. Bak *et al.*[17] studied dual-pulse laser induced breakdown in low-speed premixed ethane-air mixtures, and they found that the pulse interval for achieving the laser breakdown was longer than that for the quiescent air. Nakaya *et al.*[18] experimentally studied the flame kernel behavior for the case of dual-pulse laser–spark ignition in the lean methane-air mixture, using a combination of two laser breakdowns. It was shown that for the same discharge energy, dual-pulse laser spark ignition generates a stronger flame kernel compared with the single laser spark.

Dumitrache *et al.*[19] proposed an alternative approach for dual-pulse laser ignition using a combination of the ultraviolet and infrared laser pulses. A first ultraviolet pulse of 266 nm creates a preliminary ionization region through avalanche and multiphoton ionization, and the second near-infrared (NIR) laser pulse of 1024 nm heats the mixture. Their results indicate that such a technique leads to the reduction in the lean limit and to the increase in combustion efficiency. Moreover, the energy required for successful ignition was found to be lower (E = 60 mJ) compared to single laser pulse ignition (E = 75 mJ).[16] Tropina *et al.*[20] studied chemical pathways for dual-pulse laser ignition in the frame of the three-temperature plasma model and 1D approach, taking into account plasma and combustion chemistry. The critical initial concentration of electrons required for successful ignition by dual-pulse laser and the role of photodissociation of fuel molecules as a way to influence the ignition probability have been emphasized. Dumitrache and Yalin[21] investigated the role of hydrodynamics induced by a dual-pulse laser plasma in nitrogen and have shown that the kernel dynamics and the lobe formation depend on overlapping of focal points.

II. NUMERICAL MODEL

A. Formulation of the problem

We consider dual-pulse laser ignition in a quiescent methane-air mixture. Dynamics of the first ultra-violet pulse was not modelled but was taken into account by selecting appropriate initial conditions, as in Ref. 20, which were based on the experimental data of dual-laser pulse ignition by 10 ns 266 nm and 1064 nm pulses.[19] A significant fraction of the laser energy at those conditions is transferred into the vibrational degrees of freedom.[22] Because of the very fast vibrational-translational (VT) relaxation of oxygen, the vibrational energy is mainly stored in nitrogen molecules. At the same time, the energy transfer rate between electrons and vibrationally excited molecules is very high (around several ns[20]). Therefore, we assumed that the electron temperature was constant and its spatio-temporal evolution was not included in the model.

The mathematical model of dual-pulse laser ignition can be written as follows:

$$\frac{\partial \rho}{\partial t} + \nabla \cdot (\rho \bar{v}) = 0, \tag{1}$$

$$\frac{\partial (\rho \bar{v})}{\partial t} + \nabla \cdot (\rho \bar{v} \bar{v}) = -\nabla p + \nabla \cdot \hat{\tau}, \tag{2}$$

$$\frac{\partial (\rho h)}{\partial t} + \frac{\partial}{\partial x_i}(\rho \bar{v} h) + \frac{\partial (\rho K)}{\partial t} + \frac{\partial}{\partial x_i}(\rho \bar{v} K) = \frac{dp}{dt} + \nabla \cdot (\tau \cdot \bar{v}) + \dot{Q} + \beta \dot{Q}_j + \dot{Q}_{VT}, \tag{3}$$

$$\frac{\partial (\rho Y_k)}{\partial t} + \nabla \cdot \left[\rho(\bar{v} + v'_k) Y_k\right] = \dot{\omega}_k, \tag{4}$$

$$\frac{\partial n_j}{\partial t} + \nabla \cdot \bar{\Gamma}_j = \sum_j R_i + R_{av} + R_{mpi} = f(T, Te), \tag{5}$$

$$\frac{\partial (E_v)}{\partial t} + \frac{\partial}{\partial x_i}(E_v \bar{v}) - \frac{\partial}{\partial x_i}\left(D_{N_2} \frac{\partial}{\partial x_i} E_v\right) = (1-\beta)\dot{Q}_j - \dot{Q}_{VT}, \tag{6}$$

$$p = \rho R_u T \sum_{k=1}^{N} \left(\frac{Y_k}{M_k}\right), \quad \bar{\Gamma}_j = (-1)^{j-1} \mu_j \, n_j \bar{E} - D_j \nabla n_j + n_j \bar{v}, \tag{7}$$

$$\tau_{ij} = \mu\left(\frac{\partial v_j}{\partial x_i} + \frac{\partial v_i}{\partial x_j} - \frac{2}{3}\frac{\partial v_k}{\partial x_k}\delta_{ij}\right), \tag{8}$$

$$h = \sum\nolimits_k Y_k \left\{ h_{k,o}(T_{ref}) + \int_{T_{ref}}^{T} C_p(T) dT \right\}, \tag{9}$$

$$\dot{Q}_J = \frac{e^2 n_e I_L (\nu_m + \nu_c)}{\varepsilon_0 c m_e (\omega_L^2 + (\nu_m + \nu_c)^2)}, \quad \dot{Q}_{VT} = \hbar_w \Pi_V + \frac{E_v - E_v^0}{\tau_{VT}}, \tag{10}$$

where ρ is the density, p is the pressure, τ_{ij} is the viscous stress tensor, μ is the dynamic viscosity, h is the mixture enthalpy,

Y_k, M_k are the mass fraction and molecular weight of the k-species, R_u is the universal gas constant, and C_p is the specific heat of the mixture at constant pressure.

In the equations for the mixture enthalpy (3) and vibrational energy E_v, $\dot{Q}$ is the reaction heat, $\dot{Q}_j$ is the joule heating term, Q_{VT} is the vibrational-translational energy exchange term, T_{ref} is the standard temperature, and K is the kinetic energy.

In the equations for mass fractions of neutral gas species (5), v_k' is the diffusion velocity and ω_k is the chemical source term, which includes a k-species production and consumption rate in 325 reactions of the GRI-3.0 mechanism[23] and the low temperature oxidation mechanism of methane.[20] Additional plasma reactions included in the model are presented in Table I. The gas phase species are assumed to follow the ideal gas law. The standard molar specific heat and the standard-state values of the molar enthalpy $H_{k,0}$ at constant pressure for k species have been given as functions of the temperature according to NASA polynomials. We use the Sutherland formula for the mixture viscosity dependence on temperature.

The model includes Eq. (5) for electron and positive ions (O_2^+), where μ_j and D_j are the mobility and diffusion coefficients of positive ions (j = 1) and electrons (j = 2). The source term in Eq. (5) includes the ionization rate by the avalanche ionization R_{av} as well as the ionization rate by the multiphoton ionization, R_{mpi}, calculated as in Ref. 20. In the joule heating term $\dot{Q}_j$ [Eq. (10)], n_e and m_e are the electron number density and mass, I_L is the laser beam intensity, e is the electron charge, ε_0 is the vacuum permittivity, and ν_m, ν_c are the transport frequencies of elastic (electron-neutrals) and Coulomb electron-ion collisions defined as functions of the electron temperature. The absorbed laser energy goes to heating and vibrational excitation depending on the parameter β, reflecting the part of the laser energy, which deposits in the translational degrees of freedom. The value of the parameter β was chosen according to the data of the electromagnetic field energy transferred to the different degrees of freedom and its dependence on the electron energy.[24] At the electron temperature (T_e = 1 eV), most of the energy goes to the vibrational excitation of nitrogen molecules and parameter β = 0.3 and 1 were taken as the baseline condition. We also considered the case of β = 1 and β = 0.8, when the laser energy mainly goes to gas heating, which corresponds to the laser spark case.

Equations (3) and (6) also contain a term Q_{VT} which includes vibrational-translational (VT) relaxation in the Landau-Teller form, describing VT relaxation from the low vibrational levels with the vibrational-relaxation time τ_{VT} and an additional term responsible for the VT relaxation from the higher vibrational levels and the anharmonicity effects.[22]

TABLE I. The set of additional reactions.[33]

	Reaction	k_0 (c^{-1})	n	E_a
1	$e + O_2 \rightarrow 2e + O_2^+$	Reference 22	0	0
2	$e + O_2^+ \rightarrow O + O$	0.599×10^{-4}	1.0	0
3	$O_2^+ + O_2 + e \rightarrow O_2 + O_2$	0.346×10^{-5}	0.5	0
4	$O_2^+ + N_2 + e \rightarrow O_2 + N_2$	0.312×10^{-22}	1.5	0

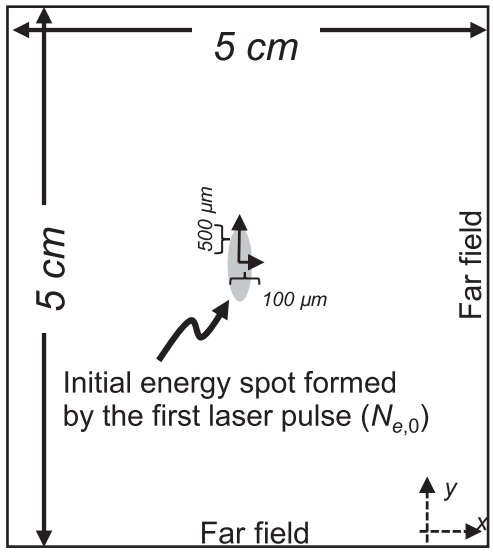

FIG. 1. Schematic diagram of the computational domain for dual-pulse laser ignition.

The schematic of the problem geometry and boundary conditions is presented in Fig. 1. In the far-field region, we assumed zero normal gradient for all variables, except static pressure, which equals to atmospheric pressure. The electron temperature was equal to T_e = 1 eV. Initial vibrational and gas

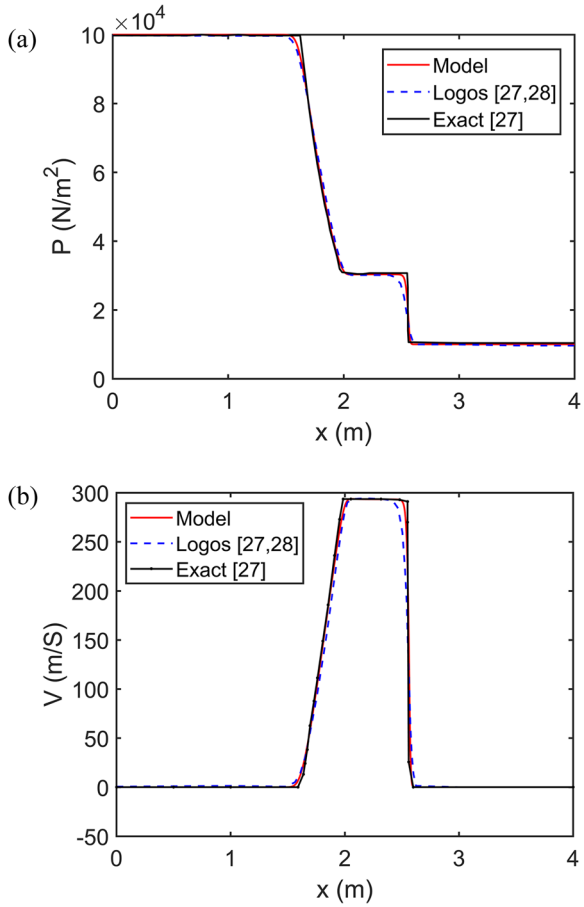

FIG. 2. Comparison of pressure and velocity distribution with the analytical[27] and numerical solutions (LOGOS code[28]) for the one-dimensional Riemann problem: (a) pressure vs distance after 1 ms and (b) velocity vs distance after 1 ms.

TABLE II. Precision tests.

Allowable error, S_{max} (%)	Grid resolution (μm)	Time step size (μs)	Number of time steps	S_{err}	Allowable number of time steps	Reliability, Rs = n_{max}/n
0.01	$15 \times 15 \times 1$	0.01	20 000	5.4×10^{11}	3.4×10^{12}	1.7×10^{08}
0.01	$15 \times 15 \times 1$	0.1	2 000	5.4×10^{11}	3.4×10^{12}	1.7×10^{09}
0.01	$100 \times 100 \times 1$	0.01	20 000	5.4×10^{08}	3.9×10^{07}	1.9×10^{03}
0.01	$100 \times 100 \times 1$	0.1	2 000	5.4×10^{08}	3.9×10^{07}	1.9×10^{04}

temperatures were equal to $T = 500\,^{\circ}$K. Initial conditions for electrons and positive ions have a form

$$n_e = n_e(0)\,\exp\left(-\frac{x^2}{x_{ch}^2} - \frac{y^2}{y_{ch}^2}\right),\quad n_{O_2}^{+} = n_{O_2}^{+}(0)\,\exp\left(-\frac{x^2}{x_{ch}^2} - \frac{y^2}{y_{ch}^2}\right), \tag{11}$$

where $n_e(0)$, $n_{O_2^+}(0)$ are the initial concentrations of electrons and oxygen ions on the axis of the plasma channel and $x_{ch} = 100$ μm and $y_{ch} = 500$ μm are the sizes of the initial ionization region created by the UV pulse. Initial concentrations of electrons on the axis after the UV pulse $n_e(0)$ have been varied and initial concentrations of ions are assumed to be inversely proportional to their ionization potential.

III. MODEL DEVELOPMENT

The system of Eqs. (1)–(6) was solved using a custom made solver on the basis of (Open FOAM) C++ libraries.[26] We use the finite volume method and the PISO (Pressure Implicit Splitting of Operators) algorithm, which includes one predictor and two corrector steps to find the velocity and pressure field. For time discretization, a second order backward Euler scheme was chosen. A second order unbounded scheme that limits toward the upwind scheme in the regions with strong gradients was the main scheme for the advection terms. A second order central difference scheme was used for diffusion terms and mass fluxes. The model includes a Strang splitting algorithm for chemistry terms and a bi-conjugate gradient method. A variable time step was adjusted dynamically to limit the maximum convective Courant-Friedrichs-Lewy (CFL) number to 0.5. The model implements a quadrilateral mesh.

The time range of the ignition problem is below the range of flow instabilities; therefore, the turbulence effects were not considered in this study. The flow dynamics was verified comparing the simulation results with the analytical and numerical

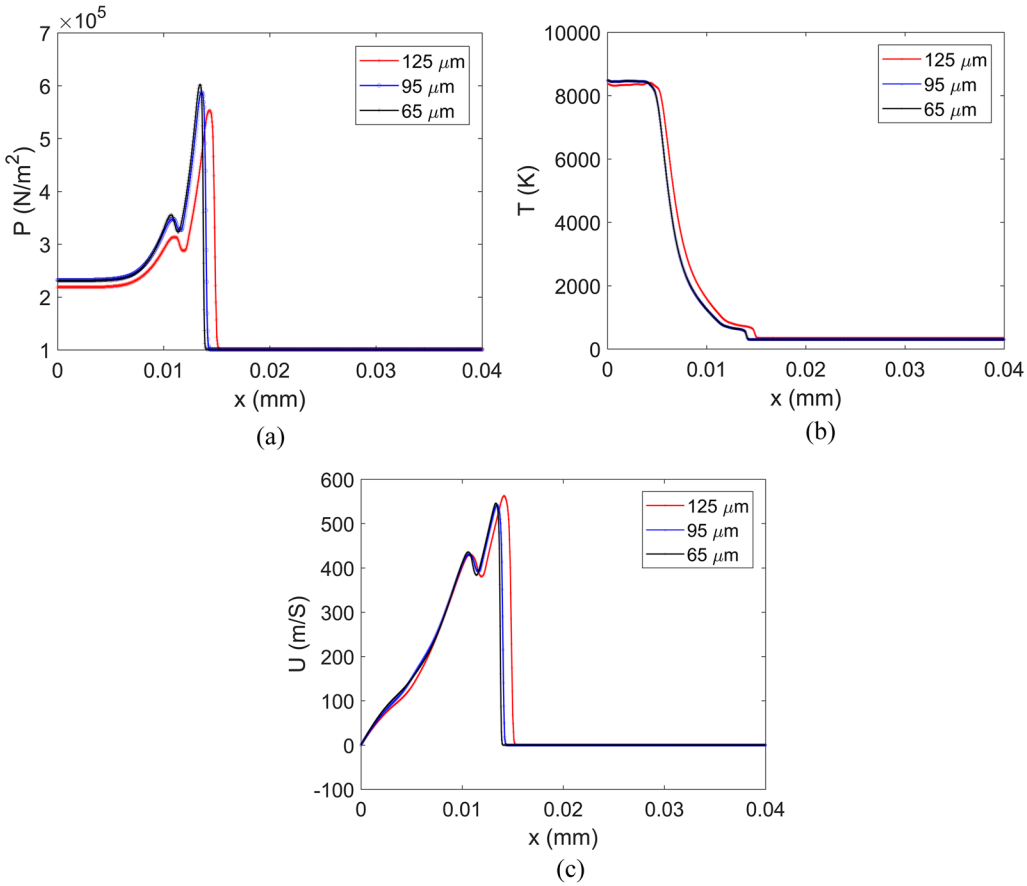

FIG. 3. Test results on the mesh size dependence. Pressure (a), temperature (b), and velocity (c) distribution along the axial direction at t = 9 μs.

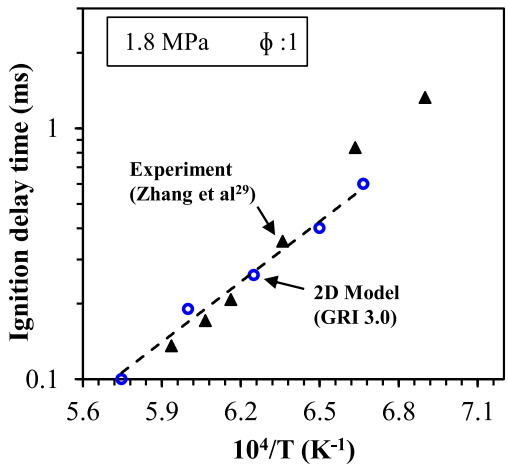

FIG. 4. Effect of the initial temperature on the ignition delay time.

solutions of the one-dimensional Riemann problem. The shock capturing capability of the method is based on the Kurganov-Tadmor scheme. We checked the evolution of the discontinuity in the initial conditions using the same approach as in Refs. 27 and 28. The pressure distribution and velocity distribution after 1 ms are presented in Fig. 2 and showed a good agreement with the analytical and numerical solutions. Thus, we concluded that the current model is capable of predicting sharp pressure gradients, which can appear in the ignition problem solution.

Additional testing of the model was based on the stochastic error evaluation as was discussed in detail by Smirnov *et al.*[27] The total error was described by the summation of relative errors in each direction, and assuming that a maximum allowable error $S_{\max} \approx 0.01\%$ for our simulation, the maximum allowable number of time steps $n_{\max}$ was evaluated as in Ref. 27. Table II shows the results of the error estimation and a significantly low accumulation of the error in our simulation.

IV. RESULTS AND DISCUSSION

For the first step, we considered the ignition of a methane-air mixture by a single laser pulse. We assumed thermal equilibrium after the laser energy deposition and treated it as an initial condition of the problem, modeled by an energy source at the center of a domain that is 5 cm × 5 cm in size (Fig. 1). The energy source is described by a Gaussian function and has an elliptical shape with a peak temperature and pressure of 6000 K and 5 atm, respectively. To choose an appropriate mesh size for the formulated model, calculations have been run for different meshes. A mesh size of ~95 μm was found to

FIG. 5. Experimental[30] and numerical schlieren images at different time (case 1 and 2) and the third lobe (case 3) for 1.5 mm gap size/initial kernel length: (a) experimental results,[30] (b) numerical schlieren of dual pulse laser dynamics in air,[21] (c) our schlieren images for dual pulse laser ignition in the stoichiometric methane-air mixture. Reproduced with permission from Kono *et al.*, "Mechanism of flame kernel formation produced by short duration sparks," Symp. Combust. **22**(1), 1643–1649 (1989). Copyright 1989 Elsevier.

provide a grid independent solution [Figs. 3(a)–3(c)] to capture the shock wave, whereas to capture the electron dynamics, the minimum required value of mesh size was of ~5 μm to keep the Courant number below 1.

For the validation purposes, we compared the calculated ignition delay time (Fig. 4) for the stoichiometric methane-air mixture with the similar experimental results from the work of Zhang *et al.*[29] The ignition criterion was based on the maximum of OH concentration. We found a close agreement between our model and the experimental data observed except a discrepancy at a low temperature region model for the estimation of longer ignition delay time which can be attributed to the boundary effects in the 2D. The model also prescribes well the strong pressure and temperature gradients (T_{shock}/T_{amb} = 1000; P_{shock}/P_{amb} = 22) generated by the source term as well as the experimental tear drop shape temperature lobe and velocity contours observed in Ref. 10.

For dual-pulse laser ignition, a stoichiometric methane-air mixture with the initial electron number density of 1×10^{18} m^{-3}, the electron temperature Te = 1 eV, and a near-infrared laser (NIR) pulse of 20 ns duration and of 20 mJ laser energy, $\beta = 1$ and $\beta = 0.3$ (30% of the energy goes to joule heating) have been chosen as base case 1 and base case 2. Figure 5 shows a comparison between our synthetic schlieren results for base case 1 (c), numerically calculated synthetic schlieren results in air[21] (b), and the experimental results[30] (a) for laser spark ignition in the stoichiometric propane-air mixture. It is seen that at the initial stage (around 25 μs) the kernel dynamics in the fuel-air mixture and in air is similar. Our results also showed a hot-toroidal kernel formation, which matched well with the experimental observation.

We have found that the kernel dynamics depends on the shape and the initial energy deposition created by the first ultraviolet laser pulse. For simplification, we considered the dual-pulse laser energy deposition in air (Fig. 6) to evaluate the effect of the initial energy spot. We observed a toroidal shape kernel structure after 60 μs for both convex and concave energy spots with the uniform initial energy distribution [Figs. 6(a) and 6(b)]. For the convex shape energy spot with a Gaussian distribution in the X-direction, a double horn-shaped temperature lobe [Fig. 6(c)] is formed, caused by the vorticity generation in the vertical direction. For the convex shape energy spot with a Gaussian distribution in both XY directions [Fig. 6(d)], we observed a completely different kernel, connected with the additional significant horizontal recirculation. The secondary horizontal recirculation tends to suppress the temperature kernel growth and shortens the kernel increment rate. Oriented on the experimental observations of the flame

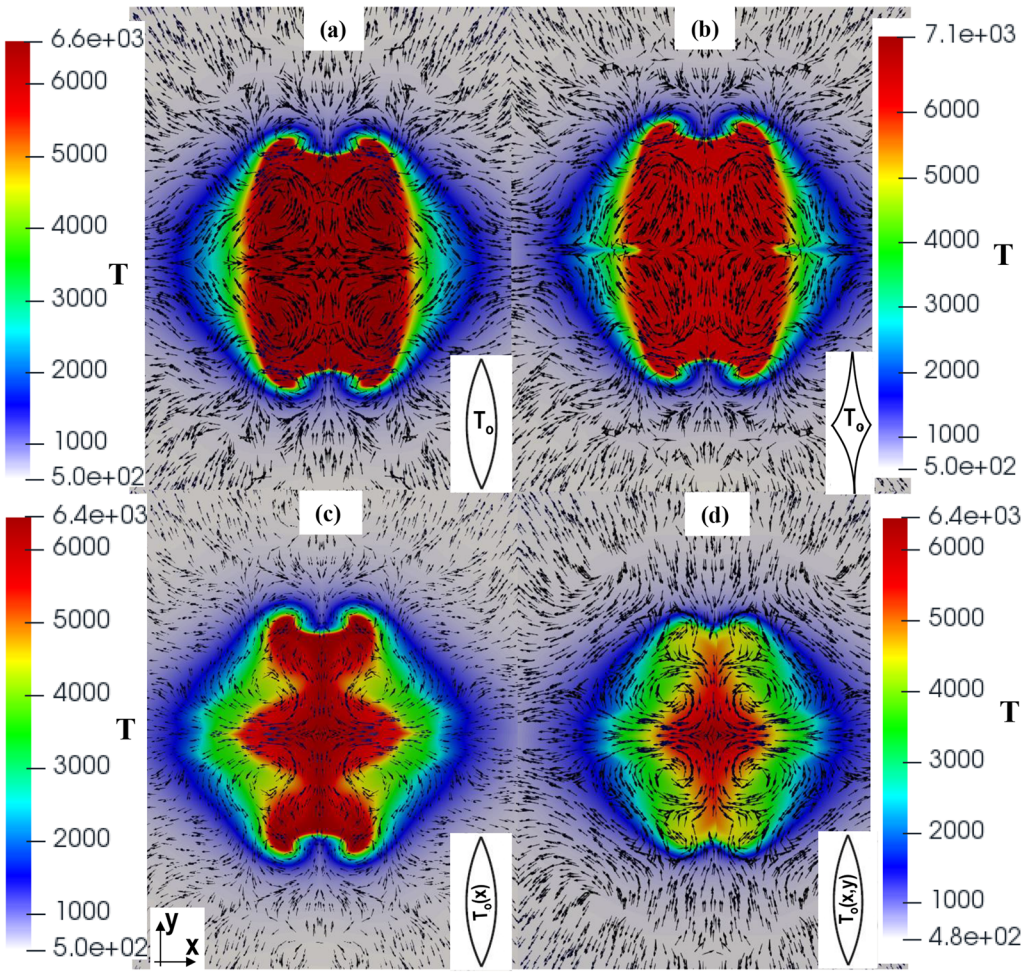

FIG. 6. Temperature and velocity distribution after 60 μs: the initial energy spot is (a) convex and uniform, (b) concave and uniform, (c) convex with Gaussian distribution in the X-direction, (d) convex with Gaussian distribution in both X and Y directions. The size of the pixel image is 2 cm × 2 cm.

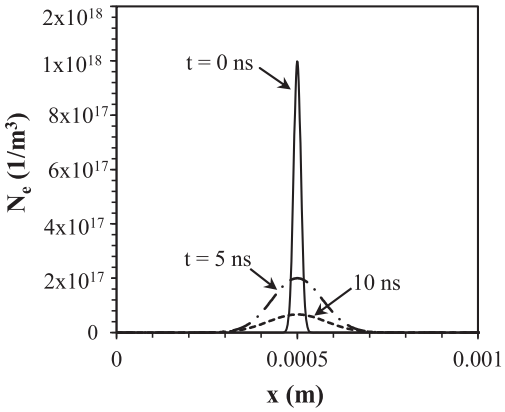

FIG. 7. Electron number density axial profiles: base case 1.

kernel dynamics, the convex initial shape profile after the first laser pulse was chosen as a base case and all the calculations of ignition and flame propagation in the fuel-air mixture were run with the same initial shape profile.

At the same time, temporal dynamics of electrons is mainly controlled by the second NIR laser pulse. It is confirmed by the electron number density axial profiles presented in Fig. 7. We observed a sharp decrease by two orders of magnitude for the electron number density at the first 10 ns. Despite that, a second laser pulse of 20 mJ energy helps sustain a relatively high electron number density to achieve ignition for both stoichiometric and lean ($\Phi = 0.7$) methane-air mixtures. The spatio-temporal flame kernel dynamics for base cases 1 and 2 is presented in Figs. 8–11. We observed different stages of the kernel formation as follows:

- After 20 ns of energy deposition, the ignition kernel still has the same elliptical shape which became millimeter in size (Fig. 8). This shape is directly related to heating caused by the shock wave propagation.
- The initial kernel expands in all directions up to 20 μs when a reverse flow started to form in the top of the kernel. As a result, a toroidal structure of the hot kernel is formed which has a maximum temperature of 3000 K (Fig. 8).
- The reverse flow shrinks the kernel in the vertical direction [Figs. 9(a) and 9(b)] and increases the curvature of the torus structures. As kernel expands in the horizontal direction, the recirculation [Fig. 9(c)] becomes larger and separates the kernel along the horizontal direction.

FIG. 8. Spatial contours of the temperature: base case 1. The size in the pixel is (1×1) cm^2.

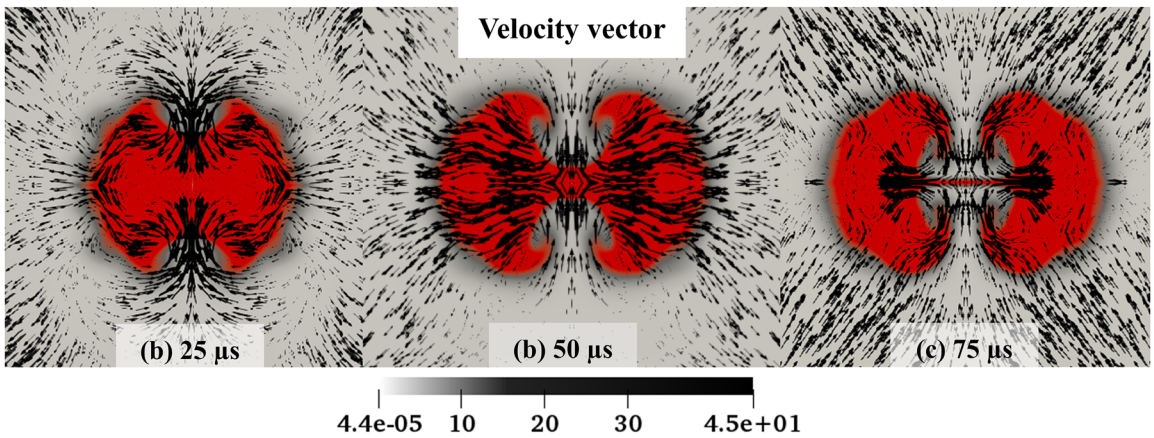

FIG. 9. Velocity vector (with respect to the temperature contour) and streamline profiles for base case 1 with respect to the temperature contour shown in Fig. 8.

FIG. 10. Spatial contours of different species after 60 μs: base case 1.

The recirculation velocity is the maximum around the heated kernel structure that can be attributed to the formation of the toroidal vortex region.

For base case 1, we observed ignition and the flame propagation started at 20 μs, which is confirmed by the CH and OH profiles presented in Fig. 10. For base case 1, the OH profiles presented in Fig. 11 also follow the same spatio-temporal pattern. A relatively early ignition event and the ignition delay time depend on the initial electron number density created by the first UV pulse and on the parameter β reflecting the heating part of the NIR laser pulse energy. Our baseline condition has an electron number density of 10^{18} ($1/m^3$), but ignition was also obtained when the initial electron number density was 10–100 times lower. However, the ignition delay time increases significantly for those conditions as well as for the non-equilibrium case. Table III shows the ignition time delay as a function of the initial electron number density assuming that 80% of the laser energy goes to heating, $\beta = 0.8$. The present results agree with previous experimental and calculation results, showing that we need a certain minimum electron/ion concentration from the first UV pulse to be able to get ignition.

Figure 12 shows the spatio-temporal profiles of the flame kernel for three different equivalence ratios (only for ignition cases) for base case 2 with vibrational non-equilibrium. It is seen for both lean and rich mixtures that OH concentration is smaller than for the stoichiometric case and the spatio-temporal kernel dynamics is slightly different compared to base case 1 (Fig. 11) due to the effect of vibrational

FIG. 11. Spatial-temporal contours of the OH formation: base case 1 ($\beta = 1$). The size in the pixel is (1×1) cm^2.

TABLE III. Ignition time delay, τ, as a function of the initial electron number density.

n_{e0}	T_{max} after 2 μs	τ (μs)
1×10^{18}	3000	130
5×10^{17}	3000	160
1×10^{17}	2000	240
1×10^{16}	500	...

non-equilibrium. Our analysis suggests that the observed difference in the ignition kernel dynamics is associated with the vibrational-translational relaxation and diffusion processes included in the vibrational energy conservation equation.

Figure 13 shows the variation of the flame kernel structure due to the change in the laser intensity or due to the change of the focal point of the second pulse. We considered 100% and 5% of the initial laser energy contributed to joule heating. As a result, after the same period of time at the 5% of the laser energy going to joule heating, a significantly lower temperature and a smaller kernel radius are observed. Due to the absence of the strong recirculation caused by the sharp temperature gradient, the kernel shape also changes. To take into account changes in the focal points by two laser pulses, we consider the case when the peak on the initial Gaussian profile of the electron number density moves 100 μm in the vertical direction. Because maximum joule heating is directly related to the maximum electron number density, when there

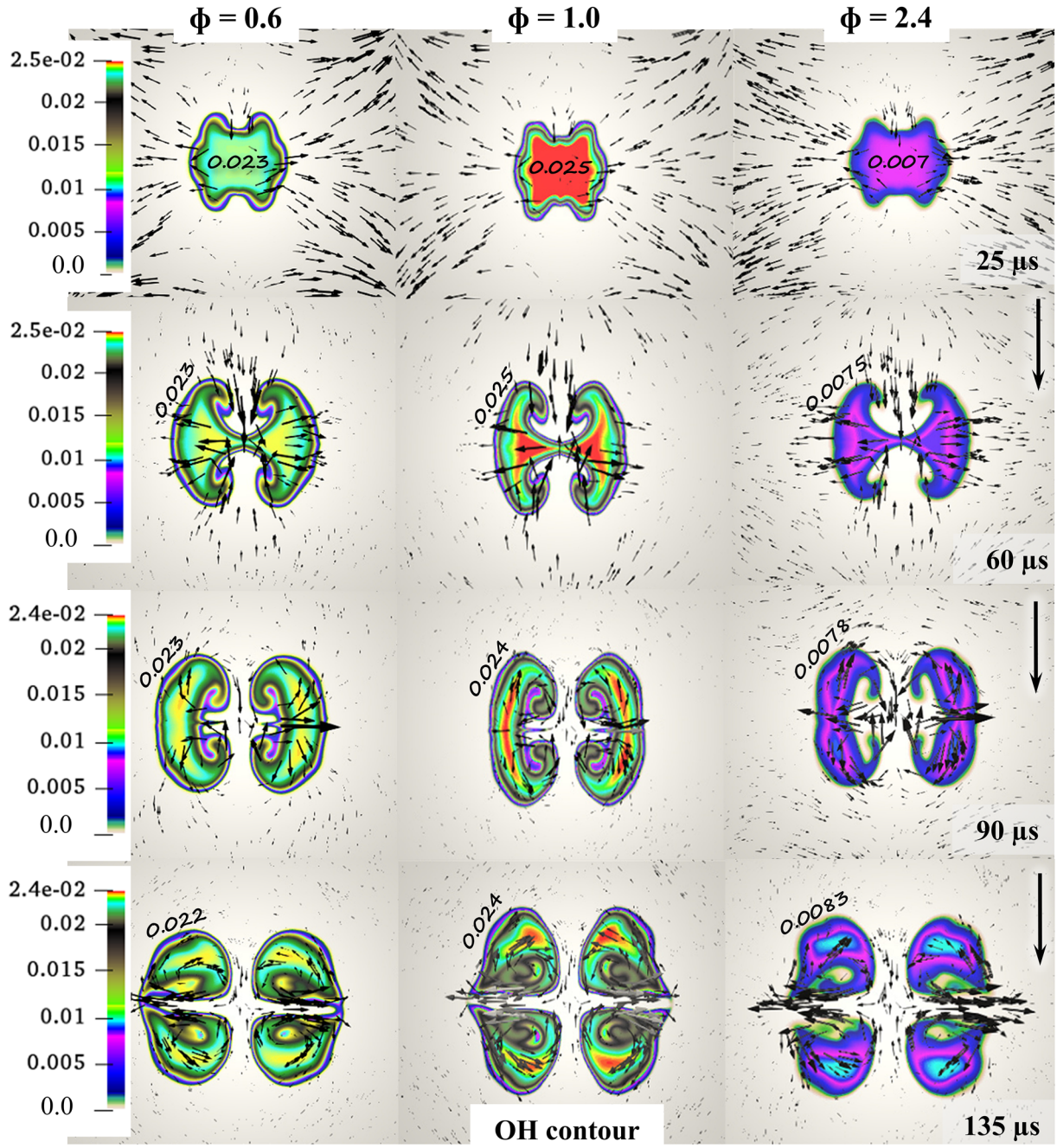

FIG. 12. Spatial-temporal contours of the OH formation: base case 2 (β = 0.3). The size in the pixel is (1 × 1) cm^2.

FIG. 13. Spatial contours of the temperature after 30 μs: (a) base case 1, β = 1; (b) β = 0.05; (c) base case 1, β = 1 but the maximum electron number density is with the 100 μm offset in the vertical direction.

is an offset to the center, we observed an asymmetric kernel formation with the smaller increment of the kernel temperature and kernel radius. In addition, the kernel expands more in the vertical direction and splits out in the earlier time, leading to the flame extinguishment later on. The last result showed some discrepancy with the experimental data observed. The explanation of that discrepancy could be connected with the influence of additional chemical reactions, electron temperature change, and turbulence effects, which are not included in the model.[34,35]

V. CONCLUSIONS

Ignition kernel dynamics for a case of dual-pulse laser ignition was studied using a 2D numerical model including vibrational non-equilibrium. The model was validated with the available experimental and calculation data. The analysis of the spatio-temporal dynamics of temperature and OH profiles has shown that the physical mechanism controlling dual-pulse laser ignition is similar to the case of laser spark ignition. Even though the main ignition mechanism is thermal, the energy deposition by a first ultraviolet laser pulse gives the option to control the kernel growth, shape, and ignition delay time. The results suggest that the kernel dynamics and ignition delay time are also affected by the laser intensity, vibrational-translational relaxation, electron number density after the UV pulse, and change of the laser focal point. The last factor was found to have a negative effect on the flame propagation and, for the case modeled, the flame extinguished after the early split up of the ignition kernel. For the high initial degree of ionization, we have obtained ignition of the lean methane–air mixture with the equivalence ratio of 0.6 which offers favorable conditions for dual-pulse laser ignition. The kernel growth and dynamics are slower for the nonequilbium case, which leads to the significant increase in the ignition delay time. We suggested that the ignition delay time can be modulated by the change in the UV laser pulse intensity (in our case by the change in the initial electron number density), time delay between pulses and the near-infrared laser pulse intensity (in our case by the change in the electron temperature and parameter β).[25,31,32]

ACKNOWLEDGMENTS

This work has been supported by internal funds of Texas A&M University and by the DOD-AFOSR award under Subcontract with Princeton University SUB0000242.

[1] P. D. Ronney, "Laser versus conventional ignition of flames," Opt. Eng. **33**(2), 510 (1994).
[2] H. Kopecek *et al.*, "Laser ignition of methane-air mixtures at high pressures and diagnostics," J. Eng. Gas Turbines Power **127**(1), 213 (2005).
[3] S. A. O'Briant, S. B. Gupta, and S. S. Vasu, "Review: Laser ignition for aerospace propulsion," Propuls. Power Res. **5**(1), 1–21 (2016).
[4] A. A. Tropina, M. N. Shneider, and R. B. Miles, "Ignition by short duration, nonequilibrium plasma: Basic concepts and applications in internal combustion engines," Combust. Sci. Technol. **188**(6), 831–852 (2016).
[5] L. V. Keldysh, "Ionization in the field of a strong electromagnetic wave," Sov. Phys. JETP **47**, 1945–1957 (1964).
[6] F. Anabitarte, A. Cobo, and J. M. Lopez-Higuera, "Laser-induced breakdown spectroscopy: Fundamentals, applications, and challenges," ISRN Spectroscopy, **2012**, 285240.
[7] Y. Zhang, G. Xiong, S. Li, Z. Dong, S. G. Buckley, and S. D. Tse, "Novel low-intensity phase-selective laser-induced breakdown spectroscopy of TiO_2 nanoparticle aerosols during flame synthesis," Combust. Flame **160**(3), 725–733 (2013).
[8] H. Steiner, W. Gretler, and T. Hirschler, "Numerical solution for spherical laser-driven shock waves," Shock Waves **8**(3), 139–147 (1998).
[9] Z. Jiang, K. Takayama, K. P. B. Moosad, O. Onodera, and M. Sun, "Numerical and experimental study of a micro-blast wave generated by pulsed-laser beam focusing," Shock Waves **8**(6), 337–349 (1998).
[10] S. Ghosh and K. Mahesh, "Numerical simulation of laser induced breakdown in air," in *46th AIAA Aerospace Sciences Meeting and Exhibit* (AIAA, 2008), p. 1069.
[11] T. X. Phuoc and F. P. White, "An optical and spectroscopic study of laser-induced sparks to determine available ignition energy," Proc. Combust. Inst. **29**(2), 1621–1628 (2002).
[12] C. Dumitrache, C. M. Limbach, and A. P. Yalin, "Laser thermal ignition using a dual-pulse approach," in *54th AIAA Aerospace Sciences Meeting* (AIAA, 2016), p. 0460.
[13] D. Bradley, C. G. W. Sheppard, I. M. Suardjaja, and R. Woolley, "Fundamentals of high-energy spark ignition with lasers," Combust. Flame **138**(1-2), 55–77 (2004).
[14] J. B. Michael, A. Dogariu, M. N. Shneider, and R. B. Miles, "Subcritical microwave coupling to femtosecond and picosecond laser ionization for

localized, multipoint ignition of methane/air mixtures," J. Appl. Phys. **108**, 093308 (2010).
[15]A. Matsuda, Y. Sekiya, R. Rosli, T. Sakai, and A. Sasoh, "Plasma behavior induced by repetitive laser pulses," in 39th Plasmadynamics and Lasers Conference, 2008, p. 3898.
[16]L. Wermer, S. Im, and M. Soo Bak, "Schlieren imaging investigation of successive laser-induced breakdowns in air," in *54th AIAA Aerospace Sciences Meeting* (AIAA, 2016), p. 0458.
[17]M. S. Bak, L. Wermer, and S. Im, "Schlieren imaging investigation of successive laser-induced breakdowns in atmospheric-pressure air," J. Phys. D: Appl. Phys. **48**(48), 485203 (2015).
[18]S. Nakaya, S. Iseki, X. Gu, Y. Kobayashi, and M. Tsue, "Flame kernel formation behaviors in close dual-point laser breakdown spark ignition for lean methane/air mixtures," Proc. Combust. Inst. **36**(3), 3441–3449 (2017).
[19]C. Dumitrache, R. VanOsdol, C. M. Limbach, and A. P. Yalin, "Control of early flame kernel growth by multi-wavelength laser pulses for enhanced ignition," Sci. Rep. **7**(1), 10239 (2017).
[20]A. A. Tropina, R. B. Miles, and M. N. Shneider, "Mathematical model of dual-pulse laser ignition," J. Propul. Power **34**(2), 408–414 (2018).
[21]C. Dumitrache and A. Yalin, "Numerical modeling of the hydrodynamics induced by dual-pulse laser plasma," in *2018 AIAA Aerospace Sciences Meeting, AIAA SciTech Forum* (AIAA, 2018), p. 0689.
[22]M. N. Shneider, M. S. Mokrov, and G. M. Milikh, "Dynamic contraction of the positive column of a self-sustained glow discharge in air flow," Phys. Plasmas **21**, 032122 (2014).
[23]G. P. Smith, "GRI-Mech 3.0," http://www.me.berkley.edu/gri_mech/, 1999.
[24]Y. P. Raizer, *Gas Discharge Physics* (Springer, Berlin, Heidelberg, 1991).
[25]A. P. Yalin, N. Wilvert, C. Dumitrache, S. Joshi, and M. N. Shneider, "Laser plasma formation assisted by ultraviolet pre-ionization," Phys. Plasmas, **21**(10), 103511 (2014).
[26]C. J. Greenshields, *OpenFOAM User Guide, Version 5* (The OpenFOAM Foundation, 2017).
[27]N. N. Smirnov, V. B. Betelin, R. M. Shagaliev, V. F. Nikitin, I. M. Belyakov, Y. N. Deryuguin, S. V. Aksenov, and D. A. Korchazhkin, "Hydrogen fuel rocket engines simulation using LOGOS code," Int. J. Hydrogen Energy **39**, 10748–10756 (2014).
[28]N. N. Smirnov, V. B. Betelin, R. M. Shagaliev, V. F. Nikitin, L. I. Stamov, and D. I. Altoukhov, "Accumulation of errors in numerical simulations of chemically reacting gas dynamics," Acta Astronautica **117**, 338–355 (2015).
[29]Y. Zhang, X. Jiang, L. Wei, J. Zhang, C. Tang, and Z. Huang, "Experimental and modeling study on auto-ignition characteristics of methane/hydrogen blends under engine relevant pressure," Int. J. Hydrogen Energy **37**(24), 19168–19176 (2012).
[30]M. Kono, K. Niu, T. Tsukamoto, and Y. Ujiie, "Mechanism of flame kernel formation produced by short duration sparks," Symp. Combust. **22**(1), 1643–1649 (1989).
[31]L. Wermer, J. Hansson, and S. Im, "Dual-pulse laser-induced spark ignition and flame propagation of a methane diffusion jet flame," Proc. Combust. Inst. **36**(3), 4427–4434 (2017).
[32]M. N. Shneider and R. B. Miles, "Laser induced avalanche ionization in gases or gas mixtures with resonantly enhanced multiphoton ionization or femtosecond laser pulse pre-ionization," Phys. Plasmas **19**, 083508 (2012).
[33]M. N. Shneider, A. M. Zheltikov, and R. B. Miles, "Tailoring the air plasma with a double laser pulse," Phys. Plasmas **18**(6), 063509 (2011).
[34]L. Cifuentes, C. Dopazo, A. Sandeep, N. Chakraborty, and A. Kempf, "Analysis of flame curvature evolution in a turbulent premixed bluff body burner," Phys. Fluids **30**, 095101 (2018).
[35]G. O. Erol, J. Hasslberger, M. Klein, and N. Chakraborty, "A direct numerical simulation analysis of spherically expanding turbulent flames in fuel droplet-mists for an overall equivalence ratio of unity," Phys. Fluids **30**, 086104 (2018).

AIAA SciTech Forum
7-11 January 2019, San Diego, California
AIAA Scitech 2019 Forum

10.2514/6.2019-0741

Modeling of dual-pulse laser ignition in a turbulent flow

A.A. Tropina[1], R.Mahamud[2], M.N. Shneider[3], R.B. Miles[4]
[1,2,4]*Texas A&M University, Aerospace Department, College Station, TX 77840*
[3]*Princeton University, Mechanical and Aerospace Department, Princeton, 08540*

We presented a mathematical model of dual-pulse laser ignition in a turbulent flow taking into account detailed combustion chemistry and non-equilibrium plasma dynamics in a frame of a three-temperature plasma model. To account for turbulence we use four semi-empirical models: $k-\varepsilon$ model, RNG $k-\varepsilon$ model and $k-\omega$ SST model. Preliminary results showed a possibility of reliable laser ignition in a turbulent flow using a dual-pulse approach. We have found that to get a better ignition probability in a turbulent flow we need to increase the initial number density of electrons seeded by the first ultra-violet pulse.

I. Nomenclature

I_L = laser beam intensity
K = kinetic energy
T_{ref} = reference temperature
P = pressure
τ_{ij} = viscous stress tensor
h = mixture enthalpy
Y_k = mixture enthalpy
M_k = molecular weight
R_u = universal gas constant
C_p = specific heat
$\dot{Q}$ = heat of reaction
$\dot{Q}_j$ = joule heating
Q_{VT} = vibrational-translational (V-T) energy exchange term
m_e = electron mass
n_e = electron number density
ω_k = chemical source term
ε_0 = the vacuum permittivity
R_{av} = avalanche ionization term
R_{av} = ionization rate by the multiphoton ionization
τ_{VT} = VT-relaxation time
v_k' = diffusion velocity
ν_T = turbulent viscosity
ν_m = transport frequency of elastic collisions
k = turbulent kinetic energy
ε = dissipation rate
ω = specific dissipation rate
L = reference length scale
I = laser intensity
μ_{eff} = effective viscosity
Π_v = VT relaxation term from the higher vibrational levels
E_v = non-equilibrium vibrational energy per molecule
E_v^0 = thermal equilibrium vibrational energy per molecule
$\hbar w$ =0.29 eV, the vibrational quanta of nitrogen
T_v = vibrational temperature
ν_c = transport frequency of Coulomb collisions

[1] Research Professor, Aerospace Engineering, AIAA Associate Fellow
[2] Postdoctoral Researcher, Aerospace Engineering, AIAA member
[3]Senior Research Scholar, Mechanical and Aerospace Engineering, AIAA Associate Fellow
[4] TEES Eminent Professor, Aerospace Engineering, AIAA Fellow

II. Introduction

Laser ignition has attracted considerable attention recently connected with its unique possibilities to locate ignition at any point inside the combustion chamber, the absence of electrodes and an increase of the ignition probability especially of lean mixtures [1-3]. At the same time one of the main disadvantages of laser ignition is the formation of the strong shock wave and losses of energy associated with high temperature spark related phenomena. A novel concept of ignition by the dual-pulse laser method [4-7] helps to avoid such losses. A main idea is to divide the ignition process by the laser plasma in two stages. The first step is to create a preliminary ionization region using the ultra-violet (UV) or high intensity, short time duration laser pulse with a small amount of energy below breakdown by multiphoton and avalanche ionization mechanisms [8]. The second step is subsequent energy addition through joule heating using a much higher energy near infrared (NIR) laser pulse. The duration of the second pulse varies between 10 and 20 ns with a total consumed energy of 20-40 mJ, which is enough to achieve ignition and to avoid energy losses connected with the strong blast wave formation [4,5]. The combination of two subsequent laser sparks [9] is an alternative approach for dual-pulse laser ignition. Experiments exploring the concept of dual-pulse laser ignition by UV and NIR laser pulses were conducted in the absence of a gas flow, so the question of dual-pulse laser ignition in a turbulent flow is still open. In our previous work [10] we presented and validated a mathematical model of dual-pulse laser ignition in a quiescent methane-air mixture, showing the influence of vibrational non-equilibrium and non-uniformity of the initial electron density distribution on the ignition kernel development.

As has been discussed in the literature, under equilibrium conditions the kernel size for a spark ignition is a strong function of time, and an ignition kernel forms a very stable structure [11]. At the early time of ignition and flame propagation, the kernel structure practically is not influenced by the turbulent fluctuations except in the case of very strong turbulence, which can lead to flame extinction. Jarzy et. al [12] have suggested that the generation of a uniform, small scale turbulence flow field near the ignition point can improve the reliability of ignition. For non-equilibrium plasma assisted ignition, this phenomenon can be slightly altered, as the energy deposition dynamics is different [10]. This paper presents a first attempt to explore the concept of dual-pulse laser ignition in a turbulent flow using numerical modeling.

III. Mathematical model

We considered a planar channel turbulent flow of premixed methane-air with inflow Reynolds numbers Re=2000-5000. The turbulent flow and subsequent ignition are described by the two-dimensional Reynolds-averaged Navier-Stokes equations. Ignition and combustion reaction schemes are taken from [7,10]. Appropriate initial conditions for electrons and ions at t=0 reflect dynamics of the first laser pulse. To model turbulence the model additionally includes equations of the standard semi-empirical models of turbulence. We use several turbulence models including the standard $k-\varepsilon$ model; the Renormalization $k-\varepsilon$ model and SST $k-\omega$ model. Initial conditions for the flow simulation are based on the solution for the non-reacting mixture turbulent flow in a two-dimensional channel geometry.

We investigate ignition of the multi-component methane-air mixture at the turbulent Prandtl number Pr_t=0.9 and Lewis numbers Le=1 for all species assuming that turbulent diffusion coefficients are the same for all components. The mathematical model of the problem in a frame of the three-temperature plasma model is as follows

$$\frac{\partial \rho}{\partial t} + \nabla.(\rho \bar{v}) = 0 \tag{1}$$

$$\frac{\partial (\rho \bar{v})}{\partial t} + \nabla.(\rho \overline{vv}) = -\nabla p + \nabla \cdot \hat{\tau} \tag{2}$$

$$\frac{\partial (\rho h)}{\partial t} + \frac{\partial}{\partial x_i}(\rho \bar{v} h) + \frac{\partial (\rho K)}{\partial t} + \frac{\partial}{\partial x_i}(\rho \bar{v} K) = \frac{dp}{dt} + \nabla.(\tau.\bar{v}) + \dot{Q} + \dot{Q}_{VT} + \dot{Q}_{TE} \tag{3}$$

$$\frac{\partial (\rho Y_k)}{\partial t} + \nabla.\left[\rho(\bar{v} + v_k^{'})Y_k\right] = \dot{\omega}_k \tag{4}$$

$$\frac{\partial n_j}{\partial t} + \nabla.\,\bar{\Gamma}_j = \sum_j R_i + R_{av} + R_{mpi} = f(T, Te)\,, \tag{5}$$

$$\frac{\partial(E_v)}{\partial t}+\frac{\partial}{\partial x_i}(E_v\bar{v})-\frac{\partial}{\partial x_i}(D_{N_2}\frac{\partial}{\partial x_i}E_v)=\dot{Q}_{VE}-\dot{Q}_{VT} \tag{6}$$

$$\frac{\partial}{\partial t}(\frac{3}{2}kn_eT_e)+\frac{\partial}{\partial x_i}(\frac{5}{2}\Gamma_e kT_e)=\dot{Q}_j-\dot{Q}_{VE}-\dot{Q}_{TE} \tag{7}$$

$$p=\rho R_u T\sum_{k=1}^{N}\left(\frac{Y_k}{M_k}\right),\ \bar{\Gamma}_j=(-1)^{j-1}\mu_j\ n_j\bar{E}-D_j\nabla n_j+n_j\bar{v} \tag{9}$$

$$\tau_{ij}=\mu(\frac{\partial v_j}{\partial x_i}+\frac{\partial v_i}{\partial x_j}-\frac{2}{3}\frac{\partial v_k}{\partial x_k}\delta_{ij}) \tag{10}$$

$$h=\sum_k Y_k\left\{h_{k,o}(T_{ref})+\int_{T_{ref}}^{T}C_p(T)dT\right\} \tag{11}$$

$$\dot{Q}_J=\frac{e^2n_eI_L(\nu_m+\nu_c)}{\varepsilon_0 cm_e(\omega_L^2+(\nu_m+\nu_c)^2)},\ \ \dot{Q}_{VT}=\hbar_w\Pi_V+\frac{E_v-E_v^0}{\tau_{VT}}; \tag{12}$$

$$E_v=x_{N_2}.N\hbar w/(exp\left(\frac{\hbar w}{k_BT_v}\right)-1); \tag{13}$$

$$E_v^0=x_{N_2}.N\hbar w/(exp\left(\frac{\hbar w}{k_BT}\right)-1). \tag{14}$$

The chemical source term, which includes a k-species production and consumption rate in 325 reactions of the GRI-3.0 mechanism and the low temperature oxidation mechanism of methane is the same as in our earlier work [10]. The source term in Eq. (5) for electrons and positive ions includes the ionization rate by avalanche ionization R_{av} as well as the ionization rate by multiphoton ionization R_{mpi} and additional plasma reactions as in [7]. The gas phase species are assumed to follow the ideal gas law. The absorbed laser energy goes to heating and vibrational excitation according to the data of the electromagnetic field energy transferred to the different degrees of freedom and its dependence on the electron energy [13]. Vibrational-translational relaxation term (12) includes vibrational-translational (VT) relaxation in the Landau-Teller form, describing VT relaxation from the low vibrational levels with the vibrational-relaxation time τ_{VT} and an additional term Π_v responsible for the VT relaxation from the higher vibrational levels and the anharmonicity effects as in [14]. Dynamics of the first ultra-violet pulse was not modelled as in [10] but was taken into account by selecting initial conditions for the electron and positive ions number density in the initial ionization region of the convex shape (Fig.1).

A stress tensor in Eq. (2) includes laminar and turbulent parts, where the turbulent viscosity was evaluated based on the choice of the turbulent model. At this stage of the model development turbulence effects on the chemical reactions rates were neglected and the model includes laminar reaction rates. Thus, we assumed that the reaction rates of plasma and combustion reactions do not depend on the local turbulence intensity, which is valid for relatively fast chemical reactions. Figure 1 presents the schematic of the problem geometry and boundary conditions.

IV. Numerical model

The system of non-stationary RANS equations is solved using a custom made solver based on Open FOAM C++ libraries [15]. We use a finite volume method and the PISO (Pressure Implicit Splitting of Operators) algorithm, which includes one predictor and two corrector steps to find the velocity and pressure fields. For time integration, a second order backward Euler scheme is chosen. A second order unbounded scheme that limits towards upwind scheme in the

regions with strong gradients is a primary scheme for the advection terms. A second order central difference scheme is used for diffusion terms and mass fluxes. The model includes a Strang splitting algorithm for chemistry terms and bi-conjugate gradient method. A variable time step is adjusted dynamically to limit the maximum convective CFL number to 0.5. A code developed in [10] for dual-pulse laser ignition in a quiescent methane-air mixture has been verified by comparison the simulation results with the analytical and numerical solutions and experimental data to check the grid independence, the shock capturing capability and the low accumulation of the error in our simulations. A validation of the ignition and the three-temperature plasma models has been carried out by the comparison of the calculated ignition delay time, ignition kernel dynamics, and numerical shlieren images with the available experimental data. To model dual-pulse laser ignition in a turbulent flow we include semi-empirical turbulent models.

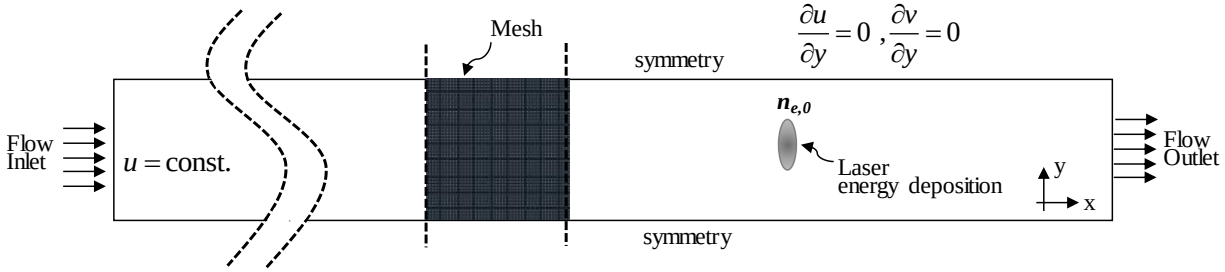

Figure. 1: Schematic of the problem geometry.

V. Results and Discussions

To validate a turbulent part of the model we performed calculations for a standard backward step facing geometry. The mean stream wise velocity profiles in the inlet, recirculation region and attached flow region are compared with the available experimental data [16] and the results are shown in Fig. 2. All the RANS models match well with the experimental data. The $k-\varepsilon$ model was found to be better than other models in the downstream region.

Simulation results of dual-pulse laser ignition for a case of the $k-\varepsilon$ turbulence model are presented in Fig.3-6. We considered a near-infrared laser (NIR) pulse of 20 ns duration and of 20 mJ laser energy. Figure 3 shows the ignition kernel structure and the selected species contours at t=5 ms at the inflow Reynolds number $Re = 2 \cdot 10^4$ and the initial electron number density $n_e^0 = 10^{17}\ m^{-3}$. It is seen, that at such an inflow velocity and preliminary ionization conditions the flow penetrates into the initial plasma spot and creates a recirculation region behind the kernel. The ignition kernel grows with time that proves a successful ignition event but compared with ignition in a quiescent methane-air mixture we do not observe a separation of the kernel (Fig.4).

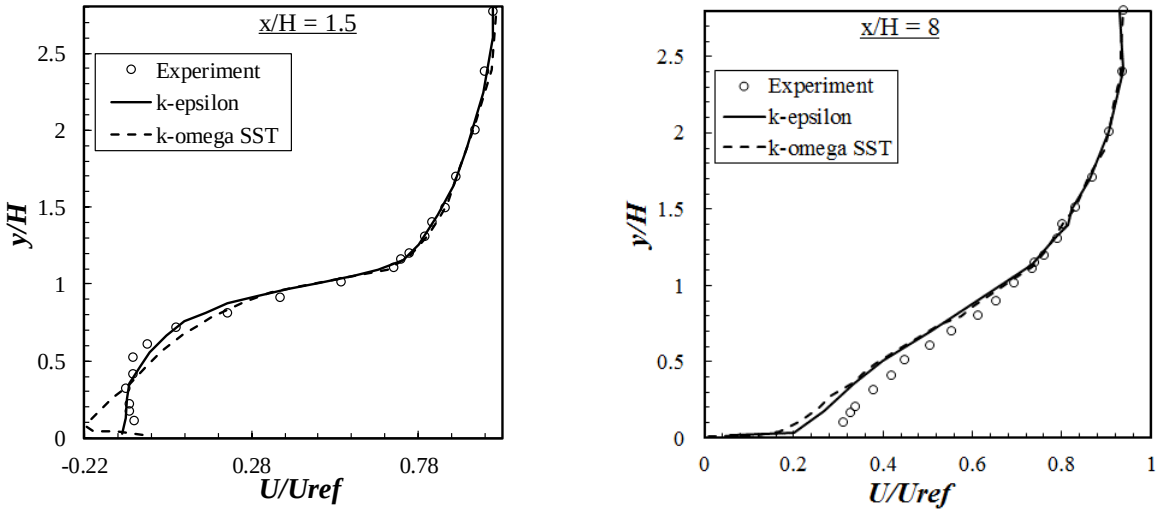

Figure. 2: The velocity profiles at different cross-sections for different turbulence models, $Re = 3 \cdot 10^4$.

To understand the dynamics of the ignition kernel in a turbulent flow Figure 4 presents a time resolved structure of the kernel during the early time of ignition. As can be observed, when the temperature of the core is high enough the flow tends to pass over the kernel followed by a recirculation region behind the kernel. At a later time, the kernel is swept away by the flow and if a flow velocity is high enough and the initial electron number density is below $n_e^0 = 10^{17}\ m^{-3}$ ignition is not observed. Thus to get a better ignition probability in a turbulent flow we need to increase a number density of electrons seeded by the first UV pulse.

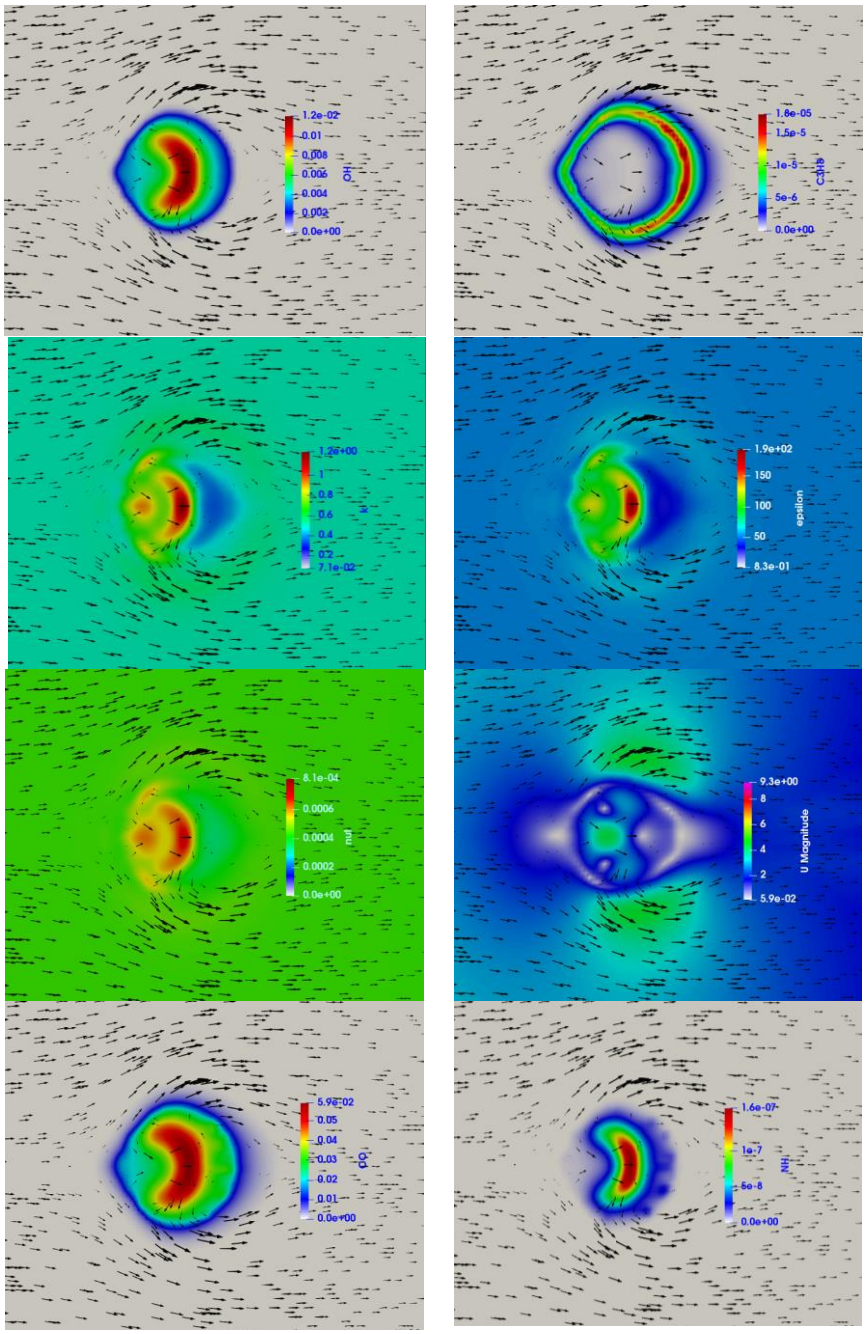

Figure 3: The ignition kernel structure and selected species contours after 5 ms at $Re = 2 \cdot 10^4$, the $k-\varepsilon$ turbulence model.

Figure 5(a) shows the centerline gas temperature profile (x=0) for three different flow regimes at time t=10 ns so during the NIR laser pulse energy deposition. The gas temperature in the core of the channel at this early time does not change significantly between the case of the turbulent flow(RNG-k-epsilon model) and the case of the laser energy deposition in a quiescent methane-air mixture. Because the Reynolds number was the same $Re = 5 \cdot 10^3$ for both laminar and turbulent flow, results for the laminar flow are inconsistent with the flow physics. The spatial distribution of the electron number density at time t=20 ns is showed in Figure 5(b) with the flow velocity field under such conditions. The flow tends to pass over the plasma kernel due to the strong shock wave generation.

If the initial number density of electrons formed by the first ultra-violet pulse becomes higher, the dynamics of the plasma kernel interaction with the flow is changed. Stronger shockwave and joule heating created by the second near-infrared laser pulse leads to more stable kernel structure at the early time of ignition, when the incoming flow does not penetrate inside the kernel (Fig.6.b). The kernel diameter increases with time, indicating a successful ignition event. In addition, the kernel diameter increases with the initial electron number density (Figure 7).

We also considered an interaction of the dual-pulse laser pulse with incoming turbulent flow. Figure 8 shows the formed flow field nearby the ignition kernel with the initial number density of electrons $n_e^0 = 10^{17}\ m^{-3}$ and $Re = 8 \cdot 10^4$. The flow pattern is quite similar; however, the RNG- $k-\varepsilon$ model predicts slightly higher velocity at the wake of the kernel compared to the k-omega SST model.

Analyzing the influence of the Reynolds number on ignition kernel dynamics, we can summarize that for the low Reynolds numbers, the kernel structure formed by dual-laser pulse is very stable and similar to that in a quiescent methane-air mixture. At high Reynolds numbers, the flow swept away the ignition kernel and the structure and shape of the kernel is changed compared with the case of ignition in a quiescent mixture (Fig.9,10). Oriented on the OH profiles estimated ignition delay time for the problem was around 120 μs.

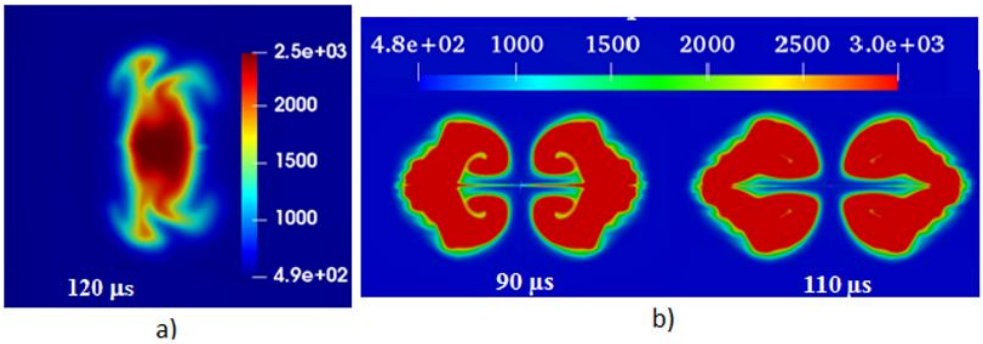

Figure 4: The ignition kernel shape: a) turbulent flow, $Re = 6.5 \cdot 10^4$; b) quiescent methane-air mixture.

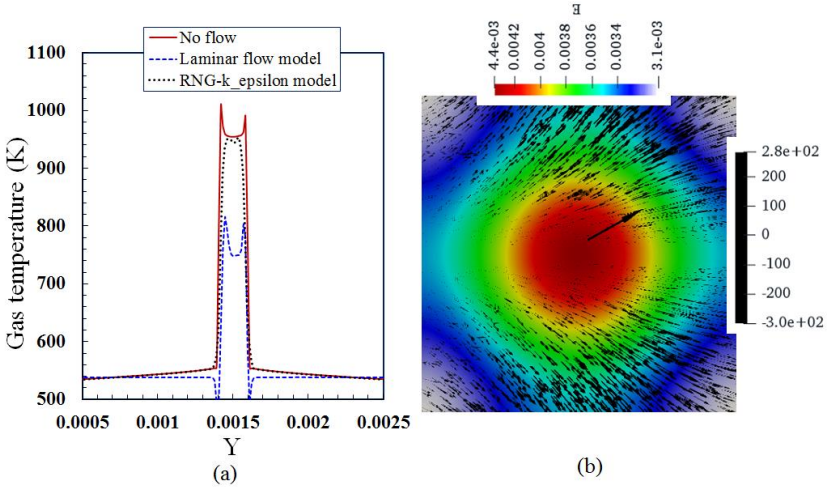

Figure 5: (a) The gas temperature profile at x=0 after 10 ns of the NIR laser pulse energy deposition; (b) The electron number density and the velocity vectors.

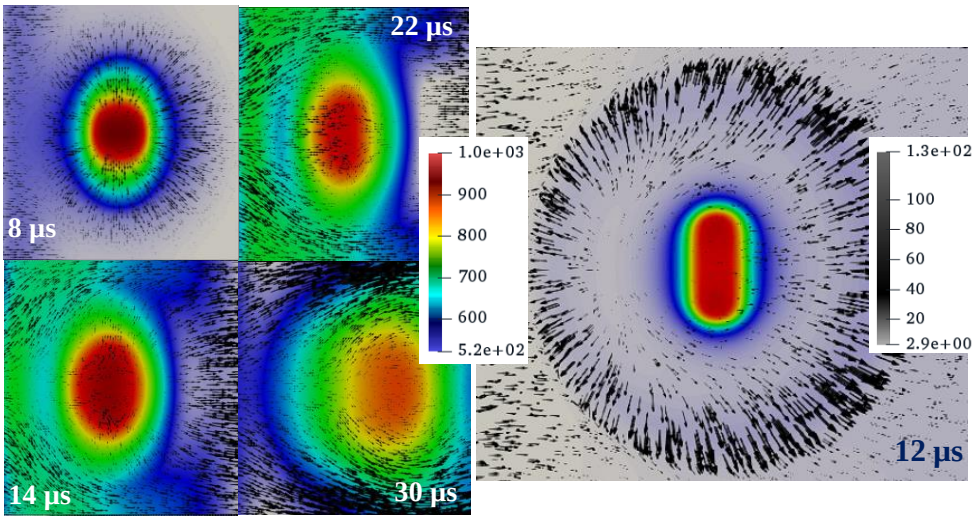

Figure 6: Gas temperature distribution for the different initial electron number density, $Re = 10^4$: a) $n_e^0 = 10^{16}\ m^{-3}$; b) $n_e^0 = 5 \cdot 10^{17}\ m^{-3}$.

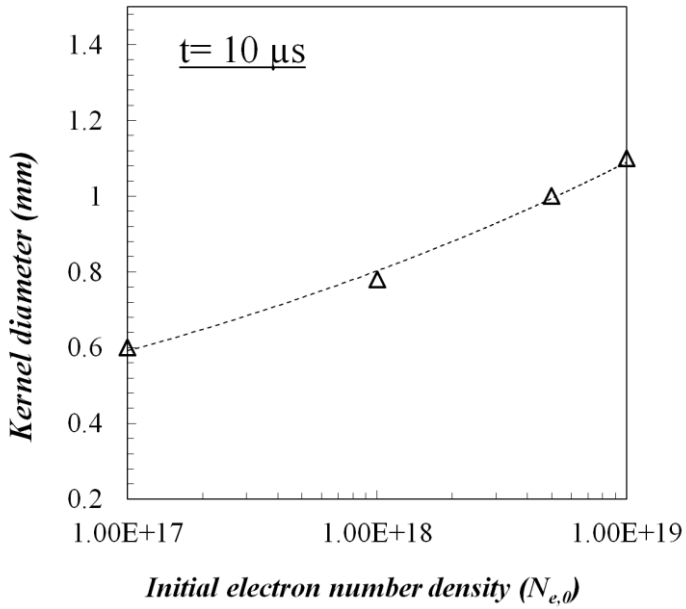

Figure 7: Dependence of the ignition kernel size on the initial electron number density (t=10 μs).

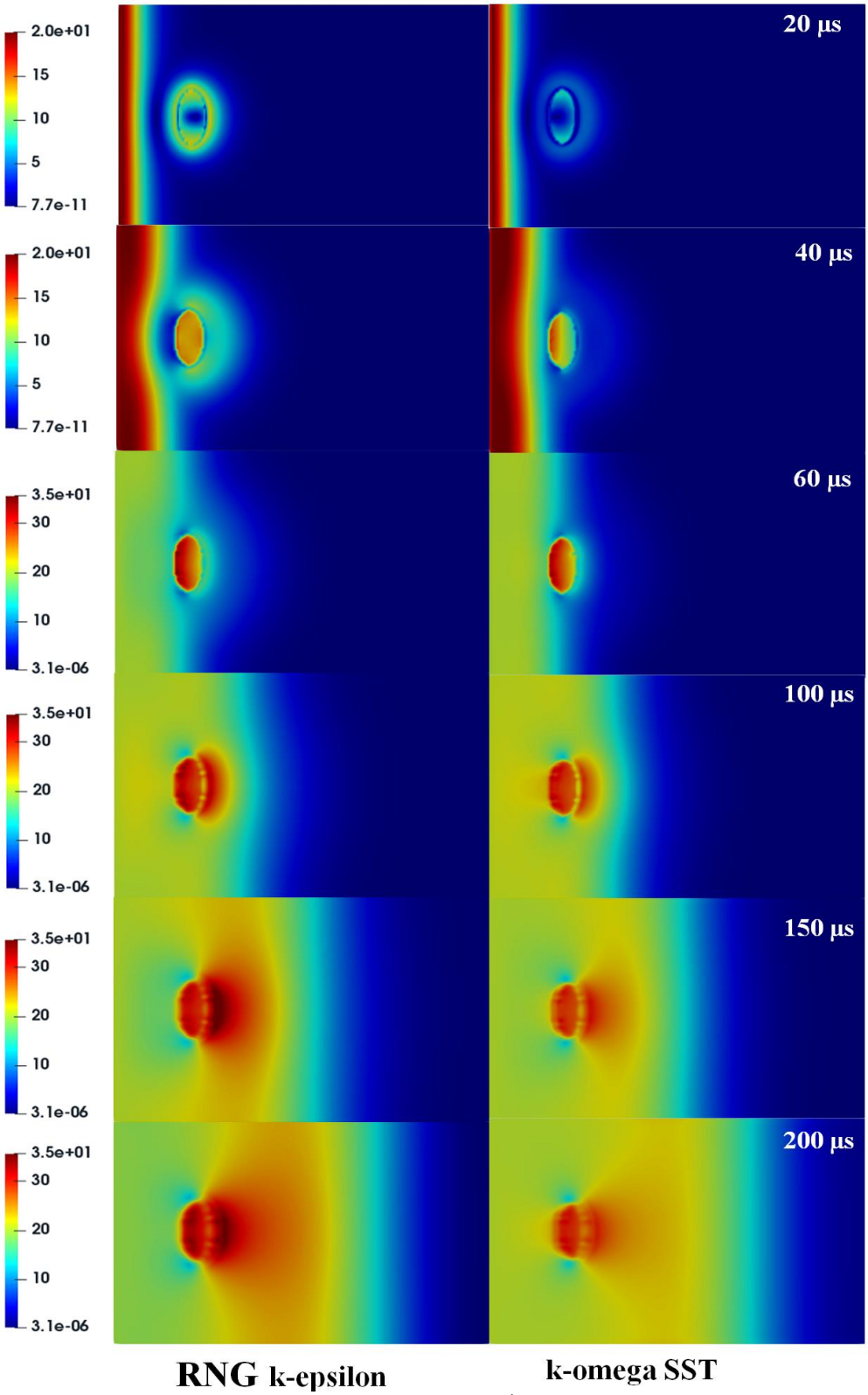

Figure 8: Spatio-temporal velocity contours at $Re = 8 \cdot 10^4$ predicted by two models of turbulence. Successful ignition event, the initial electron number density is $n_e^0 = 1 \cdot 10^{17}\ m^{-3}$..

a) RNG- $k-\varepsilon$ model; b) SST $k-\omega$ model.

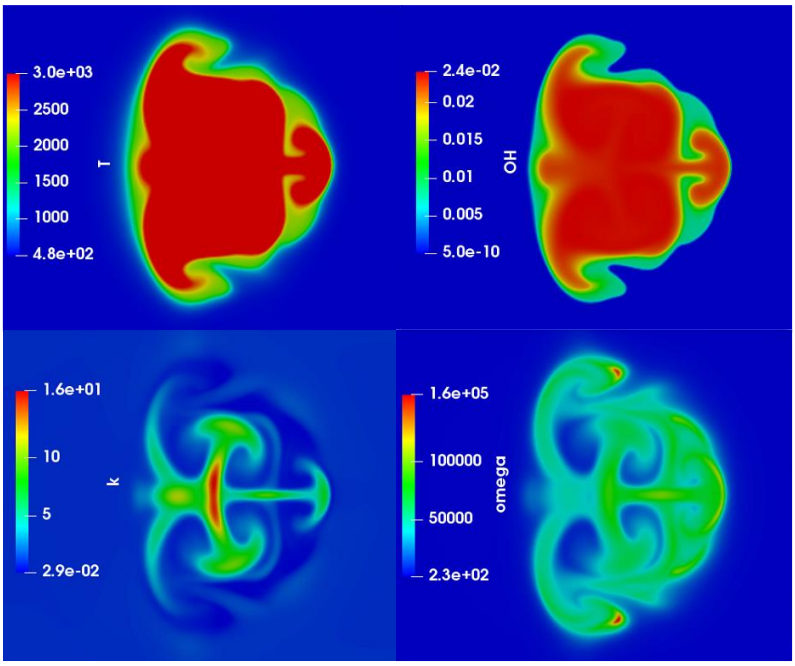

Figure 9. The ignition kernel after 300 μs, the $k-\omega$ SST model.

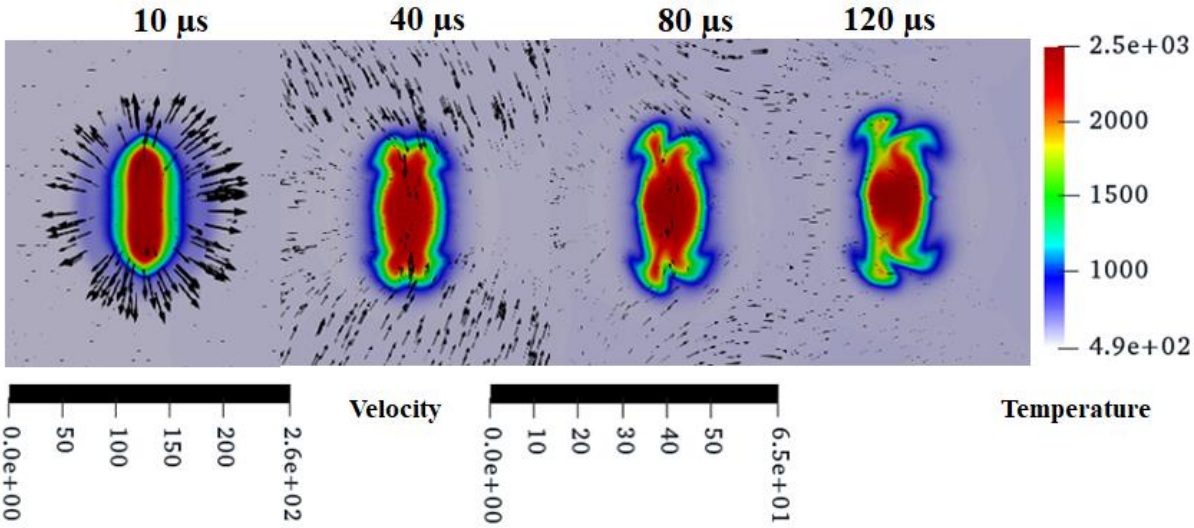

Figure 10. Plasma and ignition kernel dynamics for dual-pulse laser ignition in a turbulent flow, $Re = 5 \cdot 10^3$.

VI. Conclusions

We have presented a mathematical model of dual-pulse laser ignition in a turbulent flow taking into account detailed chemistry, electrons and ions dynamics in a frame of the three-temperature plasma model. The results showed a possibility of successful ignition in a turbulent flow using a dual-pulse laser technique. For the low Reynolds numbers and moderate initial electron number density, created by the first ionizing pulse, the kernel structures are

very stable and similar to those in a quiescent methane-air mixture. At high Reynolds numbers, the flow swept away the kernel, leading to the change of the shape and structure of the kernel. For the case of high turbulence intensity, a further development of the model is needed to understand the interactions between turbulence, ignition and plasma chemistry at the early time of ignition.

.

Acknowledgement

This work has been supported by internal funds of Texas A&M University and by the DOD-AFOSR award under Subcontract with Princeton University SUB0000242.

References

1. Ronney, P. D. Laser versus conventional ignition of flames, Opt. Eng., 1994, Vol. 33, No. 2, pp. 510-521.
2. O'Briant, S. A., Gupta, S. B, Vasu,S.S. Review: laser ignition for aerospace propulsion, Propuls. Power Res., 2016, Vol. 5, pp. 1–21.
3. Tropina, A.A., Shneider, M.N., Miles,R.B. Ignition by Short Duration, Nonequilibrium Plasma: Basic Concepts and Applications in Internal Combustion Engines, Combust. Sci. Technol.,2016, Vol. 188, No. 6, pp. 831–852.
4. Yalin,A.P., Wilvert, N., Dumitrache, C., Joshi, S., Shneider,M.N. Laser plasma formation assisted by ultraviolet pre-ionization, Phys. Plasmas, 2014, Vol. 21,No. 10, p. 103511.
5. Dumitrache, C., Limbach, C.M., Yalin, A.P. Laser Thermal Ignition Using a Dual-Pulse Approach, 54th AIAA SciTech Forum, AIAA Paper 2016-0460.
6. Dumitrache,C., VanOsdol,R., Limbach, C.M., Yalin,A.P. Control of Early Flame Kernel Growth by Multi-Wavelength Laser Pulses for Enhanced Ignition, 2017, Sci. Rep., Vol. 7, pp. 10239.
7. Tropina, A. A. , Shneider, M.N., Miles, R.B. Mathematical model of dual-pulse laser ignition, J. of Propulsion and Power, 2018, Vol. 34, No. 2, pp. 408-414.
8. Shneider, M.N., Miles, R.B. Laser induced avalanche ionization in gases or gas mixtures with resonantly enhanced multiphoton ionization or femtosecond laser pulse pre-ionization, Phys. Plasmas,2012, Vol.19, p.083508.
9. Wermer,L., Hansson, J., Im,S. Dual-pulse laser-induced spark ignition and flame propagation of a methane diffusion jet flame, Proc. Combust. Inst.,2017, Vol. 36, pp. 4427–4434.
10. Mahamud,R., Tropina, A.A., Shneider , M.N., Miles, R.B. Dual-pulse laser ignition model. Phys. of Fluids, 2018, Vol.30, p.106104
11. Kono, M., Niu, K., Tsukamoto, T. Ujiie, Y. Mechanism of flame kernel formation produced by short duration sparks, Symp. Combust.,1989, vol. 22, no. 1, pp. 1643–1649.
12. Chomiak J Flame development from an ignition kernel in laminar and turbulent homogeneous mixtures. Proc. 17th Symp. (International) on Combustion (Pittsburg: The Combustion Institute), 1979, pp.255–263.
13. Raizer,Y.P. Gas Discharge Physics. Berlin, Heidelberg: Springer Berlin Heidelberg, 1991.
14. Shneider, M.N., Mokrov, M.S., Milikh,F.M. Dynamic contraction of the positive column of a self-sustained glow discharge in air flow, Physics of Plasma, 2014, Vol. 21, pp.092122.
15. C. J. Greenshields, OpenFOAM User Guide, Version 5, 2017.
16. Steffen, C.J. A Critical Comparison of Several Low Reynolds Number k-c Turbulence Models for Flow Over a Backward-Facing Step, 29th AIAA Joint Propulsion Conf. and Exhibit, Monterey, CA, 1993, June 28-30, AIAA Paper 93-1927.

Properties of Dual-Pulse Laser Plasmas and Ignition Characteristics in Propane-Air and Methane-Air Mixtures

Carter Butte*,[1], Ciprian Dumitrache&,[2], Azer Yalin*,[3]
*Colorado State University, Fort Collins, CO, 80523, USA
&Laboratoire EM2C, CNRS, CentraleSupélec, Université Paris-Saclay, 91190 Gif-sur-Yvette, France

Abstract

This contribution characterizes the properties of dual-pulse nanosecond laser plasmas and examines their ability to ignite fuel-air mixtures. The dual-pulse plasma is generated using a UV pre-ionization pulse (λ=266 nm) of energy E_{UV}=20 mJ, followed by an NIR pulse (λ=1064 nm) of energy E_{NIR}=40 mJ delivered 15 ns after the first pulse. Rayleigh and Thomson scattering diagnostics are performed for dual-pulse plasmas in air (T_0=298 K, P_0=1 bar) to measure electron density and gas temperature over a timescale of 200 ns to 200 µs after initial plasma formation. We report a dual-pulse electron density of n_e=4.0-5.9x10^{17} cm^{-3} at time of 200 ns after the initial pulse, and a gas temperature of 1360 K at time of 10 µs, using Thomson and Rayleigh scattering techniques respectively. Temporal profiles of electron density exhibit similar trends for both the NIR and dual-pulse plasmas, while temperature profiles indicate much more rapid gas cooling for the dual-pulse plasma. Dual-pulse laser ignition was studied in non-flowing propane-air and methane-air mixtures (P_0=1 bar and T_0=323 K) yielding a lean limit of ϕ=0.6 for both fuels, though propane ignition exhibited slightly higher efficiency.

I. Introduction

Laser plasmas are of growing interest for ignition in a host of combustion applications including the aerospace field. As spark plugs and other igniter technologies reach their performance limit, emerging emphasis is placed on developing new ignition techniques, one of which is laser ignition. Laser ignition techniques have the advantage of not requiring mounts or electrodes, thus avoiding associated heat sink and flame quenching effects, as well as increased flexibility in positioning the ignition source.[1-4] Other advantages include precision timing control and potential combustion enhancement. As new fuel types, including bio-fuels, are developed for aerospace applications, there is a need for development of accompanying ignition techniques. Laser ignition has shown promise in rocket applications including deep space nuclear propulsion and ignition of non-hypergolic fuels in orbital maneuvering thrusters.[5,6,7] Ramjet and scramjet engines may benefit from spark location flexibility, rapid relight, and potentially spatially (volumetric) arrays of ignition points which contributes to increased control over intermediate reactions, leading to more stable and complete ignition.[5,6,7] Terrestrial applications include turbomachinery and reciprocating engines, where laser ignition techniques can offer reduced maintenance requirements, and have been shown to extend the lean limit, increase flame speeds[8], and reduce pollutant emissions.[9] In certain scenarios, high frequency laser induced plasmas have been shown to increase flame stability and assist in flame propagation.[10,11] However, the high energy requirements necessary for gas breakdown have proved a significant obstacle in making laser ignition industrially attractive.[9] Previous studies have found that less than 8% of breakdown energy contributes to ignition, while the rest of the plasma energy is lost through shockwave propagation and radiative processes.[12]

[1] Graduate Student, Department of Mechanical Engineering, Colorado State University, Fort Collins, CO
[2] Postdoctoral Fellow, Laboratoire EM2C, Université Paris-Saclay, Gif-sur-Yvette, France, AIAA Member
[3] Professor, Dept. of Mechanical Engineering, Colorado State Univ., Fort Collins, CO, Associate Fellow AIAA

We are examining multi-pulse plasmas, based on two nanosecond laser pulses operating at different wavelengths, as a means to expand ignition windows and tailor properties such as gas temperature, electron number density, and plasma size and hydrodynamics.[9,13-14] By decoupling the two processes responsible for plasma formation, multiphoton ionization (MPI) and electron avalanche ionization (EAI), the dual-pulse technique makes plasma properties controllable and requires less input energy than well-established laser spark ignition.[13,14] Mahamud et al. recently developed a model illustrating that properties such as kernel growth and ignition delay are made controllable through adjustment of laser intensity and focusing distance.[15] Past research has shown that UV laser ionization is dominated by MPI processes, while NIR breakdown is dominated by EAI processes.[13] Accordingly, our method uses a UV laser pulse (λ=266 nm in the present work) for pre-ionization, and a secondary NIR laser pulse (λ=1064 nm in the present work) for energy addition to seed electrons. Other research has examined the effect of time-spacing between pulses for multi-pulse and repetitive-pulse schemes and combinations of laser and microwave pulses. [11,16,17-19] Dual-pulse plasmas have been shown to cause less flame stretching and successful suppression of an undesirable third lobe, commonly observed with other laser ignition techniques.[9] These properties result in better ignition characteristics, particularly with regards to increased efficiencies and extension of the lean limit.[5,9] In high speed flows, dual-pulse plasmas (created with other wavelength/timing schemes) also have increased ignition probabilities compared to single pulse plasmas of equivalent energy.[18]

This contribution presents experimental results regarding gas temperature and electron density of laser plasms formed from the dual-pulse pre-ionization method. Additionally, ignition experiments were performed in propane-air and methane-air mixtures to demonstrate the ability of such a technique to ignite combustible mixtures, particularly around the lean limit. Section II of the paper details the experimental setup for plasma formation, Rayleigh and Thomson scattering diagnostics, and ignition and combustion in fuel-air mixtures. Section III presents the resulting electron densities and temperatures of the dual-pulse and NIR plasmas, as well as ignition efficiencies in propane-air and methane-air mixtures. Section IV draws conclusions and presents ideas for future work.

II. Experimental Setup

The dual-pulse laser plasmas are formed from two beams. The first pre-ionization pulse (λ=266 nm) is due to the fourth-harmonic output of an Nd:YAG (Continuum Powerlite 8010) and generally has energy of 20 mJ and pulse-duration of 7 ns. The second pulse (λ=1064 nm) is delivered 15 ns later and is due to the fundamental output of a second Nd:YAG (New Wave Gemini) with energy 40 mJ and pulse-duration of 10 ns. The optical setup is shown in Fig. 1. For single-pulse experiments, in the NIR, the same 1064 nm source (New Wave Gemini) is used, generally with energy of 95 mJ. For the dual-pulse case, the separate beams are spatially overlapped and combined with a beam splitter (ThorLabs HBSY134). The two beams are focused to a common location, with separate lenses both having focal length of 300 mm). Rough beam overlap is achieved with irises and pinholes, while final precise alignment is achieved by minimizing the laser energies required to spark. Initial alignment is done in open-air, after which the combustion chamber is added and minor adjustments are made.

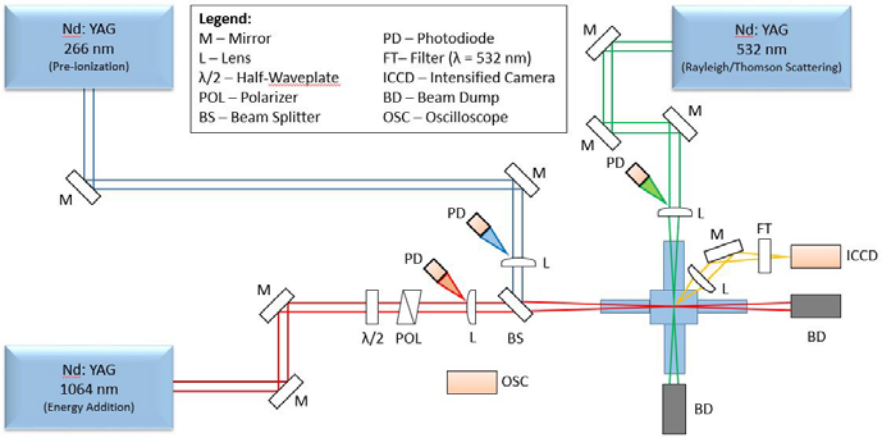

Figure 1: The optical setup for the dual-pulse plasma with Rayleigh/Thomson scattering diagnostic.

An additional Nd:YAG laser source (Spectra Physics Quanta Ray) operating at 532 nm is used for diagnostics by (combined) Rayleigh and Thomson scattering. The diagnostic probe beam is introduced into the combustion chamber using dielectric steering mirrors and focused with a plano-convex lens (f=250 mm). The diagnostic beam is orthogonal in direction to the plasma formation beams and weakly focused in the laser plasma region, possessing a beam waist diameter of approximately 190 µm (narrower than the laser plasmas that it is used to probe). The scattering signal is collected along a direction orthogonal to both the plasma formation and diagnostic beam axes with a collection lens (f=75 mm). It is then imaged through a 532 nm bandpass filter (ThorLabs FL532-10) onto an ICCD camera (pco DICAM pro). Baffles positioned inside the chamber reduce the amount of background light collected by the camera (i.e. reduce the elastic scattered laser light from the chamber windows and spurious reflections etc.). The camera imaging is executed using 2 x 2 binning, resulting in an image resolution of 512 x 640 pixels, with a spatial resolution corresponding to 11 µm/pixel. 774 images are collected for each condition (three sets of 258 images) and photodiodes are utilized to monitor the timing of each laser as well as the camera. A similar setup is used for plasma characterization studies and ignition studies, but in the latter case the chamber arms for delivery of the diagnostic beam are removed. For combustion heat-release analysis, pressure data is collected using a dynamic pressure transducer (PCB Piezotronics 113B24) and oscilloscope (Rigol DS1204B).

III. Results and Discussion

A. Energy Dependence of UV Plasma Luminosity

The goal of this investigation is to identify the ionization mechanism for the UV pre-ionization pulse employed in the dual-pulse scheme. Given the non-resonant UV excitation, it is expected that ionization should be primarily via MPI. The dependence of electron generation, for which we use optical emission as a proxy signal, on the laser pulse energy can be an indicator for the type of ionization present. Specifically, for non-resonant MPI, given the 266 nm wavelength and the ionization energy of air (mainly consisting of nitrogen), one expects a cubic dependence of electron density on laser fluence (3 photons are required for ionization).[20,21] The dependence of optical emission (obtained 200 ns after the UV pulse for shutter duration 25 ns, without spectral filtering) on the UV laser pulse energy is shown in Fig. 2. The emission data is well fit with a third order polynomial which supports that ionization is predominantly by MPI (not, e.g. 2+1 resonant enhanced MPI or a high fraction of electron generation by EAI). However, it is recognized that optical emission is not a perfect proxy for electron generation, and future efforts will include similar measurements (versus laser energy) with Thomson scattering.[22]

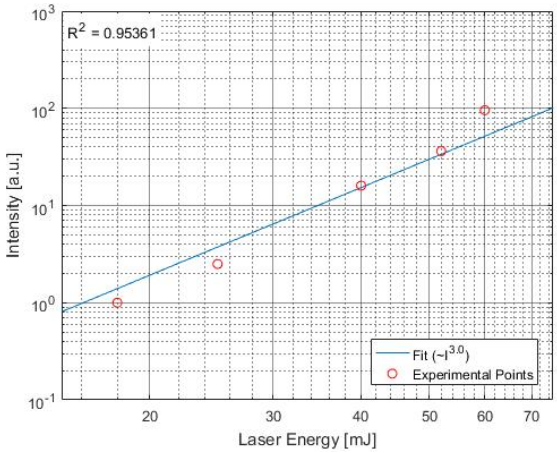

Figure 2: Optical emission intensity of the UV plasma as a function of the laser energy. Images were taken at a delay of 200 ns after plasma formation (first pulse). A cubic fit has been applied to the data to verify the ionization method.

B. Plasma Electron Density

We have performed 2-D scattering measurements of the laser plasmas to examine plasma density and gas temperature. The scatter signal is due to a combination of Rayleigh and Thomson scattering (and much weaker Raman scattering). At early times the scattering signal is primarily due to Thomson scattering, and can be used for electron density determination, while at later times the signal is primarily Rayleigh, allowing for determinations of gas temperature.[23] The transition between the two regimes can be difficult to determine and in the present case is set as the time when the central Thomson peak (clearly visible at early times) diminishes to be no longer discernible. The scattering measurements were performed for both dual-pulse and NIR induced plasmas. The dual-pulse plasma was based on E_{UV}=20 mJ and E_{NIR}=40 mJ (E_{Total}=60 mJ), while the NIR (only) plasma had E_{NIR}=95 mJ. The scattering profiles are plotted in Fig. 3 where the vertical axis shows the scatter and the horizontal axis is the spatial position transverse to the plasma formation axis. The inset shows the orientation of the probe beam relative to the laser plasma axis – the dark region in the middle is due to low density and high temperature. The scattering signal, I, is normalized by a baseline signal, I_0. The method to infer electron density, at the center position, is based on lower and upper bounds of the Thomson peak and has been described in our past work.[13] Taking the 1 μs delay profile (left of Fig. 3) as an example, one sees that far away from the center of the plasma, the signal remains unchanged (I/I_0=1), because the plasma induced shockwave has not reached this point. Working inwards, we observe a large increase in signal due to scattering from increased particle density on the leading edge of the shockwave. The reduction in intensity in the central portion is attributed to rarefaction on the trailing edge of the shockwave and the elevated temperature (reduced density) of the plasma kernel, while an upward pointing peak due to Thomson (electrons) is also present.[13,23]

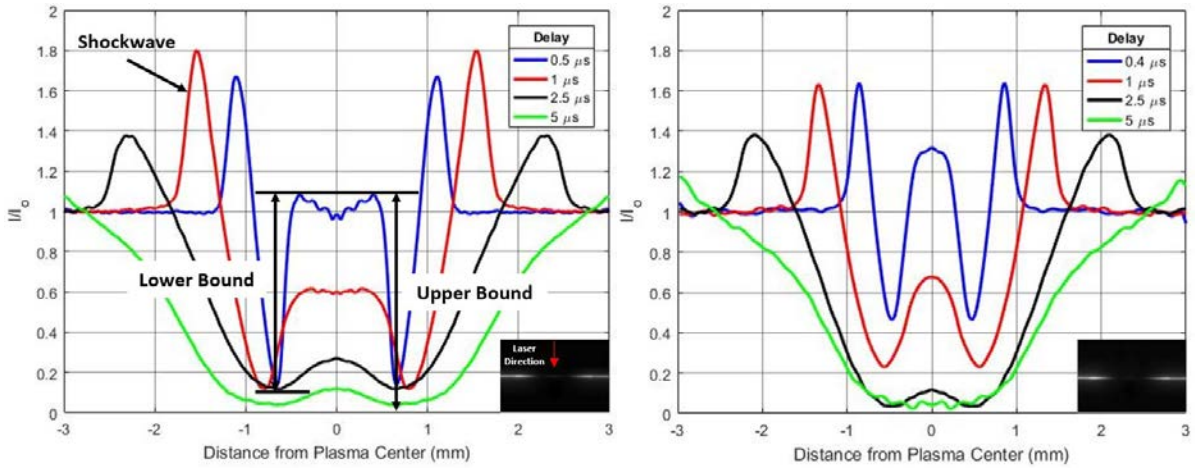

Figure 3: Rayleigh scattering signal along the transverse axis of the plasma for a NIR (left) and dual-pulse (right) laser plasma. The signal has been normalized by the intensity of the scattering beam. The rise of central portion of the signal is due to Thomson scattering. Images in the bottom right detail the raw ICCD images at a delay of 2.5 μs. The plasma formation lasers enter from the top of the image.

For the 0.5 μs delay case (left of Fig. 3), the lower and upper bounds of the Thomson scatter are shown, from which the electron density can be estimated.[13] Electron density decay for both plasmas can be seen in Fig. 4, where the uncertainty bars span between the bounding values. We find similar electron density profiles for the dual-pulse and NIR cases, with a peak value of n_e~5.0×10^{17} cm^{-3} measured for the dual-pulse at delay of 200 ns after plasma formation.

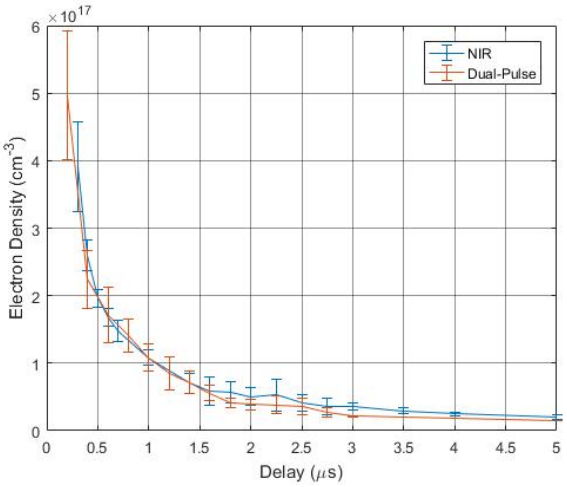

Figure 4: Electron density decay for the NIR and dual-pulse plasmas as a function of time.

C. Plasma Gas Temperature

Rayleigh scattering measurements for temperature can begin to be applied at the time when the Thomson scattering signal becomes negligible. We (somewhat crudely) estimate this to be the time at which the central region of the scattering signal begins to rise (due to cooling) rather than continues to fall (due to electron decay).[20] The corresponding time is approximately 5 µs for the dual-pulse condition and 10 µs for the NIR plasma, in reasonable agreement with literature.[13] The corresponding (Rayleigh dominated) profiles are shown in Fig. 5. At the extended delay times (left of Fig. 5 for NIR), some interesting hydrodynamic fluid behaviors become apparent. The peaks and dips are thought to be due to kernel vorticity extracting hot fluid from the central region and circulation of this fluid through two adjacent lobes.[9,24]

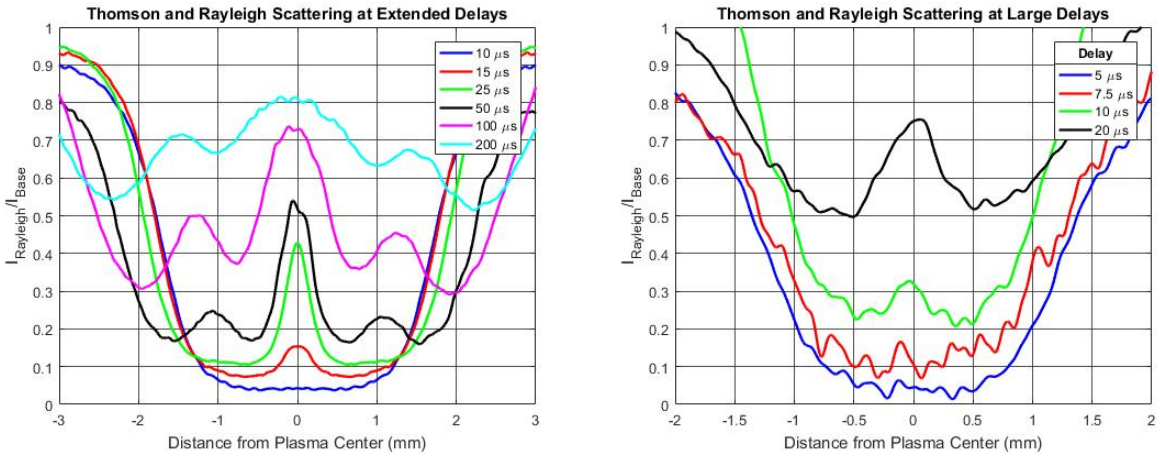

Figure 5: The normalized scattering signal at later delays for both NIR (left) and dual-pulse (right) plasmas.

The basic method to determine temperature from the Rayleigh (dominated) scattering profiles is to use a ratio approach where (at each spatial position) the intensity for a given condition of interest, *I*, is normalized by the Rayleigh signal, Io, from known reference conditions (in this case T_0=298 K, P_0=1 bar). Then, assuming the ideal gas law and uniform pressure between the two cases, the unknown temperature can be readily found from the ratio *I/Io*. Further details on the method, including background subtraction, can be found in our past work.[13]

The above approach does not account for variations of species composition (e.g. due to dissociation of nitrogen) with temperature, nor the variation of the contributing cross-sections with temperature. We have also implemented corrections on the inferred temperature to account for these effects.[25] We use the NASA CEA code to determine the

dependence of mole fractions on temperature and also compute temperature dependent cross-sections.[25] The calculations are made over the temperature range T=0–23,500 K. These values are then used to simultaneously solve Equation 1 for the temperature (T) and normalized cross section ($\frac{\sigma}{\sigma_0}$) based on the measured intensity ratio *I/Io*:

$$\frac{I}{I_0} = \frac{N_0}{N} \frac{\sigma}{\sigma_0} \left(\frac{T_0}{T} \right) \quad \textbf{(1)}$$

where T_o represents the reference temperature of 298 K, I_B is the background image with no laser beams at reference conditions (P_0=1 bar, T_0=298 K), I_P is the plasma image with no scattering beam at the reference conditions, and I_D represents the dark counts of the camera, or the image with no laser beams present at P<0.001 bar.

The resulting temperature measurements, with and without correction for cross-sections, are shown in Fig. 6 for NIR and dual-pulse cases. For the conditions shown in Figure 6, the corrected temperatures are slightly lower than those without correction. In this range, the corrected (species-averaged) cross-section is a bit below the uncorrected value (mostly due to nitrogen dissociation) meaning that, without correction, inferred densities are low, and inferred temperatures a bit high. We report a maximum gas temperatures of 5,480 K at 10 µs for the NIR case, and 3,880 K at 7.5 µs for the dual-pulse case. We find that the dual-pulse plasma cools much more rapidly than its NIR counterpart. It takes approximately 10 µs for the dual-pulse plasma to reach 1,000 K, while it takes the NIR plasma more than 100 µs. These findings warrant further investigation and we note there is an additional experimental uncertainty (~30%) present in the reported measurements due to jitter in the timing of the probe laser beam that affects its overlap with the gated detection period of the intensified camera.

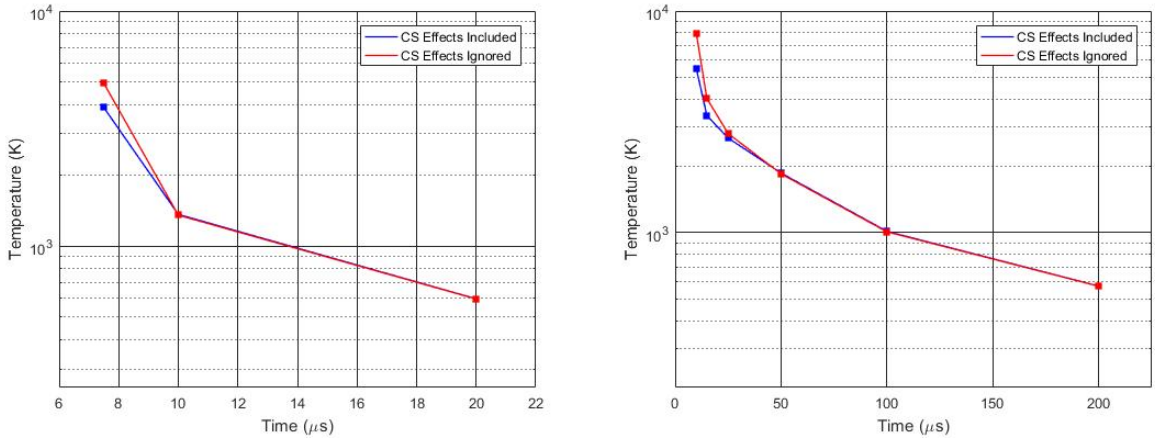

Figure 6: Temperature versus time profiles, from Rayleigh scattering, for the NIR (left) and dual-pulse (right) plasmas.

D. Ignition Testing

Dual-pulse ignition was performed in two separate fuels (methane and propane) for equivalence ratios corresponding to ϕ=0.5—1.0. The pressure traces, due to heat release, from ignition events at each equivalence ratio were recorded using an oscilloscope and dynamic pressure transducer. The results were then averaged (n>=5 replicates per condition), and are shown in Fig. 7.

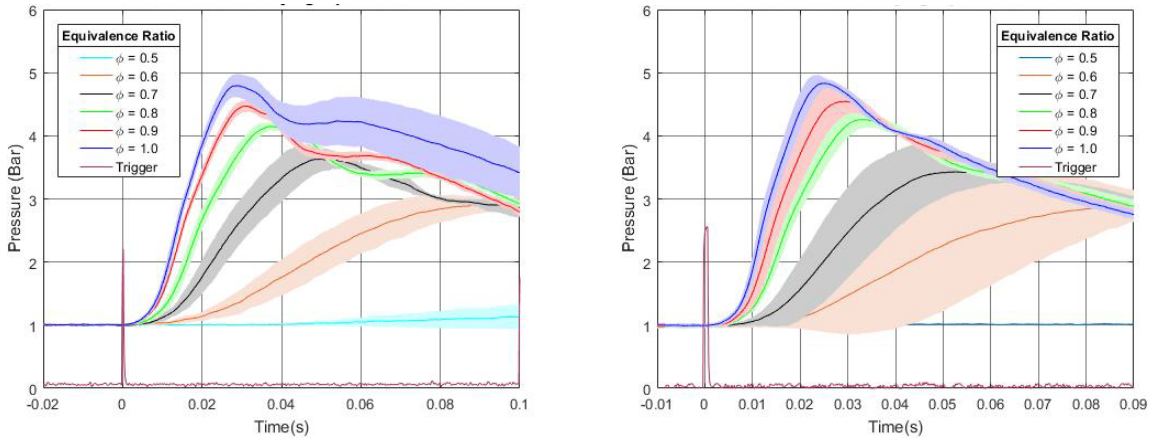

Figure 7: Recorded pressure traces at varying equivalence ratios for methane (left) and propane (right). The dual-pulse scheme uses E_{UV}=20 mJ and E_{NIR}=40 mJ. The standard deviation of the multiple traces for each condition is plotted as the shaded region. Initial conditions were P_0=1 bar and T_0=323 K.

The heat release of the ignition event can be calculated through integration of the pressure history and addition of estimated heat loss to the wall, calculated through estimation of the slope after the ignition event has occurred. Fuel energies are calculated using the lower heating value (LHV) and mass as calculated from the partial pressure. Ignition efficiency is then the ratio of the heat release to the internal energy of the fuel. Resulting efficiencies are shown in Fig. 8.

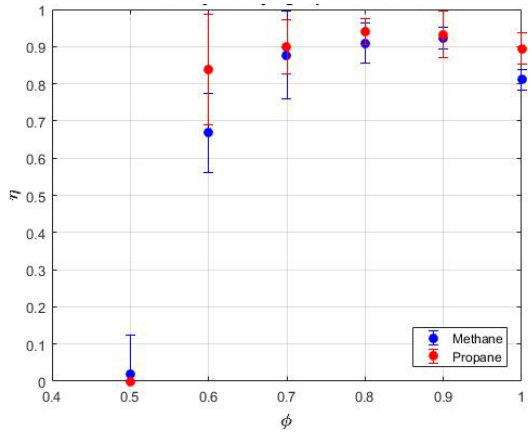

Figure 8: Combustion efficiency for ignition of propane-air and methane-air mixtures by dual-pulse laser ignition. Each data point is the average of at least five traces, where the error bars represent one standard deviation in each direction.

Both fuels exhibit similar trends, though slightly higher efficiency was experienced for propane ignition. We report a lean limit value of ϕ=0.6 for propane where all of the tests resulted in ignition, consistent with similar dual-pulse ignition in literature.[13] Methane was determined to have similar flammability limits.

IV. Conclusions and Future Work

The temporal profiles of electron density versus time are similar for both the dual-pulse and NIR cases, with peak dual-pulse plasma density of n_e~5x10^{17} cm^{-3} measured 200 ns after plasma formation. The dual-pulse plasma cools very rapidly, reaching a temperature of ~1350 K by 10 μs and ~600K by 20 μs, while the NIR plasma cools more slowly. There is some uncertainty to these measurements, due to laser timing and temperature dependent cross-sections, which will be further examined in future work. Ignition experimentation has suggested that methane and propane have similar flammability limits, though propane exhibits slightly higher ignition efficiencies. We report a lean limit value of ϕ=0.6 for both mixtures, consistent with previous findings at similar conditions.[13] Future

work will examine resonant ionization as a means to further increase the efficiency of the pre-ionization pulse, e.g. via an oxygen scheme at 287.6 nm.[27] The use of REMPI may promote more effective pre-ionization yielding further combustion benefits and/or allow use of lower energy pre-ionization pulses.[20]

References

1. Herdin, G., Klausner, J., Weinrotter, M., Graf, J., and Wimmer, A., "GE Jenbacher's Update On Laser Ignited Engines," ICEF-ASME, 2006, pp. 1–7.

2. Bradley, D., Sheppard, C. G. W., Suardjaja, I. M., and Woolley, R., "Fundamentals of high-energy spark ignition with lasers," Combustion and Flame, vol. 138, Jul. 2004, pp. 55–77.

3. Dumitrache, C., Baumgardner, M., Boissiere, A., Maria, A., Roucis, J., Marchese, A. J., and Yalin, A., "A study of laser induced ignition of methane – air mixtures inside a Rapid Compression Machine," Proceedings of the Combustion Institute, vol. 36, 2017, pp. 3431–3439.

4. Kopecek, H., Maier, H., Reider, G., Winter, F., and Wintner, E., "Laser Ignition of Methane–Air Mixtures High Pressures," Experimental Thermal and Fluid Science, vol. 27, 2003, pp. 499–503.

5. O'Briant,A., Gupta,S. B., and Vasu, S.S., "Review: Laser ignition for aerospace propulsion," Propulsion and Power Research, 2016, pp. 1–21.

6. Brieschenk, S., Kleine, H. and O'Byrne, S., "Laser ignition of hypersonic air–hydrogen flow," Shock Waves 23, 2013, pp. 439–452.

7. Negishi, J., Horisawa, H. and Kimura, I., "Mixing and reaction enhancement characteristics of laser-induced plasmas and detonations in laser-augmented scramjets." AIP Conference Proceedings, 2006, pp. 151–162.

8. Herdin, G., and Klausner, J., "Laser Ignition: A New Concept to Use and Increase the Potentials of Gas Engines," ICEF- ASME, 2005, pp. 1–9.

9. Dumitrache, C., Vanosdol, R., Limbach, C. M., and Yalin, A.P., "Control of Early Flame Kernel Growth by Multi-Wavelength Laser Pulses for Enhanced Ignition," Scientific Reports, 2017, pp. 1–8.

10. Yu, Y., Li, X., An, X., Yu, X., Fan, R., Chen, D., and Sun, R., "Stabilization of a Premixed Methane-Air Flame with a High Repetition Nanosecond Laser-Induced Plasma," Optics and Laser Technology, 2017, pp. 24-21.

11. Wermer, L., Hansson, J., and Im, S., "Dual-Pulse Laser-Induced Spark Ignition and Flame Propagation of a Methane Diffusion Jet Flame," The Combustion Institute, 2016, pp. 1-8.

12. Phuoc, T. X. and White, F. P., "An optical and spectroscopic study of laser-induced sparks to determine available ignition energy," Proceedings of the Combustion Institute. **29**, 2002, pp.1621–1628.

13. Dumitrache, C, Limbach, C., and Yalin, A., "Threshold Characteristics of Ultraviolet and Near Infrared Nanosecond Laser Induced Plasmas," AIP Physics of Plasmas **23** 093515, 2016.

14. Dumitrache, C., VanOsdol, R., Limbach, C., and Yalin, A., "Laser Ignition of Propane-Air Mixtures Using a Dual-Pulse Technique," 55th AIAA Aerospace Sciences Meeting, 2017.

15. Mahamud, R., Tropina, A., Shneider, M., and Miles, R., "Dual-Pulse Laser Ignition Model," Physics of Fluids **30** 106104, 2018.

16. Bak, M., Im, S., and Cappelli, M., "Successive Laser-Induced Breakdowns in Atmospheric Pressure Air and Premixed Ethane-Air Mixtures," The Combustion Institute, 2014, pp. 1744-1751.

17. Michael, J., Dogariu, A., Shneider, M., and Miles, R., "Subcritical Microwave Coupling to Femtosecond and Picosecond Laser Ionization for Localized, Multipoint Ignition of Methane/Air Mixtures," AIP Journal of Applied Physics **108** 093308, 2010.

18. Wermer, L., Lefkowitz, J., Ombrello, T., and Im, S., "Ignition Enhancement by Dual-Pulse Laser-Induced Spark Ignition in a Lean Premixed Methane-Air Flow," The Combustion Institute, 2018, pp. 1-8.

19. Hsu, P., Roy, S., Zhang, Z., Sawyer, J., Slipchenko, M., Mance, J., and Gord, J., "High-Repetition-Rate Laser Ignition of Fuel-Air Mixtures," Optics Letters vol. 41 No. 7, 2016.

20. Ronney, P., "Laser Versus Conventional Ignition of Flames," Optical Engineering, 1994, pp. 510-521.

21. Morgan, C.G, "Laser-Induced Breakdown of Gases," Reports on Progress in Physics **38** 621, 1975.

22. El-Rabii, H., Victorov, S. B. and Yalin, A. P., "Properties of an Air Plasma Generated by Ultraviolet Nanosecond Laser Pulses," Journal of Physics D: Applied Physics, **42**, 75203, 2009.

23. Limbach, C., and Miles, R., "Rayleigh and Thomson Scattering Diagnostics of Laser Air Sparks: A Testbed for Tailoring Laser Plasmas," 45th AIAA Plasmadynamics and Lasers Conference, 2014.

24. Bradley, D., Sheppard, C. G. W., Suardjaja, I. M. and Woolley, R., "Fundamentals of High-Energy Spark Ignition with Lasers." Combustion and Flame **138**, 2004, pp. 55–77.

25. Limbach, C. M., Dumitrache, C. and Yalin, A. P. "Laser Light Scattering from Equilibrium, High Temperature Gases: Limitations on Rayleigh Scattering Themometry," 47th AIAA Plasmadynamics and Lasers Conference, 2016, pp. 1-13.

26. Giar, R., and Scharer, J., "Focused Excimer Laser Initiated, Radio Frequency Sustained High Pressure Air Plasmas," AIP Journal of Applied Physics **110** 103301, 2011.

27. Dumitrache C., Butte C., Eickelberg A. and Yalin A., "On the Use of REMPI Pre-Ionization for Laser Plasma Formation," 2018 AIAA Aerospace Sciences Meeting, AIAA SciTech Forum, 2018.

Single and Dual-Pulse Laser Ignition of Methane-Air and Hydrogen-Air Mixtures

Carter Butte[1], Parneeth Lokini[2], Azer P. Yalin[4]
Colorado State University, Fort Collins, CO, 80523, USA

Ciprian Dumitrache[3]
CentraleSupélec EM2C, Châtenay-Malabry, France

Abstract

This investigation examines ignition characteristics of various fuel-air mixtures using both single and dual-pulse laser plasmas building off our previous work. A single pulse laser plasma (λ=1064 nm) of energy E_{SP}=60 mJ is used to ignite methane-air and hydrogen-air mixtures (T_0=298 K, P_0=1 bar) of equivalence ratios in the range of ϕ=0.1–1.0. A non-resonant dual-pulse plasma is formed using a preionization beam in the UV (λ=266 nm) and an energy addition pulse operating in the NIR (λ=1064 nm), with energies of E_{UV}=20 mJ and E_{NIR}=40 mJ, respectively. The dual-pulse plasma is used to ignite methane-air and hydrogen-air mixtures of equivalence ratios in the same range. We report lean limits of ϕ=0.53 and ϕ=0.12 for single pulse ignition of methane-air and hydrogen-air mixtures respectively, and lean limits of ϕ=0.50 and ϕ=0.11 for dual-pulse ignition of methane-air and hydrogen-air mixtures, respectively. OH* chemiluminescence shows that single and dual-pulse toroid shapes in methane-air mixtures are consistent with single pulse and dual-pulse toroids formed in propane-air mixtures, but that hydrogen-air mixtures tend to suppress third lobe development over a larger range of equivalence ratios. An investigation of dual-pulse beam axial offset effects demonstrates that downstream focusing of the energy addition pulse relative to the preionization pulse more effectively suppresses third lobe formation than upstream focusing. We also note that upstream focusing of the energy addition pulse near stoichiometric conditions can result in a fourth lobe centered around the preionization channel, and that for small axial offsets ($\Delta z \leq 0.5$ mm), variability exists in the direction of flame propagation. In terms of ignition, we show that for axial offsets above 2 mm no significant benefits (in terms of lean limit extension) are observed. Finally, the main finding of this study is that ignition probability using the dual-pulse non-resonant method is a strong function of axial offset and that downstream focusing of the energy addition pulse is preferable to upstream focusing.

I. Introduction

Progress towards more complex combustion applications has demanded more advanced and versatile ignition techniques. One attempt to address some of the concerns associated with well-established techniques such as spark plugs and igniters is laser plasma ignition. Advantages of laser ignition include flexibility of spark location and timing, reduced NO_x formation, leaner engine operation, increased combustion efficiency, and greater

[1] Graduate Student, Department of Mechanical Engineering, Colorado State University, Fort Collins, CO
[2] Graduate Student, Department of Mechanical Engineering, Colorado State University, Fort Collins, CO
[3] Postdoctoral Fellow, Laboratoire EM2C, Université Paris-Saclay, Gif-sur-Yvette, France, AIAA Member
[4] Professor, Department of Mechanical Engineering, Colorado St. Univ., Fort Collins, CO, Associate Fellow AIAA

system longevity at elevated pressures.[1-5] Additionally, the non-intrusive nature of laser plasmas results in more unperturbed kernel evolution, as proximate mounting hardware is not required. This is an advantage when compared with spark plug or igniter electrodes which typically act as heat sinks quenching the flame. However, large input energies and complications with beam delivery have impeded field implementation.[6-8]

Our approach to address these challenges uses a dual-pulse laser plasma where a UV beam preionizes a gas mixture and a secondary NIR beam increases the energy and ionization state of the gas. The use of this technique decouples the processes responsible for ionization, predominantly multiphoton ionization (MPI) and electron avalanche ionization (EAI) through inverse bremsstrahlung absorption, and allows for tailoring of plasma properties through adjustments to beam energies and delay time.[9-12] Recent work has shown that dual-pulse laser plasmas not only reduce energy requirements but also enhance ignition characteristics such as combustion efficiency, particularly around the lean limit.[6] An investigation into further energy reduction used a resonant scheme targeting molecular oxygen for preionization. Results showed that similar electron densities to single pulse plasmas and non-resonant dual-pulse plasmas could be produced with 67% of the energy, most of which was concentrated in the energy addition beam.[13] Ignition experimentation with the resonant dual-pulse plasma demonstrated extension of the lean limit for methane-air mixtures, though toroid shapes as observed using OH* chemiluminescence suggested that this was likely a result of increased laser energy deposition in the plasma. This investigation serves to fill in the voids in existing literature with regards to ignition experimentation of various fuels using single and dual-pulse laser ignition. Specifically, this investigation employs a single pulse plasma (λ_{SP}=1064 nm) for ignition of methane-air and hydrogen-air mixtures, and a non-resonant dual-pulse plasma (λ_{UV}=266 nm, λ_{NIR}=1064 nm) for ignition of methane-air and hydrogen-air mixtures. In the analysis, these experimental results are combined with past results to give a comprehensive picture of the ignition abilities of single pulse and dual-pulse plasmas in propane-air, methane-air, and hydrogen-air mixtures.[6,13]

The rest of the document is outlined as follows: Section II details the procedure and setup for ignition testing, Section III presents the results with regards to ignition efficiencies and lean limits of the fuels of interests using the plasmas of interest, and Section IV makes final remarks regarding comparisons to existing literature and future experimentation.

II. Experimental Setup

We use the fourth-harmonic (λ=266 nm) of an Nd:YAG (Continuum Powerlite 8010) for preionization and the fundamental output (λ=1064 nm) from a second Nd: YAG (New Wave Gemini) for energy addition. The two together, separated temporally by 15 ns using a pulse delay generator (Berkeley Nucleonics 555), form the dual-pulse plasma. The preionization beam is attenuated to an energy of E_{UV}=20 mJ and has a pulse duration of approximately 7 ns. The energy addition pulse has an energy of E_{NIR}=40 mJ and has a pulse duration of 10 ns. These energies were selected to match the conditions of dual-pulse plasmas used for ignition of propane-air mixtures in the past.[6] The optical layout for dual-pulse plasma formation is shown in Fig. 1. The beams are spatially overlapped using a beam splitter (ThorLabs HBSY134) and focused to a common waist using two lenses of focal length f = 300 mm. The lens for the energy addition pulse is placed on a translation stage as to be able to optimize and adjust the axial offset of the two beams. The beams are focused to the approximate center of a custom chamber of volume V = 195 cm^3 in which ignition experimentation is performed. The same 1064 nm laser used for energy addition is also used for single pulse plasma formation, where the duration is the same but the energy is raised to E_{SP}=60 mJ. A dynamic pressure transducer (PCB Piezotronics 113B24) mounted on the side of the chamber is used with an oscilloscope (Rigol DS1204B), to record pressure histories of ignition, while simultaneous OH* chemiluminescence imaging is performed using an ICCD (pco DICAM pro) and an optical bandpass filter (Andover 310FS10-50) of wavelength λ~310 nm.

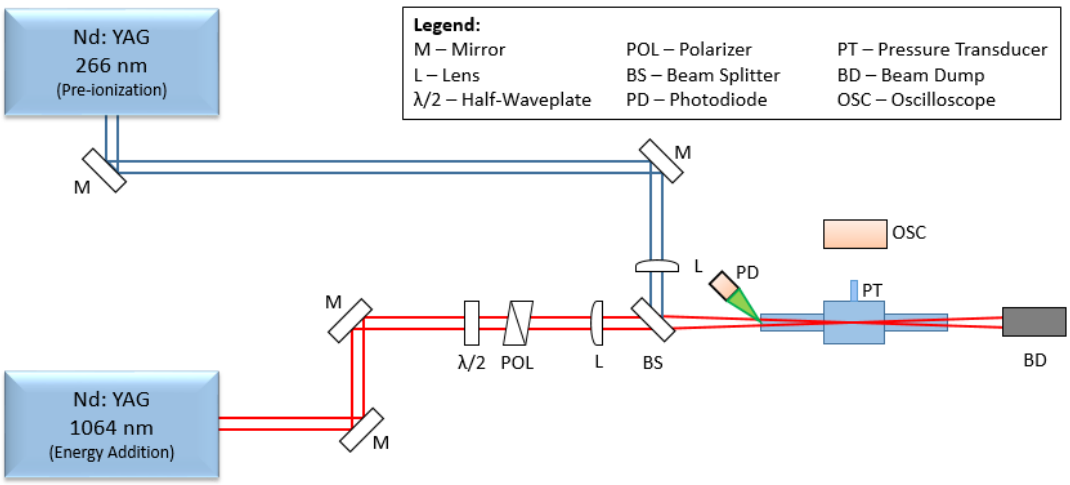

Figure 1: The optical setup for plasma ignition. Single pulse ignition uses the same setup without the 266 nm laser.

III. Results

A. Ignition Testing

Combustion of methane-air and hydrogen-air mixtures was performed using both single and dual-pulse plasmas to supplement past ignition testing of these plasmas in other fuels.[6] We examined equivalence ratios from the stoichiometric case down to the lean limit, with increasing resolution towards the lean limit. Dual-pulse methane combustion focused on lean limit determination in the region of $0.47<\phi<0.55$ to supplement existing literature published by our group in the near stoichiometric region.[14] The pressure traces presented in Fig. 2 show single and dual-pulse ignition in the first and second column, and methane-air and hydrogen-air mixtures in the first and second rows respectively. Time of zero corresponds to the time of laser energy deposition, and the central line of each pressure trace represents the average of at least n=10 individual measurements, while the shaded region represents one standard deviation in either direction of the igniting cases. As expected, we see decreasing peak pressure and increasing ignition delay and variability with increasing equivalence ratio. Note that the dual-pulse trace at ϕ=0.8 is provided from previous experimentation.[14]

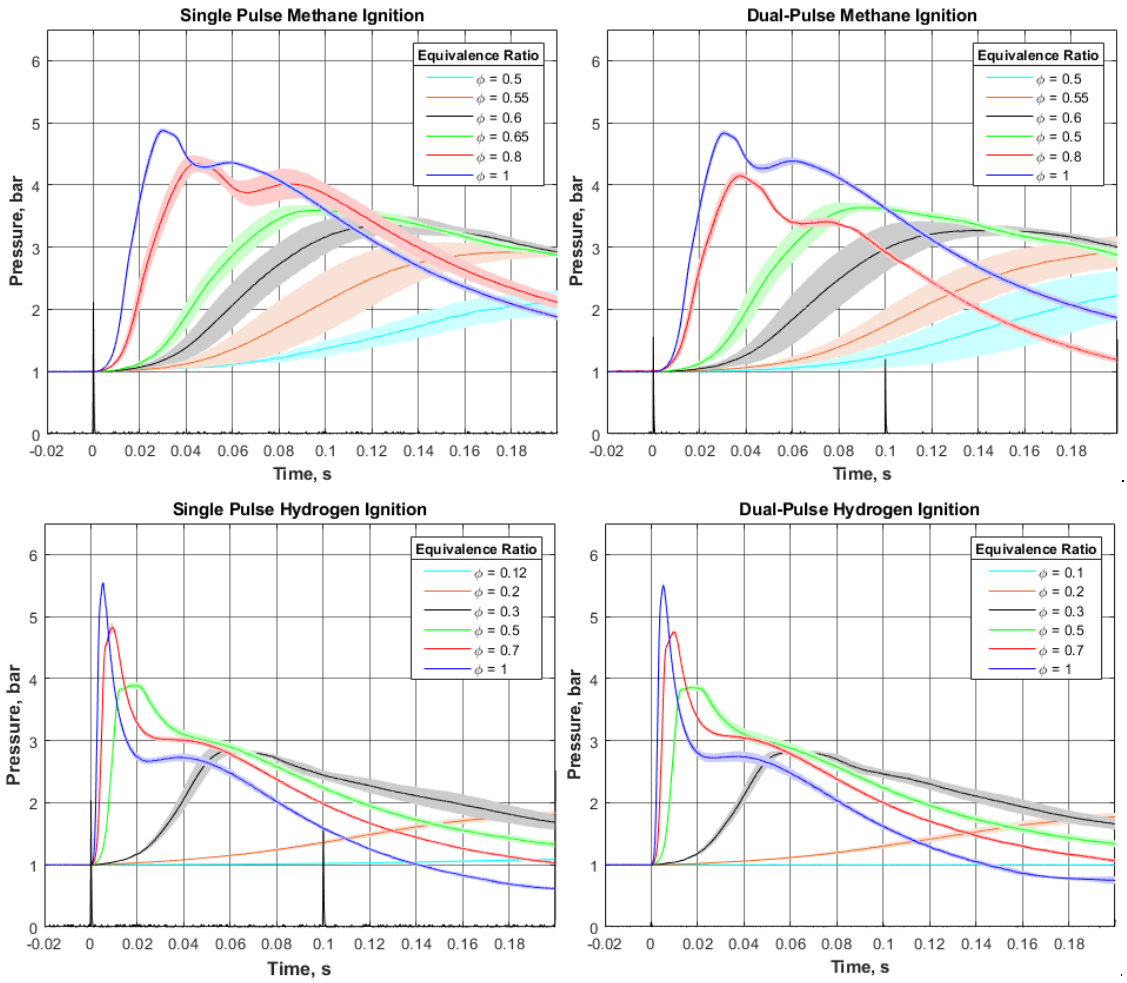

Figure 2: Combustion pressure histories for single and dual-pulse ignition of methane-air and hydrogen-air mixtures. Each trace is the result of averaging successful ignition events of at least ten trials,

We define successful ignition as any increase in pressure (as monitored by the dynamic pressure transducer) accompanied by simultaneous flame propagation as monitored through OH* chemiluminescence. This definition includes weak and partial combustion events. We define the lean limit as the leanest test case where probability of ignition met or exceeded 50%. Using the pressure traces shown above, we can extract a heat release rate from each ignition event as described in our past work.[12] By comparing to the heating values of the respective fuels, we can calculate the combustion efficiency for each ignition event. The resulting efficiencies are shown in Fig. 3 for the single and dual-pulse cases and are compared with existing information for propane from literature.[6,14] The vertical error bars are representative of the standard deviation in efficiency for each equivalence ratio, while horizontal error bars indicate the measurement uncertainty associated with the pressure gauge used to monitor partial pressures. Note that the uncertainty in equivalence ratio varies for each fuel type. The average efficiency value is calculated from the igniting cases, and excludes unsuccessful ignition events. All cases ignited 100% of the time, unless otherwise marked (shown as fractions of successful ignition events around the lean limit).

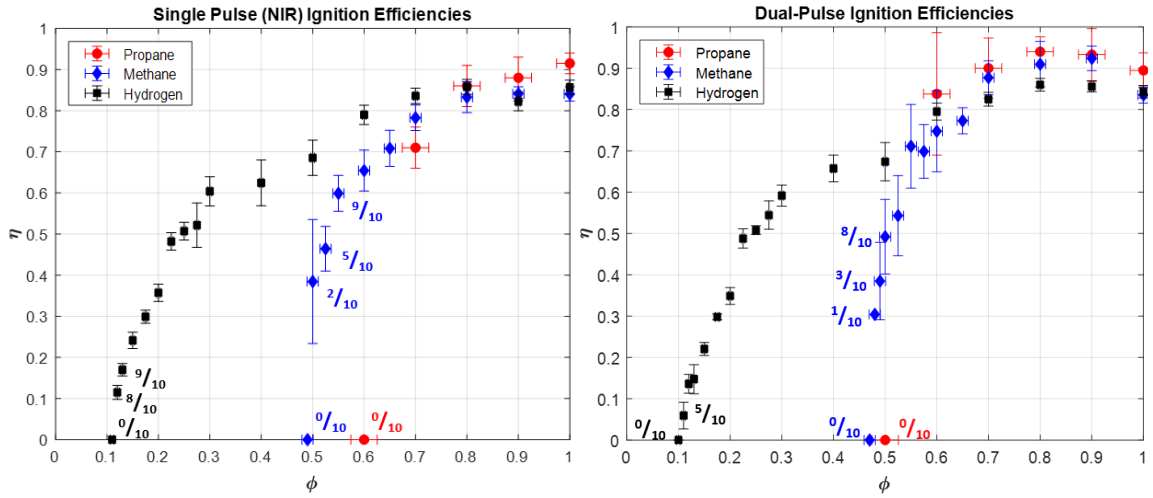

Figure 3: Ignition efficiency for propane (red), methane (blue), and hydrogen (black) fuel-air mixtures using single pulse (left) and dual-pulse (right) plasmas. Note that for the same combined energy, use of the dual-pulse plasma results in a horizontal shift of each curve to the left, extending the lean limit, and increasing ignition efficiency for the lean fuel-air mixtures.

As seen in past experimentation, we observe higher efficiency for lean mixtures, as well as extended lean limits for hydrogen-air when compared with methane-air and propane-air mixtures.[13] Near stoichiometric conditions, we see elevated efficiencies for propane. Based on our definition of the lean limit, we report single pulse NIR lean limits of ϕ=0.12 for hydrogen, ϕ=0.53 for methane, and literature reports a lean limit of ϕ=0.70 for propane.[6] For the dual-pulse plasma, we report lean limits of ϕ=0.11 for hydrogen, ϕ=0.50 for methane, and previous experimentation reports a lean limit of ϕ=0.60 for propane.[14] We find that the dual-pulse plasma results in extension of the lean limit for each fuel type relative to single-pulse (with the same total incident energy). We note the most significant difference for propane, though the resolution ($\Delta\phi$=0.1) in equivalence ratio from previous experimentation could be improved.[6] We also note that the lean limits for the dual-pulse plasma closely match those of the resonant dual-pulse plasma.[13] In terms of efficiency, we report generally higher efficiency ignition for the dual-pulse plasma in both methane-air and hydrogen-air mixtures when compared with single pulse NIR ignition, though the result is seen for nearly all equivalence ratios in the methane-air case while only for the particularly lean cases for hydrogen-air mixtures.

B. OH* Chemiluminescence

In tandem with ignition experimentation, we imaged the flame front and kernel growth using an intensified charged camera and a λ~310 nm filter corresponding to the emission from the intermediate OH* radical, known to be a species correlated with regions of heat release.[15-17] This method allows for temporal imaging of the plasma kernel evolution when ignition is repeated and the timing for the gate of the camera is altered. This method works very well when the kernel shape is consistent shot to shot, as is the case near stoichiometric conditions, but becomes difficult near the lean limit, where localized variations in fuel concentrations result in differently shaped flame fronts and flame speeds. For this reason, we tend to look at the kernel shapes near the lean limit independently rather than as a sequence. Fig. 4 shows flame kernel development of the single pulse NIR plasma in methane, revealing similar kinds of kernel shapes that are well documented in literature for other fuel-air mixtures.[18-23] Though this structure is actually an asymmetric torus, it is typically described as a series of lobes because of the shape it takes on when viewed in two dimensions. The toroid is formed by plasma induced hydrodynamics and acts as a driving mechanism through which surrounding gas is entrained and forced through its center.[2,24] The asymmetric torus can be identified in the following images as two vertical side lobes (corresponding to the cross-section image of the torus) and the expelled jet passing through the center of the torus can be identified as the third lobe propagating towards the laser.[6] In this investigation, we see third lobe formation for single pulse methane-air ignition for all equivalence ratios, and separation of the third lobe for mixtures of equivalence ratios of $\phi \leq 0.70$. We also see that near the lean limit, the flame front propagates for hundreds of microseconds, before dissipating or quenching on a several millisecond timescale. Though partial ignition does occur, the flame does not propagate to fill the chamber for some of these leaner mixtures as it does for mixtures of higher equivalence ratios. This result is expected and is similar to single pulse NIR ignition in other fuels.[6] For the flame kernels in Fig. 4, the gain for collection was constant, though the images use selective contrast to highlight the

kernel shapes. Time delays were selected to match (as close as possible) the conditions previously published by our group on ignition of propane-air mixtures.[6]

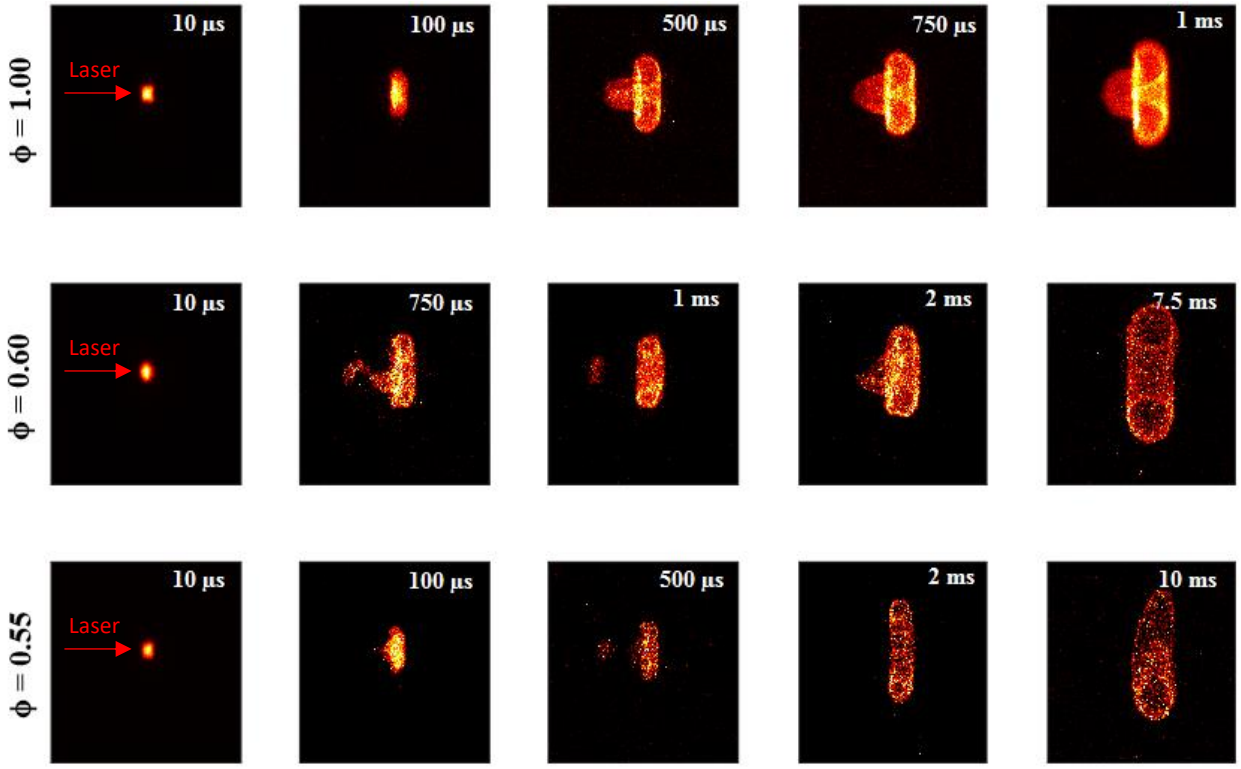

Figure 4: Flame propagation for the single pulse NIR plasma in methane-air mixtures at a variety of equivalence ratios. Indicated times are relative to laser energy deposition inside the chamber. Images have physical dimensions of 28 mm x 22 mm in the horizontal and vertical directions, respectively. Note the tendency of the third lobe to form and separate for the leaner cases.

Figure 5 details similar flame kernel evolution for single pulse NIR plasmas in hydrogen-air mixtures. Single pulse NIR combustion of hydrogen-air mixtures exhibits distinctly different kernels as compared to methane-air mixtures. Primarily, the timescale for complete combustion was much shorter. The hydrogen-air flame takes around 1 ms to fill the entire frame, while the methane-air flame takes longer than 2.5 ms. More rapid combustion can be expected based on higher predicted flame speeds associated with hydrogen.[25] This can also be seen in the pressure histories of Fig. 2. In terms of kernel shape, the main difference compared to methane is that near stoichiometric conditions we observe highly different flame speeds in the radial and longitudinal (beam propagation) directions. The images show that the kernel expands rapidly over the radial axis when compared with the longitudinal axis. The flame speed of the third lobe is significantly smaller than that of the adjacent toroid, and the result is an ovular shaped kernel and a third lobe that never fully develops. However, we hypothesize that it is possible that the third lobe attempts to form in this near stoichiometric scenario, but is accompanied by large rates of flame strain, resulting in quenching and rapid extinction of this third lobe. As the equivalence ratio decreases, we begin to see the third lobe become more pronounced, which may be due to more uniform flame speeds and reduced strain rate. By ϕ=0.65, we see the third lobe on occasion, at ϕ=0.4 we see it every time, and around ϕ=0.20 we see separation begin to occur. Below ϕ=0.20, we see separation of the third lobe, though there is still enough energy in the independent lobes to sustain combustion in localized regions. This is seen in the bottom right image where a section of the kernel has expanded above the frame and is overlaid with kernels still in the frame (ϕ=0.13, t=25 ms).

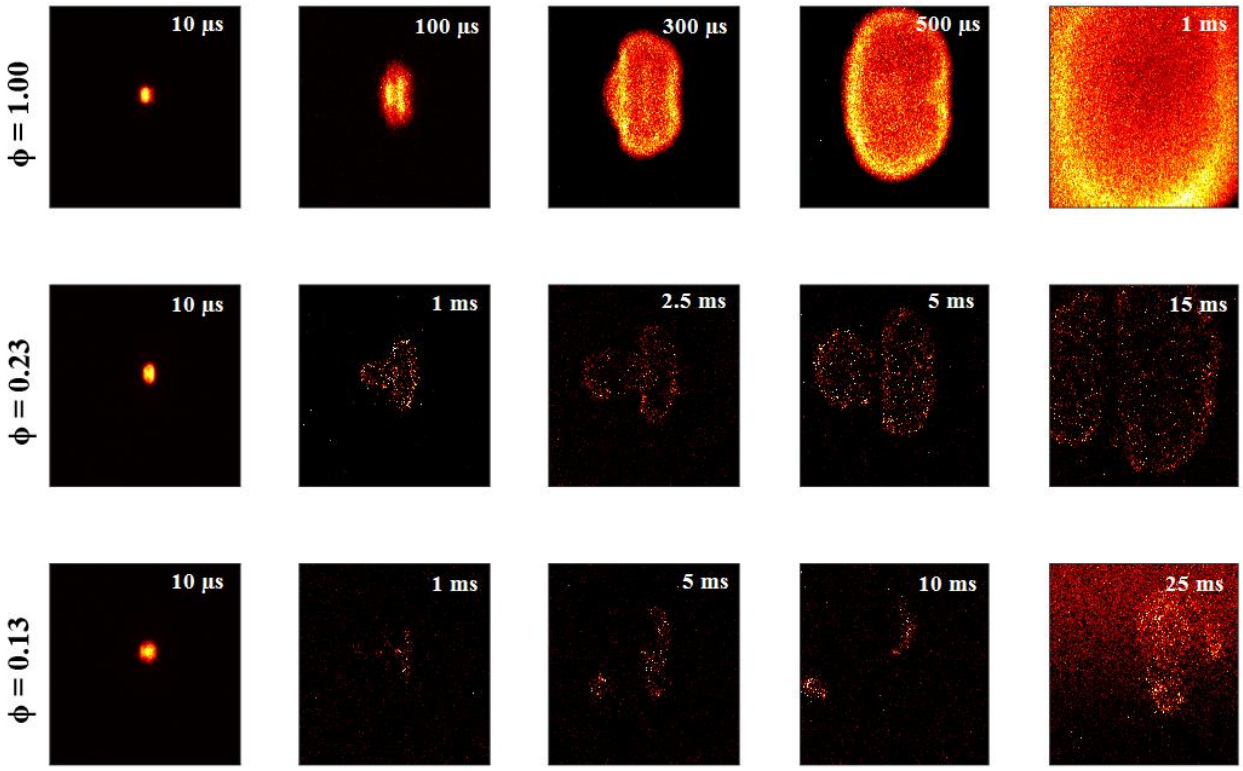

Figure 5: Flame propagation for the single pulse NIR plasma in hydrogen-air mixtures at a variety of equivalence ratios. Indicated times are relative to laser energy deposition inside the chamber. Images have physical dimensions of 28 mm x 22 mm in the horizontal and vertical directions, respectively. Note the ovular shape of the kernel as well as the segmentation that takes place for leaner mixtures, resulting in localized ignition events.

Using the same techniques presented above for the single pulse NIR plasma and kernel, we analyze the dual-pulse plasma for ignition in both methane-air and hydrogen-air mixtures. We see that in both fuel-air mixtures, for all equivalence ratios, the dual-pulse plasma kernel exhibits the characteristic shape of a preionization channel and a larger energy addition kernel over the range of tens of microseconds.[12] Fig. 6 shows methane-air ignition. For equivalence ratios in the range ϕ=1.0-0.70 the energy deposition profile suppresses the development of the third lobe.[6] For the stoichiometric case, the direction of plasma propagation (or the direction in which the third lobe would form if it did) is unpredictable. As mentioned earlier, each image represents a separate ignition event, so that each image should be evaluated individually rather than as a sequence. In eleven combustion events, we report that five of these kernels propagated towards the laser beam, while four propagated away (two were indeterminable). We attribute this to the axial overlap of the two beams, and believe that variability in propagation direction is indicative of good overlap (Δz=0), which leads to suppression of the third lobe. This is studied more rigorously in the offset investigation in Section C. Below ϕ=0.7, despite successful overlap, the third lobe is formed, but it takes a long time to develop (tens of ms), which may explain why this result was not reported on in the past for propane-air mixtures.[6] Around ϕ=0.55, we observe third lobe detachment, kernel segmenting and extinction, and localized kernels which then propagate towards a complete ignition event.

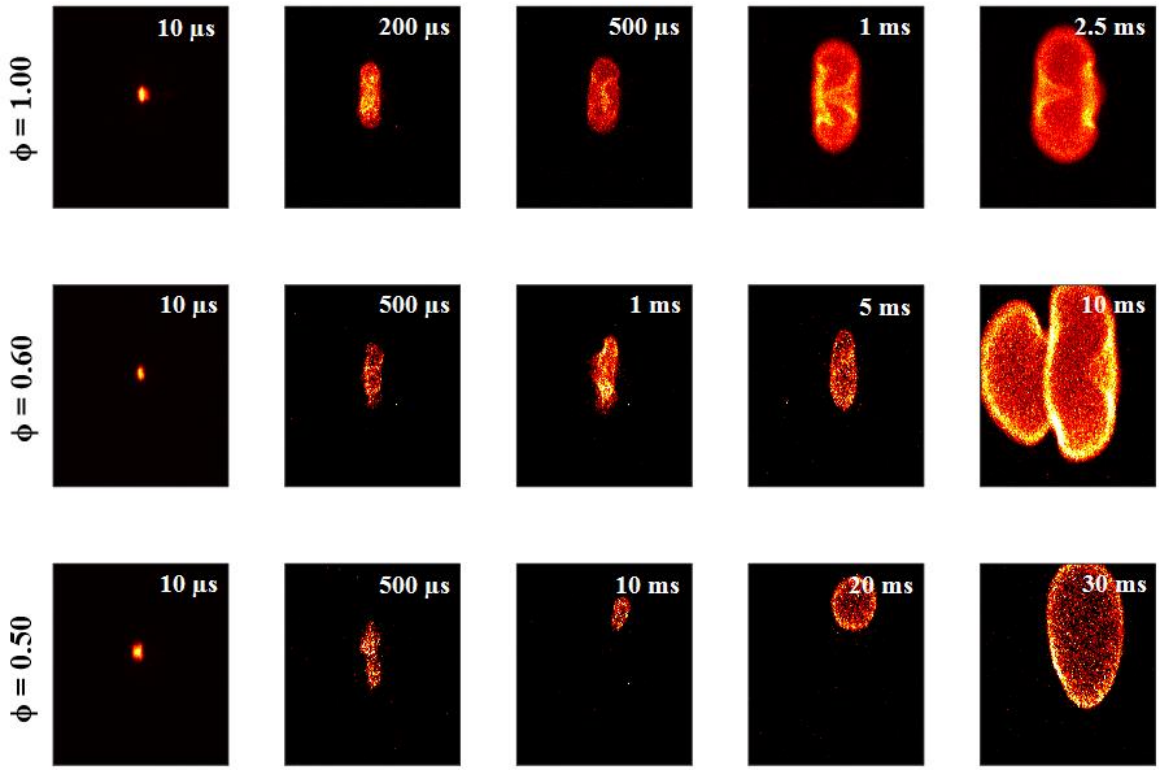

Figure 6: Flame propagation for the dual-pulse plasma in methane-air mixtures at a variety of equivalence ratios. Indicated times are relative to laser energy deposition inside the chamber. Images have physical dimensions of 28 mm x 22 mm in the horizontal and vertical directions, respectively. Note the non-existence of the third lobe for the stoichiometric case. Additionally note the timescale over which the third lobe is seen for the intermediate equivalence ratios and the localized combustion that occurs near the lean limit.

Much like the single pulse NIR plasma, kernel shapes for dual-pulse ignition of hydrogen-air mixtures were much different compared to those formed in methane air mixtures, likely due to fuel reactivity. Again, for all equivalence ratios, the dual-pulse plasma kernel exhibits a distinct preionization channel and energy addition kernel over the first few microseconds. For equivalence ratios in the range ϕ=1.0-0.5, the dual-pulse plasma kernel propagates with this characteristic cross shape all the way through the ignition process. Though this occurs for all equivalence ratios in this range, it is most visible for the ϕ=0.9 case. Below ϕ=0.5, the third lobe is formed, as a net central fluid flow is developed in the center of the toroid, forcing the third lobe in the direction of laser incidence. Around ϕ=0.2, we see segmenting and separation in the kernels, and near the limit we see localized pockets of ignition similar to those seen for single pulse ignition.

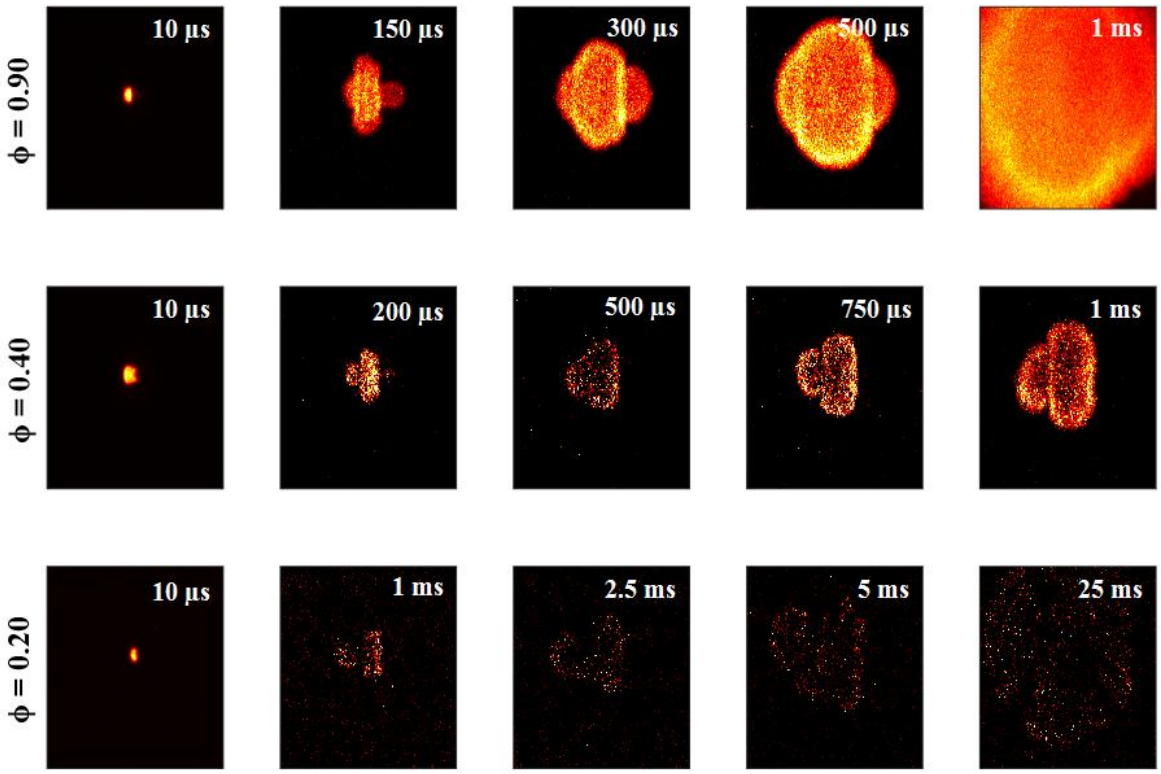

Figure 7: Flame propagation for the dual-pulse plasma in hydrogen-air mixtures at a variety of equivalence ratios. Indicated times are relative to laser energy deposition inside the chamber. Images have physical dimensions of 28 mm x 22 mm in the horizontal and vertical directions, respectively. Note the unique cross shaped kernel for the stoichiometric case.

C. Investigation of Axial Offset in Dual-Pulse Ignition

Previous work in our group has demonstrated that dual-pulse plasma kernel dynamics in propane-air mixtures are a strong function of the energy deposition profile, i.e. the focusing conditions and axial overlap of the two pulses.[6] The previous section demonstrated that third lobe formation can be inhibited near stoichiometric conditions for both methane-air and hydrogen-air mixtures. In order to better characterize this effect and the impacts of deviation from perfect overlap, a test space consisting of a series of axial offsets (Δz = -5.0, -2.0, -0.5, 0.0, +0.5, +2.0, +5.0 mm) and equivalence ratios (ϕ=0.50, 0.60, 0.80, 1.00) was developed. Example axial offsets are shown in Fig. 8 where a negative axial offset corresponds to the energy addition pulse (NIR) focusing upstream of the preionization pulse (UV) and vice versa. In practice, this is done by fixing the location of the UV beam, while moving the focus of the NIR beam via a translation stage on which the lens is mounted.[9]

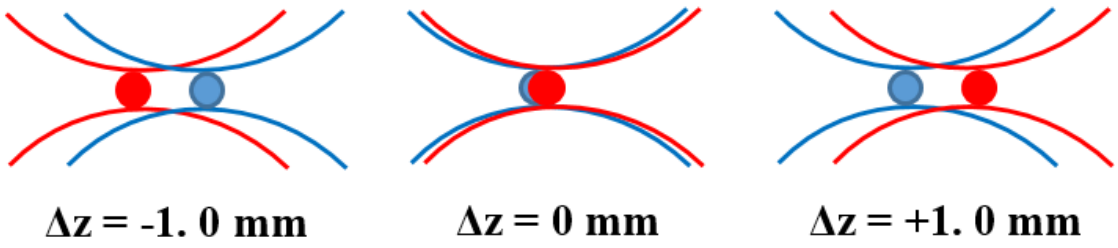

Figure 8: Example axial offsets where the red trace represents the focusing of the energy addition (NIR) beam, and the blue trace represents the focusing conditions of the preionization (UV) beam. The zero offset case is slightly shifted for visualization.

For each combination of axial offset and equivalence ratio, at least three combustion events were attempted, though for the zero offset case at least ten combustion events were averaged as described in Section A. The absolute limit to ignition was also determined as the minimum equivalence ratio for which at least one of the ignition attempts resulted in combustion of the fuel mixture. Experiments were performed in methane-air mixtures. Fig. 9 shows the effects of offset variability on kernel shapes, where each image is taken at a time of t=1 ms after laser energy deposition using an exposure value of Δt=500 µs. In these images, the laser beam enters from the left. Neither beam has sufficient energy to generate full breakdown (and ignition) independently, and therefore each flame kernel can be considered a dual-pulse flame kernel. Note that the lean scenario (shown in the top row of Fig. 9) varied with the offset in order to be able to obtain a successful ignition event. Within $\Delta z = \pm 0.5$ mm, this lean scenario corresponded to an equivalence ratio of ϕ=0.50, but outside this offset, the lean scenario corresponded to ϕ=0.525.

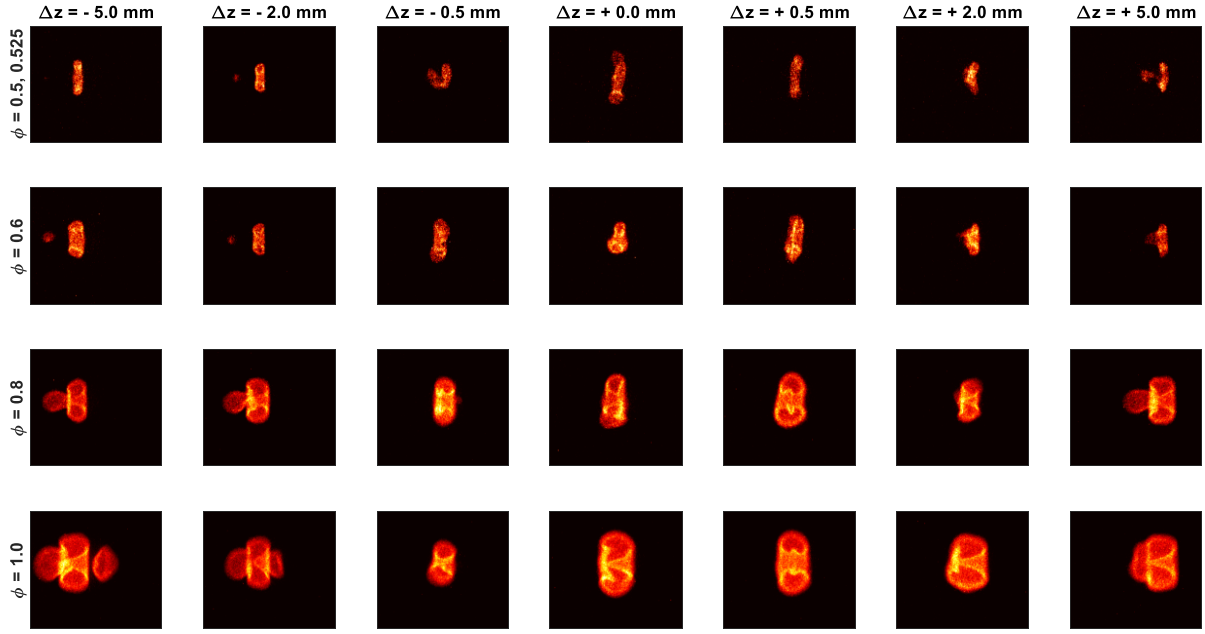

Figure 9: Flame kernel shapes from the dual-pulse plasma in methane-air mixtures at a variety of equivalence ratios and offset conditions. Each image is taken at a time of t=1 ms using an exposure of Δt=500 µs. Images have physical dimensions of 28 mm x 22 mm in the horizontal and vertical directions, respectively.

The cases for which the energy addition pulse is focused upstream of the preionization pulse tend to exhibit higher longitudinal flame speeds for the third lobe, resulting in much more common third lobe detachment than equal axial offsets that focus downstream of the preionization pulse. We hypothesize to this be to be due to the free electron densities along the longitudinal axis, and the corresponding MPI/EAI electron production proportions for each beam.[12] For the upstream case (negative axial offsets), the energy addition beam has not passed through an electron dense region when it reaches its focal point. Though some of the pulse energy gets absorbed by free electrons downstream of the focal point, the proportion of energy that reaches these free electrons is smaller, and the plasma tends to develop as if it were a single pulse plasma, where the energy addition pulse becomes responsible for both MPI and EAI. An interesting phenomenon is observed for the negative axial offset at the stoichiometric condition, where a "fourth lobe" is developed near the location of preionization focus. This suggests that in these conditions, sufficient energy deposition occurs downstream of the focal point in the preionization channel to develop another lobe. Much like the third lobe, this lobe is susceptible to separation from the main toroid, as is seen in the extreme offset case of Δz=-5.0 mm.

The cases where the energy addition pulse is downstream of the preionization pulse tend to have less flame stretching of the third lobe, and separation occurs less frequently. We hypothesize this to be due to better inverse bremsstrahlung absorption of the energy addition pulse, which in this case has to completely pass through the preionization channel before it reaches its focal point. This results in better absorption of the energy addition pulse, as it is responsible for a much smaller proportion of MPI and contributes mainly to EAI, developing kernel shapes that better suppress the third lobe. We also see in Fig. 9 that the overlap precision is difficult to discern by simply looking

at kernel shapes. As mentioned before, for the zero offset case, we see that the flame growth is unpredictable, sometimes occurring upstream and sometimes occurring downstream (seen in the first row of Fig. 6 and described in Section B). We see that within the range of $\Delta z \leq 0.5$ mm, this trend continues. Somewhere between 0.5 mm and 2 mm, this variability breaks down and the three lobe structure grows towards the laser for every ignition test.

In conjunction with imaging, pressure histories were collected so that efficiencies could be calculated. For each condition, three combustion events were attempted, and successful events were averaged. The resulting ignition efficiencies as a function of offset and equivalence ratio are shown in Fig. 10 (left). The zero offset case has increased ignition efficiency for nearly all equivalence ratios, though no observable trend exists for the other offsets at equivalence ratios far from the lean limit. Near the lean limit, the closer the axial offset to the zero offset case, the further the absolute ignition limit was extended. For the zero offset case, the absolute ignition limit was ϕ=0.48. For an axial offset of Δz=0.5 mm in either direction, the absolute ignition limit was found to be ϕ=0.50. Once the axial offset reached Δz=2.0 mm, the absolute ignition limit was ϕ=0.53. This matches the lean limit of single pulse ignition. Therefore, we conclude that in order to benefit from dual-pulse ignition lean limit extension, the axial offset between waists must be less than 2 mm, though the range of acceptable offsets is likely much smaller and further investigation is warranted.

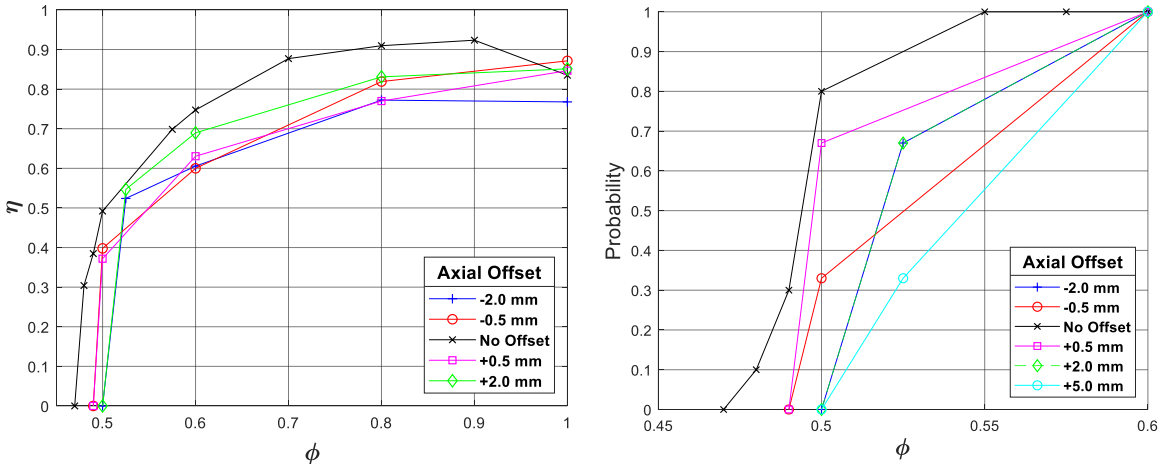

Figure 10: Combustion efficiency (left) and ignition probability (right) for a variety of axial offsets and equivalence ratios. Each point represents the average of at least three ignition attempts. Note the decreasing efficiency with increasing offset distance. Also note how increasing axial offset results in decreasing probability of ignition and how the -0.5 mm case has higher probability of ignition that the +0.5 mm case, attributed to better suppression of the third lobe seen in the OH* chemiluminescence images.

It is also informative to look at the probabilities of ignition as a function of offset. The measured probabilities of ignition are shown in Fig. 10 (right). The limited resolution step size in equivalence ratio inhibits our ability to draw thorough conclusions though we do note some important trends. We see that the probability of ignition increases with better overlap precision. Additionally, we notice an increase in probability for the downstream focusing condition when compared with the upstream condition at Δz=0.5 mm. We attribute this to the better suppression of third lobe as commented upon in the OH* chemiluminescence section of the offset investigation. Recall that this third lobe is known to transport heat and intermediate species away from the kernel, so suppression of it results in more stable combustion, therefore increasing the probability of ignition.

IV. Conclusions

We have demonstrated combustion characteristics of single pulse NIR and dual-pulse plasmas for both methane-air and hydrogen-air mixtures. We report higher efficiencies (particularly in methane-air mixtures) and slightly extended lean limits for dual-pulse plasmas when compared with single pulse plasmas. The lean limits for single pulse NIR plasmas are determined to be ϕ=0.12 for hydrogen and ϕ=0.53 for methane. Corresponding values for the dual-pulse plasma are ϕ=0.11 for hydrogen and ϕ=0.50 for methane, which matches the values reported for resonant dual-pulse plasma in previous work.[13] OH* chemiluminescence for single pulse NIR plasmas in methane-air mixtures

showed similar three lobe structures to those well established for propane-air mixtures, while hydrogen-air mixtures tended to have much more rapid radial growth when compared with longitudinal growth of the third lobe. For the dual-pulse plasma, the preionization channel was clearly seen, and had sufficient energy to dictate kernel shape for near stoichiometric conditions in hydrogen-air mixtures. Suppression of the third lobe occured in both mixtures near stoichiometric conditions, but the third lobe could be observed at extended delays for the leaner cases. Hydrogen-air mixtures ignited much more rapidly for both plasmas when compared with methane-air mixtures. An investigation into the axial offset between waists for the dual-pulse plasmas showed that it is preferable to focus the energy addition beam further downstream from the preionization pulse rather than upstream, if perfect overlap (Δz=0.0 mm) cannot be achieved. For downstream focusing, third lobe suppression is stronger and ignition probability is increased. For upstream focusing, the energy addition pulse acts more like a single pulse plasma, responsible for both MPI and EAI and forming a three lobe structure more frequently. At near stoichiometric conditions, upstream focusing can result in a four lobe structure with the fourth lobe centered near the preionization channel. This fourth lobe typically detaches from the main toroid much like the third lobe. We find that zero axial offset (Δz=0.0 mm) results in the most efficient and most probable ignition with the lowest lean limit. The benefit of lean limit extension completely ceases by an offset of 2 mm, while kernel flame propagation directions are highly variable in the region of ±0.5 mm.

V. References

1. Herdin, G., Klausner, J., Weinrotter, M., Graf, J., and Wimmer, A., "GE Jenbacher's Update on Laser Ignited Engines," ICEF-ASME 2006.

2. Bradley, D., Sheppard, C. G. W., Suardjaja, I. M., and Woolley, R., "Fundamentals of high-energy spark ignition with lasers," Combustion and Flame, vol. 138, Jul. 2004, pp. 55–77.

3. Dumitrache, C., Baumgardner, M., Boissiere, A., Maria, A., Roucis, J., Marchese, A. J., and Yalin, A., "A study of laser induced ignition of methane – air mixtures inside a Rapid Compression Machine," Proceedings of the Combustion Institute, vol. 36, 2017, pp. 3431–3439.

4. Kopecek, H., Maier, H., Reider, G., Winter, F., and Wintner, E., "Laser ignition of methane–air mixtures at high pressures," Experimental Thermal and Fluid Science, vol. 27, Apr. 2003, pp. 499–503.

5. Herdin, G., and Klausner, J., "Laser Ignition: A New Concept to Use and Increase the Potentials of Gas Engines," ICEF- ASME 2005.

6. Dumitrache, C., Vanosdol, R., Limbach, C. M., Azer, &, and Yalin, P., "Control of Early Flame Kernel Growth by Multi-Wavelength Laser Pulses for Enhanced Ignition," Scientific Reports, 2017.

7. Dumitrescu, C., Puzinauskas, P. and Yalin, A., "Fiber-Optic Spark Delivery for Gas-Phase Laser-Induced Breakdown Spectroscopy." Applied Spectroscopy 61, 2007, pp 1338-1343.

8. Yalin, A., Defoort, M., Wilson, B., and Galvanauskas, A., "Fiber Optic Delivery of Nanosecond Laser Pulses for Spark Formation in Gases." Laser Applications to Chemical, Security and Environmental Analysis, 2006, pp 1338-1343.

9. Tropina, A., Shneider, M., and Miles, R., "Modeling of Dual-Pulse Laser Ignition." 2017 AIAA Aerospace Sciences Meeting, AIAA SciTech Forum, 2017.

10. Tropina, A., Mahamud, R., Shneider, M., and Miles, R., "Mathematical Modeling of Dual-Pulse Laser Ignition in a Turbulent Flow." 2017 AIAA Aerospace Sciences Meeting, AIAA SciTech Forum, 2017.

11. Dumitrache, C., VanOsdol, R., Limbach, C., and Yalin, A., “Laser Ignition of Propane-Air Mixtures Using a Dual-Pulse Technique,” 55th AIAA Aerospace Sciences Meeting, AIAA Scitech Forum, (AIAA 2017-1976).

12. Dumitrache, C., Limbach, C., and Yalin, A., “Threshold Characteristics of Ultraviolet and Near Infrared Nanosecond Laser Induced Plasmas,” AIP Physics of Plasmas, 2018.

13. Butte C., Dumitrache C., and Yalin A., “Dual-Pulse Laser Ignition Using Oxygen REMPI Preionization,” 2019 AIAA Aerospace Sciences Meeting, AIAA Aviation Forum, 2019.

14. Butte C., Dumitrache C., and Yalin A., “Properties of Dual-Pulse Laser Plasmas and Ignition Characteristics in Propane-Air and Methane-Air Mixtures,” 2019 AIAA Aerospace Sciences Meeting, AIAA SciTech Forum, 2019.

15. Ballester, J., Hernandez, R., Sanz, A., Smolarz,A., Barroso, J., and Pina, A., “Chemiluminescence monitoring in premixed flames of natural gas and its blends with hydrogen.” Proc. Combust. Inst. 32, 2009, pp. 2983–2991.

16. He, L., Guo, Q., Gong, Y., Wang, F., and Yu G., “Investigation of OH* chemiluminescence and heat release in laminar methane—oxygen co-flow diffusion flames.” Combustion and Flame 201, 2019, pp. 12-22.

17. Kathrotia, T., Dreier, T., Riedel, U., and Shulz, C., “Strain rate and fuel composition dependence of chemiluminescent species profiles in non-premixed counterflow flames: comparison with model results.” Applied Physics B 107, 2012, pp. 561-569.

18. Morsy, M. H., and Chung, S. H., “Numerical simulation of front lobe formation in laser-induced spark ignition of CH_4/Air Mixtures.” Proc. Combust. Inst. 29, 2002, pp. 1613–1619.

19. Endo, T. et al., “An Experimental Study on the Ignition Ability of a Laser-Induced Gaseous Breakdown.” Combust. Flame 178, 2017.

20. Bradley, D., Sheppard, C., Suardjaja, I. M., and Woolley, R., “Fundamentals of High-Energy Spark Ignition with Lasers.” Combust. Flame 138, 2004, pp. 55–77.

21. Kojima, H., Takahashi, E. and Furutani, H., “Breakdown Plasma and Vortex Flow Control for Laser Ignition using a Combination of Nano- and Femto-second Lasers.” Opt. Express 22, 2014.

22. Beduneau, J., Bonggyu, K., Zimmer, L., and Ikeda, Y., “Measurements of Minimum Ignition Energy in Premixed Laminar Methane/Air Flow by using Laser Induced Sparks.” Combust. Flame 132, 2003, pp. 653–665.

23. Wermer, L., Hansson, J. and Im, S., “Dual-pulse Laser-Induced Spark Ignition and Flame Propagation of a Methane Diffusion Jet Flame.” Proc. Combust. Inst. 36, 2017, pp 4427–4434.

24. Dumitrache C., and Yalin A., “Numerical Modeling of the Hydrodynamics Induced by Dual-Pulse Plasma,” 2018 AIAA Aerospace Sciences Meeting, AIAA SciTech Forum, 2018.

25. Glassman, I., Yetter, R., and Glumac, N. *Combustion.* 2014.

Modeling of laser ignition in hydrogen-air mixture

Albina A. Tropina[1], Matthew R. New-Tolley[2], Mikhail N. Shneider[3]
[1]Texas A&M University, Aerospace Department, College Station, TX 77840
[2,3]Princeton University, Mechanical and Aerospace Department, Princeton, NJ 08544

Summary

We present a three temperature plasma model of dual-pulse laser ignition of the hydrogen-air mixture. The results suggested that the calculated ignition delay time strictly depends on the model dimension, showing the highest values for the zero-dimensional model. Kinetic scheme, which includes the avalanche and multiphoton ionization showed a good agreement with the measured ignition delay time. Analysis of energy exchange and ignition mechanisms confirmed mostly thermal effect of the near infrared laser pulse, showing dependence not only on the maximum laser intensity but also on the laser intensity profile.

Nomenclature

I_L = laser beam intensity
E_{Joule} = Joule heating
I_i = ionization potential
P = pressure
τ_{ij} = viscous stress tensor
h = mixture enthalpy
Y_k = k-species mass fraction
M_k = molecular weight
R_u = universal gas constant
C_p = specific heat
$\dot{Q}$ = heat of reaction
$\dot{Q}_j$ = joule heating
Q_{VT} = vibrational-translational (V-T) energy exchange term
m = electron mass
n_e = electron number density
ω_k = chemical source term
ε_0 = the vacuum permittivity
R_{av} = avalanche ionization term
ω_{MPI} = multiphoton ionization probability
τ_{VT} = VT-relaxation time
γ = Keldysh parameter
$v_k^{'}$ = diffusion velocity
ν_m = transport frequency of elastic collisions electrons with neutrals
ν_c = transport frequency of Coulomb collisions electrons with ions
E_v = non-equilibrium vibrational energy per molecule
E_v^0 = thermal equilibrium vibrational energy per molecule
$\hbar w$ =0.29 eV, the vibrational quanta of nitrogen
T_v = vibrational temperature
ω_L = laser angular frequency
ξ = fraction of the absorbed energy going to ionization
E_L = laser electric field

[1] Research Professor, Aerospace Engineering, AIAA Associate Fellow
[2] Graduate Student, Mechanical and Aerospace Engineering, AIAA Student Member
[3]Senior Research Scholar, Mechanical and Aerospace Engineering, AIAA Associate Fellow

Introduction

Advanced ignition systems attract lots of attention nowadays due to increased engine performance requirements, which is of high demand for internal combustion engines [1]. Furthermore, to get a reliable and stable ignition at supersonic flow conditions, when auto-ignition does not occur, new ignition concepts are also needed. It is a well-known fact that a fuel residence time in a supersonic combustor is less than the ignition delay time for the case of thermal ignition, thus advanced more-efficient and less pollutant ignition concepts are intensively developed and researched [2]. Laser ignition has many potential benefits over the conventional spark ignition, it can be achieved without electrodes, with very high flexibility of the ignition location within the combustion chamber, and in fuel-air mixture compositions below the flammability limit. Ignition mechanisms [3] strictly depend on the laser wavelength, repetition rate, the amount of energy deposited and laser focusing. At laser wavelengths below $\lambda < 250\,nm$ ignition can occur through photochemical mechanism without a significant gas ionization, when a chain initiation stage is replaced by the phodissociation of molecules, mainly molecular oxygen by a single photon-excitation. Other ignition mechanisms include thermal ionization, non-resonant and resonant laser spark ignition. Laser thermal ignition starts after optical breakdown, which occurs at laser intensities of $100 \div 300$ GW/Cm^2 and leads to the formation of laser equilibrium plasma with electron temperatures up to 100,000 K. Optical breakdown can be achieved through electron avalanche ionization, non-resonant and resonant multi-photon ionization, depending on the Keldysh parameter $\gamma = \dfrac{\omega_L \sqrt{2mI_i}}{eE_L}$ [4]. The Keldysh parameter represents a ratio of the field oscillation frequency to the electron period of motion and depending on γ optical breakdown can occur in the so-called tunneling limit (at $\gamma \ll 1$) , or in the multiphoton ionization limit (at $\gamma \gg 1$). Gas heating, which eventually causes ignition, occurs through the laser radiation coupling to the fuel-air mixture, due to elastic electron-molecule and Coulomb collisions, dissociation, recombination, attachment and detachment processes as well as heating in the processes of vibrational-translational, electron-vibrational and electron-translational energy exchange. Laser breakdown mechanisms in different media are extensively studied in optics, leading to the development of high-sensitivity laser–induced breakdown spectroscopy LIBS [5]. One issue that inhibits the application of laser ignition is the minimum ignition energy, which is greater than the minimum ignition energy for conventional sparks [6,7]. The greater values of the minimum ignition energy for a single laser pulse ignition are connected with the additional energy required for the laser optical breakdown to create initial seed electrons at the beam focus. Besides a significant amount of the deposited energy in that case is consumed by a propagating blast wave. A new concept of the laser energy deposition on the basis of the combination of ultra-violet (UV) and near infrared laser (NIR) pulses has been proposed in [8] that allows avoiding optical breakdown, minimizes energy requirements and decreases the minimum ignition energy, by tailoring both the energy deposition and heating. The main idea of the dual-laser pulse technique is that a first low energy shaped beam creates initial seeded electrons through multi-photon or tunneling mechanisms without full optical breakdown, then, a second laser pulse with a controllable delay with respect to the first pulse provides enough additional photon energy for an avalanche process, gas heating and successful ignition. This enables the triggering of optical breakdown and controllability of the energy deposition in space. The dual-pulse laser scheme of the combination of the ultraviolet 266 nm and near infrared 1064 nm laser pulses demonstrated an increase of combustion efficiency, flame speed enhancement and successful ignition of the lean fuel-air mixture below the flammability limit [9]. Furthermore, energy consumption and energy losses associated with the shockwave propagation are significantly lower for two successive laser pulses with a time interval compared with a single pulse with the same total incident energy. One and two-dimensional mathematical model of dual-pulse laser ignition using a three-temperature plasma approach [10] was developed in [11,12] to understand a role of plasma driven gas dynamics, chemical kinetics and laser physics in controllable ignition and combustion of methane-air mixtures. Computational studies [11,12] showed that using dual-pulse laser technique allows tailoring an electron temperature, electron number density, size and shape of the formed plasma kernel, which is favorable not only for ignition purposes but also for the supersonic flow control [13]. A main fuel in scramjet engines is hydrogen, so here we present a further development of the dual-pulse laser plasma model for the case of hydrogen-air ignition.

Problem formulation

Initial step in dual-pulse laser ignition is connected with the preliminary ionization by the ultraviolet laser pulse. Photon energy of the 266 nm laser pulse is 4.66 eV, for the 1064 nm pulse is 1.165 eV. Neither pulse has sufficient photon energy to create excited electronic states or ionize mixture components, thus a main ionization

channel is a multi-photon ionization. In the ultraviolet range due to the higher photon energy probability of non-resonant or resonant enhanced (REMPI) multi-photon ionization probability is much higher compared with the MPI in the infrared wavelengths. As was mentioned in [14] there still exist discrepancies between numerical predictions and experimental data on the MPI photoionization rates. Available numerical calculation results suggested that multiphonon ionization rates for hydrogen have strong angular dependence [15]. Considering the lack of other theoretical calculations and also lack of the experimental data due to the limitations of the laser interferometry sensitivity the reliability of the MPI cross-sections is still questionable. Here we evaluated the MPI probability for nitrogen, oxygen and hydrogen on the basis of the Keldych theory in the limit when the laser frequency is much greater that the electron frequency thus $\omega_{MPI} = A\omega_L m^{3/2}\left(\frac{e^2E_L^2}{8m\omega_L^2 I_i}\right)^m$. For the near infrared laser pulse main ionization mechanism is an avalanche ionization. Approximate expression for the avalanche ionization rate was taken as in the paper [16], assuming that it is determined by the ratio of the Joule heating power to the ionization potential of the corresponding mixture component, so

$$\left(\frac{\partial n_e}{\partial t}\right)_{avalanche} = \frac{\partial n_{O_2^+}}{\partial t} + \frac{\partial n_{N_2^+}}{\partial t} + \frac{\partial n_{H_2^+}}{\partial t} \approx \xi E_{Joule}\left(\frac{Y_{N_2}}{I_{N_2}} + \frac{Y_{O_2}}{I_{O_2}} + \frac{Y_{H_2}}{I_{H_2}}\right),$$

where ionization potentials $I_{N_2} = 15.6\ eV, I_{O_2} = 12.2\ eV, I_{H_2} = 15.4\ eV$ and the Joule heating power $E_{Joule} = \frac{e^2 n_e(\nu_m+\nu_c)I_L}{m\varepsilon_0 c(\omega_L^2+(\nu_m+\nu_c)^2)}$.

We run calculations for 0D, 1D and 2D problems of hydrogen-air ignition using three different kinetic schemes. The kinetic scheme 1 includes multiphoton ionization of molecular hydrogen and additional ion H_2^+ and recombination reactions associated with this ion. The kinetic scheme 2 additionally includes a possible photodissociation of molecular hydrogen, oriented on the data about a strong field dissociation of hydrogen in a linearly polarized laser field with an intensity of 10^{14} W/m^2. That effect was taken into account by initial conditions reflecting the percentage of the fuel dissociated (1%). The kinetic scheme 3 includes electronically excited states of molecular and atomic oxygen $O_2(a\ ^1\Delta_g)$ and O (^{1}D) with main reactions from [17,18].

A mathematical model includes continuity (1) and momentum (2) equations and equations for the translational temperature of the gas written in terms of enthalpy h (3), equations for the electron temperature T_e (4) and vibrational energy E_V (5) combined with the balance equations(not shown here) for positive ions $O_2^+, N_2^+, O^+, N^+, O_4^+, NO^+, H_2^+$, negative ions O_2^-, O^-, electrons and neutrals $O_2, N_2, O, N, NO, O_3, H, H_2, OH, H_2O, HO_2, H_2O_2$. Main reactions for the air plasma are from the paper [10], the hydrogen combustion scheme was taken from [19], the charge exchange and recombination reaction rates for H_2^+ were of the same order as for main air ions.

$$\frac{\partial \rho}{\partial t} + \nabla\cdot(\rho v_i) = 0 \tag{1}$$

$$\frac{\partial(\rho v_i)}{\partial t} + \nabla\cdot(\rho v_i v_i) = -\nabla p + \nabla\cdot\hat{\tau} \tag{2}$$

$$\frac{\partial(\rho h)}{\partial t} + \frac{\partial}{\partial x_i}(\rho v_i h) + \frac{\partial(\rho K)}{\partial t} + \frac{\partial}{\partial x_i}(\rho v_i K) = \frac{dp}{dt} + \nabla\cdot(\hat{\tau}\cdot\bar{v}) + \tag{3}$$

$$+\frac{3}{2}\delta_e(\nu_m+\nu_c)k_B(T_e-T) + \frac{E_v(T_v)-E_0(T)}{\tau_{VT}} + Q_{ch}$$

$$\frac{\partial}{\partial t}\left(\frac{3}{2}n_e k_B T_e\right) + \frac{\partial}{\partial x_i}\left(\frac{5}{2}\overrightarrow{\Gamma_e}k_B T_e\right) = \nabla\left(\lambda_e\frac{\partial T_e}{\partial x_i}\right) + Q_J - \tag{4}$$

$$+\frac{3}{2}\delta_e(\nu_m+\nu_c)k_B(T_e-T) - \frac{3}{2}n_e k_B(T_e-T_v)\nu_{ev}(T_e) - Q_e$$

$$\frac{\partial E_v}{\partial t} + \frac{\partial}{\partial x_i}(v_i E_v) = \nabla(D_v\frac{\partial E_v}{\partial x_i}) - \frac{E_v(T_V)-E_0(T)}{\tau_{VT}} + \frac{3}{2}n_e k_B(T_e-T_v)\nu_{ev}(T_e) \tag{5}$$

$$\tau_{ij} = 2\mu v_{ij} - \frac{2}{3}\mu v_{jj}\delta_{ij} \quad (6)$$

Equations (5,6) include the energy exchange rate of the vibrational excitation due to collisions between molecules and electrons. The electron-vibration excitation frequency ν_{ev} is a function of the electron temperature and was taken from [10]. The electron energy balance additionally includes the energy transfer rate between electronic and translational temperatures in the form $\frac{3}{2}\delta_e(\nu_m + \nu_c)k_B(T_e - T)$, which is proportional to the elastic collision frequency ν_m and Coulomb collision frequency ν_c, taken from [10]. The electron heat conductivity equals to $\lambda_e = \frac{5}{2}k_B n_e D_e$. Additional term in eq.(4) Q_e presents the electron energy loss on the ionization, excitation, attachment and detachment processes.

Initial conditions for the problem were as follows. The initial electron temperature is $T_e = 1$ eV, the vibrational and gas temperatures are equal to T=400 K in the plasma channel of the radius r=50 μm and T=300 K outside of the channel. The laser intensity on the axis I_L was varied $I_L = 2 \cdot 10^{13} \div 40 \cdot 10^{13}$ W/m^2. Initial concentration of electrons on the axis after the UV pulse $n_e(0)$ was varied and initial concentrations of ions were inversely proportional to their ionization potential. We briefly discussed details of the computational scheme, verification and validation procedures for 1D and 2D problems in our previous papers [11,12].

On the early stage of dual-pulse laser ignition formed laser plasma is in a non-equilibrium state, because a significant part of the laser energy at the electron temperatures around 1eV is spent on the vibrational excitation and mainly stored in nitrogen molecules. We used the energy exchange term between translational and vibrational temperatures in the Landau-Teller form. It is worth noting that hydrogen addition significantly influences the vibrational excitation of nitrogen ($v = 1$). This influence is demonstrated by the energy loss dependence on the reduced electric field in air and hydrogen-air mixture at atmospheric pressure and T=400 K, presented in Fig.1. Decrease of the vibrational-translational time τ_{VT} of the vibrationally excited nitrogen in the presence of molecular hydrogen was also mentioned in [20]. Millikan and White [21] expression for the vibrational-translational relaxation time gives an estimation of τ_{VT} as a function of pressure and temperature in a form $p\tau_{VT} = exp\left[A\left(T^{-1/3} - B\right) - 18.42\right]$, which presents a compilation of the available experimental data and the Landau-Teller harmonic oscillator model and $p\tau_{VT}$ is in atm·s. In our model we used recommended corrected values of coefficients A=80.87 and B=0.01753 from [20] for the hydrogen-air mixture to explain much faster VT relaxation rates in hydrogen-air mixtures compared with pure air.

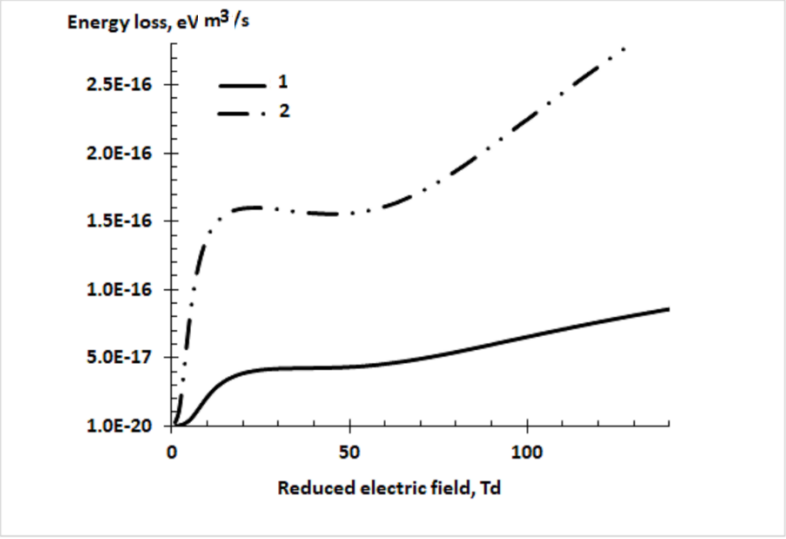

Fig.1. Energy losses in the process of the vibrational excitation of nitrogen ($v = 1$) depending on the reduced electric field: 1) stoichiometric H_2-air mixture, 2) pure air.

Results and discussion

We verified the base kinetic scheme for neutral components [19] using 0D calculations of the auto-ignition delay times of the stoichiometric hydrogen-air mixture at different temperatures. Results presented in Fig.2 showed a good agreement between calculation results and experimental measurements, confirming our choice of the base kinetic model.

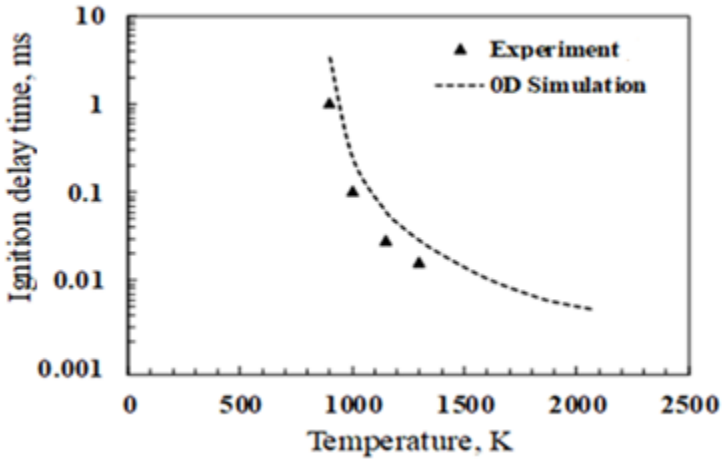

Fig.2. Ignition delay time dependence on temperature (0D problem). Experimental data are from [17].

The initial seeded electron number density after the ultra-violet pulse was varied from $n_{e0} = 10^{12}$ cm^{-3} ÷ 10^{17} cm^{-3}. The initial ionization region was of the ellipsoidal shape with the maximum elongations in *x* and *y* directions of $l_x = 500\ \mu m, l_y = 100\ \mu m$. Fig. 3 shows temporal dynamics of the formed ignition kernel at $n_{e0} = 10^{17}$ cm^{-3}. These results suggested that the first ultraviolet pulse creates a significant concentration of electrons through multiphoton ionization and following avalanche ionization.

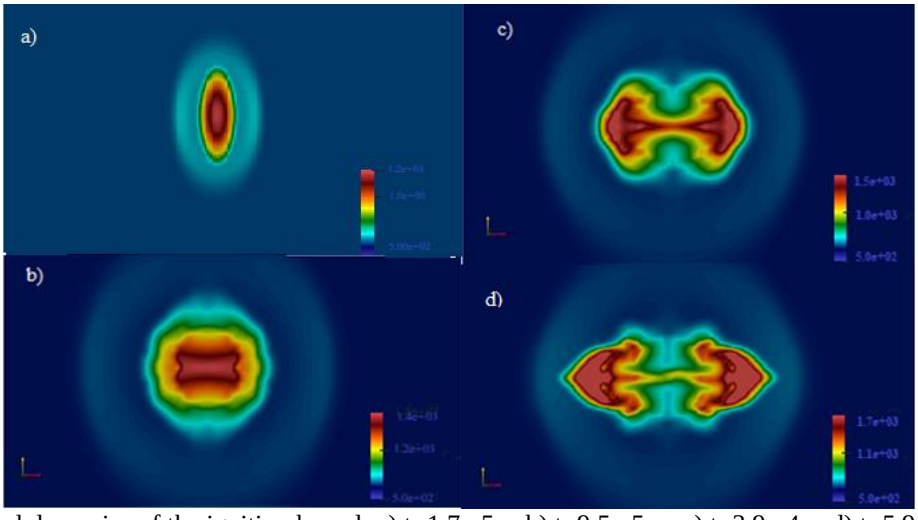

Fig.3. Temporal dynamics of the ignition kernel: a) t=1.7e-5 s; b) t=9.5e-5 s ; c) t=3.9e-4 s; d) t=5.9e-3 s.

The spatial-temporal ignition kernel dynamics is similar to dynamics observed in experiments and in our previous simulations for the methane-air mixture ignition with the formation of the reverse flow and toroidal structure of the hot kernel. We also evaluated ignition delay time using three models. In the simulations a main criterion of ignition was the largest temperature changing rate dT/dt. For the base case of dual-pulse laser ignition of the stoichiometric hydrogen-air plasma calculated ignition delay times showed a strong dependence on the dimension of the problem. Fig.4 presents a comparison between calculated and measured ignition delay time. We extracted experimental ignition delay time from the pressure traces [22] for dual pulse ignition in the hydrogen-air mixture ($\Phi = 1$), assuming that a sudden rise in pressure characterizes an onset of ignition. Calculation results for the 0D case were run at the initial temperature T=900 K. In the one-dimensional calculations we used three kinetic schemes, the two-dimensional problem was run with the kinetic scheme 1. For dual-pulse laser ignition a calculated ignition delay time for a kinetic scheme 3 with $O_2(a\ ^1\Delta_g)$ and O (^{1}D) was lower compared with calculation results for schemes 2,3, which do not include electronically excited states. This effect is well known and connected with the fact that any addition of radicals helps to chain breaking on the initial stage of ignition and promotes ignition at low temperatures, leading to the considerable decrease of the ignition delay time, as was discussed in details in [17,18]. Kinetic schemes 2,3 showed a better agreement with the experimental ignition delay time. We suggested that a main reason for that is a relatively low photon energy of the second pulse. A main possible channel of the formation of the electronically excited O (^{1}D) by the 266 nm laser pulse can be connected with the photo-dissociation of ozone, but concentration of ozone generated by the discharge plasma is too low. Furthermore, the photon energy of 1064 nm laser pulse is also lower that the energy needed to photo-dissociate molecular oxygen, a process which occurs at the laser wavelengths $\lambda < 193\ nm$. Thus, the main role of the infrared pulse was to heat a mixture to the auto-ignition temperature, as minimum.

Heating process strictly depends not only on the laser intensity, seeded initial electron number density but also on the laser intensity shaping with time. Balance of the electron energy on the plasma channel axis during the near infrared laser pulse energy deposition for the case of the stoichiometric hydrogen-air mixture ignition at $n_{e0} = 10^{12}$ cm^{-3}, $I_L = 2 \cdot 10^{14} W/m^2$ is presented in Fig.5. For clarity energy losses on vibrational excitation were scaled as $Q'_{EV} = 0.6 Q_{EV}$. It is seen, that 99% of the absorbed laser power is transferred into vibrational degrees of freedom and a small fraction of the electron energy left for ionization and gas heating through electronic-translational energy exchange. The electron-vibrational energy exchange (last term in the Eq. 5) is proportional to the electron number density and an increase of the initial concentration of electrons leads to the increase of the energy transferred to

vibrational excitation of nitrogen if the electron temperature slightly differs from 1 eV. As a result we observed a negligible heating and no ignition at the relatively high initial electron number density up to $n_{e0} = 10^{17}$ cm^{-3}. A situation cardinally changes if the shape of the heating pulse changes. Fig.6 shows two modeling profiles for the laser intensity, I_1 and I_2 with the different slope versus time with the same maximum laser intensity. For the profile I_1 we observed a negligible heating after the NIR pulse if the initial seeded electron number density was below $n_{e0} = 10^{17}$ cm^{-3}. For the profile I_2 the electron energy balance showed a significant increase of the energy spent on the ionization (Fig,5). As a result even at the initial electron number density $n_{e0} = 10^{12}$ cm^{-3} and still having a significant portion of the energy spent on the vibrational excitation after the 20 ns infrared pulse a mixture was heated to 2000 K, which was sufficient for subsequent ignition.

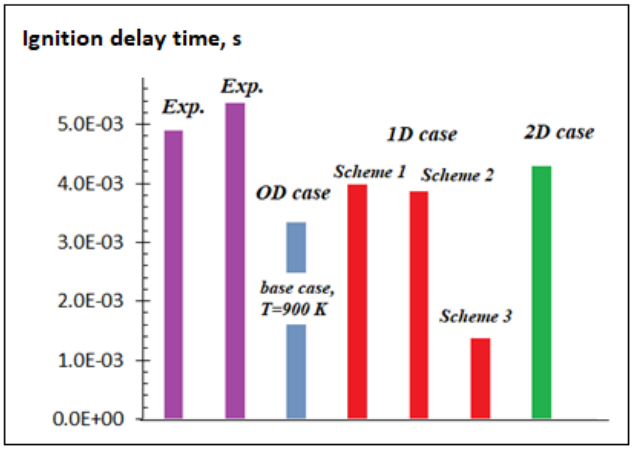

Fig.4. Ignition delay time dependence on the problem dimension.

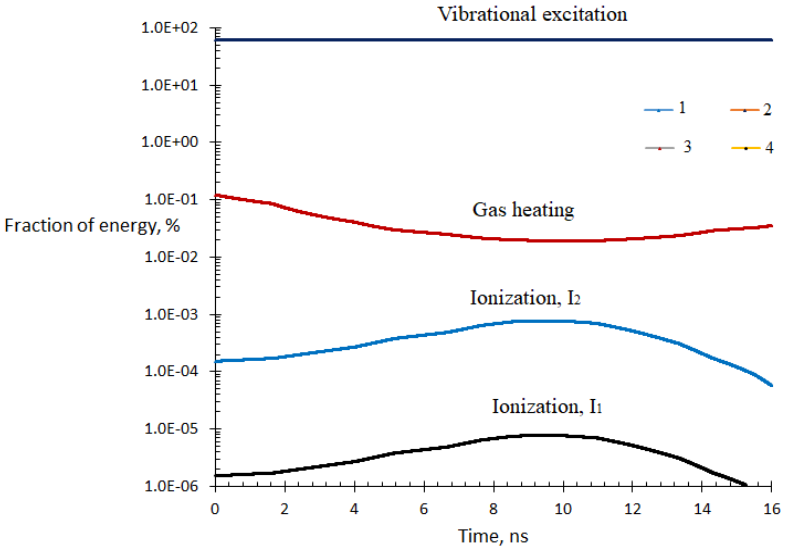

Fig.5. Fraction of the electron energy transferred to vibrational excitation, ionization and gas heating.

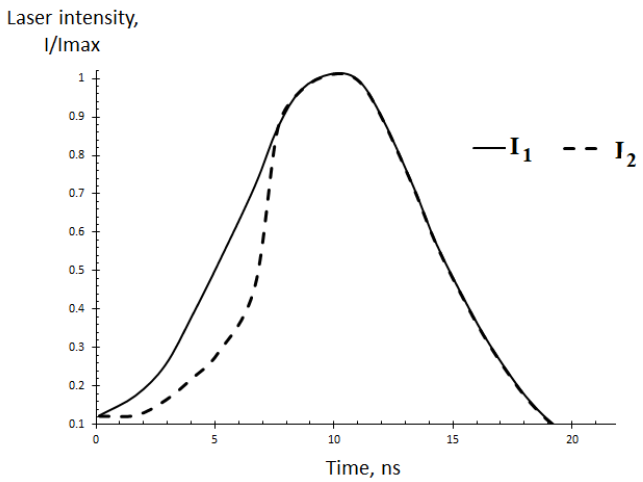

Fig.6. Modeling profiles of the laser intensity.

Conclusions

Three temperature plasma model was used to analyze ignition of the hydrogen-air mixture by the dual-pulse laser. The results showed that the calculated ignition delay time depends on the numerical model dimension. The measured ignition delay time for the case of the dual-pulse laser ignition of the stoichiometric hydrogen-air mixture was in a good agreement with simulation results for the kinetic scheme, which includes avalanche and multiphoton ionization of oxygen, nitrogen and hydrogen. Analysis of the exchange mechanisms between translation, vibrational and electronic energies confirmed mostly thermal effect of the infrared laser pulse. The results also suggested, that gas heating during the laser pulse energy deposition depends on the laser intensity profile.

Acknowledgements

This work has been supported by the DOD-AFOSR award under Subcontract with Princeton University SUB0000242.

References

1. Tropina, A.A., Shneider, M.N., Miles, R.B. ,Ignition by Short Duration, Nonequilibrium Plasma: Basic Concepts and Applications in Internal Combustion Engines, Combust. Sci. Technol., 2016, Vol. 188, No. 6, pp. 831–852.
2. O'Briant, S.A., Gupta, S.B., Vasu, S.S., Review: laser ignition for aerospace propulsion, Propulsion and Power Res., 2016, Vol. 5, No. 1, pp. 1–21.
3. Ronney, P. D., Laser versus conventional ignition of flames, Opt. Eng., 1994, Vol. 33, No. 2, pp. 510-521.
4. Keldysh, L.V. Zh. Eksp. Teor. Fiz. 47, 1945 (1964) [Sov. Phys. JETP 20, 1307 (1964)].
5. F. Anabitarte, A. Cobo, J. M. Lopez-Higuera. Laser-Induced Breakdown Spectroscopy: Fundamentals, Applications, and Challenges, ISRN Spectroscopy, Vol, 2012, 285240.
6. Brieschenk, S., O'Byrne, S., and Kleine, H., Laser-Induced Plasma Ignition Experiments in a Scramjet Inlet, AIAA Paper 2011-504.
7. Syage, J. A., Fournier, E. W., Rianda, R., and Cohen, R. B. "Dynamics of Flame Propagation Using Laser-Induced Spark Initiation: Ignition Energy Measurements", Journal of Applied physics, Vol. 34, 1988, pp.1499-1507.
8. Dumitrache, C., VanOsdol, R., Limbach, C.M., Yalin, A.P. Control of Early Flame Kernel Growth by Multi-Wavelength Laser Pulses for Enhanced Ignition, Sci. Rep., 2017, Vol. 7, No. 1, p. 10239.
9. Dumitrache, C., VanOsdol, R., Limbach, C.M., Yalin, A.P. , Laser Ignition of Propane-Air Mixtures Using a Dual-Pulse Technique, AIAA-Paper 2017-1976.

10. Shneider ,M.N., Zheltikov, A., Miles, R.B., Tailoring the air plasma with a double laser pulse, Phys. Plasmas, 2011, Vol. 18, p. 063509.
11. Tropina, A.A., Shneider, M.N., Miles, R.B., Mathematical Model of Dual-Pulse Laser Ignition, J. Propulsion and Power, 2018, Vol.34, p. 408-414.
12. Mahamud,R., Tropina, A.A., Shneider , M.N., Miles, R.B. Dual-pulse laser ignition model. Phys. of Fluids, 2018, Vol.30, p.106104.
13. Hartman D., Mahamud,R., Tropina, A.A., Dual-pulse laser energy deposition for the flow control in a supersonic flow, AIAA-paper 2019-3355.
14. Sharma, M. N. Slipchenko, M. N. Shneider, X. Wang, K. A. Rahman, A. Shashurin, Counting the electrons in a multiphoton ionization by elastic scattering of microwaves, Scientific reports, 2018, Vol. 8, p. 2874.
15. Apalategui, A. Saenz, A. Multiphoton ionization of the hydrogen molecule H_2, J. Phys. B: At. Mol. Opt. Phys., 2002, Vol.35, p.1909.
16. Yalin, A.P., Wilvert, N., Dumitrache, C., Joshi, S., Shneider, M.N., Laser plasma formation assisted by ultraviolet pre-ionization, Phys. Plasmas,2014, Vol. 21, p. 103511.
17. Popov N.A., Effect of singlet oxygen $O_2(a\ ^1\Delta_g)$ molecules produced in a gas discharge plasma on the ignition of hydrogen-oxygen mixtures, Plasma Sources Science and Technology, 2011, Vol.20, p.045002.
18. Popov, N.A. Plasma assisted ignition of combustible mixtures. Effect of electronically excited O(1D) atoms and vibrationally excited molecules. 53rd AIAA Aerospace Sciences Meeting, 5-9 Jan. 2015, Kissimmee, AIAA Paper-2015-0410.
19. Li, J., Zhao, Z., Kazakov, A., Dryer, F. An updated comprehensive kinetic model of hydrogen combustion, Int. journal of Chemical Kinetics, 2004, vol.36, p.566-575.
20. Taylor, B.D., D.A. Kessler, D.A., Oran, E.S. Estimates of Vibrational Nonequilibrium Time Scales in Hydrogen-Air Detonation Waves, 24th ICDERS, July 28 – August 2, 2013 Taipei, Taiwan.
21. Roger C. Millikan, R.C., White, D.R., Systematics of Vibrational Relaxation, J. Chem. Phys., 1963, Vol. 39, p. 3209.
22. Butte, C., Yalin, A.P., Dumitrache, C. Dual-Pulse Laser Ignition Using Oxygen REMPI Preionization, AIAA Aviation Forum, 17-21 June 2019, Dallas,TX, AIAA Paper 2019-3117.

Journal of Physics D: Applied Physics

Dynamics of dual-pulse laser energy deposition in a supersonic flow

To cite this article before publication: Rajib Mahamud *et al* 2020 *J. Phys. D: Appl. Phys.* in press https://doi.org/10.1088/1361-6463/ab7fd3

Dynamics of dual-pulse laser energy deposition in a supersonic flow

Rajib Mahamud, Daniel W. Hartman, and Albina A. Tropina
Texas A&M University, Aerospace Department, College Station, TX 77840

Abstract

Dynamics of plasma generated by the dual-pulse laser in a supersonic flow was studied numerically. The mathematical model includes species, momentum, electronic, vibrational and translational energy equations for the multicomponent ionized air. The model examines temporal dynamics of the formed air plasma and how it affects the drag, pressure signature and vorticity generation in a supersonic flow around a wedge. We observed that nonequilibrium plasmas is more effective in the drag reduction compared with the simultaneous thermal energy addition. The maximum drag reduction of around 50% and the maximum drag coefficient reduction of 30% was attained through the dual-pulse laser energy deposition. Variation of the plasma spot orientation did not significantly influence the drag reduction. We suggested that the surface pressure changes were not controlled by the vorticity generation but occurred due to the density changes and the formation of the low–density plasma spot.

Keywords: supersonic flow control, laser, energy deposition, numerical modeling

1. Introduction

The energy deposition to high speed flows can lead to a drag reduction via the decrease of surface pressure and the modification of shock wave. The deposition of energy could be realized by different techniques using plasma of spark, laser, microwave, nanosecond pulsed discharges and their combination. Experimental studies for blunt bodies in a supersonic flow [1-3] showed a significant drag reduction (up to 80%) depending on the discharge energy and geometry of the blunt body.

A new concept of the laser energy deposition on the basis of the combination of ultra-violet (UV) and near infrared laser (NIR) pulses has been proposed in [4-8] that allows avoiding optical breakdown and minimizes energy requirements by tailoring both the energy deposition and heating. The main idea is that a first shaped beam creates initial seeded electrons; then, a second laser pulse with a controllable delay with respect to the first pulse provides enough energy for an avalanche process to occur. This restricts the triggering of optical breakdown and enables the controllability of the energy deposition in space. The initial gas ionization without significant optical breakdown is achieved by the first UV laser pulse and the second near-infrared (NIR) pulse serves as a source for controllable energy deposition into the pre-ionized gas. As was shown in [8] for a case of dual-pulse laser ignition depending on the spatial electron number density profile of the first ionizing pulse, the shape of the overall laser energy deposition spot could be different. Furthermore, plasma created by the dual- pulse laser at the initial stage is non-thermal with low power requirements compared with a single laser pulse and could be beneficial for the supersonic flow control.

The basic effect of the laser energy deposition is thermal, connecting with localized flow heating by the discharge plasma. In the heated low-density region, a supersonic flow shock wave is weakened due to the local Mach number decrease, which leads to the drag reduction. The review of Knight [9] provided the analysis of thermal effects of the energy deposition on supersonic flow, presenting simulation results for different forms of steady and unsteady Gaussian energy sources and experimental observations of the pulsed energy deposition by the high frequency laser and microwave discharges. Both computational and experimental studies confirmed a possibility of the flow control and drag reduction by discharge plasma.

In the experimental and computational study [10] authors considered a single and double laser pulse energy deposition and showed that an additional mechanism leading to the shock wave weakening and drag reduction is connected with the Richtmyer-Meshkov instability and appearance of small-scale vortex structures. They also showed that the shape of the energy deposition region played a significant role in the resulting flow structure.

Numerical models [11-12] studied the generation of the Richmyer-Meshkov and shear layer instabilities and the vortex drag reduction mechanism in details. Authors concluded that a ratio of the specific heat capacities of the gas medium and the energy source significantly influenced the triple-shock configuration and the stagnation pressure. The energy deposition was modelled as the heated rarefied layer with the same velocity and pressure as in the incoming flow. In a recent study [13] authors evaluated energetic efficiency of the single laser pulse energy deposition in the quiescent air and upstream of the hemisphere cylinder at M=2. Authors used the full thermochemistry model for the ionized air and simulated the laser energy deposition as a heat source located upstream of the hemisphere tip. Authors concluded that a main effect of the high-repetition laser energy deposition is connected with the pressure decrease and generation of vortices.

It should be noted that the generation of such vortices [13] driven by the Richtmyer-Meshkov instability is one of the mechanisms of the pressure decrease. Vortices originate at the boundary of the laser energy deposition region and at the interaction zone between the low-density region and a bow shock. In both cases, a vortex strength could be manipulated by the change of the density gradient and local non-uniformity created by the formed plasma plume. Authors of the paper [14], considering a plasma sheet actuator interaction with a shock wave, concluded that the effect of the non-uniform energy deposition cannot be neglected and can lead to the generation of large –scale coherent vortices and transition to turbulence. A parametrical study [15] suggested that the vortex energy strength is proportional to the radius of the low –density region generated by the laser discharge. For optical discharges, the intense laser pulse propagating over large distances creates the low density and high temperature filament upstream of the blunt body. The recent experimental study showed that the plasma filament created by the ultrashort laser pulse

forms a low-density region that interacts with the bow shock [16]. A number of recent numerical studies also confirmed the formation of vorticity on the interaction of low density region and bow shock, that results a modulation of drag coefficient and flow separation in the high speed flows [17-21]. However, dynamics of the formed laser plasma was not modeled in those studies.

This paper explores a concept of the dual-pulse laser energy deposition in the supersonic flow, considering a laminar flow past a wedge at M=2 in the frame of the three-temperature plasma model, taking into account temporal dynamics of electrons and ions and vibrational non-equilibrium [7,8]. We examined an influence of the initial ionization level and non-uniformity of the formed laser plasma on the pressure distribution, vorticity generation and drag reduction.

2. Problem formulation

Geometry of the problem and boundary conditions are presented in Figure1. The simulations were based on the Navier-Stokes equations for a compressible ideal gas with free stream conditions

$$M_\infty = 2, T_\infty = 300\ K, P_\infty = 101325\ Pa, \rho_\infty = 1\ \frac{kg}{m^3}, Re_\infty = 4 \cdot 10^5, Y_{N_2} = 0.765, Y_{O_2} = 0.235$$

On the first stage of calculations, we obtained the convergent solution for the steady laminar supersonic flow past the wedge in the channel. Results of those calculations are initial conditions for the dual-pulse laser energy deposition model. Dynamics of the first ultra-violet pulse was not modelled but was taken into account by appropriate initial conditions considering a multi-photon ionization as a dominant ionization process and assuming a Gaussian shape profile for charged species so

$$n_{O_2^+} = n_{O_2^+}(0)\exp\left(-\frac{(x^2+y^2)}{r_f^2}\right),\ n_{N_2^+} = n_{N_2^+}(0)\exp\left(-\frac{(x^2+y^2)}{r_f^2}\right),\ n_e = n_e(0)\exp\left(-\frac{(x^2+y^2)}{r_f^2}\right),$$

where $n_{O_2^+}(0), n_{N_2^+}(0), n_e(0)$ are the initial number densities of positive ions and electrons on the axis of the plasma channel. We also modelled experimentally observed left or right offset cases, when a maximum of the initial electron number density moved to the left or right from the center. The initial electron number density $n_e(0)$ was varied in limits 10^{16}~10^{18} $\left[-\frac{(x^2+y^2)}{r_f^2}\right]$ cm^{-3} and initial number densities of positive ions were inversely proportional to their ionization potential. The value of initial electron number density depends on laser intensity, pulse width, wavelength and photoionization rates. For example, a laser pulse with an intensity of 4×10^{13} W/cm^2 and a pulse width of 100 fs would result in an initial number density of 1×10^{17} $\left[-\frac{(x^2+y^2)}{r_f^2}\right]$ cm^{-3} [6]. The initial ionization region was of the ellipsoidal shape with the maximum elongations in *x* and *y* directions of $l_x = 500\ \mu m, l_y = 100\ \mu m$ and a channel diameter was d=12 cm. An initial electron temperature was $T_e = 1\ eV$ and vibrational and gas temperatures were equal to T= $300\ K$. Based on this initial number density we assume that the NIR pulse energy absorbed by the gas varies in limits $E_L = 25$ ~$250\ mJ$. .

A mathematical model includes continuity (1) and momentum (2) equations and equations for the translational temperature of the gas written in terms of enthalpy *h* (3), equations for the electron temperature T_e (4) and vibrational energy E_V (5) combined with balance equations (not shown here) for positive ions $O_2^+, N_2^+, O^+, N^+, O_4^+, NO^+$, negative ions O_2^-, O^-, electrons and neutrals O_2 , N_2 , O, N, NO, O_3 . A description of the plasma model is described in reference [7]. Main reactions for the air plasma can be found in reference [6].

$$\frac{\partial \rho}{\partial t} + \nabla \cdot (\rho v_i) = 0 \quad (1)$$

$$\frac{\partial (\rho v_i)}{\partial t} + \nabla \cdot (\rho v_i v_i) = -\nabla p + \nabla \cdot \hat{\tau} \quad (2)$$

$$\frac{\partial(\rho h)}{\partial t}+\frac{\partial}{\partial x_i}(\rho v_i h)+\frac{\partial(\rho K)}{\partial t}+\frac{\partial}{\partial x_i}(\rho v_i K)=\frac{dp}{dt}+\nabla\cdot(\dot{\tau}\cdot\bar{v})+ \quad (3)$$

$$+\frac{3}{2}\delta_e(\nu_m+\nu_c)k_B(T_e-T)+\frac{E_v(T_v)-E_0(T)}{\tau_{VT}}$$

$$\frac{\partial}{\partial t}\left(\frac{3}{2}n_e k_B T_e\right)+\frac{\partial}{\partial x_i}\left(\frac{5}{2}\overrightarrow{\Gamma_e}k_B T_e\right)=\nabla\left(\lambda_e\frac{\partial T_e}{\partial x_i}\right)+Q_J- \quad (4)$$

$$+\frac{3}{2}\delta_e(\nu_m+\nu_c)k_B(T_e-T)-\frac{3}{2}n_e k_B(T_e-T_v)\nu_{ev}(T_e)-Q_e$$

$$\frac{\partial E_v}{\partial t}+\frac{\partial}{\partial x_i}(v_i E_v)=\nabla(D_v\frac{\partial E_v}{\partial x_i})-\frac{E_v(T_V)-E_0(T)}{\tau_{VT}}+\frac{3}{2}n_e k_B(T_e-T_v)\nu_{ev}(T_e) \quad (5)$$

$$\tau_{ij}=2\mu v_{ij}-\frac{2}{3}\mu v_{jj}\delta_{ij} \quad (6)$$

We used the energy exchange term between translational and vibrational temperatures in the Landau-Teller form with the vibrational relaxation time τ_{VT} [22]. Equations (5,6) also include the energy exchange rate of the vibrational excitation due to collisions between molecules and electrons. The electron-vibration excitation frequency ν_{ev} is a function of the electron temperature and was taken from [23]. The electron energy balance additionally includes the energy transfer rate between electronic and translational temperatures in the form $\frac{3}{2}\delta_e(\nu_m+\nu_c)k_B(T_e-T)$, which is proportional to the elastic collision frequency ν_m and Coulomb collision frequency ν_c, taken from [23]. The joule heating term has a form $Q_J=\frac{e^2 n_e I_L(\nu_m+\nu_c)}{\varepsilon_0 c m_e[w_L^2+(\nu_m+\nu_c)^2]}$, where the laser intensity equals to $I_L=E_L S_f$ and the laser frequency is $\omega_L=\frac{2\pi c}{\lambda}$. The electron heat conductivity equals to $\lambda_e=\frac{5}{2}k_B n_e D_e$. Additional term in eq.(4) Q_e presents losses of the electron energy on the ionization, excitation, attachment and detachment processes.

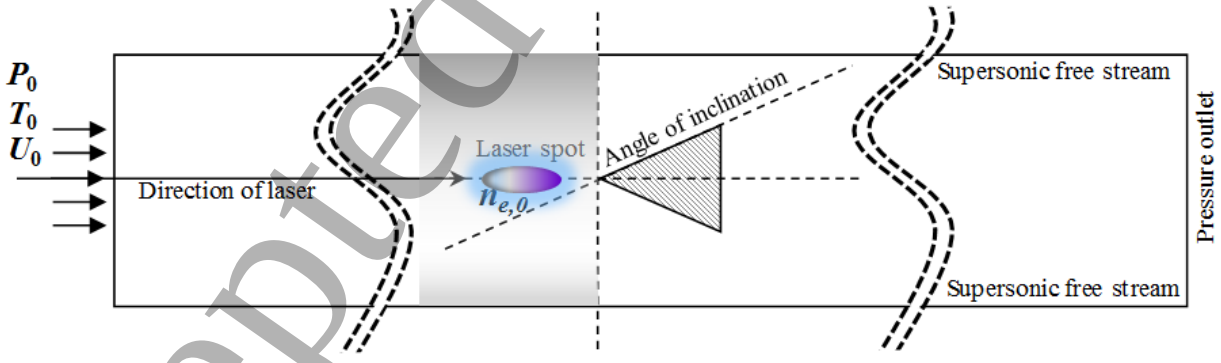

Figure1. A schematic of the computational domain.

The system of equations was solved using a custom made solver based on OpenFOAM C++ libraries [24]. We utilize a finite volume method and a PIMPLE algorithm to couple the continuity and momentum equations, which is a combination of SIMPLE and PISO algorithms. The PIMPLE algorithm provides stability at high Courant numbers (CFL>>1) and therefore, the time step can be increased drastically. The GAMMA differencing scheme was used for the discretization of the spatial terms and capture shock in supersonic flow conditions. We used the first-order implicit Euler scheme for the discretization of the temporal term and a second-order unbounded scheme for the advection terms, which limits the upwind scheme in the regions with strong gradients. A second-order central difference scheme

was chosen for diffusion terms and mass fluxes. To limit the maximum convective CFL number to CFL =1 we suggested an adjustable time step. The model implements unstructured quadrilateral mesh.

The efficiency of the laser energy deposition can be estimated by the ratio of work done and the energy deposited into the medium. The energy deposition Q_{plasma} depends on the initial electron number density created by the first ionizing pulse, on the laser intensity and on the duration of the second pulse. We introduced aerodynamic efficiency, as a ratio of the energy saved due to the drag reduction $W_{D,red}$ to the total energy Q_{plasma} deposited by the discharge. Thus,

$$\eta_{aerodynamic} = \frac{W_{D,red}}{Q_{plasma}}, \tag{7}$$

where $W_{D,red} = \int_{\tau=t1}^{t2}(F_{d,base} - F_{d,plasma})\, U\, d\tau$, $F_{d,base}, F_{d,plasma}$ are the drag force for the base case (no plasma) and the drag force for the case with the dual pulse laser energy deposition. In addition, the power effectiveness of the laser energy deposition can be defined as follows

$$\eta_{power} = \frac{(F_{D,reduced}]_{max} \cdot U}{Q_{plasma}/t}, \tag{8}$$

where t_D is the time of drag force changes due to the laser energy deposition.

Table 1 shows main baselines conditions for the problem considered.

Table 1: Baseline conditions for dual-pulse laser energy deposition

Variables	
u (m/s)	500 ~ 800
Ma	1.5-3
$n_{e,0,max}$ (1/cm^3)	10^{16}~10^{18}
τ(ns)	20
α	8°
$T_\infty\ (K)$	300
$T_{e,0}\ (K)$	12000
$T_{v,0}\ (K)$	600
$P_\infty (Pa)$	101325
Re_∞	10^5 ~ 10^6
C_d	0.51, 0.46, 0.41,0.36

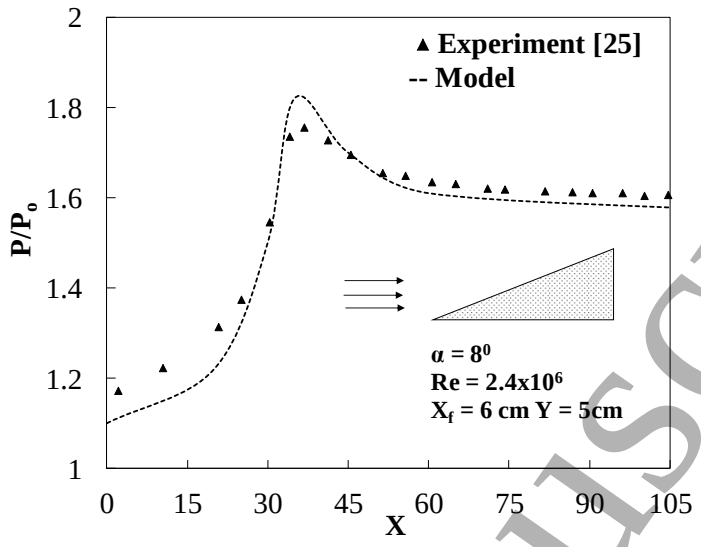

Figure 2. A comparison of numerical results with experiment [25] for the axial pressure distribution of flow over a wedge for a high speed flow.

3. Results and Discussion

For the validation of the model, we took the experimental data from [25], where the authors studied a flow field and surface pressure distribution for the laminar supersonic flow around wedges at Mach number M=2.25 having different incidences α with respect to the freestream. The calculated and measured surface pressure distributions are shown in Figure 2 for the wedge with $\alpha = 8^{\circ}$. In Figure 2, the pressure was normalized with the free-stream pressure and was plotted at a distance from the leading edge, where the location *x=0* corresponds to the shock wave position. The Reynolds number of the problem, Re=2.4×10^6 , was based on the measured boundary layer thickness of 2.2 mm. It is seen that calculations and experimental results not only exhibit common trends in the pressure distribution but also showed a good quantitative agreement. Details of the validation and verification procedure of the three-temperature plasma model for the dual-pulse laser energy deposition were discussed in our previous work [8].

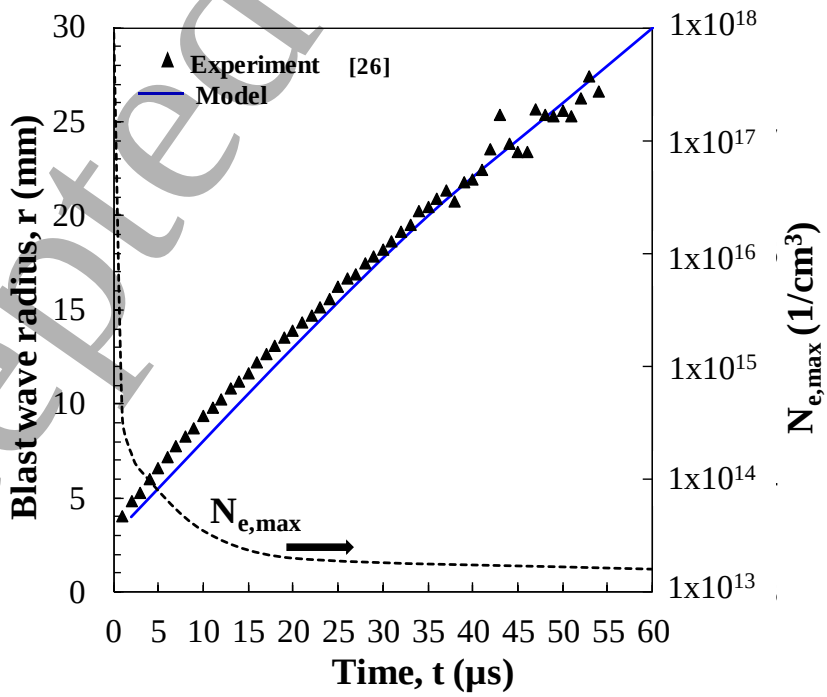

Figure 3. A blast wave radius as a function of time for the laser energy deposition in the quiescent air.

We additionally validated the shock capturing capability of the model by the comparison between the experimental and numerical blast wave radius. A blast wave is formed after the energy deposition by the rapid expansions of the high pressure and temperature area and propagates into the ambient air. We determined the position of the blast wave by locating the maximum pressure along the radial distance from the center of the energy deposition area. For that case, the initial electron number density $n_e(0) = 10^{17}\ cm^{-3}$ and energy deposited by the second pulse was E= 250 mJ. Figure 3 shows temporal profiles of the electron number density and measured and calculated blast wave radius. The experimental blast wave radius [26], based on Rayleigh scattering, measured the radial location of the spherical blast wave in quiescent air. Though, the experimental conditions simulates laser induced optical breakdown in air, a reasonable agreement between experimental and model data was observed. Therefore, it can be deduced that the plasma life time or breakdown conditions have a minimal effect on the blast wave that has formed initially and propagated away from the core. The energy deposition in the experiment was performed with a focused Nd; YAG laser that has a pulse width of 10 nanoseconds generating two pulses at a maximum rate of 200 mj energy per seconds. A higher energy deposition in the experiment indicate significant energy losses in the air. Oriented on the electron number density, the plasma life time for this particular case was around $5\sim20\ \mu s$.

To model the laser energy deposition in the air flow, first, we simulated a steady supersonic flow around the wedge with $\alpha = 8^{\circ}$ (Figure1) at atmospheric pressure conditions and Reynolds number $Re_D = 2 \times 10^5$, where the characteristic length scale was the diameter of the channel. Figure 4 shows the velocity, temperature and pressure distribution in the calculation domain, which clearly indicated the supersonic flow structure.

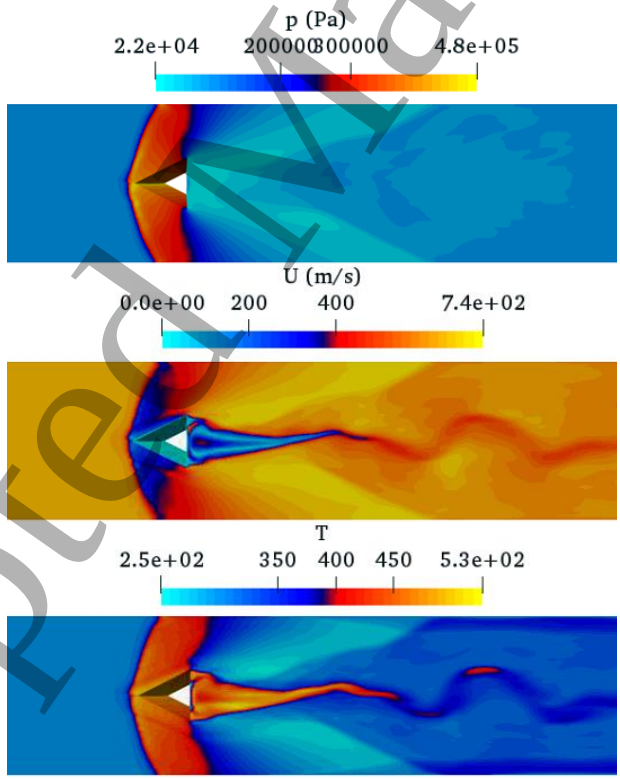

Figure 4. Steady supersonic flow past a wedge at M=2.

To negate the effect of any transient flow conditions, the dual pulse laser energy was deposited in the converged solution of the steady supersonic flow. The initiation of plasma kernel formation in a high speed flow requires a significantly higher energy than that of a quiescent condition [27]. It was assumed that an initial ionization region of the ellipsoidal convex shape was created ahead of the wedge at *x=0.2m*, located symmetrically on the wedge axis. A duration of the second laser pulse was 100 ns and the laser discharge energy absorbed by air was E_L =100 mJ and

E_L =150 mJ. The initial electron number density on the axis was varied in limits $n_{e0}(0) = 10^{16}$~10^{18} cm^{-3}. In these conditions a role of the second laser pulse was to support and extend plasma life without transition to breakdown. Figure 5 depicts temperature distribution and velocity vectors for two initial electron number densities at specified times for the energy absorbed E_L =100 mJ. It is seen from Figure 5 that temporal dynamics of the dual-pulse laser energy deposition depends on the initial ionization level created by the first ionizing pulse. Changes in the initial electron number density lead to the changes in the strength of the formed blast wave, level of gas heating , magnitude of vorticity, non-uniform temperature distribution and also change of low density core, which streaming over the wedge and interacts with the shock wave.

Thus, depending on the initial electron number density we observed two modes of the temperature distribution in the plasma kernel. A relatively undisturbed mode for the case of $n_{e0}(0) = 10^{17}$ cm^{-3} is seen in Figure 5 (pictures on the left hand side), when the thermal spot generated by the dual-pulse laser is moving and elongated with the flow, but still remains of the toroidal shape for some time until it reaches the wedge, forming a low density region and starting to interact with the bow shock. The second highly disturbed mode, presented in Figure5 (pictures on the right hand side) for the case of the higher initial electron number density $n_{e0}(0) = 10^{18}$ cm^{-3} shows the larger elliptical kernel and a significant deformation of the initial toroidal kernel by the supersonic flow.

We did not observe a significant influence of the blast wave formed by the dual-pulse laser energy deposition on the bow shock, compared with the cases of the single laser pulse or combined laser-microwave energy deposition. For the low initial electron number density $n_{e0}(0) = 10^{16}$ cm^{-3} generated blast wave is relatively weak and the Mach number is significantly less than the Mach number of the freestream flow. A main effect of the dual-laser pulse energy deposition on the flow in our case is connected with the interaction of the low-density region with the bow shock. Structure of the formed low-density region for both cases is strictly non-uniform and a size of the region along the x-axis increases practically linear with the initial electron number density $n_{e0}(0)$. It also leads to the different vorticity generated for two cases considered.

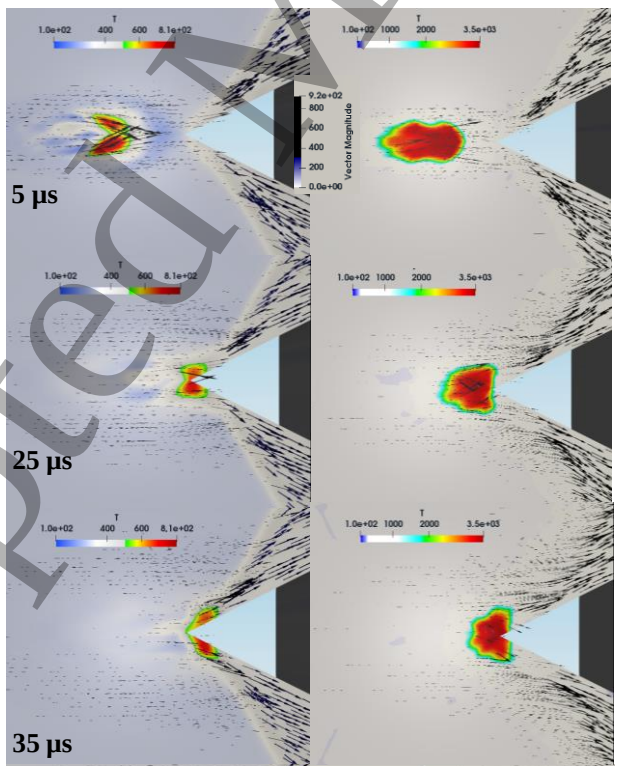

Figure 5. Temperature distribution and velocity vectors: left - $n_{e0}(0) = 10^{17}$ cm^{-3}, right - $n_{e0}(0) = 10^{18}$ cm^{-3}.

Main source of the vorticity generation was a baroclinicity effect, which increased with the initial electron number density. Because of the strong temperature non-uniformity in the heated plasma spot, which depends on the initial ionization level, on the initial electron number density profile as well as on the energy exchange between electrons and neutrals, a density and pressure gradient are not collinear. That leads to the production of vorticity in the area where $\frac{1}{\rho^2}\nabla p \times \nabla \rho \neq 0$, and eventually induces a velocity field that increases the baroclinic torque due to the Rayleigh-Taylor instability. Considering the boundary of the heated plasma spot as a density stratified interface with the density ratio $\alpha < 1$, when the shock passes into a region with a lower sound speed, it could be noted that, an angle between the bow shock and the boundary of the heated plasma region also changes depending on the initial conditions, leading to the appearance of the Richtmyer-Meshkov instability [12]. Results presented in Figure 6 show, that for a case of the higher initial ionization level the interaction of the low-density region with a bow shock lasts the longer time and leads to the higher levels of the vorticity generated. Note, that plasma itself generates vorticity in the process of the plasma channel expansion. Formed vortices travel along the wedge surface, when the thermal spot started to interact with the bow shock (at t= $t = 0.36\ \mu s$ in Figure7). This mechanism of the surface pressure decrease combined with the formation of the low density region itself leads to the local Mach number decrease and local attenuation of the bow shock. Let's consider a laser energy deposition oriented on the some angle to .the wedge axis, for example, at the angle $\alpha = 41.8°$, which corresponds to the oblique shock angle for our wedge. In that case, we can suppress a formation of the vorticity due to the baroclinicity effect, because $\nabla p \times \nabla \rho \approx 0$ and a main source of the drag reduction and surface pressure change is a change in density. We did not observe significant modifications in the drag force with the change in the plasma spot orientation which confirms our conclusion.

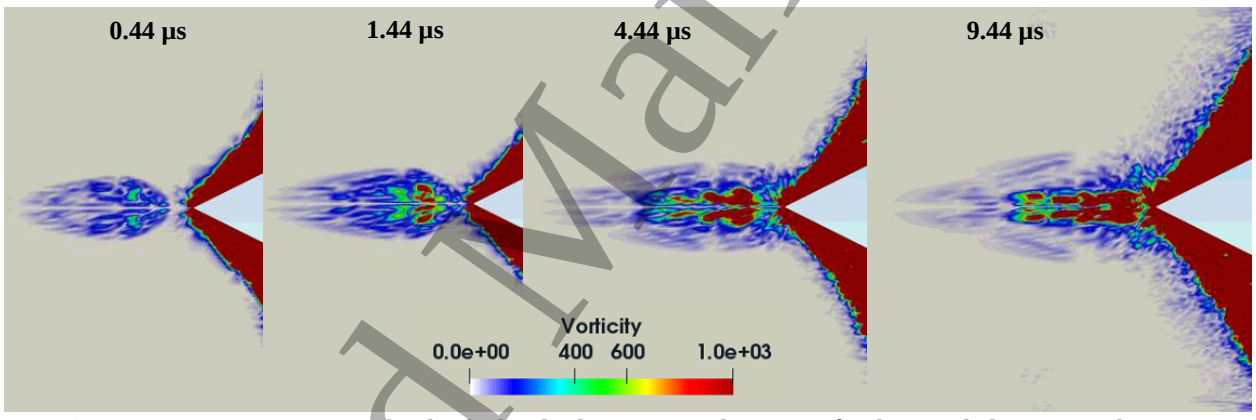

Figure 6. Vorticity generation by the dual-pulse laser energy deposition for the initial electron number density: $n_{e,I} = 10^{17}\ cm^{-3}$.

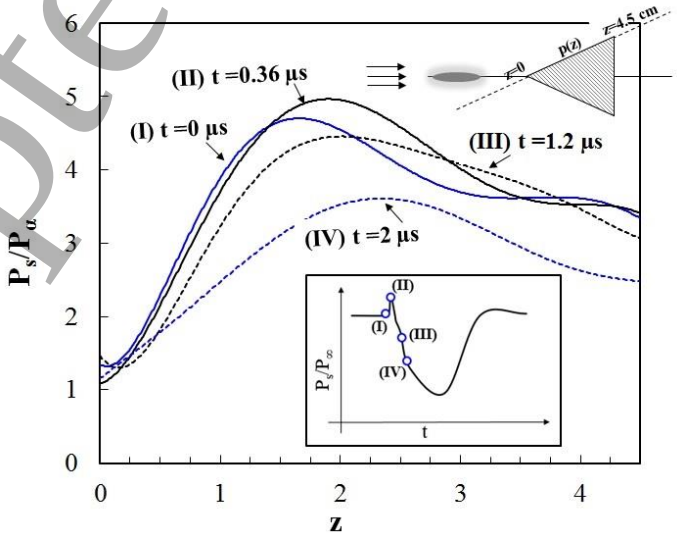

Figure 7. Normalized surface pressure profiles along the upper wedge wall at $n_{e,0} = 10^{17}\ cm^{-3}$.

Temporal behavior of the maximum pressure and maximum temperature in the area close to the wedge leading edge also changes depending on the initial degree of ionization. Figure 8 a) shows that for the higher initial electron number density with the same energy addition by the second pulse E_L =100 mJ, the reduction of pressure takes place for an extended time, which is closely related to the maximum temperature increase due to the dual-pulse laser energy deposition as shown in Fig 8(b). Furthermore, for any specific energy deposition, due to the surface pressure decrease we observed the drag force decrease (Figure 9 a), which reaches its maximum at the initial electron number density $n_{e,0} = 5 \times 10^{16}\ cm^{-3}$. We also consider a case of the simultaneous energy addition in the same location with the same absorbed energy of the laser discharge E_L =100 mJ assuming that we have a thermal equilibrium and all the deposited laser energy goes to gas heating (Eq.3). It is worthy to note, that a drag reduction was observed for both equilibrium and non-equilibrium plasma cases (Figure9a) but for the latter case it was higher and lasted for a longer time. A magnitude of the drag force decrease changes with the Reynolds number as shown in Figure 9 (b), where curves presented have the same initial electron number density $n_{e,0} = 5 \times 10^{16}\ cm^{-3}$ and the same amount of energy E_L =100 mJ provided by the second laser pulse.

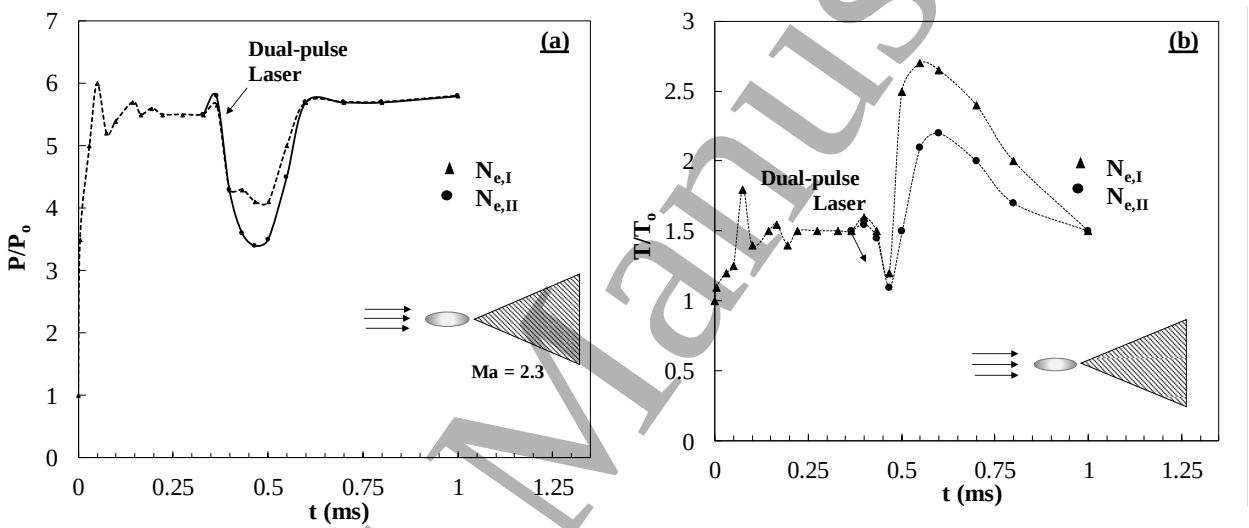

Figure 8. Temporal behavior of (a) the maximum pressure and (b) the maximum temperature (on the wedge axis nearby the wedge tip) for the different initial ionization level ($n_{e,I} = 10^{17}\ cm^{-3}, n_{e,II} = 10^{16}\ cm^{-3}$.

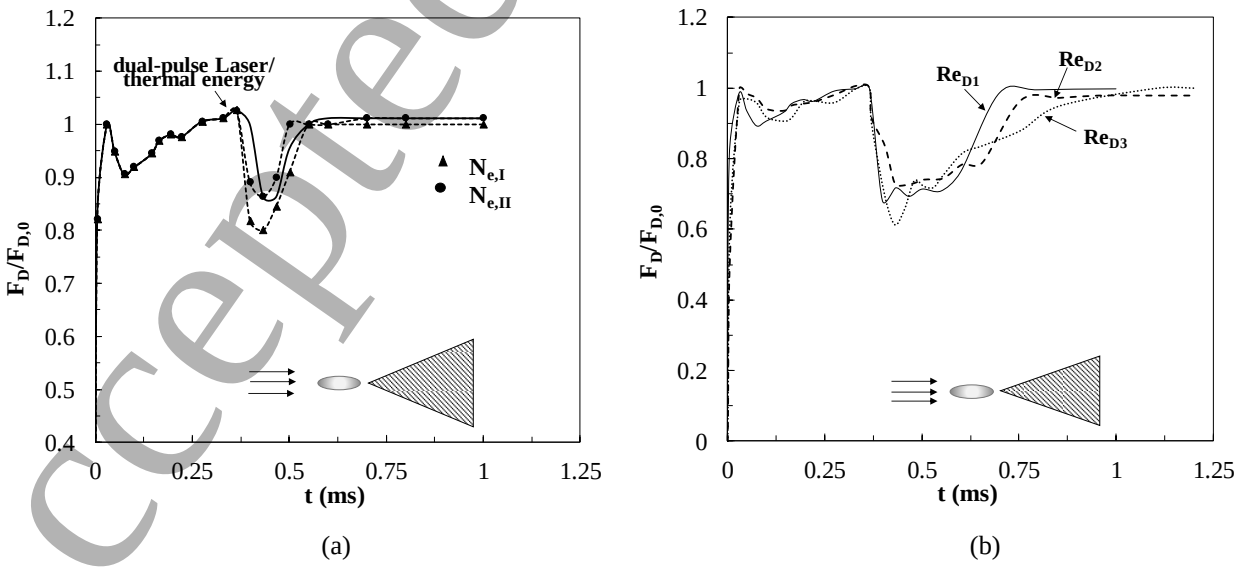

(a) (b)

Figure 9. Temporal behavior of the drag force:
a) at the different initial ionization levels ($n_{e,I} = 10^{17}\ cm^{-3}, n_{e,II} = 10^{16}\ cm^{-3}$);

b) for the different inflow Reynolds number (Re_{D1}= 4.8×10^{06}, Re_{D2}= 6×10^{06}, and Re_{D3}= 7×10^{06})

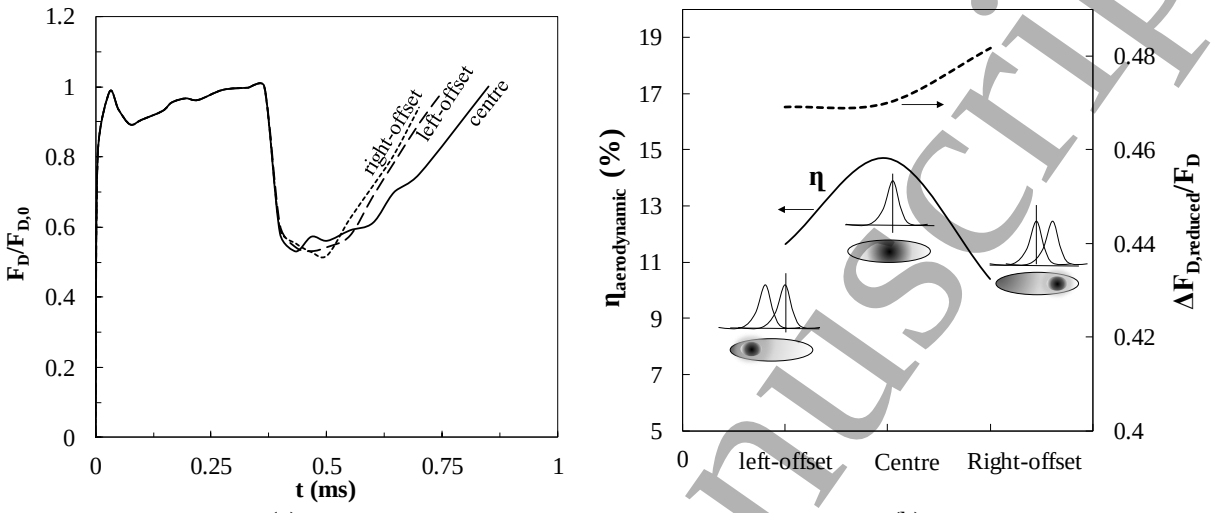

(a) (b)

Figure 10. (a) Temporal behavior of the drag force (b) Maximum drag reduction and aerodynamic efficiency of the dual-pulse laser energy deposition depending on the offset of the second pulse with respect to the first one.

We also observed that by changing the location of the maximum electron number density of the initial profile yields varying in the drag decrease (Figure10). Because varying parameters can affect the performance of the laser system, we also analyzed how the aerodynamic laser efficiency defined by Eq.7 changes depending on the initial profile of the electron number density. As seen in Figure10a, each of the three methods exhibit roughly the same maximum drag reduction. The aerodynamic laser efficiency changes between each of these methods as the effective plasma interaction time is variable. The highest aerodynamic laser efficiency comes when the maximum of the initial electron number density is in the center of the energy deposition area (Figure10b). Furthermore, we see an adverse effect on the reduction in drag as the critical value moves toward the oblique shock. We gain marginal increases in the reduced drag with critical values further from the oblique shock away from a centrally distributed configuration despite losing aerodynamic laser efficiency. This linear shift in the critical value creates a time delay between the impact of the bulk energy deposit and the shear layer. The varying geometry also causes local changes in the concentration of pressure waves in the boundary layer directly impacting drag. Integrating the power curve by a linearly scaled distribution of drag yields this result for the same power requirement. Figure 11 shows how the aerodynamic efficiency and the maximum drag force increases with the inflow Reynolds number for the same amount of energy deposition.

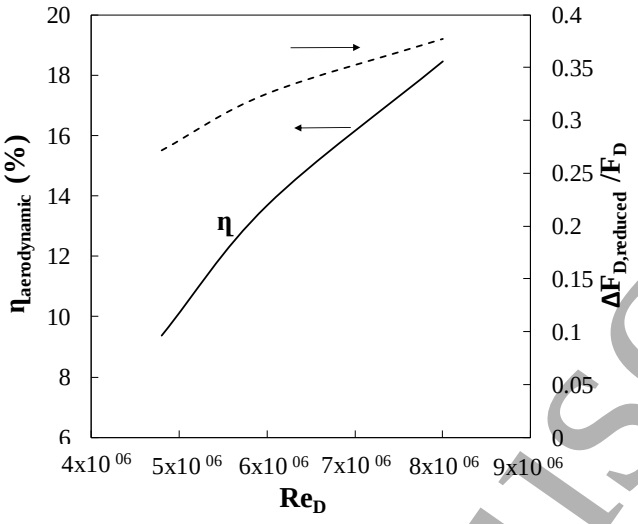

Figure 11. Aerodynamic efficiency of the energy deposition and the maximum drag reduction with respect to Reynolds number.

It is worth noting that the introduced aerodynamic laser efficiency parameter can be used to compare the effects of different supersonic flow control systems. A large reduction over a short time can have the same aerodynamic laser efficiency as a small reduction over a large period. The effect of initial electron number density on the drag reduction and the drag coefficient is presented in Figure 12. Higher degree of initial ionization increases the area of low density region and its interaction with the wedge. This significantly improves the drag reduction capability of the dual-pulse laser system. With the increment of initial electron number density, however, and consequently enhancement of the maximum drag reduction, a significant improvement of drag coefficient performance was observed.

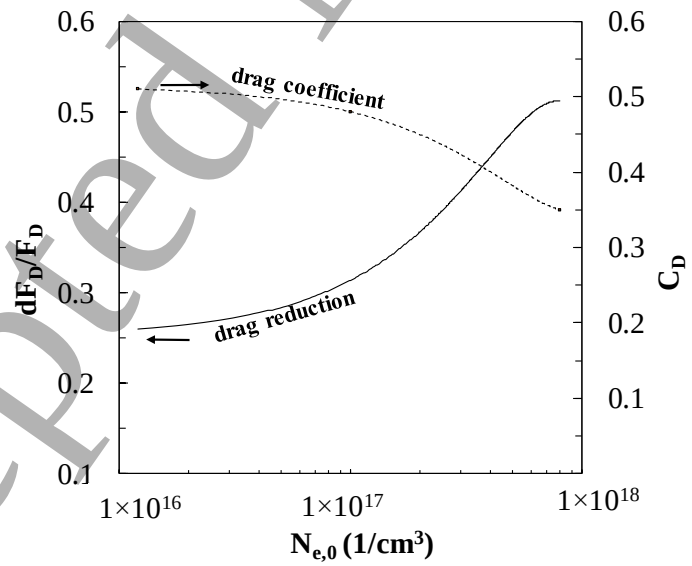

Figure 12. Maximum drag reduction and aerodynamic efficiency of the dual-pulse laser energy deposition depending on the initial electron number density profile.

4. Conclusions

A mathematical model was presented for the dual-pulse laser energy deposition in the supersonic flow. The developed model takes into account the temporal dynamics of the formed laser plasma in the frame of the three-temperature model. Results of the simulations showed that the pressure drop over the wedge and a baroclinic production of the vorticity depend on the initial ionization level created by the first laser pulse. Simulation results also suggested that nonequilibrium plasma was more favorable compared with the thermal plasma in the drag force reduction in a supersonic flow, assuming the same laser energy was absorbed by the gas. Effects of different laser direction on the surface pressure were studied by changing the plasma kernel orientation. The surface pressure did not change significantly with the change of the initial kernel orientation (0 ~ 90 degrees). Thus the main effect of plasma on the supersonic flow in our conditions can be attributed to a low-density core formation.

Acknowledgements

The research was supported by the internal funds of Texas A&M University.

References

[1] Riggins D, Nelson H, and Johnson E 1999 Blunt-Body Wave Drag Reduction Using Focused Energy Deposition *AIAA J.* **37** 460-467

[2] Kim J, Matsuda A, Sakai T, and Sasoh A 2011 Wave Drag Reduction with Acting Spike Induced by Laser-Pulse Energy Depositions *AIAA J.* **49** 2076-2078

[3] Kianvashrad N et al 2017 Effect of Off-Body Laser Discharge on Drag Reduction of Hemisphere Cylinder in Supersonic Flow *AIAA Paper 2017-3478*

[4] Dumitrache C, VanOsdol R, Limbach C, and Yalin A 2017 Control of early flame kernel growth by multi-wavelength laser pulses for enhanced ignition *Sci. Rep.* ***7*** *10239*

[5] Yalin A, Wilvert N, Dumitrache C, Joshi S, and Shneider M 2014 Laser plasma formation assisted by ultraviolet pre-ionization *Phys. Plasmas* ***21*** 103511

[6] Shneider M, Zheltikov A, and Miles R 2011 Tailoring the air plasma with a double laser pulse *Phys. Plasmas* ***18*** 063509

[7] Tropina A, Shneider M and Miles R 2018 Mathematical Model of Dual-Pulse Laser Ignition *J. Propulsion and Power* ***34*** 408-414

[8] Mahamud R, Tropina A, Shneider M and Miles R 2018 Dual-Pulse Laser Ignition model *Phys. of Fluids* ***30*** 106104

[9] Knight D 2008 Survey of aerodynamic drag reduction at high speed by energy deposition. *J. Propulsion Power* ***24*** 1153-1167

[10] Schulein E, Zheltovodov A, Pimonov E and Loginov M 2009 Study of the Bow Shock Interaction With Laser-Pulse-Heated Air Bubbles *AIAA Fluid Dynamics Conference 3568*

[11] Azarova O and Knight D 2015 Interaction of microwave and laser discharge resulting "Heat spots" with supersonic combined cylinder bodies *Aerosp. Sci. Technol.* ***43*** *343-349*

[12] Azarova O and Gvozdeva L 2017 Control of triple-shock configurations and vortex structures forming in high speed flows of gaseous media past an AD body under the action of external energy sources *Aerospace* ***4*** 2017-9

[13] Kianvashrad N and Knight D 2019 Numerical Simulation of laser energy discharges for flight control *J. Phys. D: Appl. Phys.* ***52*** 49005

[14] Koroteeva E, Znamenskaya I, Orlov D and Sysoev N 2017 Shock wave interaction with a thermal layer produced by a plasma sheet actuator *J. Phys. D: Appl. Phys.* ***50*** 085204.

[15] Ogino Y, Ohnishi N, Taguchi S and Sawada K 2009 Baroclinic vortex influence on wave drag reduction induced by pulse energy deposition *Physics of fluids* ***21*** 066102

[16] Elias P et al 2018 Experimental Investigation of Linear energy Deposition using Femtosecond Laser Filamentation in a M=3 Supersonic Flow *AIAA paper* 2018-4896

[17] Joarder R, Padhi U, Singh A and Tummalapalli H 2017 Two dimensional numerical simulations on laser energy deposition in a supersonic flow over a semi-circular body *Int. J. of Heat Mass Transfer* ***105*** 723-740

[18] Wang W, Li J, Jin D, Tang M, Wu Y and Xiao L 2018 High-frequency counter-flow plasma synthetic jet actuator and its application in suppression of supersonic flow separation *Acta Astronautica* ***142*** 45-56

[19] Abdollahzadeh M, Pascoa J and Oliveira P 2016 Implementation of the classical plasma–fluid model for simulation of dielectric barrier discharge (DBD) actuators in OpenFOAM *Comput. Fluids* ***128*** 77-90

[20] Rezaei A et al 2018 Influence of repetitive laser pulse energy depositions on supersonic flow over a sphere, cone and oblate spheroid *Aerosp.Sci.Technol.****76*** 72–81

[21] Alberti A, Munafo A, Pantano C and Panesi M 2019 Supersonic and hypersonic non-equilibrium flow control using laser energy deposition *AIAA paper 2019-2867*

[22] Macheret S, Shneider M and Miles R 2002 Magnetohydrodynamic control of hypersonic flows and scramjet inlets using electron beam ionization, *AIAA Journal* ***40*** 74-81

[23] Raizer Y 1997 Gas Discharge Physics (New York: Springer)

[24] Greenshields C 2017 *OpenFOAM User Guide* ***5***

[25] Degres G and Ginoux J 1984 Surface phenomena in a three-dimensional skewed shock wave/laminar boundary layer interaction, *AIAA Journal* **22** 1764-1769

[26] Adelgren R., Elliott G, Knight D, Zheltovodov A and Beutner 2001 Energy deposition in Supersonic Flows *AIAA paper* 2001-0885

[27] Tropina A, Mahamud R, Shneider MN and Miles RB, Mathematical modeling of dual-pulse laser ignition in a turbulent flow AIAA paper 2019-0741

Nomenclature

c = Speed of light, m/s

D_e = Electron diffusion coefficient, m^2/s

D_v = Vibrational diffusion coefficient, m^2/s

E_0 = Thermal equilibrium vibrational energy, J

E_L = Energy absorbed by the gas from the laser, J

E_V = Nonequilibrium vibrational energy, J

h = Enthalpy, J

I_L = Laser intensity, W/m^2

K_B = Boltzmann constant, J/K

l_x = Laser Deposition size in the x direction

l_y = Laser Deposition size in the y direction

Ma = Local Mach Number

M_∞ = Free Stream Mach Number

m_e = mass of electron, kg

n_Y = Number density of any species Y

n_e = Electron number density

P = Pressure, N/m^2

P_∞ = Free Stream Pressure, N/m^2

Q_e = Electron energy losses on the ionization, electronic and vibrational excitation, J/s

Q_J = Joule heating term, J/s

Re_∞ = Free Stream Reynolds Number

r_f = Focal radius, m

S_f = Focal area, m^2

t = time, s

T_∞ = Free Stream Gas Temperature, K

T = Temperature, K

v= velocity, m/s

Y= Mass fraction for a species

T_v = Vibrational temperature, K

T_e = Electron temperature, K

Symbols

α = Wedge angle

δ_e = Reduced Mass Ratio

ρ = Density, kg/m^3

ρ_∞ = Free Stream Density, kg/m^3

λ = Laser wavelength, mm

λ_e = Electron Heat Conductivity, W/m/K

ν_{ev} = Electron − vibration excitation frequency, $1/s$

ν_m = Elastic Collision Frequency, $1/s$

ν_c = Coulomb Collision Frequency, $1/s$

τ_{VT} = Vibrational relaxation time, s

ω_L = Laser frequency, 1/s

Subscripts

∞ =Free Stream Quantity

0 = Total/Thermal Property

c = Coulomb Property

D = drag

e = Electronic State Property

f = Focal Parameter

L = Related to the Laser

m =Pertaining to Elastic or Momentum

T = Translational/Time related

v = Vibrational Mode Property

x = Spatially related to the x direction

y = Spatially related to the y direction

Y = Denotes any species, Y may be replaced with the molecular formula (e.g. O_2)

Research Article | Vol. 28, No. 4 / 17 February 2020 / Optics Express 5835
Optics EXPRESS

Gas dynamics and vorticity generation in laser-induced breakdown of air

CIPRIAN DUMITRACHE[1] AND AZER P. YALIN[2,*]

[1]Laboratoire EM2C, CNRS, CentraleSupélec, Université Paris-Saclay, 91190 Gif-sur-Yvette, France
[2]Center for Laser Sensing and Diagnostics, Colorado State University, Fort Collins, CO 80523, USA
*azer.yalin@colostate.edu

Abstract: Research has shown that the ignition characteristics of laser-induced plasmas in fuel-air mixtures are influenced by the gas dynamics effects induced during the gas breakdown stage. Here, we present the numerical modeling of the fluid mechanics induced by breakdown (plasma formation) from a nanosecond near-infrared (NIR) laser pulse in air. The simulations focus on the post-discharge kernel dynamics with the goal of developing a better understanding of how vorticity is generated during the kernel cooling phase. Initial conditions (ICs) of kernel shape, temperature, and pressure (corresponding to the end of the laser pulse) are found from experimental Rayleigh scattering data. It is shown that this method for determining ICs is preferred versus the use of the Taylor-Sedov blast wave theory as it provides a more accurate description of the starting field. Past experimental observations have revealed that the gas dynamics of nanosecond laser sparks typically lead to the formation of an asymmetric torus with a frontal lobe propagating towards the laser source. We show that the development of the asymmetric torus is governed by strong vorticity generated through baroclinic torque arising from the blast wave that forms at the kernel boundary. Initially, the blast takes the shape of the teardrop kernel but then evolves into a spherical front during the first ~10 μs because the blast wave strength varies along its circumference. This spatial variation leads to a misalignment between the pressure and density gradients and generation of vorticity by baroclinic torque. Ultimately, the observed flow-field is dictated by how the energy was initially deposited around the beam waist during breakdown. As such, one can tailor the aerodynamics induced during the cooling and recombination phase by controlling the energy deposition profile.

1. Introduction

Laser induced breakdown has been studied for a wide range of combustion applications including as an ignition source for reciprocating engines [1–3], gas turbines [4–6] and rocket engines [7,8], and as a means to provide flame stabilization in high speed diffusion jet flames [9–12]. For widely used nanosecond pulses, a typical breakdown event is governed by two processes. An initial pool of free electrons is formed by multi-photon ionization (MPI) whereby a gas molecule becomes ionized through the absorption of multiple-photons within the molecule's excitation lifetime. This is followed by the plasma growth stage via electron avalanche ionization (EAI). During EAI, the free electrons generated by MPI are accelerated in the presence of the laser's electric field (i.e., inverse bremsstrahlung absorption) and generate further gas ionization through collisions with the nearby gas molecules. During this period, the plasma rapidly reaches high temperatures (~30,000 K) and high pressures (several tens of bar) [13,14]. The initial plasma kernel has a characteristic teardrop shape with the axial length governed by the focusing conditions and beam energy. The plasma kernel grows with high velocity (~0.1-1 km/s) during the first microsecond after the pulse [13]. An interesting feature of the kernel's subsequent development is the presence of vorticity within the plasma even when the breakdown was generated in an initially quiescent gas. Vorticity in the fluid leads to the collapse of the teardrop kernel along its optical axis and, ultimately, to the formation of an asymmetric torus with a lobe feature pointing in the direction

#385430 https://doi.org/10.1364/OE.385430
Journal © 2020 Received 11 Dec 2019; revised 30 Jan 2020; accepted 3 Feb 2020; published 14 Feb 2020

Optics EXPRESS

of the laser, at several tens of microseconds later. When experimentally viewed by (planar) 2-D imaging methods, the flow structure appears as a "three-lobe" pattern due to the persisting torus and frontal lobe (also referred to as "third lobe") [15–17]. Shown in Fig.. 1 is an example of a kernel investigated as part of this work which has collapsed into an asymmetric torus at 100 µs after the laser pulse.

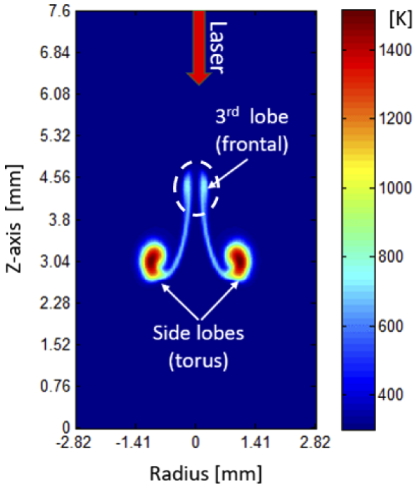

Fig. 1. Temperature contours showing an asymmetric torus obtained 100 µs after a laser spark. The image shows the three-lobe structure that is typically encountered in laser ignition by nanosecond NIR pulses.

The gas dynamics involved in the breakdown process, in particular the vorticity generation mechanism leading to the creation of the three-lobe structure, have not been sufficiently explained in the literature. The formation mechanism of the third lobe was first discussed by Bradley et al. [13] who posited that the third lobe forms due to the interaction between the rarefaction waves (which constitute the tail end of the blast wave) and the hot gas kernel present at the beam focus. The inward flow induced by the passing rarefaction during first ~5-10 µs is key to the mechanism proposed by Bradley. Similar to a Taylor instability, the gas of lower density (hotter) is accelerated more by this outward pressure gradient than the neighboring layer of gas that has higher density (colder). The resulting torque generates a pair of counter-rotating vortices–one at the upstream (laser incident) side and one at the downstream side of the kernel. This (nearly adjacent) vortex pair causes the hot gas kernel left after breakdown to collapse into a torus. The imbalance of vortex strength between the pair also generates the third (frontal) lobe. However, no actual measurements or computational fluid dynamics (CFD) simulations were performed to confirm this mechanism. Moreover, detailed analysis of the kernel topology has suggested that vorticity might be present at even earlier times, before the blast wave has separated from the kernel. In another study, Dors et al. [18] conducted a CFD analysis of a breakdown kernel from a 10 ns Nd:YAG laser (1064 nm) pulse with E_{pulse}=25 mJ. Their study assumed that the plasma is in equilibrium and the initial kernel profile was determined from experimental observations. Interestingly, while their results predict the formation of an asymmetric toroid, the direction of propagation of the third lobe was towards the cooler side of the post-breakdown kernel which is contrary to what has been experimentally reported [19,20]. This suggests that obtaining the correct direction of fluid rotation induced by vorticity is very sensitive to the initial conditions.

It is important to note the significant role of vorticity for practical applications including the viability of flame ignition. Endo et al. [21] indicated that the plasma-driven fluid dynamics dictates the flame kernel topology. Furthermore, they suggest that flame vorticity entrains the

Optics EXPRESS

surrounding combustible mixture which leads to an increase of the effective kernel energy in the early stages of flame development. A comparative experimental study between single- and dual-pulse laser breakdown ignition by the present authors showed that the plasma-induced vorticity is responsible for the flame kernel extinction at the lean limit [22]. Moreover, it was shown that by controlling how the energy is deposited in the gas along the optical axis, one can control the direction of fluid rotation including changing the direction of the third lobe (i.e. making it appear towards or away from the incoming beam) or even completely suppressing it. Therefore, understanding the mechanisms through which vorticity is generated in a laser spark (and tailoring it) can have a wide range of benefits such as reducing flame stretching in highly turbulent combustion devices (e.g. aero-turbines), flame stabilization in ramjet or scramjet propulsion systems, increase in combustion efficiency for stationary natural gas engines, and optimization of plasma aerodynamic flow control devices.

In this paper we use computational fluid dynamics to investigate the gas dynamic effects induced by a nanosecond laser spark in atmospheric air. Initial conditions (after the end of the incident pulse) are found from experimental studies. The temporal evolution of the flow field and the corresponding kernel dynamics are modeled under the 2-D axis-symmetric assumption. A vorticity equation analysis shows that vorticity is generated mainly by baroclinic torque due to misalignment between the pressure and density gradients within the kernel. Pressure contours show that the strength of the blast wave varies along its circumference during the first ~10 μs after the laser pulse, which results in a misalignment of the pressure gradient with respect to the density gradient (which follows the temperature gradient). We find that, ultimately, the initial shape of the breakdown kernel dictates the subsequent gas dynamics. The teardrop kernel gives rise to two zones of significant recirculation at the front (facing the laser source) and the back (away from the laser source) of the kernel that have different strengths. These two vortices govern the collapse of the laser kernel into the three-lobe structure observed experimentally. These findings provide new insight into the vorticity generation, and its implications to the flow field, relative to the current literature.

2. Mathematical model

The fluid mechanics generated by the laser breakdown process were numerically modeled using a Riemann solver developed in-house based on the Navier-Stokes equations. At this stage, the model neglects the effects of plasma kinetics and focuses exclusively on the fluid dynamics induced by the hot gas kernel in a non-reactive air gas mixture (assumed to be 79% N_2 and 21% O_2). As such, the simulations presented here begin after the laser pulse has ended with initial conditions determined from experiments (see below). Future work will include kinetics, including attempting to model the ionization (laser on) phase, but it is important to note that several past studies have found that the observed gas dynamics effects are dominated by the interaction between the blast wave and the hot gas kernel after the pulse (i.e. not depending on kinetics) [13,15,23,24]. Moreover, post-discharge heating by vibrational-translational (V-T) relaxation reactions or by quenching of metastable states take place on a longer timescale (hundred of microseconds) compared to the timescale of blast-wave detachment and kernel collapse (~0.5-10 μs). The blast itself is created by the ultra-fast heating mechanism of electron avalanche ionization which takes place during the laser pulse. This mechanism is taken into account in the current simulations through initial conditions based on the plasma properties measured using Rayleigh/Thomson scattering at the end of the pulse. Hence, neglecting the plasma chemistry should still allow modeling and insight into how the flow field develops provided that correct profile of pressure and temperature at the end of the pulse are used in computations.

The governing equations written in cylindrical coordinates with axial symmetry (zero azimuthal velocity) are presented below in conservative form:

$$U_t + F(U)^a{}_r + G(U)^a{}_z = F(U)^d{}_r + G(U)^d{}_z + S(U) \tag{1}$$

Optics EXPRESS

where:

$$U = \begin{bmatrix} \rho \\ \rho u \\ \rho v \\ E \end{bmatrix}; \quad F(U)^a = \begin{bmatrix} \rho u \\ \rho u^2 + p \\ \rho uv \\ u(E+p) \end{bmatrix}; \quad G(U)^a = \begin{bmatrix} \rho v \\ \rho uv \\ \rho v^2 + p \\ v(E+p) \end{bmatrix};$$

$$F(U)^d = \begin{bmatrix} 0 \\ \tau_{rr} \\ \tau_{rz} \\ u\tau_{rr} + v\tau_{rz} - q_r \end{bmatrix}; \quad G(U)^d = \begin{bmatrix} 0 \\ \tau_{rz} \\ \tau_{zz} \\ u\tau_{rz} + v\tau_{zz} - q_z \end{bmatrix}; \tag{2}$$

$$S(U) = -\frac{1}{r}\begin{bmatrix} \rho u \\ \rho u^2 - \tau_{rr} \\ \rho uv - \tau_{rz} \\ u(E+p) + u\tau_{rr} - v\tau_{rz} + q_r \end{bmatrix}$$

In Eq.. (2), U is the vector of conservative variables, $F(U)^a$ and $G(U)^a$ describe the advection flux (in the r and z direction respectively), $F(U)^d$, $G(U)^d$ represent the diffusion flux, and $S(U)$ is the source term that is the result of the coordinate system transformation from Cartesian to cylindrical. ρ is the gas density, p is pressure, u and v are the radial (r-) and axial (z-) components of velocity, E is the total energy (the sum of kinetic and internal energy), $\tau_{i,j}$ are the shear stress component, and q_i represents the i^{th} component of the conductive heat flux. In this coordinate system the incident laser is oriented along the z-axis.

The system of conservation laws is complemented with two additional relations that describe the thermodynamic state of the system:

$$p = \rho R_g T$$

$$E = \rho\left(h - \frac{p}{\rho} + \frac{u^2 + v^2}{2}\right) \tag{3}$$

where the first relation in Eq.. (3) is the ideal gas law (R_g is the specific gas constant), and the second is the caloric equation of state (h is the specific enthalpy).

The caloric perfect gas assumption does not fully apply in the case of the high-temperature laser plasma; however, the numerical model assumes a thermally perfect gas which involves solving an implicit nonlinear equation in temperature in each computational cell and at each time step. The following relation for temperature is derived from Eq. (3):

$$T = \frac{-E + \rho\left(\frac{u^2+v^2}{2}\right) + \rho h(T)}{\rho R_g} \tag{4}$$

In Eq.. (4) the enthalpy, $h(T)$, is computed using the Shomate interpolation polynomials for molecular nitrogen and oxygen according to the NIST database [25]. Viscosity is modeled using Sutherland's law, assuming a Newtonian fluid with temperature-dependent viscosity, and the conductive fluxes are calculated with temperature-dependent thermal conductivities [26].

The conservation equations given in Eq.. (1) are numerically integrated using a dimensional splitting approach. The advection terms are solved using Roe's flux differencing scheme with slope limiters [27] and the diffusion terms are solved using a second order centered difference

Optics EXPRESS

scheme [28]. Finally, the resulting ODEs are integrated with an explicit 4th order Runge-Kutta IV method.

The governing equations are solved on a structured Cartesian grid using a control volume discretization approach. A piece-wise distribution of initial data over the computational cells is employed where the value at the center of a cell represents the average of each variable over the cell. An optimum cell resolution is required in order to resolve the phenomenon of interest while minimizing the computational requirements. Experimental results indicate that kernel evolution takes place over two timescales suggesting that two different cell sizes can be used in the simulation. In the first 20 μs the kernel grows significantly; the temperature drops by more than half of its initial value and vorticity is generated via baroclinic torque (see Section 3.4 for a detailed description). Over this time interval, an optimum cell size of 15 microns was determined through a grid sensitivity analysis. At times greater than 20 μs, the cell size is doubled to 30 microns in order to save computational time since the gradients of pressure and temperature are much weaker and the toroidal structure has already formed. Additionally, the axial-symmetric nature of the kernel under investigation allows for modeling only half of the kernel which further reduce the computational cost. The code uses non-reflective boundary conditions at the edge of the domain. This allows the blast wave to leave the computational domain with minimal disturbances [29,30].

3. Results and discussion

3.1. Determination of initial conditions

Since the current simulations do not model the optical breakdown process, the choice of the initial conditions (corresponding to the end of the laser pulse) becomes critical. These initial conditions are found from experimental studies based on breakdown from a focused Nd:YAG beam (1064 nm) with representative parameters of 10 ns pulse duration, 70 mJ energy and waist of 170 µm. The initial kernel shape is based on broadband optical emission images taken immediately after the pulse has ended [31]. The pressure and temperature of the kernel at the end of the discharge are determined from 1-D Rayleigh/Thomson scattering measurements [32]. A typical scattering image is show in the left of Fig. 1 [32–34]. The right of Fig. 2 shows the resulting 1-D gas density profiles (normalized by ambient density, ρ_0) along the Rayleigh probe beam for different times after the end of the breakdown pulse. At all times, far from the plasma (where the gas is undisturbed) the density remains unchanged, i.e. ρ/ρ_0=1. Moving inwards (from either side) toward the center of the domain there is a sharp increase in density due to the shock wave at the front of the blast that accompanies the breakdown process. At regions inside the blast, the density steadily drops due to progressively higher temperatures. (At early times, an increase in signal is observed right at the center of the kernel due to the presence of Thomson scattering from the free electrons; this signal contribution does not correspond to the true gas density and is excluded from determination of initial conditions.)

These density profiles (right of Fig. 2) contain information on the shock wave location, blast wave strength and kernel size, at various times after the breakdown, and are thus well suited for determination of initial conditions for the simulation. The method used to determine the initial conditions (corresponding to the end of the breakdown pulsed) is as follows. We assume a teardrop shape (major axis along the laser propagation direction) for the starting kernel from our past imaging measurements [31]. We then iteratively run the CFD model for various values of peak temperature and kernel size and compare the resulting density profiles to their experimental counterparts (right of Fig. 1), seeking the best agreement. The pressure profile is linked to the temperature profile using the ideal gas equation of state under the assumption that the gas density should remain unchanged during the laser energy deposition phase. This hypothesis is valid as long as the laser pulse duration is much shorter than the acoustic-time scale (where the latter is given by the radial length of kernel, divided by the speed of sound). The simulated density

Optics EXPRESS

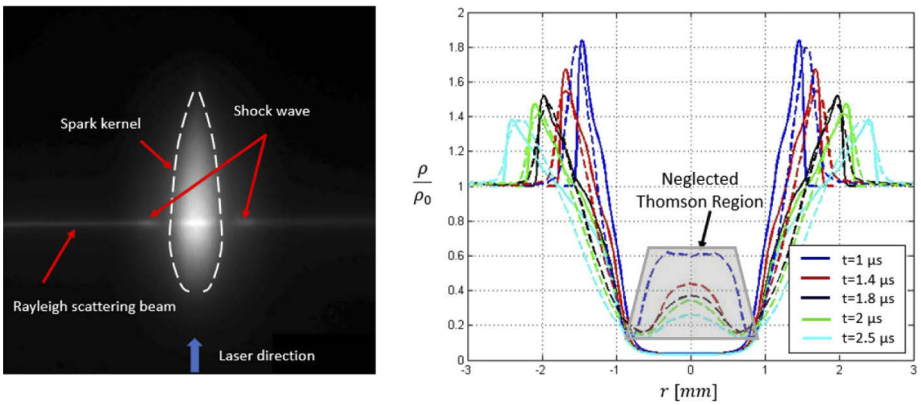

Fig. 2. Left: Experimental 1-D Rayleigh scattering performed on a laser spark kernel at t = 1 μs. Right: Resulting normalized density profiles along the Rayleigh scattering beam at different times after the breakdown pulse. Experimental data is shown with broken lines and the simulation with solid lines.

profiles are shown with solid lines in the right of Fig. 2. In terms of selecting the needed initial conditions (for end of laser pulse) we set a criterion that both the location and the amplitude of the peak of the blast wave should agree, between simulated and Rayleigh profiles, to better than 5%. If one considers how much the (initial condition) pressure and temperature fields can vary, while still satisfying the 5% agreement criterion, one finds that the peak temperature varies be less than ~3% (i.e. ~500 K maximum change in peak temperature of ~15,000 K). Such a small temperature change will not change the hydrodynamic effects presented here. The initial temperature and pressure profiles are shown in Fig. 3.

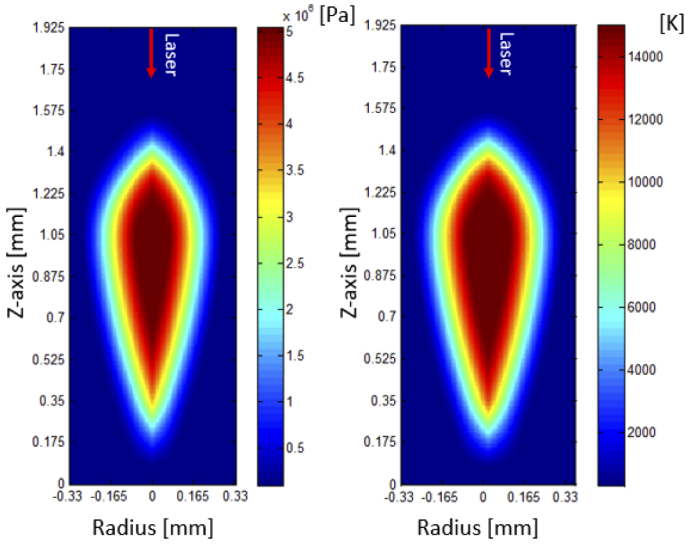

Fig. 3. Initial kernel profile used for the CFD simulations corresponding to end of the breakdown pulse. Pressure (left) and Temperature (right).

An important contribution of this study is the method, outlined above, of using Rayleigh scattering profiles to infer the pressure and temperature of the breakdown plasma at the end of the laser pulse. Previous work in the field has typically used Taylor-Sedov blast wave theory which

Optics EXPRESS

relies on matching the experimentally observed blast wave radii (usually from schlieren) with those predicted from the theory. However, we find that that this method grossly over-estimates the kernel's thermodynamic state at the end of the pulse. Taylor's blast wave analysis assumes a perfectly spherical shock wave front. However, this is not true for a typical laser spark that more closely resembles a cylinder than a sphere. In this case, the blast wave speed varies strongly with location along the circumference thus confounding analysis based on a simpler spherical wave. Additionally, Taylor-Sedov analysis assumes an instantaneous explosion from an infinitesimally small volume. This means that, while the Taylor-Sedov theory can be used to determine the energy released based on measurements of the shock wave radii once it becomes spherical, one cannot simply extrapolate temperature and pressure immediately after the end of the nanosecond pulse. Our analysis shows that the size of the initial kernel plays a key role in determining the correct temperature and pressure immediately after the pulse. To illustrate this point, Fig. 4 shows simulated cases for two different starting kernel configurations that result in similar blast wave radius and strength variations over time. We see that when considering both size and temperature, one can get nearly degenerate blast wave evolution for different parameter combinations, indicating that the size also plays a significant role in determining the correct thermodynamic state at the end of the laser pulse. If this size effect is ignored the kernel temperature is grossly over-estimated, with previous literature using Taylor-Sedov analysis reporting temperatures in excess of 100,000 K and pressures between 5,000-10,000 bar [13,35,36].

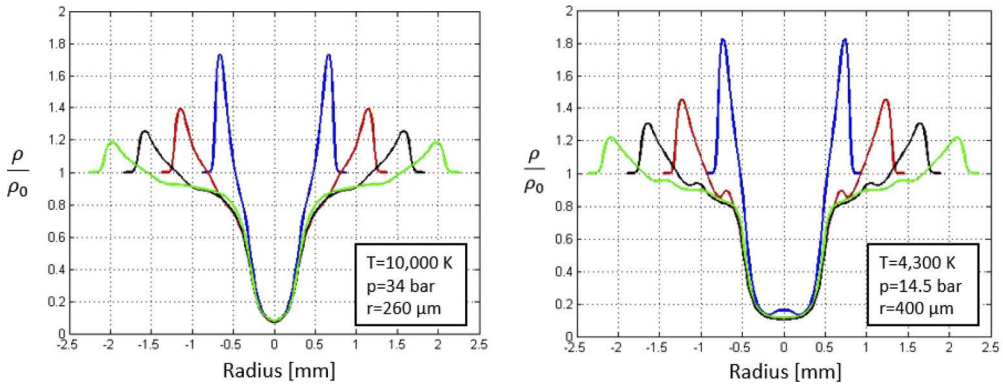

Fig. 4. Computed 1-D Rayleigh scattering profiles for two different initial laser spark profiles: smaller, hotter kernel (left) and larger, colder kernel (right).

3.2. Kernel dynamics

A comparison between experimental and synthetic schlieren images showing the kernel development after the breakdown pulse is presented in Fig. 5. The synthetic images were obtained by plotting the contours of the vertical density gradient (which would correspond to a horizontal knife edge orientation in experiments). The images show that the kernel maintains its initial teardrop shape for the first ~5 µs after the pulse. However, its volume has increased by approximately a factor of 4 during this initial stage. This is followed by compression of the kernel along the optical propagation axis between ~5-30 µs. At 30 µs after the pulse, the kernel presents two strong indentations at the leading and trailing edge. As will be shown in detail in the following section, this is caused by two significant recirculation regions that entrains the cold surrounding air from either side and push this air towards the center of the kernel. At 50 µs, the three-lobe structure (i.e., the two side lobes and the frontal lobe) is already formed. In 3-D, this structure resembles an asymmetric torus in which the plane of stagnation at the center is broken

Optics EXPRESS

because the re-circulation at the back of the kernel is stronger. In the final stages of the kernel development, the frontal lobe continues to grow towards the laser source as more surrounding fluid is pushed through the middle of the torus. The kernel maintains this shape for several hundred of microseconds until it is completely dissipated by Rayleigh-Taylor instabilities formed inside the flow. The actual lifetime of the three-lobe structure depends on the energy absorbed inside the gas and the focusing conditions, but it is typically between 0.1-1 ms.

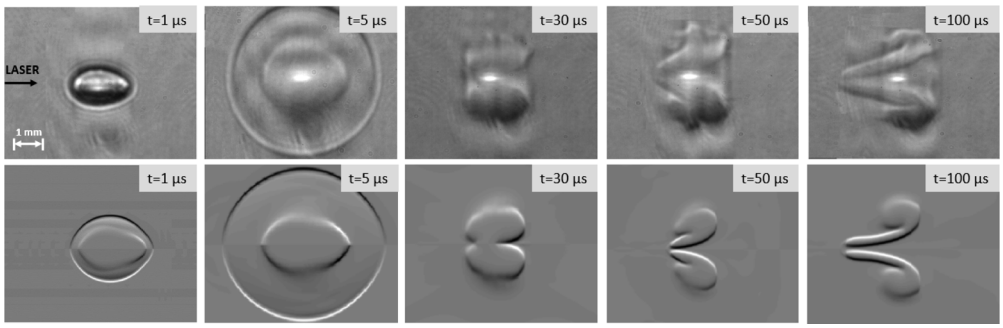

Fig. 5. Experimental (top) and synthetic (bottom) schlieren images showing the evolution of the kernel and the formation of the asymmetric torus (E_{laser}=70 mJ). Both sets of images use the same scale.

A comparison between the evolution of maximum kernel temperature obtained experimentally by Rayleigh scattering and CFD is shown in in Fig. 6. Interestingly, the temperature decay presents three successive regions: (a) a region of sharp temperature decrease associated with fast kernel expansion at times <~1 µs, (b) a region where the rate of temperature decrease slows between ~1-15 µs, and (c) a region governed by toroidal dynamics in which gradual kernel cooling is observed between 15-200 µs after the pulse. The relatively uniform temperature in region (b) is a new finding and is due to heat diffusion from the kernel being balanced by heating of the kernel center caused by the axial compression that was previously described. Temperature measurements at earlier times are not shown as Thomson scattering and pressure changes precludes temperature determination by the current Rayleigh scattering method. The comparison shows that the CFD simulation captures the temperature evolution during the toroidal development stage.

3.3. Blast wave propagation

Previous work on laser breakdown has outlined the importance of blast wave dynamics in the generation of vorticity. Blast waves are observed in many types of ultrafast heat releases from point sources. A typical blast wave front consists of a leading shock wave that compresses and heats the gas ahead of it and a trailing rarefaction wave which acts to reduce the gas density behind the wave returning it to its initial (unperturbed) state. During the interaction between the heated gas and the rarefaction, a zone of pressure gradient reversal is observed when the pressure behind the blast becomes smaller than the ambient pressure. In bomb detonations, this is typically referred as a “blast wind” which tends to suck destroyed items back towards the epicenter of the explosion.

Figures 7 and 8 show the computed pressure fields for times before and after blast wave detachment respectively. Since the laser energy is deposited inside the gas on a much shorter timescale (nanoseconds) compared to the hydrodynamic scale of the laser plasma (order microseconds based on speed of sound and characteristic spark dimension), a pressure buildup inside of the plasma kernel accompanies the rise in temperature during the energy addition process. In the early stages of the kernel development, acoustic waves coalesce at the edge of the kernel

Optics EXPRESS

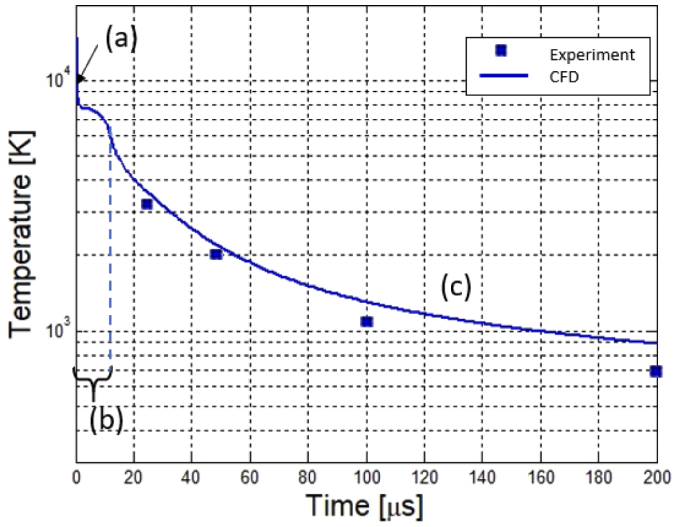

Fig. 6. Evolution of maximum kernel temperature evolution during the cooling phase. Experimental points (squares) have vertical error bars of ~± 20 K.

thereby forming a strong blast wave. This process is accompanied by a fast decrease in pressure at the center of the kernel during the first few hundred nanoseconds. Interestingly, an increase in pressure at the center of the kernel is observed at ~300 ns after the pulse, corresponding to the formation of a secondary pressure front (see below). Despite being weaker in amplitude, this front propagates faster than that of the main blast since the density of the fluid around it is much lower than that of the far-field; this secondary pressure front then catches up (and merges) with the main blast wave at around ~1.5 μs after the pulse. The resulting blast initially takes the shape of the post-laser breakdown teardrop kernel (Fig. 3). However, as the time evolves the blast wave front becomes progressively more spherical. This phenomenon is described in more detail below and has a significant impact on vorticity generation.

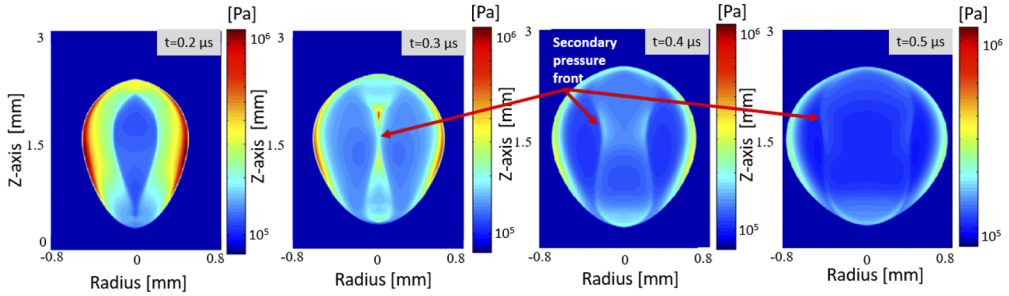

Fig. 7. Pressure contours showing the early kernel evolution (prior to blast wave detachment). A secondary pressure front is observed during this development phase.

Once the blast wave detaches from the kernel (at time ~1 μs), the pressure at the epicenter gradually decreases. At 1 μs after the pulse, the rarefaction wave that closely follows behind the shock front begins to decrease the pressure inside the gas kernel until it becomes smaller than the ambient pressure. The outward pointing pressure gradient observed in the 2.5 μs and 5 μs frames at the center of the kernel gives rise to a fluid flow directed towards the center of the kernel. This inward flow initiates the observed kernel collapse into the asymmetric torus shown in Fig. 6.

Optics EXPRESS

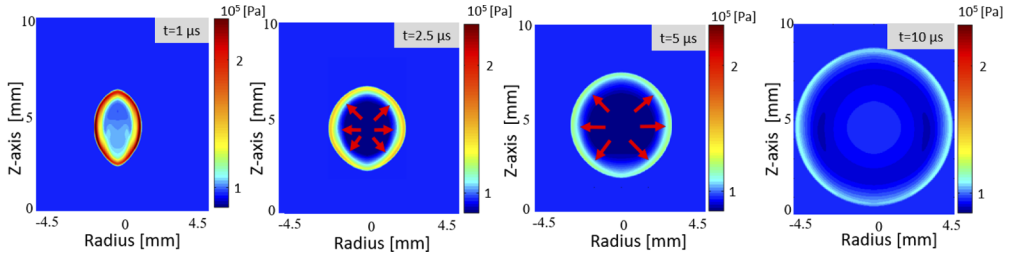

Fig. 8. Pressure contours showing the evolution of the blast wave after kernel detachment and until it becomes spherical. The red arrows shown at 2.5 μs and 5 μs indicate the direction of the pressure gradient inside of kernel. This is responsible for the observed kernel collapse (pressure at the epicenter becomes smaller than the ambient pressure).

Finally, the pressure at the center of the kernel recovers to atmospheric in ~10-15 μs after the pulse and the blast wave becomes fully detached and perfectly spherical.

A more detailed analysis of the secondary pressure wave observed between 0.3-1.5 μs is warranted as this feature has not been previously observed to our knowledge. The wave velocity is subsonic (e.g. ~600 m/s corresponding to M = 0.3 at 0.3 μs after the pulse) meaning the wave is not a secondary blast. Being subsonic, this secondary front does not appreciably compress the fluid which is why it is not visible in either schlieren or Rayleigh scattering measurements. The source of this secondary front is revealed in Fig. 9. Inspecting the velocity profiles at 0.4 μs after the pulse reveals that significant recirculation takes place inside of the kernel. Since the pressure at the epicenter is still above atmospheric there is a net acceleration towards the outside. However, the strong source of vorticity near the kernel boundary tends to recirculate the fluid back to the kernel center leading to a temporary increase in gas pressure. This is a significant finding because previous research attribute the presence of vorticity within the kernel to (only) the interaction between the rarefaction and the remaining hot gas kernel behind the blast [13], yet the present results suggest that vorticity is generated within the kernel even during the (earlier) blast wave formation process. This result has been checked for grid resolutions as small as 1 μm and it does not appear to be a numerical artefact. A comprehensive discussion of vorticity generation is given in the next section.

3.4. *Mechanism of vorticity generation*

Figure 10 provides vorticity contours for various time delays during the kernel development. Positive vorticity means that the fluid is rotating counter-clockwise in the plane of the figure (color coded red in the images below) while negative vorticity indicates clockwise rotation (shown in blue). As previously noted, vorticity is generated during the first few hundred of nanoseconds after the laser pulse, well before the leading blast wave has detached itself from the main kernel. The two counter rotating vortices push the fluid radially inwards, thus causing the formation of the secondary pressure front observed between ~0.3-1.5 μs. This source of vorticity persists until the outward pressure gradient is established inside the kernel (due to formation of the rarefaction wave at the kernel boundary). As the kernel collapses, the two vortices change their direction of rotation and entrain the surrounding cold fluid and push it along the optical axis towards the center of the kernel (between ~2 and 100 μs). This causes the kernel to compress faster over the optical axis than radially (compare the images for 4 and 7 μs). At 7 μs, one notices indentations at the top and bottom of the kernel which grow as time progresses. The vortices gradually move towards the center of the kernel during the collapse, until they collide with each other a few tens of microseconds after the pulse (note that the rotations of the vortices are opposite in the images for 7 μs versus 100 μs in Fig. 10), and ultimately pass one another. When the vortices collide, the

Optics EXPRESS

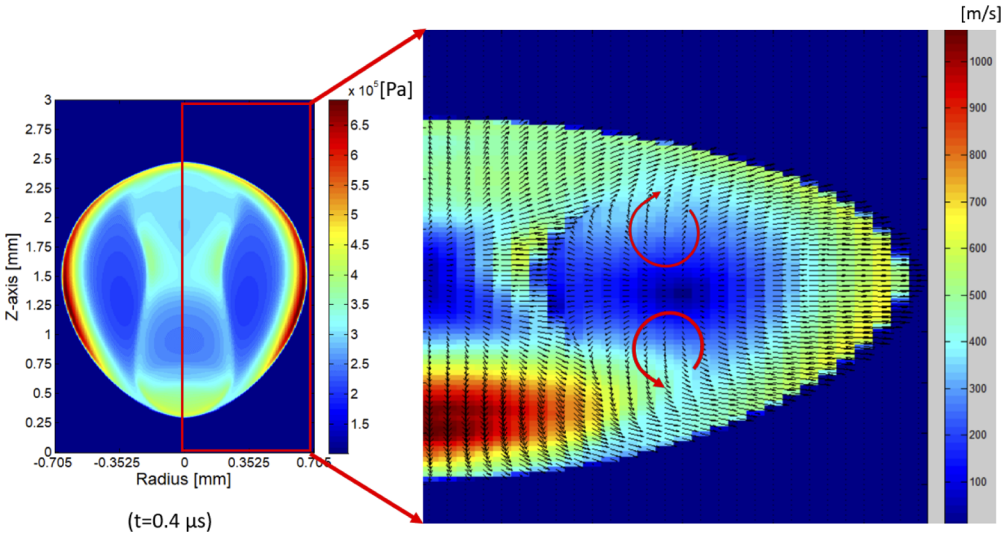

Fig. 9. Left: Pressure contours showing the secondary pressure front propagating inside of the hot kernel (see also Fig. 7). Right: Velocity field imposed on velocity contours showing the presence of vorticity at early times during the kernel development (t = 0.4 µs is shown here). The region used for the right panel is shown with the red rectangle in the left panel, i.e. the right plot is made for half of the kernel.

stronger vortex (originally at the bottom) is able to displace the weaker vortex (originally at the top) radially outwards and continue its upward motion. Finally, the stronger vortex, positioned at the top, continues to entrain surrounding fluid from the bottom which is expelled at the top giving rise to the frontal lobe which propagates towards the laser source. The kernel boundary (shown with dashed black lines in Fig. 10 and Fig. 11) was determined using an edge finding algorithm that tracks the location of maximum temperature gradient along the perimeter of the kernel.

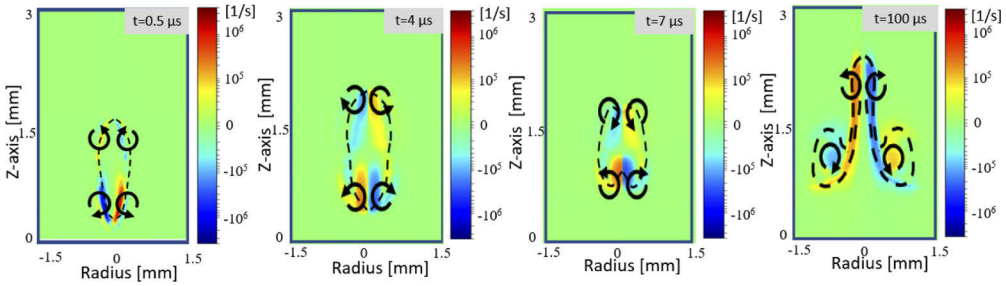

Fig. 10. Vorticity contours for various time delays during the kernel development into an asymmetric torus. The arrows indicate the direction of rotation. The kernel boundary is sketched using dotted lines for each time delay.

To better understand the mechanism(s) through which vorticity is generated, each of the terms in the vorticity equation are evaluated individually in CFD post-processing:

$$\frac{D\vec{\omega}}{Dt} = (\vec{\omega}\cdot\vec{\nabla})\vec{u} - \vec{\omega}(\vec{\nabla}\cdot\vec{u}) + \nu\vec{\nabla}^2\vec{\omega} + \frac{1}{\rho^2}[\vec{\nabla}\rho\times\vec{\nabla}p] \tag{5}$$

The first term on the right-hand side describes enhancement of vorticity by stretching and tilting due to the presence of velocity gradients. This is the mechanism through which turbulent eddies

Optics EXPRESS

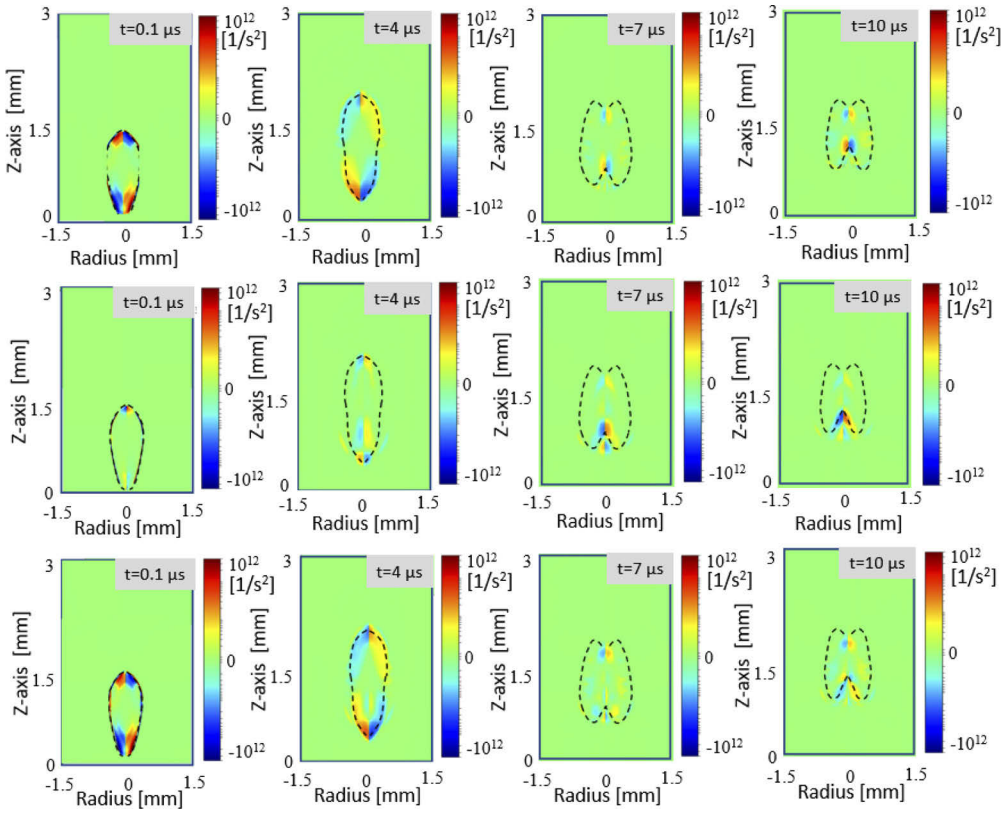

Fig. 11. Rate of vorticity generation by baroclinic torque (top) and kernel contraction (middle) compared to the total rate of vorticity generation (bottom). The shape of the actual spark kernel is shown with dotted line contour. The images show how vorticity is generated during the kernel collapse phase (t = 0.1-10 µs).

transfer energy to smaller scales in turbulent flows. The second term describes the effects of flow compressibility on the vorticity generation. This term enhances vorticity through the flow-field as the flow undergoes expansion or contraction. The third term describes the effects of viscous diffusion on vorticity generation. Finally, the last term describes vorticity generation by baroclinic torque, i.e. misalignment between density and pressure gradients. Evaluating each term shows that baroclinic torque is the main mechanism through which vorticity is generated with some contribution also from the compressibility (contraction) term. Figure 11 shows 2-D contours of the rate of vorticity from the dominant terms as well as the total rate. The images show that vorticity is generated predominantly by baroclinic torque and that the expansion term only acts as a source of enhancement/dissipation of vorticity that has already been generated in the fluid. Most of vorticity is generated during the first ~5 µs after the laser pulse with the baroclinic torque accounting for ~90% of the total vorticity generated at this stage. At ~10 µs after the pulse, the blast wave becomes fully detached and perfectly spherical thus removing the main source of baroclinicity. As time progresses, the contribution of the expansion term to the total vorticity generation increases. The kernel compression (which was initially induced by baroclinic torque) now gradually becomes the main contributor to vorticity enhancement. However, the rate of vorticity generation has dropped by two orders of magnitude: from $\sim 10^{12}$ $1/s^2$ at 4 µs down to $\sim 10^{10}$ $1/s^2$ at 10 µs.

Optics EXPRESS

A comparison between the pressure contours presented in the previous section and Fig. 11 shows that the generation of baroclinic torque is related to the blast wave dynamics. Baroclinic torque is generated in two stages. Before the shock wave detaches from the kernel surface, baroclinic torque induces vorticity which leads to the generation of the secondary pressure front discussed earlier. Then, after the formation of the rarefaction wave at the tail of the blast, the direction of baroclinic torque is reversed. As show in Fig. 11, baroclinic torque is the main contributor to the axial collapse of the kernel during this stage. After ~10 μs the effect of baroclinic torque becomes negligible (note that the rate of vorticity generation drops by two orders of magnitude between 1-10 μs). This time delay also corresponds to the complete blast wave separation from the kernel.

A physical explanation of the mechanism that generates baroclinic torque is provided with the aid of Fig. 12. As the shock wave is formed at the boundary of the kernel during the early stages of kernel development, it has a non-uniform pressure around its circumference. The pressure contours in the top of Fig. 12 show that the blast is stronger on the sides of the kernel where the front is more planar compared to the top and bottom where the front is more spherical. This is to be expected because the energy is dissipated more quickly in a spherical shock versus a planar one due to stretching of the wavefront during the associated increase in perimeter. A consequence of the non-uniform pressure field is that the pressure gradient at the "corner" of the kernel is slightly tilted towards the higher pressure part (side region) of the shock front. In

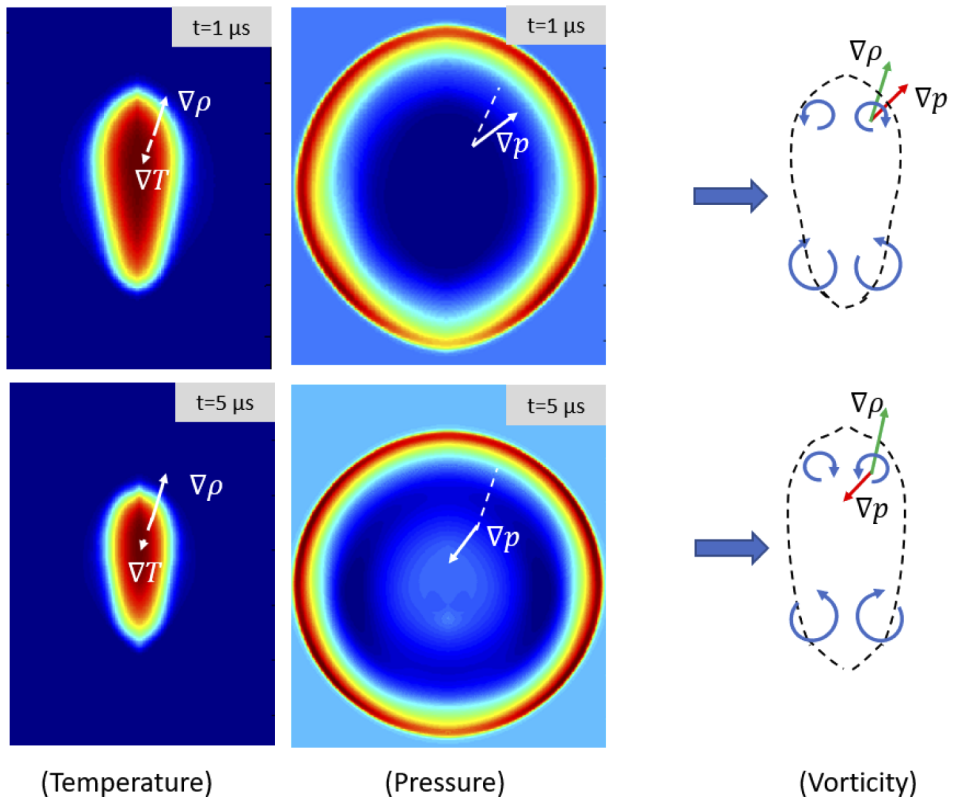

Fig. 12. Temperature and pressure contours showing the misalignment between the density and pressure contours at 1 μs (top) and 5 μs (bottom). The images show that, once the pressure gradient is reversed inside the kernel, baroclinic torque changes the direction of fluid rotation.

Optics EXPRESS

contrast, the gradient of density simply follows the temperature gradient (which points directly towards the epicenter of the blast) but it is inverted since higher temperature leads to lower density in a region of constant pressure. The broken line in the central panel of Fig. 12 indicates the orientation of the density gradient (as determined from the left panel). The two gradients and the ensuing vorticity direction are shown together schematically in the right panel of Fig. 12. This misalignment between the density and pressure gradients at the corners of the kernel leads to the generation of vorticity by baroclinic torque. At t~1.5-2 μs after breakdown, the detachment of the blast wave from kernel establishes an inward pointing pressure gradient which is caused by the inward flow induced by the rarefaction wave. This leads to a decrease, and ultimately to a direction reversal, of the vorticity generated by baroclinic torque. The bottom part of the blast wave has an even tighter radius of curvature than the top leading to similar behavior but with larger gradient misalignment, thus making the vortex at the bottom stronger than the one at the top. As discussed previously, this will ultimately dictate the direction of propagation of the third lobe, i.e., towards the direction of the plasma forming laser for the present case where the energy deposition leads to a stronger vortex on the downstream (bottom) side. Many of these ideas can be conceptually understood by considering the blast wave dynamics of a kernel initially shaped as a long thin cylinder: In this case the blast comprises two spherical fronts from the top and bottom of the cylinder and a planar front from the sides; the planar side front will propagates faster eventually catching up to the spherical fronts and ultimately become spherical (with baroclinic torque again generated at the "corners" until the wave is fully spherical). In this scenario, a perfectly symmetric torus will be obtained (with no third lobe observed) since the vortex pair will have equal strength. Such kernel dynamics are sometimes encountered in nanosecond pin-to-pin discharges when the energy is distributed homogenously inside the electrode gap [23,37,38]. Moreover, while the present focus is on NIR laser sparks, the mechanism described here can also be used to explain the hydrodynamics observed in visible and ultra-violet laser induced plasma.

4. Conclusions and future work

A numerical study of the gas dynamics induced by a laser spark was presented in this manuscript. It was found that the blast wave dynamics play a key role in the development of the experimentally observed asymmetric torus (three-lobe structure). Initially, the kernel takes the shape of a teardrop with the hotter region facing towards the laser propagation direction. This will ultimately influence how vorticity is being generated inside the kernel during its subsequent evolution. The strength of the ensuing blast wave, which initially takes the shape of the kernel, varies along its circumference during the early stages of kernel development. This leads to misalignment between the density and pressure gradient and generates vorticity by baroclinic torque. An analysis of the vorticity equation shows that baroclinic torque is the main mechanism that governs the collapse of the initial teardrop kernel into an asymmetric torus. Baroclinic torque is formed in two stages: first, before the shock wave detaches from the boundary of the kernel, baroclinic torque generates vorticity that brings fluid radially inwards and leads to the formation of a secondary pressure front within the kernel; second, several microseconds after the pulse, the rarefaction wave generates a pressure gradient reversal inside the kernel. This changes the direction of rotation induced by the baroclinic torque and leads to the axial collapse of the kernel. Past explanations of vorticity generation in the laser induced plasmas, in particular from Bradley [13], considered vorticity formation due to the (later) interaction of the rarefaction wave and kernel but not the possibility of (earlier) vorticity formation before detachment of the shock wave.

Ultimately, what dictates the direction in which the third lobe propagates is which of the two counter-rotating vortices is stronger. This depends primarily on the initial kernel topology. If the kernel is hotter at the front (which is the typical configuration for the optical breakdown process in which EAI is the dominant ionization mechanism), then the vortex at the bottom will be stronger (due to larger misalignment between the pressure and the density gradients from the

Optics EXPRESS

tighter radius) causing entrained gas to expel a lobe towards the front side (laser incident side). From a practical point of view, the following finding is important: if one desires to control the kernel dynamics in applications such as ignition, flame stabilization or aerodynamic flow control, one needs to control how the energy is deposited around the beam waist. This is consistent with our past work using dual-pulse laser plasma showing that the lobe can present at the front or back sides of the kernel, or not at all, depending on energy deposition [22].

Funding

Air Force Office of Scientific Research (FA9550-18-1-0239).

Acknowledgements

None.

Disclosures

The authors declare no conflicts of interest.

References

1. J. D. Dale, P. R. Smy, D. Way-Nee, and R. M. Clements, "Laser-ignited internal combustion engine," Combust. Flame **30**, 319–320 (1977).
2. S. Joshi, F. Loccisano, A. P. Yalin, and D. T. Montgomery, "On Comparative Performance Testing of Prechamber and Open Chamber Laser Ignition," J. Eng. Gas Turbines Power **133**(12), 122801 (2011).
3. N. Pavel, M. Tsunekane, K. Kanehara, and T. Taira, "Composite All-Ceramics, Passively Q-switched Nd:YAG/Cr^{4+}:YAG Monolithic Micro-Laser with Two-Beam Output for Multi-Point Ignition," Opt. Express **19**(10), 9378–9384 (2011).
4. J. D. Mullett, P. B. Dickinson, A. T. Shenton, G. Dearden, and K. G. Watkins, "Multi-cylinder laser and spark ignition in an IC gasoline automotive engine: A comparative study," *SAE Tech. Pap.* 2008 (2008).
5. D. L. McIntyre, S. D. Woodruff, M. H. McMillian, S. W. Richardson, and M. Gautam, "Lean-Burn Stationary Natural Gas Reciprocating Engine Operation With a Prototype Miniature Diode Side Pumped Passively Q-Switched Laser Spark Plug," *ASME 2009 Internal Combustion Engine Division Spring Technical Conference* pp 405–413 (2008).
6. S. Barbosa, P. Scouflaire, S. Ducruix, and G. Gaborel, "Comparisons Between Spark Plug and Laser Ignition in a Gas Turbine Combustor," *Proceedings of the European Combustion Meeting* pp 2–7 (2007).
7. M. Börner, C. Manfletti, and M. Oschwald, "Experimental Study of a Laser-Ignited Liquid Cryogenic Rocket Engine Conventional ignition methods of cryogenic rocket engines," *Laser Ignition Conference* pp 1–19 (2015).
8. C. Manfletti and G. Kroupa, "Laser ignition of a cryogenic thruster using a miniaturised Nd:YAG laser," Opt. Express **21**(S6), A1126 (2013).
9. L. Wermer, J. Hansson, and S. Im, "Dual-pulse laser-induced spark ignition and flame propagation of a methane diffusion jet flame," Proc. Combust. Inst. **36**(3), 4427–4434 (2017).
10. S. Brieschenk, S. O'Byrne, and H. Kleine, "Ignition characteristics of laser-ionized fuel injected into a hypersonic crossflow," Combust. Flame **161**(4), 1015–1025 (2014).
11. S. Brieschenk, S. O'Byrne, and H. Kleine, "Laser-induced plasma ignition studies in a model scramjet engine," Combust. Flame **160**(1), 145–148 (2013).
12. A. M. Starik, N. S. Titova, L. V. Bezgin, and V. I. Kopchenov, "The promotion of ignition in a supersonic H2–air mixing layer by laser-induced excitation of O2 molecules: Numerical study," Combust. Flame **156**(8), 1641–1652 (2009).
13. D. Bradley, C. G. W. Sheppard, I. M. Suardjaja, and R. Woolley, "Fundamentals of high-energy spark ignition with lasers," Combust. Flame **138**(1-2), 55–77 (2004).
14. T. X. Phuoc, "Laser spark ignition: Experimental determination of laser-induced breakdown thresholds of combustion gases," Opt. Commun. **175**(4-6), 419–423 (2000).
15. M. H. Morsy and S. H. Chung, "Numerical simulation of front lobe formation in laser-induced spark ignition of ch 4 /air mixtures," Proc. Combust. Inst. **29**(2), 1613–1619 (2002).
16. I. A. Mulla, S. R. Chakravarthy, N. Swaminathan, and R. Balachandran, "Evolution of flame-kernel in laser-induced spark ignited mixtures: A parametric study," Combust. Flame **164**, 303–318 (2016).
17. J. L. Beduneau, N. Kawahara, T. Nakayama, E. Tomita, and Y. Ikeda, "Laser-induced radical generation and evolution to a self-sustaining flame," Combust. Flame **156**(3), 642–656 (2009).
18. I. G. Dors and C. G. Parigger, "Computational fluid-dynamic model of laser-induced breakdown in air," Appl. Opt. **42**(30), 5978–5985 (2003).
19. N. Glumac, G. Elliott, and M. Boguszko, "Temporal and Spatial Evolution of the Thermal Structure of a Laser Spark in Air," *43rd AIAA Aerospace Sciences Meeting and Exhibit* pp 1–16 (2005).

Optics EXPRESS

20. S. A. Ramsden and P. Savic, "A Radiative Detonation Model for the Development of a Laser-Induced Spark in Air," Nature **203**(4951), 1217–1219 (1964).
21. T. Endo, Y. Takenaka, Y. Sako, T. Johzaki, S. Namba, and D. Shimokuri, "An experimental study on the ignition ability of a laser-induced gaseous breakdown," Combust. Flame **178**, 1–6 (2017).
22. C. Dumitrache, R. Vanosdol, M. Limbach C, and A. P. Yalin, "Control of Early Flame Kernel Growth by Multi-Wavelength Laser Pulses for Enhanced Ignition," Sci. Rep. **7**(1), 10239 (2017).
23. M. Kono, K. Niu, T. Tsukamoto, and Y. Ujiie, "Mechanism of flame kernel formation produced by short duration sparks," Symp. (Int.) Combust., [Proc.] **22**(1), 1643–1649 (1989).
24. S. Ghosh and K. Mahesh, "Numerical simulation of laser – induced breakdown in air," *46th AIAA Aerospace Sciences Meeting* pp 1–22 (2008).
25. M. W. Chase, "NIST-JANAF Themochemical Tables, Fourth Edition," J. Phys. Chem. Ref. Data, Monogr. **9**, 1–1951 (1998).
26. B. N. Srivastava and R. C. Srivastava, "Thermal conductivity and eucken correction for diatomic gases and binary gas mixtures," J. Chem. Phys. **30**(5), 1200–1205 (1959).
27. E. Toro, *Riemann Srolvers and Numerical Methods for Fluid Dynamics* (Springer-Verlag, 1999).
28. J. R. Edwards, "A low-diffusion flux-splitting scheme for Navier-Stokes calculations," Comput. Fluids **26**(6), 635–659 (1997).
29. T. J. Poinsot and S. K. Lelef, "Boundary conditions for direct simulations of compressible viscous flows," J. Comput. Phys. **101**(1), 104–129 (1992).
30. K. W. Thompson, "Time dependent boundary conditions for hyperbolic systems," J. Comput. Phys. **68**(1), 1–24 (1987).
31. C. Dumitrache and A. Yalin, "Laser-induced heating using a non-resonant dual-pulse approach with application to laser ignition," *46th AIAA Plasmadynamics and Lasers Conference* (2015).
32. C. Dumitrache, C. M. Limbach, and A. P. Yalin, "Threshold characteristics of ultraviolet and near infrared nanosecond laser induced plasmas," Phys. Plasmas **23**(9), 093515 (2016).
33. A. B. Murphy , and A. J. D. Farmer, "Temperature measurement in thermal plasmas by Rayleigh scattering," J. Phys. D: Appl. Phys. **25**(4), 634–643 (1992).
34. E. Carbone and S. Nijdam, "Thomson scattering on non-equilibrium low density plasmas: Principles, practice and challenges," Plasma Phys. Controlled Fusion **57**(1), 014026 (2015).
35. T. Phuoc and F. White, "Laser-induced spark ignition of CH 4/air mixtures," Combust. Flame **119**(3), 203–216 (1999).
36. T. A. Spiglanin, A. Mcilroy, E. W. Fournier, R. B. Cohen, and J. A. Syage, "Time-resolved imaging of flame kernels: Laser spark ignition of H2/O2/Ar mixtures," Combust. Flame **102**(3), 310–328 (1995).
37. S. Stepanyan, N. Minesi, A. Salmon, G. D. Stancu, and C. O. Laux, "Spatial evolution of the plasma kernel produced by nanosecond discharges in air," J. Phys. D: Appl. Phys. **52**(29), 295203 (2019).
38. M. Castela, S. Stepanyan, B. Fiorina, A. Coussement, O. Gicquel, N. Darabiha, and C. O. Laux, "A 3-D DNS and experimental study of the effect of the recirculating flow pattern inside a reactive kernel produced by nanosecond plasma discharges in a methane-air mixture," Proc. Combust. Inst. **36**(3), 4095–4103 (2017).

scientific reports

Check for updates

OPEN

Resonant dual-pulse laser ignition technique based on oxygen REMPI pre-ionization

Ciprian Dumitrache[1], Carter Butte[2] & Azer Yalin[2]✉

This contribution investigates a novel laser ignition method based on a dual-pulse resonant pre-ionization scheme. The first laser pulse efficiently creates initial gas ionization (seed electrons) through a 2 + 1 resonantly-enhanced multiphoton ionization (REMPI) scheme targeting molecular oxygen (λ ~ 287.6 nm). This pulse is followed by a second non-resonant near-infrared pulse (λ = 1064 nm) for energy addition into the gas via inverse bremsstrahlung absorption. The sequence of two pulses creates a laser induced plasma that exhibits high peak electron number density and temperature ($n_e \sim 8 \times 10^{17}$ cm^{-3} at t = 100 ns and T ~ 8000 K at t = 10 μs, respectively). These plasma parameters are similar to those attained for typical single-pulse near-infrared laser plasmas but with the advantage of substantially lower pulse energy (by factor of ~ 2.5) in the dual-pulse REMPI case. A combustion study focusing on ignition of propane/air mixtures shows that the dual-pulse REMPI method leads to an extension of the lean flammability limit, and an increase in combustion efficiency near the lean limit, as compared to laser ignition with a single NIR pulse. The measurement results and observed gas dynamics are discussed in the context of their impact on combustion applications.

The ever-increasing push for energetically efficient and environmentally friendly energy conversion systems, in particular combustion technologies, has driven the interest in laser ignition (LI) as an alternative to conventional ignition systems. LI systems are potentially attractive in this regard, for example, when applied to industrial reciprocating natural gas engines, LI has shown reduction in NO_x emissions and extension of the lean limit[1–3]. The technology is of interest to a variety of combustion applications including reciprocating engines, aero-turbines, and rocket engines[4–10]. System level features of LI, as contrasted to conventional igniter technology, include: the lack of electrodes (which tend to act as heat sinks) within the combustion chamber, the ability to achieve fine control over ignition timing, flexibility in locating the ignition source (based on focusing optics), and potentially systems with favorable cost, packaging and reliability parameters.

Recent approaches towards LI have examined dual (or multiple) pulse laser plasmas based on pre-ionization, i.e. where a first laser pulse primarily ionizes the gas (to produce seed electrons) and then subsequent pulse(s) primarily heat and add energy to the plasma gas kernel via inverse Bremsstrahlung (IB)[11,12]. In general, short wavelength is better suited for the preionization (owing to more efficient multi-photon ionization) while longer wavelength radiation is better suited for energy addition (owing to more efficient IB). The preionization approach relies on synergistic effects between the two pulses, in particular the increased absorption of the second pulse caused by the preionization. This is distinct from multi-pulse approaches (usually at a single-wavelength) where the individual pulses each independently cause breakdown[13,14] Experimentally, Yalin et al. showed that preionization due to an ultraviolet (UV) 266 nm beam in air reduces the breakdown requirement of an overlapped near-infrared (NIR) energy addition beam at 1064 nm[12]. When applied to combustion, Dumitrache et al. showed that the dual-pulse preionization scheme allowed ignition of leaner propane-air mixtures as compared to single-pulse ignition with the same pulse energy[15]. Subsequent modeling work has further elucidated aspects of the pre-ionization laser plasmas. A computational fluid dynamics (CFD) analysis has shown the role of plasma-driven gas dynamics to enhance the early kernel growth, in particular an ability to tailor the resulting laser plasma (by adjusting the axial offset of the two laser pulses) to either suppress or admit the typical 3rd lobe feature which in turn is linked to the ability to ignite lean mixtures[16]. Kinetic modeling has examined nonequilibrium and electron dynamics in the dual-pulse preionization laser plasmas[17].

Specifying required plasma parameters for ignition in practical applications is challenging owing to the different possible fuel mixtures and flowfields (e.g. ignition of reciprocating engines versus aero-turbines versus

[1]Plasma and Radiation Physics, Solid-State Quantum Electronics Lab., National Institute for Laser, 077125 Bucharest, Romania. [2]Department of Mechanical Engineering, Colorado State University, Fort Collins 80525, USA. ✉email: azer.yalin@colostate.edu

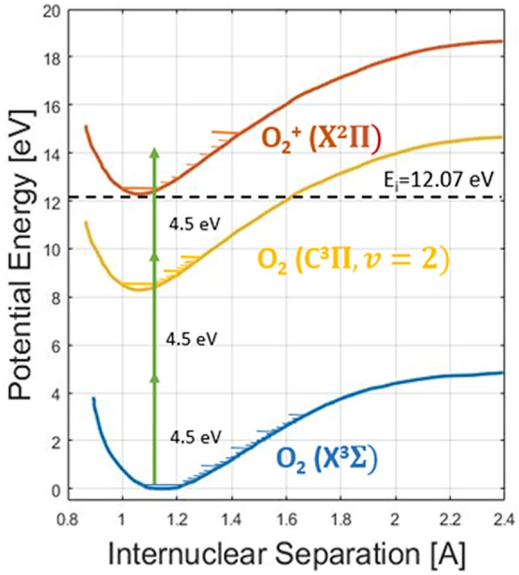

Figure 1. Simplified energy level diagram of molecular oxygen showing the targeted 2 + 1 REMPI scheme (green arrows).

scramjets). The ignition kernel volume, in particular, is expected to be of great importance in combustion devices (e.g. some fuel-injected engines) that exhibit poor mixing of the fuel-and-air[18] since the larger volume is statistically more likely to overlap ignitable (well-mixed) regions. Our past work has shown larger kernel volumes (more elongated along the optical axis) when preionization is employed[19]. In general, high temperature will benefit ignition owing to promoting chain initiation reactions (rates exponential with temperature)[20], and higher electron density and temperature can increase the production of radicals and metastables from electron impact reactions[21]. However, the situation is also complicated by the associated gas dynamics, in particular fluid entrainment and vortex formation/ejection, which has also been shown to play an important role in early kernel growth[22]. An example of translating to applications is provided by past studies in a rapid compression machine where we showed successful ignition of methane–air mixtures over a range of equivalence ratios with NIR plasmas[3]. While the present work makes the first examination of the dual-pulse REMPI approach in quiescent, room temperature mixtures, future work should include detailed parametric studies tailored to specific applications.

In the present contribution, we investigate the use of a resonant preionization step, specifically the use of oxygen resonant enhanced multiphoton ionization (REMPI) at ~ 287 nm, in place of the 266 nm excitation. As will be shown herein, the resonant scheme allows more efficient electron generation (with the preionization) for much lower total pulse energy (e.g., we obtain $n_e = 1.3–3.7 \times 10^{17}$ cm^{-3} using a 3 mJ REMPI pulse compared to $n_e = 2.5–6.1 \times 10^{16}$ cm^{-3} using a non-resonant (1064 nm) 20 mJ pulse with the same beam waists). When the REMPI and NIR pulses are combined, the resonant dual-pulse scheme provides similar gas temperatures and ignition characteristics as compared to the 266/1064 nm scheme but with overall lower energy requirements ($E_{REMPI+NIR} = 40$ mJ vs. $E_{UV+NIR} = 60$ mJ). In general, the use of UV wavelengths (harmonic generation) is less energetically efficient on the laser source side. This aspect (along with size, cost, chance of optical damage) should be evaluated at the system level while keeping in mind that in many combustion applications the power of the ignition source is negligible compared with the thermal power of the flame[23].

Figure 1 shows a simplified energy level diagram for molecular oxygen including the 2 + 1 REMPI transition of interest. In the 2 + 1 notation, the 2 corresponds to the 2-photon excitation step from the oxygen ground state ($X^3\Sigma^-_g$ ($v'' = 0, J''$)) to the intermediate state ($C^3\Pi_g(v' = 2, J')$) which, when excited by a single additional photon (+ 1) is finally excited to an ionized level of molecular oxygen (O_2^+ $X^2\Pi$). At high laser intensities, any molecule reaching the intermediate state will also be subsequently ionized such that, as investigated herein, the overall ionization rate scales as the square of the laser intensity (i.e. step-wise ionization is limited by the 2-photon step)[24]. In terms of laser plasma formation, this REMPI transition has been investigated by Adams et al. for breakdown and guiding of discharges[25] and for thermometry based on microwave scattering from the laser plasma[26,27] . At high laser intensities effects of anomalous laser absorption can also become important[28,29].

The remainder of the paper focuses on our investigation of laser plasma formation and ignition using REMPI pre-ionization. We first examine the electron generation (preionization) as a function of laser wavelength in the vicinity of the REMPI transition and confirm resonant 2 + 1 excitation. Next, through the use of Rayleigh and Thomson scattering diagnostics, we consider the temporal profiles of gas temperature and electron density for the dual-pulse preionization plasmas (287 nm followed by 1064 nm pulses). We find that peak temperature and electron density is quite comparable to the corresponding values for single-pulse excitation, but with considerably lower (total) pulse energy in the dual-pulse REMPI case. In terms of ignition, the dual-pulse REMPI case extends the lean limit for propane-air ignition when compared to a single laser pulse (and again with lower pulse energy). The final investigation examines the gas dynamics and vorticity generation in the laser induced plasma

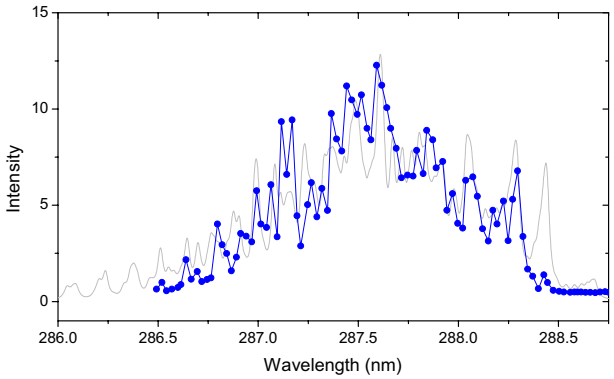

Figure 2. Thomson scattering signal from oxygen (T = 300 K, P = 1.0 atm) as function of pre-ionization laser wavelength. Blue symbols and lines are from experiment while the grey line is simulation (see text).

revealing the important role of the 3rd lobe in the flame growth. Conclusions and outlook for future research are also presented.

Results and discussion

Preionization of air by resonant enhanced multiphoton ionization of oxygen. The first set of experiments was to confirm the role of the oxygen REMPI in the preionization step based on our experimental scheme using focused nanosecond lasers in air (see "Methods" section for full setup). To this end, we have studied both the wavelength- and energy- dependence of the laser preionization step. We employ laser Thomson scattering (with an additional probe laser—see "Methods" section) as a diagnostic for plasma density[30]. Briefly, laser Thomson scattering yields a scattering spectrum due to elastic scattering of photons by electrons which, in the incoherent (non-collective) regime ($\alpha << 1$), yields a Gaussian spectrum with amplitude proportional to electron density (and probe laser power) and width proportional to the electron temperature. However, for all the scattering measurements reported here a wavelength integrated scattering signal was used. Figure 2 shows the resulting Thomson scattering signal (indicative of electron generation) as a function of the wavelength of the preionization laser. For these data, the Thomson scattering signals were recorded immediately after the end of pre-ionization pulse (~ 1 ns after the pulse, when the signal strength was maximum). Also shown in Fig. 2 is a simulated REMPI spectrum for the same transition based on the model described by Wu et al.[27] Note that the spectrum here refers to the dependence of the full (wavelength-integrated) Thomson signal as a function of the wavelength of the REMPI laser (not the spectrum of Thomson scattered light). The modeled spectrum requires detailed knowledge of the two-photon line strengths and includes Voigt convolution of laser linewidth with the thermal and natural line-broadening. The spectrum is due to the rotational structure of the vibronic transition from the molecular oxygen ground state to the intermediate state, i.e. $C^3\Pi_g(v'=2,J') \leftarrow\leftarrow X^3\Sigma^-_g\ (v''=0,J'')$, as this is the rate-limiting step of the 2 + 1 step-wise ionization. The reasonable agreement between model and experiment, including the fact that we observe no Thomson signal when detuned from the transition, confirm that ionization is via REMPI, as opposed to via (non-resonant) multi-photon ionization (MPI) and/or EAI. The discrepancies that are present are likely due to a combination of: (1) laser pulse energy (and beam quality) variations over the broad scanning interval and (2) the need to further tune the detailed line strengths and linewidths in the model. The REMPI assumption was further examined by measuring the dependence of the Thomson scatter signal on the energy of the pre-ionization pulse (at fixed wavelength of ~ 287.62 nm). These experiments showed that the Thomson scatter intensity varied with the square of the intensity of the pre-ionization beam (i.e. $n_e \sim I^2$) which further confirms plasma excitation via the 2 + 1 REMPI[31]. This result can be contrasted with similar studies (based on optical emission as a proxy for ionization) where, for 266 nm ionization, we found a cubic dependence (i.e. $n_e \sim I^3$) indicative of oxygen MPI (based on $E_{I,O2} = 13.6$ eV and $E_{photon,266\ nm} = 4.66$ eV)[19]. In summary, these tests confirm the role of the oxygen REMPI pre-ionization in the first step of our dual-pulse scheme. For all subsequent experiments, the wavelength of the REMPI beam was set to ~ 287.62 nm at the approximate peak of the spectrum.

Electron density of dual-pulse REMPI plasmas. 1-D Rayleigh and Thomson scattering measurements were performed to determine the plasma temperature and electron number density profiles. Figure 3 shows the resulting electron density during the post-discharge phase (0.1–1 μs after the pulses) for three cases: O_2 REMPI pulse on its own ($\lambda = 287.6$ nm, E = 3 mJ), single NIR pulse ($\lambda = 1064$ nm, E = 95 mJ), and the dual-pulse REMPI ($\lambda = 287.62$ nm, E = 3 mJ and $\lambda = 1064$ nm, E = 37 mJ). The measurements were conducted in a pressure cell filled with zero-grade air at $p_0 = 1$ bar and $T_0 = 298$ K. Even with the relatively low REMPI pulse energy a significant degree of ionization is still achieved. For example, we find electron number density of $n_e = (1.9 \pm 0.8) \times 10^{17}$ cm^{-3} at 100 ns after the pulse). In contrast, the non-resonant near-infrared (NIR) pulse does not achieve measurable ionization (breakdown) at such low energies. Indeed, for single-pulse NIR, a pulse energy of 95 mJ was adopted for testing as it was the lowest energy for which consistent (visible) breakdown was achieved. However, once formed, the NIR plasma is found to be almost an order of magnitude denser as compared to the (lower

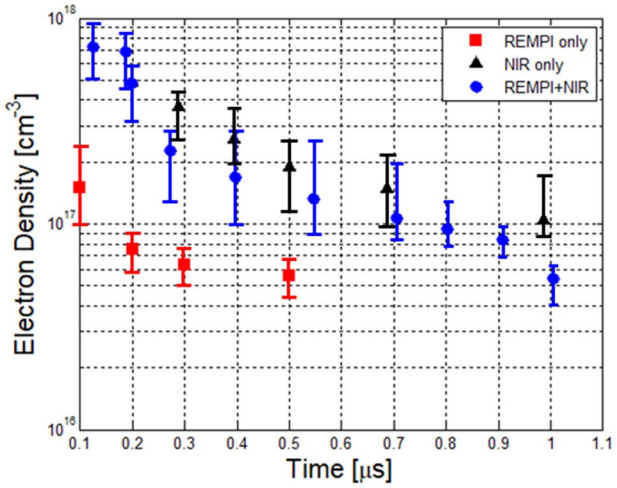

Figure 3. Temporal profiles of electron number density after breakdown for three different laser-generated plasmas: O_2 REMPI: $E_{287\ nm} = 3$ mJ (red), single-pulse NIR: $E_{1064\ nm} = 95$ mJ (black) and dual-pulse REMPI: $E_{287+1064\ nm} = 40$ mJ (blue).

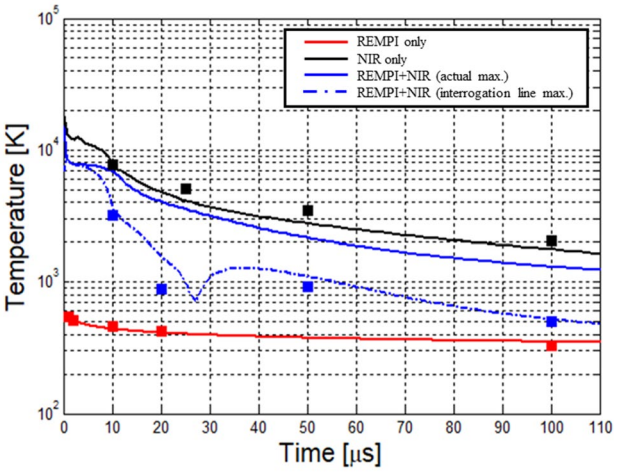

Figure 4. Gas temperature as a function of time after breakdown for three different types of laser-generated plasma: 2 + 1 O_2 REMPI (red), NIR (black) and combined REMPI + NIR (blue). Gas temperature profiles predicted by CFD modeling are shown with lines.

pulse energy) REMPI case, for example $n_e = (8.3 \pm 1.3) \times 10^{17}$ cm^{-3} at 110 ns after the pulse. These results are largely explained by the different mechanism involved in non-resonant breakdown at 1064 nm where most of the free-electrons are generated by electron avalanche ionization (as opposed to MPI or REMPI) which also results in a stronger threshold behavior[19]. For the dual-pulse REMPI case, the resulting plasma is similarly dense as compared to the single-pulse NIR pulse but using approximately 2.5 times less total pulse energy, i.e. 40 mJ (= 3 mJ + 37 mJ) total for dual-pulse REMPI versus 95 mJ for single-pulse NIR. The fast decay in electron density is explained by two main factors: kinetics (rapid recombination and attachment) and gas-dynamics (both experiments and simulations showed that the hot kernel expands very quickly during the first microsecond after plasma formation thus leading to a decrease in density[22]). In all cases presented in Fig. 3, the vertical error bars are due to the uncertainty in discriminating between the Thomson and Rayleigh scattering contributions at early times.

Temperature of single- and dual-pulse REMPI plasma. Gas temperature measurements are performed from Rayleigh scattering signals using the same experimental setup as was used for electron density (including the same pulse energies). The Rayleigh signals can only be accurately analyzed (with no Thomson interference) at sufficiently late times after the plasma forming laser pulses[11,19,32]. Figure 4 presents gas temperature measurements begininng 10 μs after the excitation. For the earlier delays, temperature is inferred using numerical simulations of the hot plasma kernel (see "Methods" section for details). The CFD-predicted tempera-

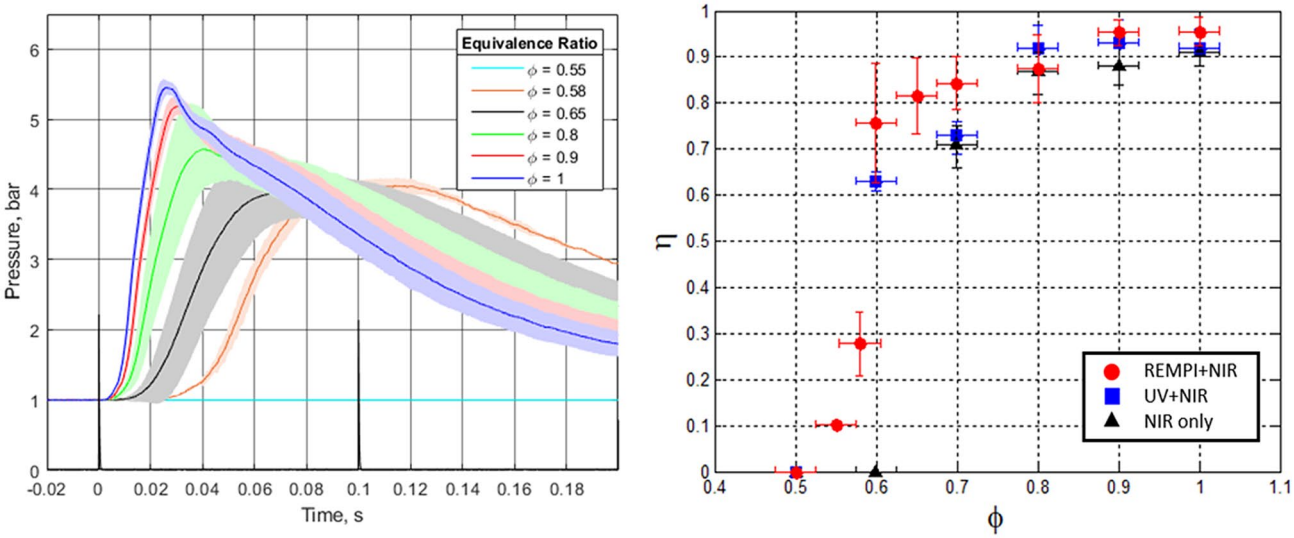

Figure 5. Left: Pressure traces due to dual-pulse REMPI ignition of propane–air mixtures. The different curves correspond to different equivalence ratios. Right: Combustion efficiency for 3 cases of laser ignition of propane–air mixtures: dual-pulse REMPI (red), non-resonant dual-pulse (blue), and single-pulse NIR (black). Each point represents the average of at least three tests and the error bars are ± 1 standard deviation.

ture profiles are shown with solid lines in Fig. 4. The tempeature profile shows that the 2 + 1 O_2 REMPI plasma is extremly cold (given the degree of ionization) with a maximum measured temperature of ~ 530 K at 1 μs after the discharge. This is to be expected in a rezonant ionization process where most of the laser energy goes directly into ionization, in this case forming $O_2^+(X)$ and free electrons, as opposed to joule heating induced by IB. For the NIR breakdown case, we find considerably higher temperatures in excess of 8300 K at 10 μs after the pulse (~ 15,000 K predicted by CFD at t = 0, i.e. at the end of the excitation pulse). As with the electron density results reported above, the dual-pulse REMPI allows similar plasma parameters (temperature in this case) when compared to single-pulse (NIR) but with only ~ 40% of the total pulse energy. The temperatures plotted in Fig. 4 correspond to the maximum temperature of the laser plasma at the given time. For the single-pulse experiments (REMPI only and NIR only) this was achieved by iteratively moving the Rayleigh probe beam at each time delay; however, owing to the potentially more complex flowfield, the dual REMPI + NIR case used a fixed measurement location. For this reason, we present two curves for the REMPI dual-pulse case in Fig. 4: the maximum temperature at a fixed location across the kernel shown in dashed blue line (data which matches well with the experimental data) and the overall peak plasma temperature from CFD. The sudden increase in temperature between 30 and 40 μs (dashed blue line) is due to strong gas dynamics associated with the motion of a hot lobe towards the side of the incoming laser during gas cooling phase. This peak does not appear in the other three curves which track overall maximum temperature because the frontal lobe never becomes the hottest part of the kernel. Finally, each experimental point includes a vertical error bar of ± 20 K, mostly due to shot-noise, but the error bars do not show on the semi-logarithmic plot.

Ignition testing and combustion efficiency. Laser ignition experiments were conducted in a pressure cell with mixtures of propane-air at initial conditions of $T_0 = 323$ K and $p_0 = 1$ bar. Combustion events were monitored based on the temporal evolution of pressure inside the cell. Pressure traces corresponding to ignition of C_3H_8/Air mixtures via the combined REMPI + NIR pulses are shown in Fig. 5-left below. The end-time of the plasma forming laser pulses defines t = 0 in the pressure traces. After a certain delay (which depends on the mixture's equivalence ratio, ϕ), a pressure rise is observed in the mixtures that ignited successfully. The pressure rise is due to heat release by chemical reactions which raise the temperature of the fixed-volume cell. As leaner mixtures are tested, the peak pressure reduces. This is mainly a consequence of the reduction in mixture reactivity. However, for the ultra-lean cases ($\phi < 0.7$), a decrease in combustion efficiency is also observed. This is shown in Fig. 5-right, where the combustion efficiency, i.e. the fraction of starting fuel energy that gets converted into heat, η, is plotted for each equivalence ratio.

We contrast the performance of the dual-pulse REMPI ($\lambda = 287.62$ nm, E = 3 mJ and $\lambda = 1064$ nm, E = 37 mJ) ignition scheme with past (baseline) measurements of combustion efficiencies for single-pulse NIR ($\lambda = 1064$ nm, E = 95 mJ) and non-resonant dual-pulse ($\lambda = 266$ nm, E = 20 mJ and $\lambda = 1064$ nm, E = 40 mJ)[15] as also shown in Fig. 5-right. The experimental results indicate the dual-pulse REMPI technique can ignite leaner mixtures as compared to single-pulse NIR ($\phi_{Min} = 0.55$ for the dual-pulse REMPI and $\phi_{Min} = 0.7$ for single-pulse NIR, respectively), as well as achieving higher combustion efficiency for the leanest ignited mixtures. Additionally, the REMPI + NIR technique exhibits higher combustion efficiency towards the lean limit as compared to the non-resonant dual-pulse. Ignition using the REMPI pulse on its own (with no accompanying 1064 nm beam) was unsuccessful due to the low temperature generated by the resonant plasma (Fig. 4). The shaded bands around the pressure traces in Fig. 5-left correspond to ± 1 standard deviation after averaging multiple ignition events.

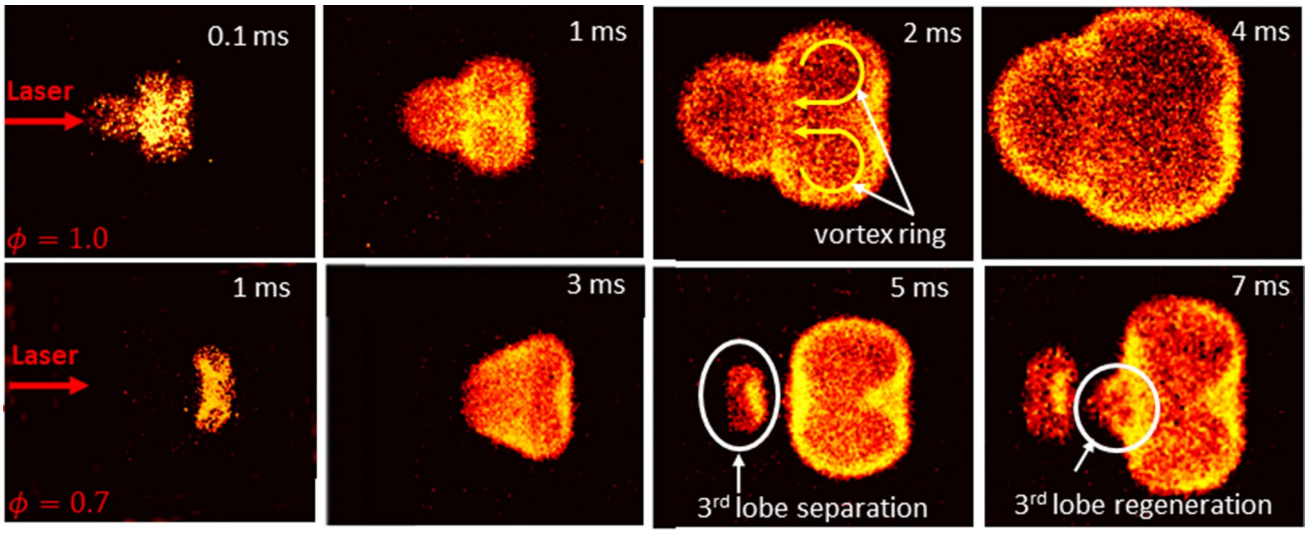

Figure 6. OH* chemiluminescence images showing the early flame kernel dynamics for stoichiometric: $\phi = 1.0$ (top) and lean: $\phi = 0.7$ (bottom) mixtures due to laser ignition with the dual-pulse REMPI configuration.

In general, the pressure traces become more variable as the equivalence ratio is reduced. Finally, the vertical error bars in the combustion efficiency plot correspond to one standard deviation in calculated combustion efficiency based on each individual pressure trace. The horizontal error bars for equivalence ratio correspond to the uncertainty in the pressure gauge reading used for mixing the gases.

Gas dynamics of dual-pulse REMPI plasmas. The flame dynamics induced by the laser plasma kernels are investigated based on OH* chemiluminescence images. The image sequences shown in Fig. 6 are due to ignition of C_3H_8/Air mixtures at stoichiometric ratio of $\phi = 1.0$ (top) and a fuel-lean condition of $\phi = 0.7$ (bottom) using the dual-pulse REMPI laser technique (λ = 287.62 nm, E = 3 mJ and λ = 1064 nm, E = 37 mJ). At stoichiometric conditions, the flame dynamics exhibit similar behavior as has been observed in the post-discharge of NIR laser plasmas[33–38]. Specifically, one observes an asymmetric toroidal flame structure having two side lobes (due to slicing of the actual toroidal feature with the 2-D section) and a third (frontal) lobe that tends to propagate towards the laser source.

Interestingly, lean mixtures appear to exhibit a rapid quenching of the third lobe within the first few hundred microseconds (note that already at 1 ms in Fig. 6 below, the frontal lobe is missing from the images). Nonetheless, vorticity generated inside the toroid continues to entrain combustible fluid through its hot center and back towards the laser source. This effect appears to cause multiple lobe re-ignition and separation events during the combustion event. The detachment and extinction of the 3rd lobe has been previously observed in single-pulse (NIR) laser breakdown[15,39]. However, the regeneration of the third lobe at later times has not, to our knowledge, been reported before. This might suggest that the dual-pulse REMPI breakdown generates stronger (more persistent) vorticity resulting in the observed gas-dynamics in the lean mixtures case, as compared to other LI modes.

Summary

The current study presents a new laser ignition technique based on resonant pre-ionization of oxygen molecules at ~ 287.6 nm. For subsequent energy addition, we employ a dual-pulse sequence where the first 287.6 nm resonant pulse is followed by a NIR 1064 nm pulse. The presence of resonant photoionization was confirmed via rotationally resolved spectra for the two-photon excitation of the $C^3\Pi_g(v' = 2) \leftarrow X^3\Sigma_g^-(v'' = 0)$ transition using laser Thomson scattering. The plasma was further characterized using Thomson and Rayleigh scattering to determine the electron number density and gas temperature evolution after the spark. The REMPI plasma was compared with the plasma due to a typical NIR single-pulse (1064 nm) and it was noted that a significant degree of ionization can be obtained using only a fraction of the laser energy. Gas heating induced by the REMPI plasma was noted to be minimal; however, when combined with a lower energy NIR pulse, one could get similar temperatures to a NIR breakdown plasma by only using ~ 40% of the total laser energy. Finally, ignition testing with the dual-pulse REMPI technique showed the possibility of increased combustion efficiency at lean conditions as compared to other laser ignition schemes. Ignition testing also showed that the lean limit can be extended from $\phi = 0.7$ (for single-pulse NIR breakdown) to $\phi = 0.55$ using the dual-pulse REMPI technique.

Methods

Optical layout. The experiments were conducted using the basic setup shown in Fig. 7. The REMPI pre-ionization beam is due to the ($\lambda \sim 287$ nm) output (doubled-signal beam) from an optical parametric oscillator (OPO) laser system (Continuum Sunlite). The OPO is pumped by a seeded Nd:YAG laser (Continuum Powerlite 8010). For dual-pulse schemes, the energy addition pulse was the fundamental output (λ = 1064 nm) from a second Nd:YAG (New Wave Gemini PIV). The energy of this laser could be changed by a variable attenuator com-

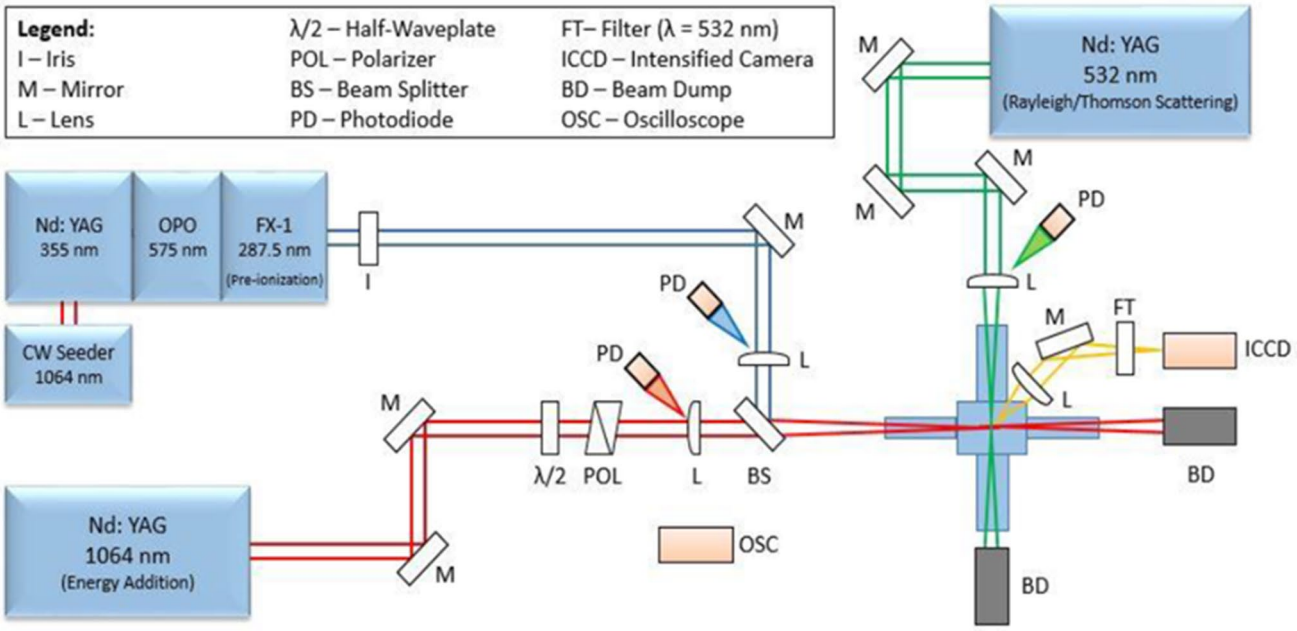

Figure 7. Optical layout used for the laser ignition experiments. Dual-pulse REMPI experiments uses overlapped beams from the 287 nm and 1064 nm laser outputs. An additional 532 nm beam is for scattering diagnostics.

Laser type	Wavelength (nm)	Pulse duration (ns)	Waist diameter (μm)	M^2 factor	Energy (mJ)
REMPI	286–290	7	150	3.4	3
UV	266	7	150	1.9	20
NIR	1064	10	150	3.2	95
Thomson/Rayleigh scattering	532	12	170	2.1	5

Table 1. Laser parameters used in the experiments.

prised of a half-wave plate and polarizer pair. The two beams are spatially overlapped (with precision ~ 10 μm) using a beam splitter and focused inside the combustion chamber using two $f = 300$ mm plano-convex lenses (one in each beam path). To vary the offset between the two beams in the axial direction (i.e. along the beam propagation direction), a translation stage was used to move the focusing lens of the 1064 nm beam. Fine-tuning of the overlap of the two beams (REMPI and NIR) is achieved by minimizing the beam energies required for plasma formation in lab air. For the non-resonant UV + NIR dual-pulse measurements, the UV pulse was obtained from the same Continuum Powerlite 8010 by replacing the third harmonic crystal with a fourth harmonic crystal (266 nm) and overriding the OPO path. For the Rayleigh/Thomson scattering experiments a third probe beam, due to the 532 nm output of another Nd:YAG laser (Spectra-Physics Quanta-Ray), was brought in orthogonally to the two plasma-formation (287 nm and 1064 nm) lasers using a set of dielectric mirrors and a plano-convex lens (f = 250 mm). A series of photodiodes and energy meters were used to monitor laser pulse durations and pulse energies of each beam leg (i.e. 287 (or 266) nm and 1064 nm) both before and after passage through the focal region and combustion chamber. The axial overlap and the beam diameters at the focus were measured using a beam profiler (Ophir SP503). The beam characteristics for each laser beam used are summarized in Table 1. Beam intensities can be determined from pulse energy, duration, and beam diameter. For a full description of the laser beam parameters, the M^2 beam quality factor is also provided in Table 1. Spatial- and temporal- intensity fluctuations within multi-mode beams can influence the efficiency of the multiphoton ionization process[40].

Thomson/Rayleigh scattering measurements. Diagnostic measurements of gas temperature and electron density of the laser plasmas were performed by Rayleigh and Thomson scattering. Details on these methods have been presented in our past publications[19,41,42] and here we summarize the essential features. The probe beam is nominally aligned to pass through the center of the laser plasma to allow 1-D (line) measurement of (combined) Rayleigh and Thomson scattering from the laser plasma (see Fig. 8). Baffles are introduced into the chamber to reduce stray light scattering from the chamber windows. The plasma is imaged using a broadband collection lens (f = 75 mm) and a silver-coated steering mirror into an ICCD camera (pco DICAM pro) which observes the scattering volume orthogonally from above. A bandpass filter at 532 nm (Thorlabs FL532-

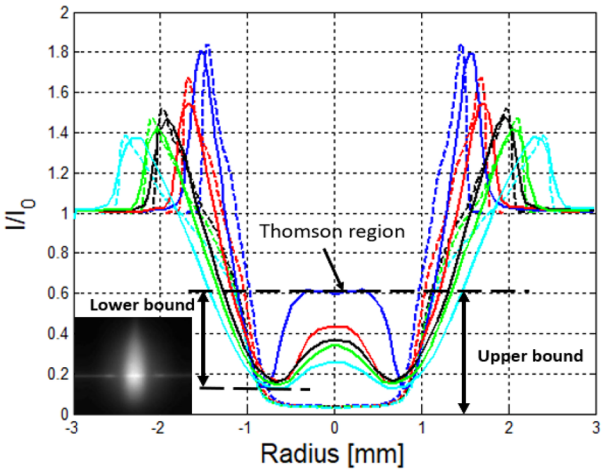

Figure 8. 1-D profiles of combined Rayleigh/Thomson scatter signal along the direction perpendicular to the plasma formation laser beams. The scattering intensity has been normalized to a reference condition of Rayleigh scattering in air. The signal rise near the center at early times (small delays) is attributed to Thomson scattering from free electrons. The insert shows a raw ICCD image from the plasma (before background subtraction and normalization) at delay of 100 ns. Experimental profiles are shown with solid lines and CFD-generated best-fit profiles are shown with dashed lines.

10) is used to suppress background light. For scattering measurements, 768 images are averaged at each point of interest (3 sets of 256 images averaged on the camera chip) using 2 × 2 binning, resulting in a detector array of 513 × 460 pixels.

Each scattering measurement is based on a ratio-normalization approach whereby scattering at a given measurement condition (i.e., at some known delay relative to laser plasma formation) is divided by the scattering from a reference condition (i.e,. scattering from air at ambient temperature and pressure). The following relations are used to obtain the plasma electron number density and temperature at each pixel in the images:

$$n_e = n_0 \frac{I_0 - I_B - I_P + I_D}{I - I_B} \frac{\sigma_R}{\sigma_T} \tag{1}$$

$$T = T_0 \frac{I_0 - I_B}{I - I_B} \frac{\sigma_R}{\sigma_{R0}}(T) \tag{2}$$

where n_e is the electron number density, n_0 is the gas density corresponding to 1 bar, T represents the plasma temperature, T_0 is the reference ambient temperature, I is the Rayleigh signal with plasma turned on, I_0 is the intensity at reference conditions (no plasma), and I_B, I_P, and I_D correspond to background counts, plasma luminosity counts, and dark counts, respectively. This approach automatically normalizes for variations in laser spatial intensity along the beam. Finally, the maximum electron number density (or temperature) is extracted from the images by averaging a 4 × 4 pixel matrix around the maximum along the direction of the probe beam.

Depending on the delay time, one can infer the gas temperature via Rayleigh scattering or electron density via Thomson scattering. Both measurements are based on previously published data for the Thomson, σ_T, and Rayleigh, σ_R, scattering cross-sections[43] where the ratio approach serves to cancel out constants such as the light collection solid-angle and detector efficiency. The Thomson measurement uses an upper- and lower-bound to yield the corresponding bounds of the electron density estimate. These bounds are shown in Fig. 8 and also described in detail in our previous work[19]. Shot noise (caused by photon counting) is another contribution to the uncertainty. This type of error is more prevalent at the early times when plasma luminosity has to be subtracted from the images (see Eq. 1) but it is still below 10% of the total uncertainty. For Rayleigh scattering measurements shot noise is the major contributor to the error bars shown in Fig. 4. Another potential source of uncertainty is the change in Rayleigh cross-section. In this work, the plasma's Rayleigh cross section dependence on temperature is taken into account under the assumption of thermal plasma kernel as explained in some of our previous works[42–44]. In this case, the plasma species concentration is determined using a chemical equilibrium code for a given temperature and the mixture's Rayleigh scattering is thus determined. We have shown previously that, even if the temperature correction to the Rayleigh scattering cross-section is completely neglected, the error on temperature is less than 5% at temperature below 8500 K[44]. Moreover, the error decreases as the plasma cools down.

In some cases, we also employ a computational fluid dynamics (CFD) model to analyze the temperature evolution of the laser plasmas. The CFD simulations are performed using a Riemann solver developed in-house based on the Navier–Stokes equations[16,45,46]. Previous work by the authors has demonstrated that the initial (end-of-the pulse) state of the NIR breakdown kernel can be obtained iteratively by fitting the experimental 1-D scattering profiles at early times as shown in Fig. 8. We remark that this CFD analysis is useful in determining the gas temperature for t < 10 μs, when uncertainties in the Rayleigh cross-sections as well as the concomitant presence of

both Thomson and Rayleigh scattering renders the experimental measurement of temperature very challenging. To select the best initial (end-of-the pulse) conditions, we require that both the location and the amplitude of the blast wave peak should agree, between simulated and measured Rayleigh profiles, to better than 5%. An example of the best fit is shown in Fig. 8 below with dashed lines for the breakdown of the NIR pulse. The corresponding NIR plasma kernel (at its very earliest formation time) is an ellipsoid with major axis of 1.5 mm, and minor axis (in the radial direction) of 0.3 mm, yielding an overall volume of 0.5 mm^3. By comparison a dual-pulse kernel takes an almost cylindrical shape with a height of 2 cm and a radius of 0.3 mm, yielding an overall volume of 5.5 mm^3. More details about the CFD model and the fitting procedure can be found in our previous work[22].

In particular, CFD is introduced in Fig. 4 to correct the experimental temperature measurements for the REMPI dual pulse case. Due to the strong gas dynamics effects involved in the kernel's post-discharge development, the scattering probe beam has to be re-adjusted at each time delay in order to find the location of maximum temperature. Instead, here the beam was kept at a fixed location that corresponded to the highest Thomson signal at the early time delays (those reported in Fig. 3) and temperature was tracked over time at this fixed location throughout the experiment. In our numerical simulations we show that a good agreement with experiments can be obtained if the experimental configuration is replicated (i.e. fixing the interrogation region).This gives us confidence to report the overall kernel peak temperature using solid blue line as predicted by the CFD model. We find that a change of 500 K in terms of initial (post laser-pulse) plasma temperature profile in the model changes the fit of the experimental Rayleigh scattering radial profiles (shown in Fig. 8) by less than 5%. In terms of using the CFD output to correct for the change in hot-spot location (solid blue curve of Fig. 4), we find that the predicted temperature profiles (at plotted points of $t \geq 10$ us) change by $< 2\%$ due to 500 K change of the initial (post laser-pulse) plasma temperature.

Ignition testing. Combustion studies were performed in a chamber with central volume of ~ 0.195 L and two side arms of length ~ 20 cm with 2.54 cm diameter circular windows for optical access. Pressure traces were recorded using a piezoelectric transducer (PCB: 113B24) mounted flush on the inner wall of the chamber. At least ten pressure traces were collected for each equivalence ratio, and the results were averaged. The traces shown in Fig. 5-left are the average traces among those that ignited individually (with uncertainty band also due to igniting traces). The average combustion pressure traces due to all events at the given condition (whether or not ignited) were used to determine the lean limit and the combustion efficiency in each test case (Fig. 5-right). The rate of pressure rise is proportional to the rate of heat release. Thus, integrating the pressure curve over time gives the total heat release during the combustion event. The actual combustion efficiency is determined as the ratio of the apparent heat release and the total available chemical energy of the fuel: $\eta = Q/\left(m_{fuel} \times LHV\right)$, where Q is the total heat release obtained by integration, m_{fuel} is the mass of fuel added in the reaction chamber and LHV is the lower heating value of the fuel. This calculation also takes into account the heat losses to the wall as well as the changes in the mixture's specific heat ratio throughout the combustion process. A detailed description of the procedure can be found in one of our earlier works[47].

Additionally, chemiluminescence images of the OH^* radical were acquired with the same ICCD camera used in the scattering experiments. The electronically excited hydroxyl radical is generated during the combustion of hydrocarbon fuels through the chain branching reaction: $CH + O_2 = OH^* + CO$. The excited OH^* emits light at ~ 310 nm as it relaxes to the ground state[48]. For CL imaging of this transition a 310 nm bandpass filter (Andover: 310FS10-50, FWHM: 10 nm) was placed in front of the ICCD.

The combustion experiments presented in this study were due to propane-air mixtures at initial pressure of 1 bar. Equivalence ratios ranging from ϕ~0.6–1.0 were tested with mixtures prepared inside the chamber based on partial pressures recorded from a gage (Omega DGP409) mounted downstream of the chamber valve. The equivalence ratio is defined as the ratio of the actual fuel/air ratio to the stoichiometric fuel/air ratio (so that $\phi = 1$ corresponds to a stoichiometric mixture and leaner mixtures have $\phi < 1$). After filling the chamber, but prior to measurements, we waited at least 10 min to allow thorough mixing of the fuel and air components. The chamber was evacuated and pumped down after each experiment to eliminate any effects of residual gases on subsequent experiments.

Received: 24 June 2020; Accepted: 2 November 2020
Published online: 16 November 2020

References

1. Herdin, G. & Klausner, J. Laser ignition: a new concept to use and increase the potentials of gas engines. *ICEF-ASME* **2005**, 1–9. https://doi.org/10.1115/ICEF2005-1352 (2005).
2. Gupta, S. B., Bihari, B., Sekar, R., Klett, G. M. & Ghaffarpour, M. Ignition characteristics of methane-air mixtures at elevated temperatures and pressures. in *ICES2005-1064* 1–7 (2005). https://doi.org/10.4271/2005-01-2189
3. Dumitrache, C. *et al.* A study of laser induced ignition of methane–air mixtures inside a rapid compression machine. *Proc. Combust. Inst.* **36**, 3431–3439 (2017).
4. Joshi, S., Loccisano, F., Yalin, A. P. & Montgomery, D. T. On comparative performance testing of prechamber and open chamber laser ignition. *J. Eng. Gas Turbines Power* **133**, 122801 (2011).
5. McIntyre, D. L., Woodruff, S. D., McMillian, M. H., Richardson, S. W. & Gautam, M. Lean-burn stationary natural gas reciprocating engine operation with a prototype miniature diode side pumped passively Q-switched laser spark plug. in *ASME 2009 Internal Combustion Engine Division Spring Technical Conference* 405–413 (2008). https://doi.org/10.1115/ICES2009-76013
6. Barbosa, S., Scouflaire, P., Ducruix, S. & Gaborel, G. Comparisons between spark plug and laser ignition in a gas turbine combustor. in *Proceedings of the European Combustion Meeting* 2–7 (2007).
7. Bihari, B., Gupta, S. B., Sekar, R., Gingrich, J. & Smith, J. Development of Advanced Laser Ignition System for Stationary Natural Gas Reciprocating Engines. in *ASME 2005 Internal Combustion Engine Division Fall Technical Conference (ICEF2005)* 601–608 (2005). doi:https://doi.org/10.1115/ICEF2005-1325

8. Manfletti, C. & Kroupa, G. Laser ignition of a cryogenic thruster using a miniaturised Nd:YAG laser. *Opt. Express* **21**, A1126–A1139 (2013).
9. Brieschenk, S., O'Byrne, S. & Kleine, H. Laser-induced plasma ignition studies in a model scramjet engine. *Combust. Flame* **160**, 145–148 (2013).
10. Börner, M., Manfletti, C. & Oschwald, M. Experimental study of a laser-ignited liquid cryogenic rocket engine conventional ignition methods of cryogenic rocket engines. in *Laser Ignition Conference* 1–19 (2015). doi:https://doi.org/10.1364/LIC.2015.Th2A.5
11. Shneider, M. N., Zheltikov, A. M. & Miles, R. B. Tailoring the air plasma with a double laser pulse. *Phys. Plasmas* **18**, 063509 (2011).
12. Yalin, A. P., Wilvert, N., Dumitrache, C., Joshi, S. & Shneider, M. N. Laser plasma formation assisted by ultraviolet pre-ionization. *Phys. Plasmas* **21**, 103511 (2014).
13. Bak, M. S., Im, S. & Cappelli, M. A. Successive laser-induced breakdowns in atmospheric pressure air and premixed ethane–air mixtures. *Combust. Flame* **161**, 1744–1751 (2014).
14. Hsu, P. S. *et al.* High-repetition-rate laser ignition of fuel–air mixtures. *Opt. Lett.* **41**, 1570–1573 (2016).
15. Dumitrache, C., Vanosdol, R., Limbach, C. M. & Yalin, A. P. Control of early flame kernel growth by multi-wavelength laser pulses for enhanced ignition. *Sci. Rep.* **7**, 1–8. https://doi.org/10.1038/s41598-017-10457-0 (2017).
16. Dumitrache, C. & Yalin, A. P. Numerical modeling of the hydrodynamics induced by dual-pulse plasma. in *AIAA 2018-0689* 1–12 (2018).https://doi.org/10.2514/6.2018-0689
17. Mahamud, R., Tropina, A. A., Shneider, M. N. & Miles, R. B. Dual-pulse laser ignition model. *Phys. Fluids* **30**, 106104 (2018).
18. Sevik, J. *et al.* Influence of injector location on part-load performance characteristics of natural gas direct-injection in a spark ignition engine. *SAE Int. J. Engines* **9**, 2262–2271 (2016).
19. Dumitrache, C., Limbach, C. M. & Yalin, A. P. Threshold characteristics of ultraviolet and near infrared nanosecond laser induced plasmas. *Phys. Plasmas* **23**, 093515 (2016).
20. Glassman, I. *Combustion* 3rd edn. (Academic Press, New York, 1997).
21. Starikovskiy, A. Physics and chemistry of plasma-assisted combustion. *Philos. Trans. R. Soc. Lond. A Math. Phys. Eng. Sci.* **373**, 20150074 (2015).
22. Dumitrache, C. & Yalin, A. Gas dynamics and vorticity generation in laser-induced breakdown of air. *Opt. Express* **28**, 5835–5850 (2020).
23. Lee, T. W., Jain, V. & Kozola, S. Measurements of minimum ignition energy by using laser sparks for hydrocarbon fuels in air: Propane, dodecane, and jet-A fuel. *Combust. Flame* **125**, 1320–1328 (2001).
24. Mori, H., Ishida, T., Hayashi, S., Aoki, Y. & Tomohide, N. A study of REMPI as measurement technique for highly rarefied gas flows (simulations and its fundamental properties of REMPI spectra). *JSME Int. J.* **43**, 400–406 (2000).
25. Adams, S., Miles, J. & Laber, A. Resonant laser induced breakdown for fuel-air ignition. *48th AIAA Aerosp. Sci.* 1–5 (2010).
26. Wu, Y., Zhang, Z. & Adams, S. F. O2 rotational temperature measurements by coherent microwave scattering from REMPI. *Chem. Phys. Lett.* **513**, 191–194 (2011).
27. Wu, Y., Zhang, Z. & Adams, S. F. Temperature sensitivity of molecular oxygen resonant-enhanced multiphoton ionization spectra involving the C 3Πgintermediate state. *Appl. Phys. B Lasers Opt.* **122**, 1–10 (2016).
28. Rowland, H. L. Anomalous absorption of electromagnetic radiation. *Phys. Fluids B* **4**, 3883–3889 (1992).
29. Turnbull, D. *et al.* Anomalous absorption by the two-plasmon decay instability. *Phys. Rev. Lett.* **124**, 185001 (2020).
30. Hutchinson, I. H. *Principles of Plasma Diagnostics* (Cambridge University Press, Cambridge, 2005).
31. Dumitrache, C., Butte, C., Eickelberg, A. & Yalin, A. P. On the use of REMPI pre-ionization for laser plasma formation. in *AIAA 2018–1431* (2018). https://doi.org/10.2514/6.2018-1431
32. Yalin, A. P. *et al.* Laser plasma formation assisted by ultraviolet pre-ionization. *Phys. Plasmas* **21**, 103511–103516 (2014).
33. Bradley, D., Sheppard, C. G. W., Suardjaja, I. M. & Woolley, R. Fundamentals of high-energy spark ignition with lasers. *Combust. Flame* **138**, 55–77 (2004).
34. Dumitrache, C., Wilvert, N., Yalin, A. & Shneider, M. Laser plasma formation using dual pulse pre-ionization. in *AIAA 2013–2632* 10 (2013).
35. Beduneau, J. L., Kawahara, N., Nakayama, T., Tomita, E. & Ikeda, Y. Laser-induced radical generation and evolution to a self-sustaining flame. *Combust. Flame* **156**, 642–656 (2009).
36. Spiglanin, T. A., Mcilroy, A., Fournier, E. W., Cohen, R. B. & Syage, J. A. Time-resolved imaging of flame kernels: Laser spark ignition of H_2/O_2/Ar mixtures. *Combust. Flame* **102**, 310–328 (1995).
37. Mulla, I. A., Chakravarthy, S. R., Swaminathan, N. & Balachandran, R. Evolution of flame-kernel in laser-induced spark ignited mixtures: A parametric study. *Combust. Flame* **164**, 303–318 (2016).
38. El-Rabii, H. & Rolon, J. Experimental study of laser ignition of a methane/air mixture by planar laser-induced fluorescence of OH. in *Proc. PSFVIP* 1–4
39. Morsy, M. H. & Chung, S. H. Numerical simulation of front lobe formation in laser-induced spark ignition of ch 4 /air mixtures. *Proc. Combust. Inst.* **29**, 1613–1619 (2002).
40. Morgan, C. G. Laser-induced breakdown of gases. *Rep. Prog. Phys.* **38**, 621–665 (1975).
41. Dumitrache, C., VanOsdol, R., Limbach, C. M. & Yalin, A. P. Laser ignition of propane-air mixtures using a dual-pulse technique. in *2017–1976* 1–8 (2017).
42. Butte, C., Dumitrache, C. & Yalin, A. P. Dual-pulse laser ignition using oxygen REMPI preionization. in *AIAA 2019-3117* 1–17 (2019).https://doi.org/10.2514/6.2019-3117
43. Limbach, C. M., Dumitrache, C. & Yalin, A. P. laser light scattering from equilibrium, high temperature. in *47th AIAA Plasmadynamics and Lasers* 1–13 (2016).
44. Butte, C., Dumitrache, C. & Yalin, A. Properties of dual-pulse laser plasmas and ignition characteristics in propane-air and methane-air mixtures. in *AIAA 2019-0464* 1–9 (2019).https://doi.org/10.2514/6.2019-0464
45. Dumitrache, C. *Novel Laser Ignition Technique Using Dual-Pulse Pre-ionization* (Colorado State University, Fort Collins, 2017).
46. Dumitrache, C. *et al.* Hydrodynamic regimes induced by nanosecond pulsed discharges in air: mechanism of vorticity generation. *J. Phys. D. Appl. Phys.* **52**, 364001 (2019).
47. Dumitrache, C. *et al.* A study of laser induced ignition of methane-air mixtures inside a rapid compression machine. *Proc. Combust. Inst.* **36**, 3431–3439 (2017).
48. Bozkurt, M., Fikri, M. & Schulz, C. Investigation of the kinetics of OH* and CH* chemiluminescence in hydrocarbon oxidation behind reflected shock waves. *Appl. Phys. B Lasers Opt.* **107**, 515–527 (2012).

Acknowledgements

The authors acknowledge support from Air Force Office of Scientific Research (FA9550-18-1-0239). The authors also acknowledge Dr. Zhili Zhang for his assistance with modeling the oxygen REMPI spectrum.

Author contributions

C.D. conducted the following experimental investigations: laser ignition of propane-air mixtures using the non-resonant dual-pulse and the NIR breakdown techniques, collected the rotationally resolved spectra for the

two-photon excitation transition using laser Thomson scattering to confirm the 2+1 O2 REMPI channel, Rayleigh/Thomson scattering measurements for the REMPI pulse. In addition, C.D, performed the CFD simulations to obtain the temperature profiles in the post-discharge. C.B. developed the experimental setup for the resonant dual-pulse method (REMPI+NIR) and performed the Rayleigh/Thomson scattering as well as the laser ignition tests for the REMPI+NIR technique. A.Y. was the principal investigator of this research project. He defined the overall research plan, provided continuous guidance to the research team including help with data interpretation. Additionally, A.Y. performed the spectrum modeling of the vibronic transition from the molecular oxygen ground state to the intermediate state. Both A.Y. and C.D. contributed to the writing of the submitted manuscript.

Competing interests

The authors declare no competing interests.

Additional information

Correspondence and requests for materials should be addressed to A.Y.

Reprints and permissions information is available at www.nature.com/reprints.

Publisher's note Springer Nature remains neutral with regard to jurisdictional claims in published maps and institutional affiliations.

International Journal of Heat and Mass Transfer 161 (2020) 120302

Contents lists available at ScienceDirect

International Journal of Heat and Mass Transfer

journal homepage: www.elsevier.com/locate/hmt

Gas dynamic regimes observed in dual-pulse laser ignition

Ciprian Dumitrache[a], Azer P. Yalin[b,*]

[a] National Institute for Laser, Plasma and Radiation Physics, Solid-State Quantum Electronics Lab., Bucharest R-077125, Romania
[b] Colorado State University, Fort Collins, CO 80523, United States

ARTICLE INFO

Article history:
Received 24 May 2020
Revised 23 July 2020
Accepted 6 August 2020

Keywords:
Laser ignition
Laser breakdown
Laser energy deposition
Plasma-induced gas dynamics
Combustion
Post-discharge gas cooling

ABSTRACT

A numerical study of the gas dynamics induced by a dual-pulse laser pre-ionization plasma used in laser ignition applications is presented herein. Past experimental observations have revealed important differences in the gas dynamics of the dual-pulse plasma, generated by overlapping a pair of ultraviolet (UV) and near-infrared (NIR) pulses, as compared to those of single-pulse (typically near-infrared) laser breakdown that has been more commonly studied. The simulation results reported here show that the dual-pulse pre-ionization scheme can lead to various gas dynamic regimes depending on the axial offset of the focal points of the two beams along the optical axis. If the UV and NIR pulses are perfectly overlapped (no offset) the energy deposition is uniform along the optical axis, leading to the formation of a toroidal structure in the post-discharge cooling phase. Alternatively, if the NIR energy addition pulse is focused with a small axial offset, (i.e., upstream or downstream of the UV pre-ionization pulse by ~0.5 mm) then an asymmetric torus forms that exhibits a third lobe which propagates away from the main kernel (to the side where the NIR was focused). Finally, if the two beams are focused with a larger offset of ~2.5 mm (weaker coupling), then another regime with a fourth lobe can arise. The four main flow regimes revealed from the model are in agreement with OH* experimental chemiluminescence images. These flow regimes influence the development of the early flame kernels, therefore playing an important role in practical laser ignition applications.

Published by Elsevier Ltd.

1. Introduction

Over the years, laser generated plasma has been investigated for a variety of practical applications including providing a source of ignition for reciprocating engines [1–3] and aerospace jet engines [4,5], a light source for laser induced breakdown spectroscopy (LIBS) [6,7], and conduits for lightning protection and microwave waveguides [8]. In a typical nanosecond laser breakdown event, an initial pool of electrons is created through multi-photon ionization (MPI) after which breakdown is achieved primarily by electron avalanche ionization (EAI). During EAI, the free electrons gain energy via (electron-neutral and electron-ion) inverse Bremsstrahlung and collide with other gas molecules thereby creating further ionization in a cascade process [9,10]. The resulting plasma reaches high temperatures (~10,000 - 50,000 K) and high pressures (~10–100 bar) [11,12]. Depending on the focusing optics, the initial plasma kernel has an axial length of several millimeters (along the beam optical axis) and grows with high velocity (~0.1–1 km/s) during the first microsecond after the pulse. The hydrodynamic (gas dynamic) regime induced in the post-discharge/cooling phase typically takes the shape of an asymmetric torus with a frontal lobe propagating towards the laser [13–15]. Sometimes, in the literature, this lobe is also referred to as a 3rd lobe (where the 1st and 2nd are due to the counter-rotating vortices that make up the torus as viewed in two-dimensional slices) [16–18].

Past research has shown that using such laser sparks as a source of ignition in engines can present distinct advantages when compared to conventional sparks (i.e. capacitive spark plugs) such as: decreasing the lean limit, elevating flame speeds, providing freedom to optimally position the ignition kernel inside the combustion chamber, and eliminating spark plug erosion challenges [19,20]. By implementing laser ignition with fiber optic delivery [21], it may be possible to locate the source remotely from the combustion location and/or to ignite multiple locations with a single source. However, there are also certain disadvantages associated with laser ignition due to the breakdown process being energetically inefficient [22] and potentially leading to an increase in nitrogen oxides (NO_x) formation [23]. The higher energy is primarily due to the fact that a significant portion of the laser energy is transported away from the ignition zone by the strong blast wave that follows the breakdown process [24]. Note that even with these higher ignition energies, the impact of the ignition system to the

* Corresponding author.
E-mail address: azer.yalin@colostate.edu (A.P. Yalin).

https://doi.org/10.1016/j.ijheatmasstransfer.2020.120302
0017-9310/Published by Elsevier Ltd.

overall power balance of the combustion is close to negligible, but the energies are important from the point of view of the size and cost of the laser source (as well as the prospects for fiber delivery of such pulses).

Recent experimental studies conducted by the authors' group have shown that a dual-pulse technique using an UV laser pulse to achieve initial gas pre-ionization followed a few nanoseconds later (~5–10 ns) by a NIR pulse for energy addition allows one to tailor plasma properties such as gas temperature and electron number densities [25,26]. Fundamental to this approach is that the first (UV) pulse only pre-ionizes the plasma without creating full gas breakdown. The resulting pool of electrons then acts as a seed to promote absorption of the second (NIR) pulse. The approach has also been shown to extend the lean limit of propane-air mixtures as compared to classical (single-pulse) laser breakdown ignition while also reducing the required (total) pulse energy. An important finding from OH* chemiluminescence images was that the early flame development is different for the dual-pulse versus single-pulse (NIR), laser ignition [27]. In particular, differences in the early plasma kernels and their lobe formation were shown to play an important role in the subsequent flame growth and ability to ignite lean mixtures.

The present study fills a gap in the need to understand and numerically model the gas dynamics associated with the dual-pulse plasma kernels. Previous modeling work on the topic of dual-pulse laser ignition has also been performed by Mahamud et al. [28] with an emphasis on plasma kinetics impact on flame development. They report that ignition delay and kernel development depend strongly on laser intensity, plasma-generated radicals, and initial electron number density. The current study emphasizes on the accurate determination of the initial kernel profile and provide more detail on the mechanisms of vorticity generation for each overlap configuration. In particular, we perform a modeling study to examine the possible gas dynamic regimes including the influence of the pulse overlap (axial offset). To this end, four different overlap configurations were investigated: 1) UV and NIR focuses are perfectly overlapped (leading to a 2-lobe symmetric torus); 2 and 3) UV and NIR pulses have a small axial offset of ~0.5 mm in either direction (leading to an asymmetric torus with a 3rd lobe that moves towards the side of the NIR focus; 4) UV and NIR pulses have a weaker coupling due a larger offset of ~2.5 mm (leading to an asymmetric torus that has an additional 4th lobe). The cases labeled as 2 and 3 are near mirrors of one another and so they are handled as a single case in much of the discussion.

The manuscript is structured as follows: Section II presents the mathematical model and assumptions used in the CFD code while in Section III modeling results for the dual-pulse hot kernels are presented. Finally, Section IV completes this paper with conclusions and plans for future work.

2. Methods

The gas dynamics induced by the hot gas kernel left after the laser breakdown process were modelled numerically using a Navier-Stokes solver developed in-house [29]. At this stage, the model neglects the effects of chemical kinetics and focuses exclusively on the fluid dynamics. While this represents a simplifying approximation, it is important to note that several past studies have indicated that the observed gas dynamics effects are predominantly induced by the interaction between the blast wave and the hot gas kernel left after breakdown (and therefore not depending on the chemical kinetics) [13,18,30,31]. Additionally, previous work done by the authors has shown that the gas dynamic and the vorticity generation mechanisms of an NIR laser kernel can be accurately predicted with a very similar gas dynamic model [32]. This is because post-discharge heating by vibrational-translational (V-T) relaxation reactions or by quenching of metastable states tends to be weak in laser plasmas and takes place on a longer timescale compared to the timescale of blast-wave detachment and kernel collapse. The blast itself is created by the Joule heating mechanism of electron avalanche ionization which takes place during the laser pulse. This mechanism enters the current simulations through the temperature (and pressure) profiles corresponding to the end of the laser pulse(s), which are adopted as initial conditions for the model (and determined based on experimental measurements as discussed herein).

The governing equations for conservation of mass, momentum and energy are written in cylindrical coordinates assuming axial symmetry (and zero azimuthal velocity). Additionally, a non-reactive species transport equation is added to the model to describe the advection of hydroxyl radical generated during breakdown.

$$U_t + F(U)^a{}_r + G(U)^a{}_z = F(U)^d{}_r + G(U)^d{}_z + S(U) \tag{1}$$

Where:

$$= \begin{bmatrix} \rho \\ \rho u \\ \rho v \\ E \\ \rho Y_i \end{bmatrix};\ F(U)^a = \begin{bmatrix} \rho u \\ \rho u^2 + p \\ \rho uv \\ u(E+p) \\ \rho u Y_i \end{bmatrix};\ G(U)^a = \begin{bmatrix} \rho v \\ \rho uv \\ \rho v^2 + p \\ v(E+p) \\ \rho v Y_i \end{bmatrix};$$

$$F(U)^d = \begin{bmatrix} 0 \\ \tau_{rr} \\ \tau_{rz} \\ u\tau_{rr} + v\tau_{rz} - q_r \\ 0 \end{bmatrix};\ G(U)^d = \begin{bmatrix} 0 \\ \tau_{rz} \\ \tau_{zz} \\ u\tau_{rz} + v\tau_{zz} - q_z \\ 0 \end{bmatrix}; \tag{2}$$

$$S(U) = -\frac{1}{r}\begin{bmatrix} \rho u \\ \rho u^2 - \tau_{rr} \\ \rho uv - \tau_{rz} \\ u(E+p) + u\tau_{rr} - v\tau_{rz} + q_r \\ \rho u Y_i \end{bmatrix}$$

In Eq. (2), U is the vector of conservative variables, $F(U)^a$ and $G(U)^a$ describe the advection flux (in the r and z direction respectively), $F(U)^d$, $G(U)^d$ represent the diffusion flux, and $S(U)$ is the source term that is the result of the coordinate system transformation from cartesian to cylindrical. ρ is the gas density, p is pressure, u and v are the radial (r-) and axial (z-) components of velocity, E is the total energy (the sum of kinetic and internal energy), τ_{ij} are the shear stress component, q_i represents the i^{th} component of the conductive heat flux, and Y_i is the mass fraction of species i. In this coordinate system the incident laser is oriented along the z-axis. The thermodynamic state of the system is additionally described by two state equations:

$$p = \rho R_g T \tag{3}$$

$$E = \rho\left(h(T) - \frac{p}{\rho} + \frac{u^2+v^2}{2}\right) \tag{4}$$

where Eq. (3) is the ideal gas law (R_g is the specific gas constant), and Eq. (4) is the caloric equation of state. The transport properties are calculated in agreement with the thermally perfect gas assumption. A detailed description on how the relevant thermodynamic properties are computed can be found in our previous work [32,33]. Numerical modeling showed that in fact viscous/diffusive effects have very little influence on the simulated flow fields with the post-discharge development being dominated by compressibility effects.

The conservation equations given in Eq. (1) are numerically integrated using a dimensional splitting approach. The advection terms are solved using Roe's flux differencing scheme with slope limiters [34,35] and the diffusion terms are solved using a sec-

ond order centered difference scheme [36]. To enforce the preservation of mass fraction positivity, the technique proposed by Larrouturou for solving the convective term of the species transport equation was used [37]. Finally, the resulting ODEs are integrated with an explicit 4th order Runge-Kutta IV method. The governing equations are solved on a structured Cartesian grid using a control volume discretization approach. A piece-wise distribution of initial data over the computational cells is employed where the value at the center of a cell represents the average of each variable over the cell. The optimum cell resolution required to resolve the phenomena of interest was determine by conducting a grid sensitivity analysis over the first 10 μs of the simulation (where the strongest gas dynamics effects are observed). The optimal cell size was determined through a grid sensitivity study in which various cell sizes (between 5 and 50 μm) were tested. It was found that a cell size of 20 μm gave less than 5% difference in pressure and density fields after 10 μs when compared to the smallest cell sized domain. As such, all simulations were run using a 20 μm cell size. The computational time is reduced by taking advantage of the axial and radial symmetry (where available) of the kernels under investigation and by employing non-reflective boundary conditions at the edge of the domain to allow the blast wave to leave the domain with minimal disturbances [38,39].

3. Results & discussions

3.1. Specification of initial conditions

The simulations focus on kernel evolution after the laser energy deposition has ended (i.e., after initial heating and ionization from the pair of laser pulses has taken place). We therefore use spatially resolved temperature and pressure fields, corresponding to the end of the laser pulses, as initial conditions (ICs) for the model. The velocity is assumed to be zero at the end of the pulse under the assumption that during the short laser pulse (~10 ns) there is not enough time for significant flow to establish itself within the kernel. The initial shape and dimensions of the hot kernel induced by the dual-pulse are determined from schlieren and Rayleigh scattering measurements from previous studies [25,40,41]. In general, the schlieren informs the size and shape of the profiles while the Rayleigh data provides quantitative property values.

In each (overlap) case, the IC profiles of temperature and pressure are due to a combination of contributions from the UV and NIR beams. It is important to note that changes in the coupling between the two beams influences the shape and initial state (pressure and temperature) at the end of the pulse as discussed below. Fig. 1 shows an example schlieren image for the case in which the NIR pulse is focused slightly upstream of the UV pulse (where upstream refers to the side from which the lasers are incident). The image shows that the overall plasma kernel contains two features: an elongated channel formed by the UV pre-ionization beam and a roughly elliptical plasma growth due to the addition of the NIR pulse. The channel-like, less localized, UV contribution is because the MPI rate at this wavelength is a much weaker function of intensity ($\sim I^3$).

These distinctly different shapes relate to the relative roles of the breakdown for the different wavelengths [25]. If the NIR pulse is used on its own, the MPI process is very ineffective in generating seed electrons and exhibits a very strong dependence on the laser intensity of $\sim I^{14}$ (as opposed to $\sim I^3$ for the UV pulse). This means that the ionization process is effective only over a small region around the focus where the photon flux is high enough to allow ionization. As a consequence, the NIR electron avalanche is very localized around the laser focal point (since I^{14} falls off very quickly away from this location), thereby giving rise to the observed point-like kernel shape. On the other hand, the higher energy photons of the UV pulse enable the MPI process to develop along a longer section of the focused beam leading to the formation of an elongated plasma channel. If the NIR pulse is overlapped on the pre-existing ionization channel of the UV one notices a combined effect with the electron avalanche of the NIR tending to develop over larger distances. This leads to the formation of hotter an elongated kernel that combines the characteristics of both wavelengths such as the one shown in Fig. 1.

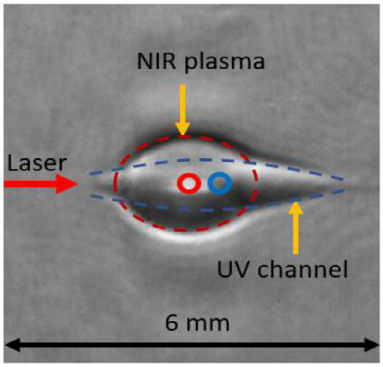

Fig. 1. Schlieren image of a dual-pulse laser plasma in atmospheric air at 500 ns after the first pulse. Image shows the pre-ionization channel generated by the UV pulse and the spherical plasma growth induced by the addition of the NIR pulse. The NIR pulse was delivered after a 10 ns delay from the beginning of the UV pulse. The blue and red circles mark the focal spots of the (initial) UV and NIR pulses, respectively. (For interpretation of the references to colour in this figure legend, the reader is referred to the web version of this article.)

To examine spatial offset effects, and compare against experiments, three different dual-pulse beam-offsets are examined, with both laser beams parallel and incident in the same direction in all cases. The three cases are: 1) the beam waists of the UV and NIR pulses are perfectly overlapped (zero offset between focal points), 2) the NIR pulse is focused 0.5 mm upstream from the focus of the UV pulse, and 3) the NIR pulse is focused 2.5 mm upstream from the focus of the UV pulse (weaker coupling between the two laser-generated plasma). Note that the 0.5 mm simulation in fact covers 2 cases, as it also describes the case of 0.5 mm with the UV upstream, simply by mirroring the output by 180°. Note that the perfect overlap case is meant to correspond to experimental results where the foci of the beams were exactly overlapped in the axial direction; however, the experimental resolution of this parameter was ~+/−0.1 mm. We found that this condition gave a very symmetric energy deposition (IC) profile that yielded a symmetric torus in the post-discharge gas-dynamics. However, in practice the most symmetric energy addition profile may in fact correspond to a small non-zero offset.

In all cases investigated the initial temperature was determined from Rayleigh/Thomson scattering measurements [42]. The temperature and pressure fields that are the ICs for case 1 (zero offset) case 2 (0.5 mm offset) are shown in Fig. 2. The initial peak temperature is estimated to be T_{max}=3.5 $\times$ 10^4 K based on the previous measurements for the dual-pulse plasma. The pressure profile could not be measured experimentally but is linked to the temperature profile using the ideal gas equation of state under the assumption that the gas density remains unchanged during the laser energy deposition phase. This hypothesis remains valid as long as the laser pulse duration is much shorter than the acoustic-time scale (where the latter is given by the radial length of the kernel divided by the speed of sound and is on the order of hundreds of nanoseconds). Using this assumption, the peak pressure is found as p_{max}=2.2 $\times$ 10^7 Pa. Moreover, past experimental work has shown that the energy absorbed inside of the kernel remains nearly constant as long as the offset of the two pulses is relatively small,

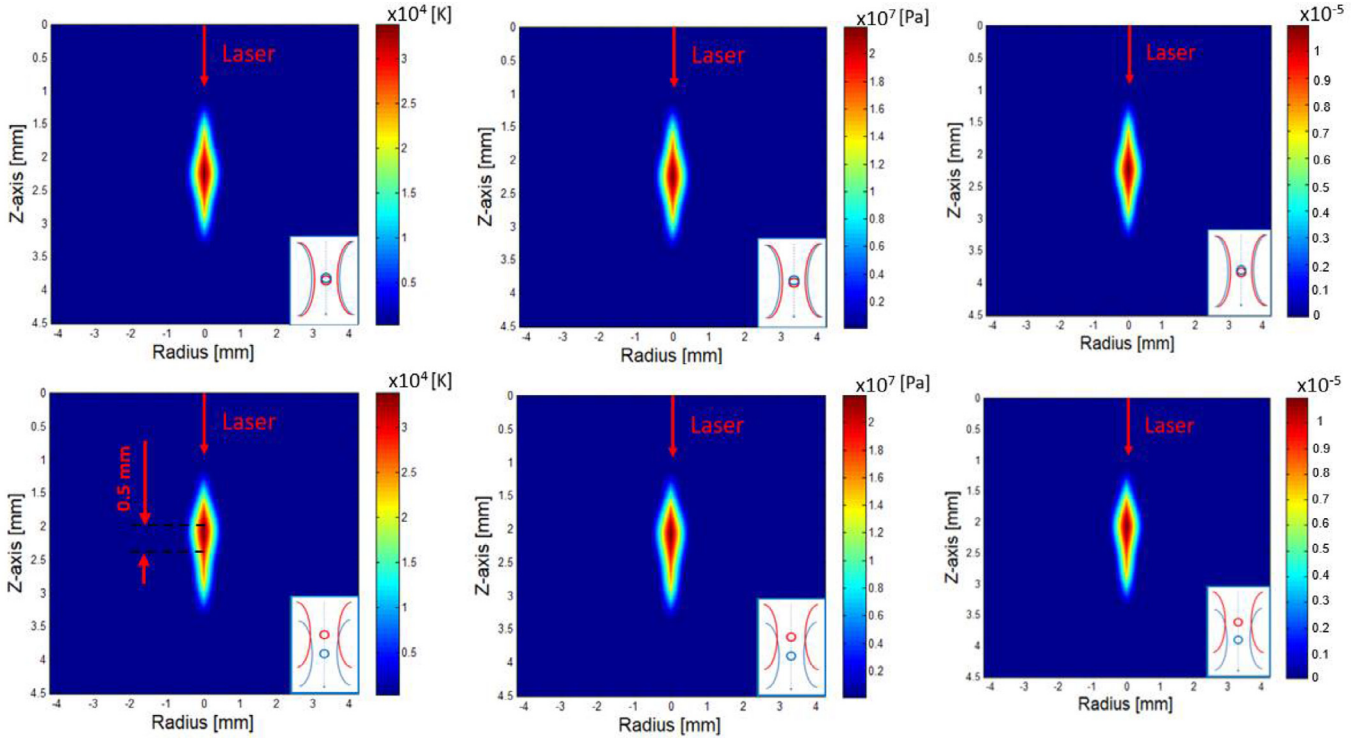

Fig. 2. Initial temperature, pressure and OH mass fraction profiles of the dual-pulse kernels for the case of perfect overlap (zero offset) between the pulses (top) and for the 0.5 mm offset case (bottom).

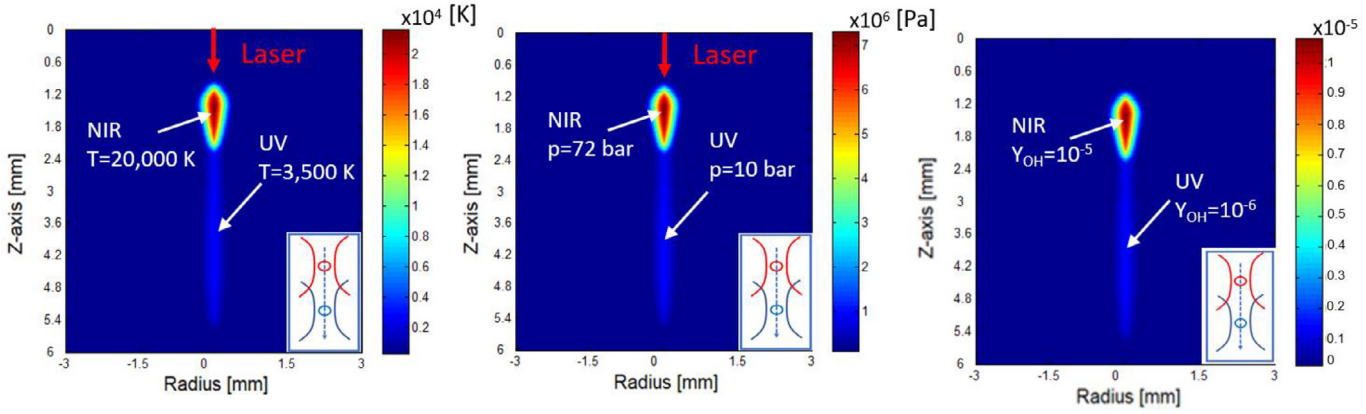

Fig. 3. Initial temperature, pressure and OH mass fraction profiles for the large offset dual-pulse case presenting a weak overlap. The NIR pulse is focused 2.5mm upstream of the UV pulse.

i.e., <~1 mm in our experiments [27]. As such, the same maximum pressure and temperature conditions were used for both test cases. This experimental finding also justifies the use of the same mirrored ICs for the two 0.5 mm offset cases, where the beams are offset in either direction. To obtain a smooth variation between the peak conditions and the far-field ($T = 300$ K, $p = 1.01 \times 10^5$ Pa) a Gaussian blending filter was also employed in the generation of the initial profiles presented in Fig. 2 and Fig. 3. The essential difference in the initial profiles for the zero and small (0.5 mm) offset cases is that for the former case the NIR ellipsoid is centered on the UV channel whereas for the latter case it is offset from the center (by 0.5 mm).

To facilitate comparison with experimental results (OH* chemiluminescence image), we also incorporate a non-reactive species transport equation to describe the advection of hydroxyl radical generated during breakdown. In the simulations, the OH was introduced through the initial conditions having a profile similar to those used for initial temperature and pressure (shown in Fig. 2-3) with a maximum mass fraction corresponding to 10^{-5} at the center and the rest being air. In experiments, the OH will come from the water vapor in the surrounding air. Therefore, it is appropriate that the OH profiles match the temperature profiles (since higher temperature will lead to more water dissociation). This is further supported by several past experimental studies [15,43] that report on OH-PLIF measurements in thermal plasma kernels similar to ours. Note that the OH radical is not destroyed nor created in the simulation. Instead, we are only interested in the advective transport of OH that takes place due to the plasma-driven gas dynamics. This was shown to be a valid assumption by previous optical emission measurements by Phuoc et al. [44,45] that demonstrated the existence of long-lived emission from OH in the post-discharge, prior to ignition.

In the case of a large offset between the two pulses the initial conditions are a bit less straightforward. Due to the weak

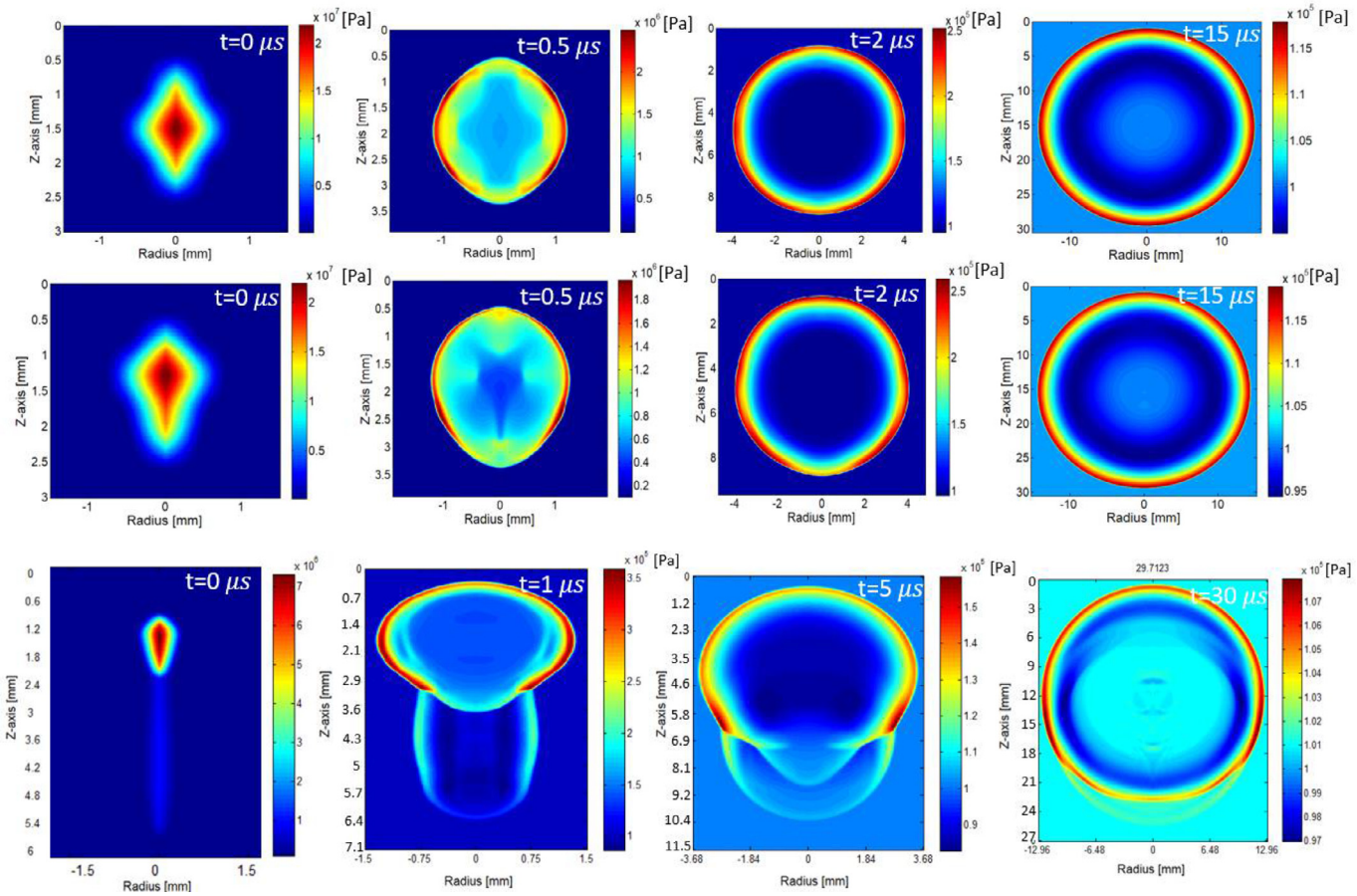

Fig. 4. Pressure contours showing evolution of the shock wave for the perfectly overlapped case (top), small (0.5 mm) offset case (middle) and large (2.5 mm) offset case (bottom). These 3 cases correspond to the ICs of Fig. 2 top, Fig. 2 bottom, and Fig. 3 respectively. Note the different spatial and pressure scales. The laser beams are incident from the top.

coupling between the two plasma kernels, the initial (end-of-the pulse) peak temperature and pressure of the NIR and UV contributions are chosen as if the two plasma were formed by each pulse on their own. This yields slightly lower peak temperature/pressure than in the previous two cases. Moreover, the geometry of the initial temperature/pressure profiles also changes. Since the NIR focus is far from the epicenter of the homogenous source of seed electrons provided by the UV pre-ionization channel, the elliptical NIR contribution used previously is now replaced with the more characteristic teardrop shape of the NIR breakdown that has been widely reported in the past [17,46,47]. This kernel topology appears because the NIR plasma tends to grow asymmetrically towards the laser source (where the avalanche ionization process can be more easily sustained by the laser radiation due to its stronger dependence on MPI than the UV). On the other hand, the UV pulse will still yield the same thin pre-ionization channel seen previously. However, its temperature is lower due to the absence of Joule heating from the NIR pulse near the focus. In the large offset case where the NIR pulse is focused 2.5 mm in front of the UV pulse, a peak temperature of 20,000 K was used for the NIR contribution and the UV pre-ionization channel was set to 3500 K. These temperatures were determined via Rayleigh scattering studies for each of the pulses since the coupling between the pulses is weak. The initial profiles for this configuration are shown in Fig. 3.

3.2. Shock wave propagation

Since the laser energy is deposited inside the gas on a much smaller timescale (nanoseconds) than the hydrodynamic timescale of the gas mixture (hundreds of nanoseconds), a strong pressure buildup accompanies the rise in temperature during the energy addition process. In the early stages of kernel development, acoustic waves tend to coalesce at the surface of the kernel thereby forming a strong blast wave. After a few hundred nanoseconds, a blast wave begins to detach from the kernel and starts propagating outward dissipating a significant portion of the kernel's energy. As shown in Fig. 4, initially the blast takes the shape of the kernel perimeter. However, as time progresses, it becomes more spherical reaching an almost perfectly spherical front within 15–30 μs after the end of the laser pulse. This finding is true for all three cases simulated and shows that, independent of the initial shape of the plasma, the non-uniform acceleration generated by the pressure gradients ultimately leads to the development of a spherical shock. This phenomenon is discussed in more detail in Section III.D as it plays a major role in vorticity generation.

3.3. Kernel dynamics and experimental validation

Fig. 5 shows the temporal evolution of temperature profiles as simulated for the dual-pulse kernels for the 3 studied offsets (0, 0.5 and 2.5 mm). It is interesting to note that while the shock wave development was nearly identical for the overlapped and small offset cases, their kernel dynamics are distinctly different. In both cases, during the first ~3–5 μs, the kernel expands very quickly while both temperature and pressure decay. The kernels approximately double their initial size during this time period. After ~5 μs, kernel collapse begins in all three cases and their evolution takes different paths after this point. The kernel formed by the

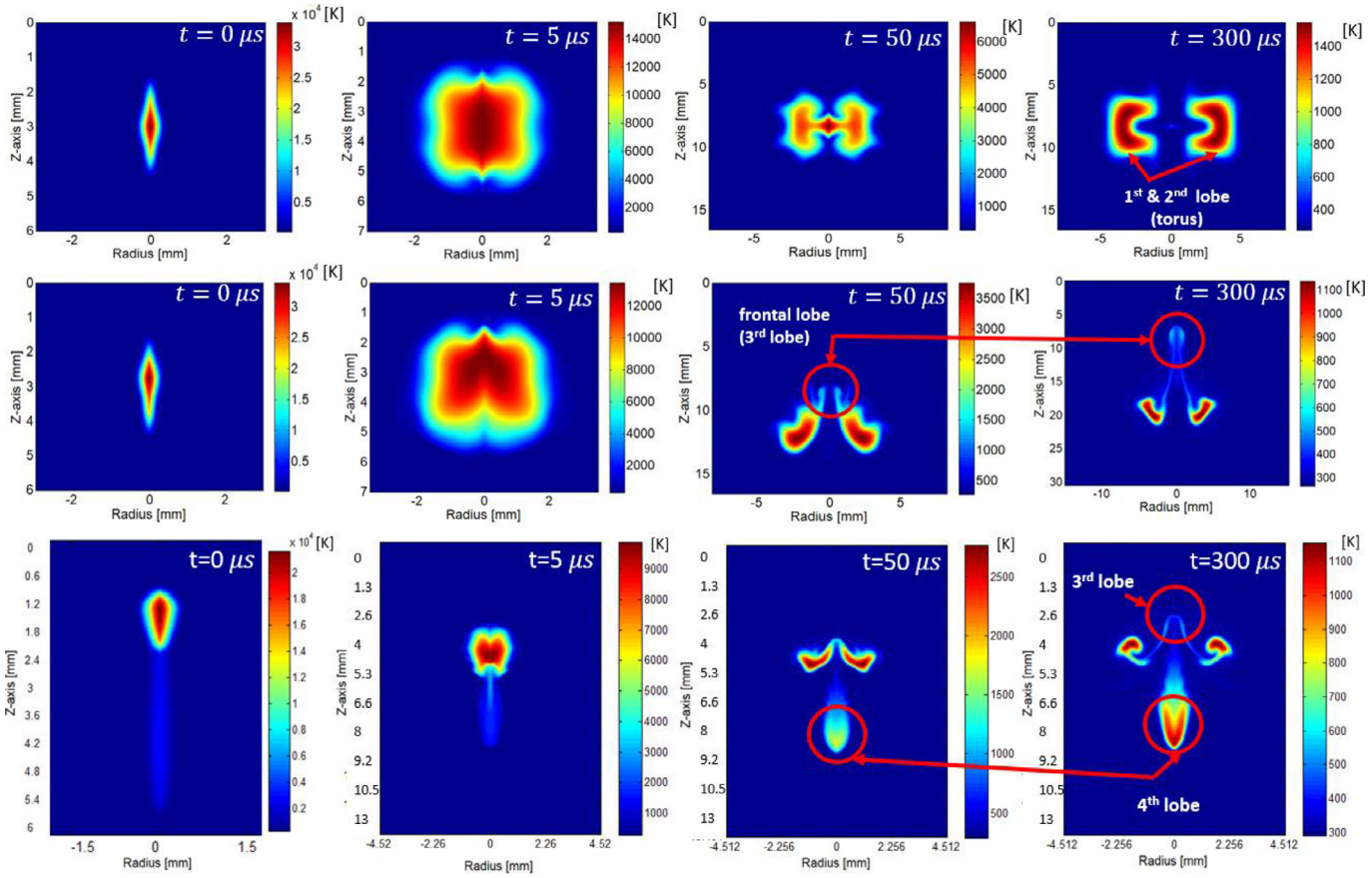

Fig. 5. Temperature contours showing the kernel evolution for the overlapped (top), small (0.5 mm) offset (middle), and large (2.5 mm) offset (bottom) cases. These 3 cases correspond to the ICs of Fig. 2 top, Fig. 2 bottom, and Fig. 3 respectively. Note the different spatial and temperature scales of the panels. The laser beams are incident from the top.

overlapped pulses (Fig. 5-top) starts to grow significantly in the radial direction as it collapses along the optical axis due to vorticity generated at the top and bottom of the kernel. At ~50 μs, this leads to the formation of a torus having a flow stagnation point at its epicenter. As time evolves, cold fluid from the surroundings is transported along the optical axis (from both top and bottom of Fig. 5) towards the center and the torus increases its radius as it gradually cools down. On the other hand, for the small (0.5 mm) offset case with NIR upstream of UV pulse (Fig. 5-middle), the kernel collapse induces a net flow (from the downstream/UV side of the kernel) along the optical axis towards the point where the temperature was initially the highest (i.e. the upstream/NIR side). This leads to rapid cooling of the kernel epicenter and formation of the so-called third lobe widely reported in laser ignition literature (generally for NIR breakdown) [13–18]. As discussed, given the symmetry of the problem and ICs, this small offset case also corresponds to that with the UV beam upstream of the NIR, in which case the resulting flow field would be essentially the same (but vertically mirrored relative to the one plotted) and with the lobe propagating also towards the NIR side (now downstream). Finally, in the case when the NIR pulse is focused 2.5 mm upstream of the UV pulse (Fig. 5-bottom), the kernel collapse leads to the formation of a four-lobe structure which is a combination of the gas dynamics effects induced by the NIR breakdown (with the typical three-lobe structure having a front lobe that propagates towards the laser source) and a compressing fourth lobe that is the result of the UV pre-ionizing channel slowly collapsing over the optical axis. In the next section we discuss vorticity generation as a means to explain the differing kernel topology regimes.

The simulated kernels for the different offsets are consistent with results of published dual-pulse experiments [48]. The dual-pulse technique using UV pre-ionization has been previously demonstrated for laser ignition of propane-air mixtures. The results indicated an extension of the lean flammability limit and an overall reduction of the laser energy required for ignition [26,49]. Presented in Fig. 6 (top) are OH* chemiluminescence images showing the early flame kernel development corresponding to the modeled cases, i.e. zero offset (to within experimental resolution of ~+/- 0.1 mm), small (0.5 mm) offset for both sub-cases of NIR upstream of UV and vice versa, and large (2.5 mm) offset with the NIR upstream. The focal spots of the incident UV and NIR beams are shown with blue and red circles, respectively. The corresponding simulated images are shown in the bottom of Fig. 6. As time progresses, we simply observe the OH transport due to the gas dynamics effects involved in the kernel cooling phase. In summary, we find good agreement between experiment and simulation with a 2-lobe symmetric torus for the perfect overlap case, formation of an asymmetric torus with a 3rd lobe (that moves towards the NIR side) in the small (0.5 mm) offset case, and formation of an asymmetric torus with an additional (4th) lobe (propagating away from the third lobe) for the large (2.5 mm) offset case. It is worth noting that in experiments we have observed inconsistent (and infrequent) generation of a 4th lobe even at a 2 mm offset, though this case typically resulted in a 3-lobe configuration. However, a small fraction also exhibited a 4th lobe. This inconsistency is thought to be caused by fluctuating hot-spots (due to the multi-mode beam) along the UV pre-ionization channel which act to induce a small shift in the breakdown location of the NIR

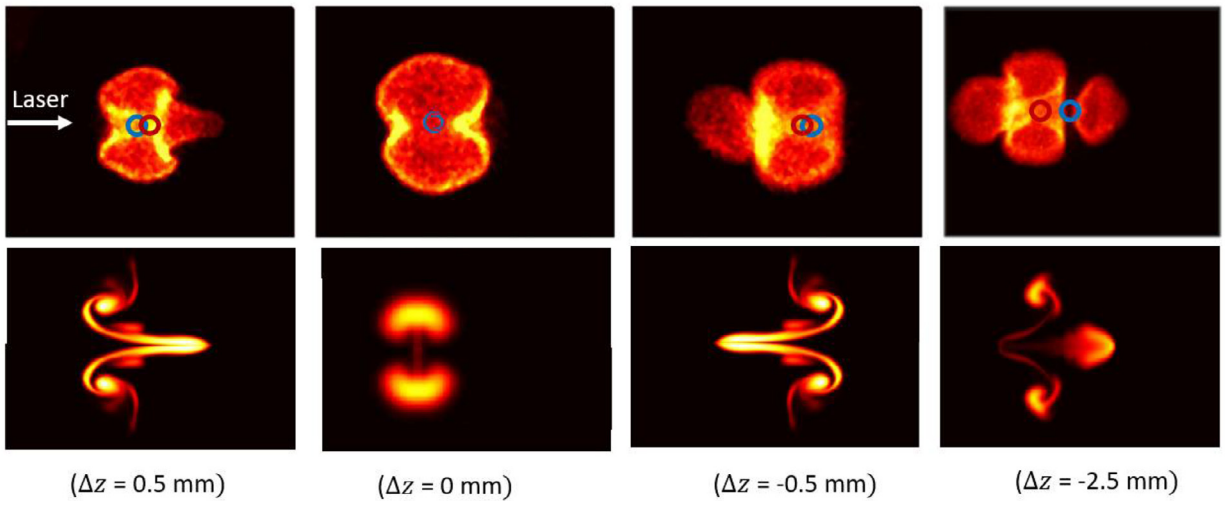

Fig. 6. Comparison between experiment (top) and simulated (bottom) OH* chemiluminescence images of a propane-air igniting kernel ($\phi = 1.0$) at time of 500 μs after the incident laser pulses. The blue and red circles show approximate positions of the focused UV and NIR beams respectively. Each image from the top frame has field of view: 22 mm × 16 mm. Images on the bottom have a field of view of: 16 mm x 10 mm. (For interpretation of the references to colour in this figure legend, the reader is referred to the web version of this article.)

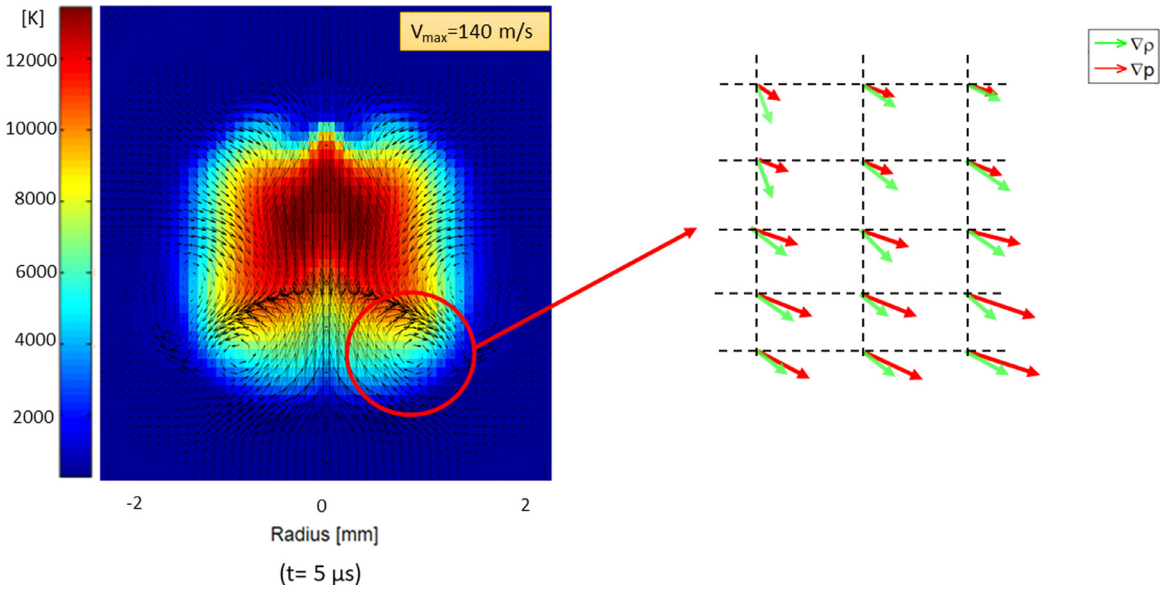

Fig. 7. (Left) Velocity field overlaid on top of temperature contours for the small (0.5 mm) offset kernel at delay of 0.5 $\boldsymbol{\mu s}$ after the initial pulses. (Right) Zoomed-in view showing the misalignment of the density (green) and pressure (red) gradients which lead to vorticity generation by baroclinic torque. (For interpretation of the references to colour in this figure legend, the reader is referred to the web version of this article.)

pulse. The apparent differences between experiments and simulation are partly due to the fact that the CFD contours are planar (2-D) sections while the experimental chemiluminescence images are path integrated (and therefore may obscure some of the finer features that are captured by the model). Moreover, the experimental images capture the light emitted from the electronically excited hydroxyl radical generated by a chain branching reaction in the flame ($CH+O_2 \rightarrow OH^*+CO$), whereas the CFD contours are representative of the OH that was generated during the discharge itself. In addition, the experimental kernels exhibit somewhat faster lobe growth (note the different spatial scales) which is attributed to chemical heat release enhancement as these were igniting stoichiometric cases (yet the simulation does not include combustion chemistry). It is important to note, at least for propane, that the main features of the kernel for igniting cases remain similar to those of non-igniting cases (see also Fig. 10 of [18]) with the later flame kernel following the "imprint" of the earlier plasma kernel (due to its baroclinic torque). The comparisons of Fig. 6 thus provide validation of the main flow field features of the dual-pulse plasma and flame kernels.

3.4. Vorticity generation

The post-discharge plasma kernel topology is largely governed by the vorticity generated during the blast wave formation and separation phase (i.e. during the first ~ 10 μs after the pulse). Several previous studies have provided detailed analysis of the mechanisms through which vorticity is generated in related plasma kernels [29,31–33,50]. The general consensus is that vorticity is primarily generated through the mechanism of baroclinic torque, i.e. due to misalignment of the density and pressure gradients, at the edges of the kernel. Fig. 7 shows the velocity field (left) along with pressure and density gradients (right) for a time of 5 μs after the pulse for the small (0.5 mm) offset case. The gradients are shown

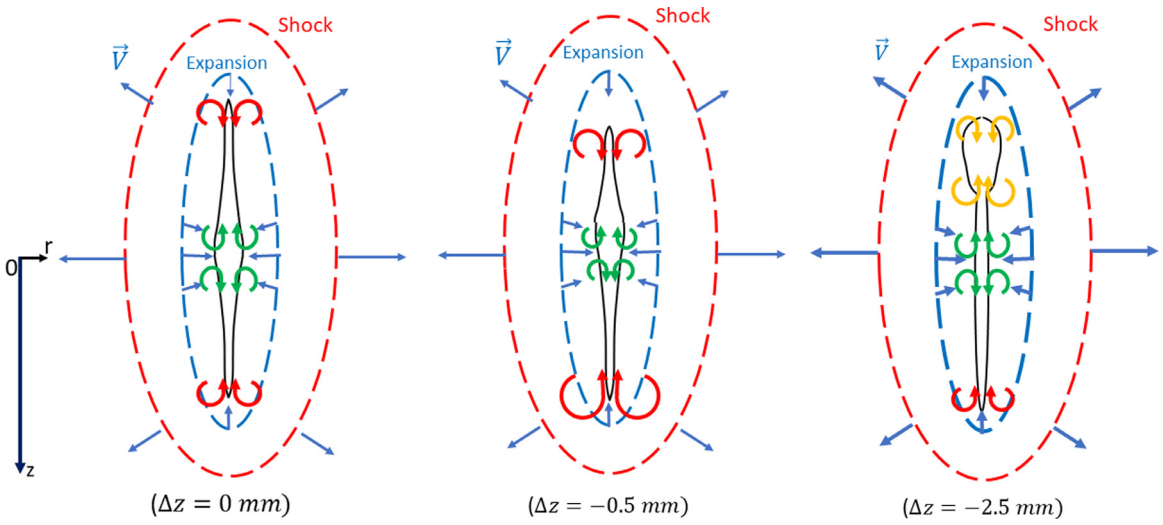

Fig. 8. Schematic showing the mechanism of vorticity generation through baroclinic torque inside of an idealized plasma kernel generated by an UV and NIR pulse for cases of perfect overlap, small (0.5 mm) offset and large (2.5 mm) offset between the two pulses. The size of the straight and curled arrows represents the amplitude of velocity and vorticity, respectively. The laser beams are incident from the top. The red and blue dashed lines represent the leading shock and rarefaction waves respectively, and the black solid line contours represent the boundaries of the hot gas kernels themselves at early time delays (prior to kernel collapse, t<~5 μs). (For interpretation of the references to colour in this figure legend, the reader is referred to the web version of this article.)

for a zoomed-in region of the domain where vorticity is clearly evident, and the vorticity formation is primarily due to the misalignment of these gradient vectors.

Vorticity generation is related to the blast wave dynamics as shown schematically in Fig. 8. A typical blast wave comprises of a leading high-pressure shock wave front that compresses the surrounding gas, followed by isentropic rarefaction waves which bring the inner fluid back to equilibrium after the passage of the blast. It is important to observe in Fig. 4 that the pressure is not constant along the entire perimeter of the blast. For example, during the first 5 μs, one observes in all cases that the blast is stronger laterally where the front is more planar (really cylindrical) compared to the top and bottom where the front is more spherical. This is because the energy is dissipated more quickly in a spherical shock versus a cylindrical one due to greater stretching of the wavefront in the former case. A consequence of the non-uniform pressure field is that the pressure gradient at the "corner" of the kernel is slightly tilted towards the higher-pressure side (lateral region) of the shock front. (By corner we mean the approximate location where the spherical and cylindrical waves meet.) On the other hand, Fig. 7 shows that the density gradient within the kernel is aligned (anti-parallel) to the temperature gradient (which points directly towards the epicenter of the blast) since the pressure variation is negligible within the kernel once the blast detaches from the kernel surface. The result is a misalignment between the pressure and density gradients which leads to generation of vorticity at the corners of all three configurations investigated due to baroclinic torque.

The positions and strengths of these vortical structures are different for the different cases studied and this has profound effects on the ensuing gas dynamics. The strongest sources of vorticity for the different cases are shown schematically in Fig. 8 using red (except for the large offset/weakly coupled cases where we used yellow to show the vorticity generated at the corners of the NIR kernel). Green is used to show regions of weaker vorticity generation by baroclinic torque near to the kernel center. In the case of the perfectly overlapped pulses ($\Delta = 0$mm), the vortices at the top and bottom of the kernel slowly overcome the weaker sources of vorticity at the center (green) and the kernel begins to collapse to form the asymmetric torus observed in Fig. 5-top. For the small ($\Delta z = -0.5$mm) offset case, the vortex at the bottom of the kernel (red) is somewhat stronger than the one at the top (red), due to the smaller radius of curvature at the bottom which causes a larger offset between the density and pressure gradients at that location. As a consequence, the bottom vortex overcomes the one on top thereby forming an asymmetric torus which entrains surrounding fluid and pushes it towards the laser source as observed in Fig. 5-middle. Lastly, for the large ($\Delta z = -2.5$mm) offset, we have a combination of effects. The NIR teardrop kernel presents its own top and bottom vortices (yellow) which lead to its collapse and to the formation of an asymmetric torus with lobe formation to the upstream side (this is similar to the case having a 0.5 mm offset as well as the well-known collapse mechanism for the NIR pulse on its own [18]). What is left from the UV pre-ionization channel also slowly begins to collapse under the influence of the bottom (red) and central (green) vortices; however, the high-aspect ratio of the UV preionization channel (large distance between these two vortices), along with the low temperature of the channel, means that the collapse is too slow (fluid moves slower through higher density/low temperature fluid) to lead to the formation of another asymmetric torus at the bottom of the kernel. Instead, a 4th lobe (only) is formed during this slow compression of the leftover gas. Note that, based on Fig. 5, the temperature of the 4th lobe changes only very slightly between 50 and 300 μs. By comparison, the temperature of the two side lobes changes by a factor of ~3 in the same time interval. The extended period of elevated temperature of the 4th lobe is due to the gas compression induced by the vorticity. For the sake of completeness, the configuration corresponding to the NIR pulse being focused far downstream from the UV focus ($\Delta z = 2.5$mm) was also tested. Such a configuration is equivalent to translating the NIR teardrop at the bottom of the UV channel. In this case, the vorticity is still strongest at the bottom of the teardrop leading to the formation of a third lobe moving upwards into the UV pre-ionization channel The resulting gas-dynamics are similar to those observed for the $\Delta z = -0.5$mm case.

Summary & future work

We have presented a numerical modeling study of the gas-dynamics induced by dual-pulse laser pre-ionization plasmas. Four different kernel configurations were examined: 1) energy is de-

posited approximately symmetrically along the optical axis (corresponding to the case of overlapped focal spots); 2) and 3) Energy deposition has a small offset (NIR focal spot is ~0.5 mm upstream/downstream of UV); and 4) Energy deposition has a large offset (NIR focal spot ~2.5 mm upstream of the UV. In Case 1), the formation of the third lobe was suppressed and the kernel developed into a symmetric toroid. Cases 2) and 3) lead to formation of an asymmetric torus with a third lobe that propagates towards the side of the initial NIR focus. Finally, Case 4) gives rise to an asymmetric torus with an additional 4th lobe that moves in the opposite direction of the third lobe. All such configurations were also observed experimentally via OH^* chemiluminescence images collected during the ignition of propane-air mixtures. These gas-dynamic features are driven by vorticity and we have presented an analysis of vorticity generation for each case. The main mechanism for vorticity generation is baroclinic torque which manifests differently for the different cases.

Importantly, the different gas dynamics arising from the various offset cases investigated may have significant implications for combustion. For example, our prior work has suggested that the 3rd lobe separation for NIR sparks could be responsible for the observed flame kernel quenching at the lean limit, whereas successful ignition was achieved at the same conditions when a zero-offset dual-pulse laser ignition was used. The persistence of elevated temperature in the various plasma kernels can also impact ignition and we find that the temperature of the kernel decays much more quickly if there is an offset between the two pulses. For example, at time 50 μs the maximum temperature is almost twice as high for the dual-pulse overlapped kernel when compared to the small offset case (~6500 K in the former case versus ~3500 K in the latter case, see Fig. 5). The overlapped (higher temperature) configuration may therefore better promote ignition at lean conditions as it is more robust to quenching (cooling). On the other hand, the small offset configuration may benefit applications in high-speed reacting flows if one judiciously arranges the two pulses such that the plasma-driven vorticity increases the ignition residence time (e.g. making the 3rd lobe propagate in a counter-flow direction). Finally, the four-lobe configuration resulting from the large offset case may benefit applications where early flame development is critical (e.g. lean ignition in moving flows), since the fourth lobe remains relatively hot for a longer time after the pulse (e.g., the temperature of the fourth lobe at 300 μs is similar to that of the two side lobes making the torus, i.e. T~1100 K). A reactive 4th lobe could actively participate in the flame propagation leading to an increase in the rate of heat release (resulting in an elevated flame speed). Future work will focus on the addition of plasma and combustion chemistry in the mathematical model as well as examining cases where the kernels are formed in moving flows.

Funding

One of the authors A.Y., acknowledges support from Air Force Office of Scientific Research (FA9550-18-1-0239).

Author Statement

C.D. conducted the following experimental investigations related to the modeling: laser ignition of propane-air mixtures using dual-pulse breakdown techniques. In addition, C.D, performed the CFD simulations to obtain the profiles discussed in the manuscript. A.Y. was the principal investigator of this research project. He defined the overall research plan, provided continuous guidance to the research team including help with data interpretation. Both A.Y. and C.D. contributed to the writing of the submitted manuscript.

Declaration of Competing Interest

The authors declare that they have no known competing financial interests or personal relationships that could have appeared to influence the work reported in this paper.

References

[1] J.D. Dale, P.R. Smy, D. Way-Nee, R.M. Clements, Laser-ignited internal combustion engine, Combust. Flame 30 (1977) 319–320.
[2] D.L. McIntyre, S.D. Woodruff, M.H. McMillian, S.W. Richardson, M. Gautam, Lean-burn stationary natural gas reciprocating engine operation with a prototype miniature diode side pumped passively Q-switched laser spark plug, in: ASME 2009 Internal Combustion Engine Division Spring Technical Conference, 2008, pp. 405–413.
[3] N. Pavel, M. Bärwinkel, P. Heinz, D. Brüggemann, G. Dearden, G. Croitoru, O.V. Grigore, Laser ignition - Spark plug development and application in reciprocating engines, Prog. Quantum Electron. 58 (2018) 1–32.
[4] C. Manfletti, G. Kroupa, Laser ignition of a cryogenic thruster using a miniaturised Nd:YAG laser, Opt. Express 21 (2013) A1126–A1139.
[5] P.S. Hsu, S. Roy, Z. Zhang, J.C. Sawyer, M.N. Slipchenko, J.G. Mance, J.R. Gord, High-repetition-rate laser ignition of fuel – air mixtures, Opt. Lett. 41 (2016) 1570–1573.
[6] J.L. Gottfried, F.C. De Lucia, C.a. Munson, A.W. Miziolek, Laser-induced breakdown spectroscopy for detection of explosives residues: a review of recent advances, challenges, and future prospects, Anal. Bioanal. Chem. 395 (2009) 283–300.
[7] S. Joshi, D.B. Olsen, C. Dumitrescu, P.V. Puzinauskas, A.P. Yalin, Laser-induced breakdown spectroscopy for in-cylinder equivalence ratio measurements in laser-ignited natural gas engines, Appl. Spectrosc. 63 (2009) 549–554.
[8] V. Zvorykin, Control of extended high-voltage electric discharges in atmospheric air by UV KrF-laser radiation, Quantum Electron. 41 (2011) 227–233.
[9] L.J. Radziemski, D. Cremers, Lasers-Induced Plasmas and Applications, Marcel Dekker, INC., New York, 1989.
[10] Y. Raizer, Laser-Induced Discharge Phenomena, Consultants Bureau, New York, 1977.
[11] N. Glumac, G. Elliott, M. Boguszko, Temporal and spatial evolution of the thermal structure of a laser spark in air, in: AIAA 2005-204, 2005, pp. 1–16.
[12] C. Limbach, R. Miles, Simultaneous temperature, density and velocity measurements in laser-generated plasmas by rayleigh and filtered rayleigh scattering, in: AIAA 2014-0143, 2014, pp. 1–28.
[13] M.H. Morsy, S.H. Chung, Numerical simulation of front lobe formation in laser-induced spark ignition of ch 4 /air mixtures, Proc. Combust. Inst. 29 (2002) 1613–1619.
[14] T.a. Spiglanin, a. Mcilroy, E.W. Fournier, R.B. Cohen, J.a. Syage, Time-resolved imaging of flame kernels: laser spark ignition of H2/O2/Ar mixtures, Combust. Flame 102 (1995) 310–328.
[15] I.A. Mulla, S.R. Chakravarthy, N. Swaminathan, R. Balachandran, Evolution of flame-kernel in laser-induced spark ignited mixtures: a parametric study, Combust. Flame 164 (2016) 303–318.
[16] T.X. Phuoc, Laser-induced spark ignition fundamental and applications, Opt. Lasers Eng. 44 (2006) 351–397.
[17] L. Wermer, J. Hansson, S. Im, Dual-pulse laser-induced spark ignition and flame propagation of a methane diffusion jet flame, Proc. Combust. Inst. 36 (2017) 4427–4434.
[18] D. Bradley, C.G.W. Sheppard, I.M. Suardjaja, R. Woolley, Fundamentals of high-energy spark ignition with lasers, Combust. Flame 138 (2004) 55–77.
[19] G. Herdin, J. Klausner, Laser ignition: a new concept to use and increase the potentials of gas engines, in: ICEF-ASME 2005, 2005, pp. 1–9.
[20] H. Kopecek, M. Lackner, F. Winter, E. Wintner, Laser-induced ignition of methane-air mixtures at pressures up to 4MPa, LASER Phys. 13 (2003) 1365–1369.
[21] A. Yalin, High power fiber delivery for laser ignition applications, Opt. Express 21 (2013) 515–517.
[22] J. Beduneau, K. Bonggyu, L. Zimmer, Y. Ikeda, Measurements of minimum ignition energy in premixed laminar methane/air flow by using laser induced spark, Combust. Flame 132 (2003) 653–665.
[23] N. Pavel, R. Chiriac, A. Birtas, F. Draghici, M. Dinca, On the improvement by laser ignition of the performances of a passenger car gasoline engine, Opt. Express 27 (2019) A385.
[24] T.X. Phuoc, Laser spark ignition: experimental determination of laser-induced breakdown thresholds of combustion gases, Opt. Commun. 175 (2000) 419–423.
[25] C. Dumitrache, C.M. Limbach, A.P. Yalin, Threshold characteristics of ultraviolet and near infrared nanosecond laser induced plasmas, Phys. Plasmas 23 (2016) 093515.
[26] C. Butte, P. Lokini, C. Dumitrache, A.P. Yalin, Single and dual-pulse laser ignition of methane-air and hydrogen-air mixtures, in: AIAA 2020-1893, AIAA Scitech, Orlando, 2020, pp. 1–13.
[27] Dumitrache C., VanOsdol R., Limbach C.M. and Yalin A.P. 2017. Laser ignition of propane-air mixtures using a dual-pulse technique *2017-1976* (Dallas, TX), pp 1–8.
[28] R. Mahamud, A.A. Tropina, M.N. Shneider, R.B. Miles, Dual-pulse laser ignition model, Phys. Fluids 30 (2018) 106104.

[29] C. Dumitrache, Novel Laser Ignition Technique Using Dual-Pulse Pre-Ionization, Colorado State University, 2017.
[30] M. Kono, K. Niu, T. Tsukamoto, Y. Ujiie, Mechanism of flame kernel formation produced by short duration sparks, Symp. Combust. 22 (1988) 1643–1649.
[31] S. Ghosh, K. Mahesh, Numerical simulation of laser – induced breakdown in air, in: 46th AIAA Aerospace Sciences Meeting, 2008, pp. 1–22.
[32] C. Dumitrache, A. Yalin, Gas dynamics and vorticity generation in laser-induced breakdown of air, Opt. Express 28 (2020) 5835–5850.
[33] C. Dumitrache, A. Gallant, N. Minesi, S. Stepanyan, G.D. Stancu, C.O. Laux, Hydrodynamic regimes induced by nanosecond pulsed discharges in air: mechanism of vorticity generation, J. Phys. D. Appl. Phys. 52 (2019) 364001.
[34] E. Toro, Riemann Solvers and Numerical Methods For Fluid Dynamics, Springer-Verlag, 1999.
[35] P.L. Roe, J. Pike, Efficient construction and utilisation of approximate Riemann solutions, Comput. methods Appl. Sci. Eng. VI (1984) 499–518.
[36] J.R. Edwards, A low-diffusion flux-splitting scheme for Navier-Stokes calculations, Comput. Fluids 26 (1997) 635–659.
[37] B. Larrouturou, How to preserve the mass fractions positivity when computing compressible multi-component flows, J. Comput. Phys. 95 (1991) 59–84.
[38] T.J. Poinsot, S.K. Lelef, Boundary conditions for direct simulations of compressible viscous flows, J. Comput. Phys. 101 (1992) 104–129.
[39] K.W. Thompson, Time dependent boundary conditions for hyperbolic systems, J. Comput. Phys. 68 (1987) 1–24.
[40] C. Dumitrache, N. Wilvert, A. Yalin, M. Shneider, Laser plasma formation using dual pulse pre-ionization, AIAA 2013-2632, 2013.
[41] C. Butte, C. Dumitrache, A. Yalin, Properties of dual-pulse laser plasmas and ignition characteristics in propane-air and methane-air mixtures, in: AIAA 2019-0464, 2019, pp. 1–9.
[42] C. Dumitrache, C.M. Limbach, A.P. Yalin, Threshold characteristics of ultraviolet and near infrared nanosecond laser induced plasmas, Phys. Plasmas 23 (2016) 093515.
[43] S. Stepanyan, N. Minesi, A. Salmon, G.D. Stancu, C.O. Laux, Spatial evolution of the plasma kernel produced by nanosecond discharges in air, J. Phys. D Appl. Phys (2019) 1–17.
[44] T.X. Phuoc, F.P. White, An optical and spectroscopic study of laser-induced sparks to determine available ignition energy, Proc. Combust. Inst. 29 (2002) 1621–1628.
[45] T.X. Phuoc, C.M. White, D.H. McNeill, Laser spark ignition of a jet diffusion flame, Opt. Lasers Eng. 38 (2002) 217–232.
[46] G.C. Gebel, T. Mosbach, W. Meier, M. Aigner, Optical and spectroscopic diagnostics of laser-induced air breakdown and kerosene spray ignition, Combust. Flame 162 (2015) 1599–1613.
[47] Y. Chen, J.W.L. Lewis, C. Parigger, Spatial and temporal profiles of pulsed laser-induced air plasma emissions, J. Quant. Spectrosc. Radiat. Transf. 67 (2000) 91–103.
[48] C. Dumitrache, R. Vanosdol, C.M. Limbach, Azer, P. Yalin, Control of early flame kernel growth by multi-wavelength laser pulses for enhanced ignition, Sci. Rep. (2017) 1–8.
[49] C. Dumitrache, R. Vanosdol, C.M. Limbach, A.P. Yalin, Control of early flame kernel growth by multi-wavelength laser pulses for enhanced ignition, Sci. Rep. 7 (2017).
[50] J.M. Wang, D.A. Buchta, J.B. Freund, Hydrodynamic ejection caused by laser-induced optical breakdown, J. Fluid Mech. (2020) 1–31.

Single and Dual-Pulse Laser Ignition of Methane-Air and Hydrogen-Air Mixtures

Carter Butte[1], Parneeth Lokini[2], Azer P. Yalin[4]
Colorado State University, Fort Collins, CO, 80523, USA

Ciprian Dumitrache[3]
CentraleSupélec EM2C, Châtenay-Malabry, France

Abstract

This investigation examines ignition characteristics of various fuel-air mixtures using both single and dual-pulse laser plasmas building off our previous work. A single pulse laser plasma (λ=1064 nm) of energy E_{SP}=60 mJ is used to ignite methane-air and hydrogen-air mixtures (T_0=298 K, P_0=1 bar) of equivalence ratios in the range of ϕ=0.1–1.0. A non-resonant dual-pulse plasma is formed using a preionization beam in the UV (λ=266 nm) and an energy addition pulse operating in the NIR (λ=1064 nm), with energies of E_{UV}=20 mJ and E_{NIR}=40 mJ, respectively. The dual-pulse plasma is used to ignite methane-air and hydrogen-air mixtures of equivalence ratios in the same range. We report lean limits of ϕ=0.53 and ϕ=0.12 for single pulse ignition of methane-air and hydrogen-air mixtures respectively, and lean limits of ϕ=0.50 and ϕ=0.11 for dual-pulse ignition of methane-air and hydrogen-air mixtures, respectively. OH* chemiluminescence shows that single and dual-pulse toroid shapes in methane-air mixtures are consistent with single pulse and dual-pulse toroids formed in propane-air mixtures, but that hydrogen-air mixtures tend to suppress third lobe development over a larger range of equivalence ratios. An investigation of dual-pulse beam axial offset effects demonstrates that downstream focusing of the energy addition pulse relative to the preionization pulse more effectively suppresses third lobe formation than upstream focusing. We also note that upstream focusing of the energy addition pulse near stoichiometric conditions can result in a fourth lobe centered around the preionization channel, and that for small axial offsets ($\Delta z \leq 0.5$ mm), variability exists in the direction of flame propagation. In terms of ignition, we show that for axial offsets above 2 mm no significant benefits (in terms of lean limit extension) are observed. Finally, the main finding of this study is that ignition probability using the dual-pulse non-resonant method is a strong function of axial offset and that downstream focusing of the energy addition pulse is preferable to upstream focusing.

I. Introduction

Progress towards more complex combustion applications has demanded more advanced and versatile ignition techniques. One attempt to address some of the concerns associated with well-established techniques such as spark plugs and igniters is laser plasma ignition. Advantages of laser ignition include flexibility of spark location and timing, reduced NO_x formation, leaner engine operation, increased combustion efficiency, and greater

[1] Graduate Student, Department of Mechanical Engineering, Colorado State University, Fort Collins, CO
[2] Graduate Student, Department of Mechanical Engineering, Colorado State University, Fort Collins, CO
[3] Postdoctoral Fellow, Laboratoire EM2C, Université Paris-Saclay, Gif-sur-Yvette, France, AIAA Member
[4] Professor, Department of Mechanical Engineering, Colorado St. Univ., Fort Collins, CO, Associate Fellow AIAA

system longevity at elevated pressures.[1-5] Additionally, the non-intrusive nature of laser plasmas results in more unperturbed kernel evolution, as proximate mounting hardware is not required. This is an advantage when compared with spark plug or igniter electrodes which typically act as heat sinks quenching the flame. However, large input energies and complications with beam delivery have impeded field implementation.[6-8]

Our approach to address these challenges uses a dual-pulse laser plasma where a UV beam preionizes a gas mixture and a secondary NIR beam increases the energy and ionization state of the gas. The use of this technique decouples the processes responsible for ionization, predominantly multiphoton ionization (MPI) and electron avalanche ionization (EAI) through inverse bremsstrahlung absorption, and allows for tailoring of plasma properties through adjustments to beam energies and delay time.[9-12] Recent work has shown that dual-pulse laser plasmas not only reduce energy requirements but also enhance ignition characteristics such as combustion efficiency, particularly around the lean limit.[6] An investigation into further energy reduction used a resonant scheme targeting molecular oxygen for preionization. Results showed that similar electron densities to single pulse plasmas and non-resonant dual-pulse plasmas could be produced with 67% of the energy, most of which was concentrated in the energy addition beam.[13] Ignition experimentation with the resonant dual-pulse plasma demonstrated extension of the lean limit for methane-air mixtures, though toroid shapes as observed using OH* chemiluminescence suggested that this was likely a result of increased laser energy deposition in the plasma. This investigation serves to fill in the voids in existing literature with regards to ignition experimentation of various fuels using single and dual-pulse laser ignition. Specifically, this investigation employs a single pulse plasma (λ_{SP}=1064 nm) for ignition of methane-air and hydrogen-air mixtures, and a non-resonant dual-pulse plasma (λ_{UV}=266 nm, λ_{NIR}=1064 nm) for ignition of methane-air and hydrogen-air mixtures. In the analysis, these experimental results are combined with past results to give a comprehensive picture of the ignition abilities of single pulse and dual-pulse plasmas in propane-air, methane-air, and hydrogen-air mixtures.[6,13]

The rest of the document is outlined as follows: Section II details the procedure and setup for ignition testing, Section III presents the results with regards to ignition efficiencies and lean limits of the fuels of interests using the plasmas of interest, and Section IV makes final remarks regarding comparisons to existing literature and future experimentation.

II. Experimental Setup

We use the fourth-harmonic (λ=266 nm) of an Nd:YAG (Continuum Powerlite 8010) for preionization and the fundamental output (λ=1064 nm) from a second Nd: YAG (New Wave Gemini) for energy addition. The two together, separated temporally by 15 ns using a pulse delay generator (Berkeley Nucleonics 555), form the dual-pulse plasma. The preionization beam is attenuated to an energy of E_{UV}=20 mJ and has a pulse duration of approximately 7 ns. The energy addition pulse has an energy of E_{NIR}=40 mJ and has a pulse duration of 10 ns. These energies were selected to match the conditions of dual-pulse plasmas used for ignition of propane-air mixtures in the past.[6] The optical layout for dual-pulse plasma formation is shown in Fig. 1. The beams are spatially overlapped using a beam splitter (ThorLabs HBSY134) and focused to a common waist using two lenses of focal length f = 300 mm. The lens for the energy addition pulse is placed on a translation stage as to be able to optimize and adjust the axial offset of the two beams. The beams are focused to the approximate center of a custom chamber of volume V = 195 cm^3 in which ignition experimentation is performed. The same 1064 nm laser used for energy addition is also used for single pulse plasma formation, where the duration is the same but the energy is raised to E_{SP}=60 mJ. A dynamic pressure transducer (PCB Piezotronics 113B24) mounted on the side of the chamber is used with an oscilloscope (Rigol DS1204B), to record pressure histories of ignition, while simultaneous OH* chemiluminescence imaging is performed using an ICCD (pco DICAM pro) and an optical bandpass filter (Andover 310FS10-50) of wavelength λ~310 nm.

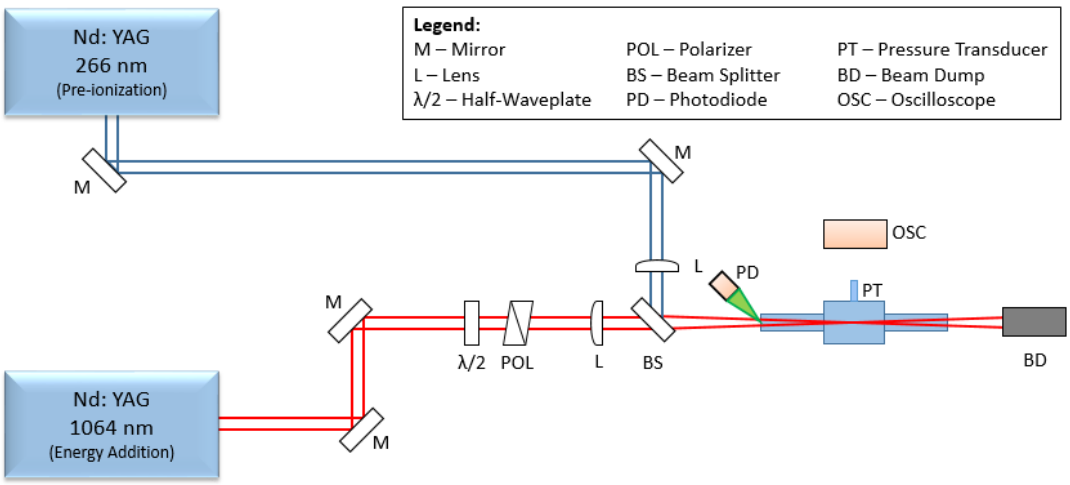

Figure 1: The optical setup for plasma ignition. Single pulse ignition uses the same setup without the 266 nm laser.

III. Results

A. Ignition Testing

Combustion of methane-air and hydrogen-air mixtures was performed using both single and dual-pulse plasmas to supplement past ignition testing of these plasmas in other fuels.[6] We examined equivalence ratios from the stoichiometric case down to the lean limit, with increasing resolution towards the lean limit. Dual-pulse methane combustion focused on lean limit determination in the region of $0.47<\phi<0.55$ to supplement existing literature published by our group in the near stoichiometric region.[14] The pressure traces presented in Fig. 2 show single and dual-pulse ignition in the first and second column, and methane-air and hydrogen-air mixtures in the first and second rows respectively. Time of zero corresponds to the time of laser energy deposition, and the central line of each pressure trace represents the average of at least n=10 individual measurements, while the shaded region represents one standard deviation in either direction of the igniting cases. As expected, we see decreasing peak pressure and increasing ignition delay and variability with increasing equivalence ratio. Note that the dual-pulse trace at ϕ=0.8 is provided from previous experimentation.[14]

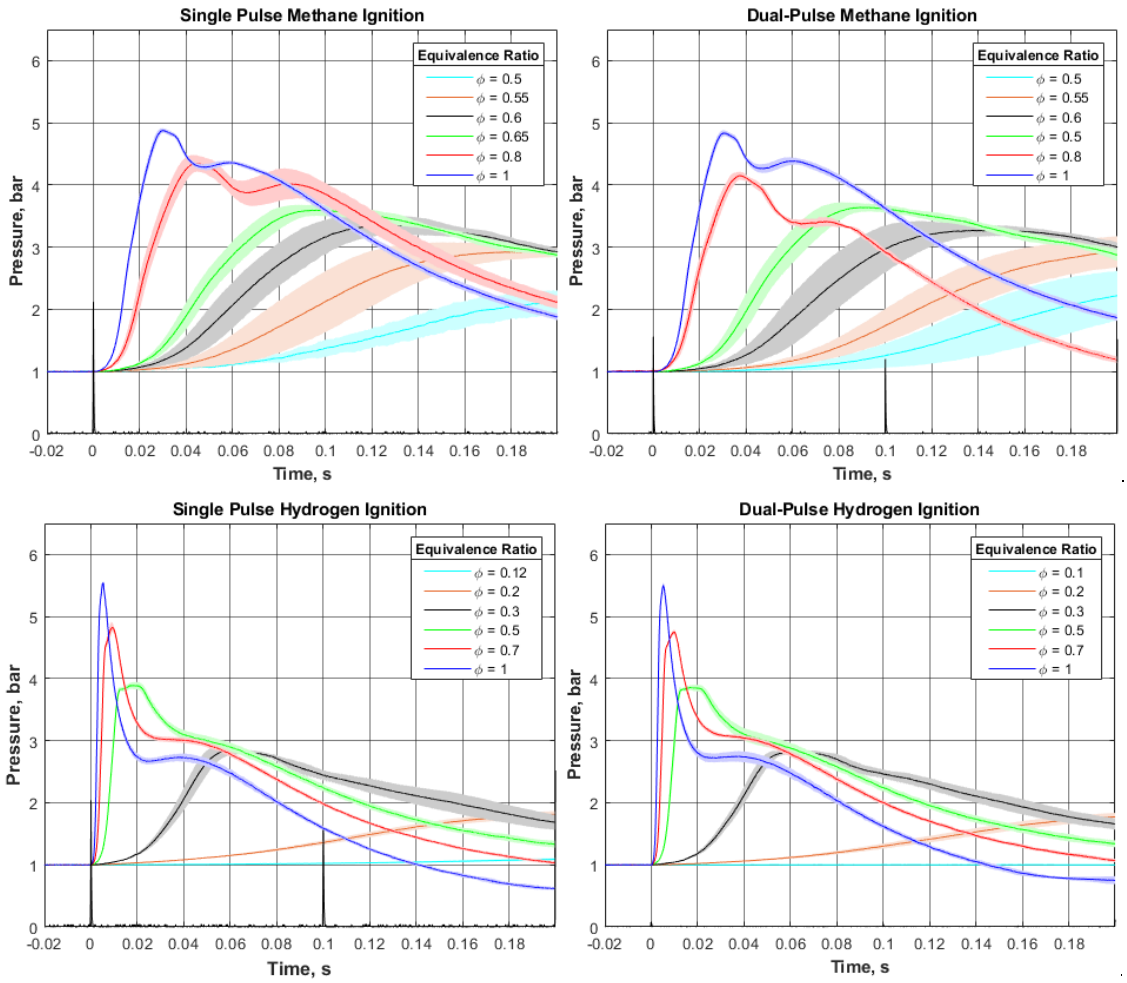

Figure 2: Combustion pressure histories for single and dual-pulse ignition of methane-air and hydrogen-air mixtures. Each trace is the result of averaging successful ignition events of at least ten trials,

We define successful ignition as any increase in pressure (as monitored by the dynamic pressure transducer) accompanied by simultaneous flame propagation as monitored through OH* chemiluminescence. This definition includes weak and partial combustion events. We define the lean limit as the leanest test case where probability of ignition met or exceeded 50%. Using the pressure traces shown above, we can extract a heat release rate from each ignition event as described in our past work.[12] By comparing to the heating values of the respective fuels, we can calculate the combustion efficiency for each ignition event. The resulting efficiencies are shown in Fig. 3 for the single and dual-pulse cases and are compared with existing information for propane from literature.[6,14] The vertical error bars are representative of the standard deviation in efficiency for each equivalence ratio, while horizontal error bars indicate the measurement uncertainty associated with the pressure gauge used to monitor partial pressures. Note that the uncertainty in equivalence ratio varies for each fuel type. The average efficiency value is calculated from the igniting cases, and excludes unsuccessful ignition events. All cases ignited 100% of the time, unless otherwise marked (shown as fractions of successful ignition events around the lean limit).

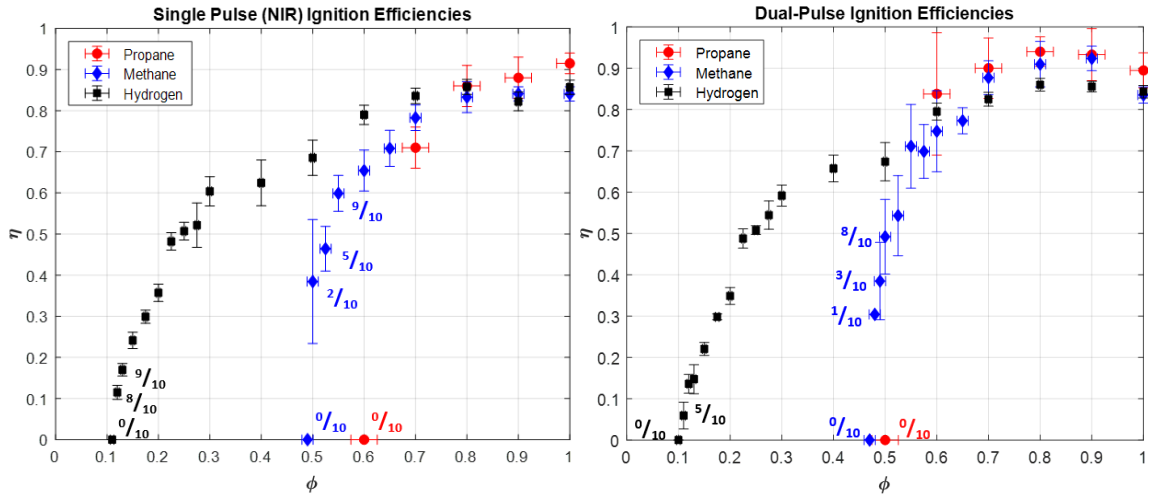

Figure 3: Ignition efficiency for propane (red), methane (blue), and hydrogen (black) fuel-air mixtures using single pulse (left) and dual-pulse (right) plasmas. Note that for the same combined energy, use of the dual-pulse plasma results in a horizontal shift of each curve to the left, extending the lean limit, and increasing ignition efficiency for the lean fuel-air mixtures.

As seen in past experimentation, we observe higher efficiency for lean mixtures, as well as extended lean limits for hydrogen-air when compared with methane-air and propane-air mixtures.[13] Near stoichiometric conditions, we see elevated efficiencies for propane. Based on our definition of the lean limit, we report single pulse NIR lean limits of ϕ=0.12 for hydrogen, ϕ=0.53 for methane, and literature reports a lean limit of ϕ=0.70 for propane.[6] For the dual-pulse plasma, we report lean limits of ϕ=0.11 for hydrogen, ϕ=0.50 for methane, and previous experimentation reports a lean limit of ϕ=0.60 for propane.[14] We find that the dual-pulse plasma results in extension of the lean limit for each fuel type relative to single-pulse (with the same total incident energy). We note the most significant difference for propane, though the resolution ($\Delta\phi$=0.1) in equivalence ratio from previous experimentation could be improved.[6] We also note that the lean limits for the dual-pulse plasma closely match those of the resonant dual-pulse plasma.[13] In terms of efficiency, we report generally higher efficiency ignition for the dual-pulse plasma in both methane-air and hydrogen-air mixtures when compared with single pulse NIR ignition, though the result is seen for nearly all equivalence ratios in the methane-air case while only for the particularly lean cases for hydrogen-air mixtures.

B. OH* Chemiluminescence

In tandem with ignition experimentation, we imaged the flame front and kernel growth using an intensified charged camera and a λ~310 nm filter corresponding to the emission from the intermediate OH* radical, known to be a species correlated with regions of heat release.[15-17] This method allows for temporal imaging of the plasma kernel evolution when ignition is repeated and the timing for the gate of the camera is altered. This method works very well when the kernel shape is consistent shot to shot, as is the case near stoichiometric conditions, but becomes difficult near the lean limit, where localized variations in fuel concentrations result in differently shaped flame fronts and flame speeds. For this reason, we tend to look at the kernel shapes near the lean limit independently rather than as a sequence. Fig. 4 shows flame kernel development of the single pulse NIR plasma in methane, revealing similar kinds of kernel shapes that are well documented in literature for other fuel-air mixtures.[18-23] Though this structure is actually an asymmetric torus, it is typically described as a series of lobes because of the shape it takes on when viewed in two dimensions. The toroid is formed by plasma induced hydrodynamics and acts as a driving mechanism through which surrounding gas is entrained and forced through its center.[2,24] The asymmetric torus can be identified in the following images as two vertical side lobes (corresponding to the cross-section image of the torus) and the expelled jet passing through the center of the torus can be identified as the third lobe propagating towards the laser.[6] In this investigation, we see third lobe formation for single pulse methane-air ignition for all equivalence ratios, and separation of the third lobe for mixtures of equivalence ratios of $\phi \leq 0.70$. We also see that near the lean limit, the flame front propagates for hundreds of microseconds, before dissipating or quenching on a several millisecond timescale. Though partial ignition does occur, the flame does not propagate to fill the chamber for some of these leaner mixtures as it does for mixtures of higher equivalence ratios. This result is expected and is similar to single pulse NIR ignition in other fuels.[6] For the flame kernels in Fig. 4, the gain for collection was constant, though the images use selective contrast to highlight the

kernel shapes. Time delays were selected to match (as close as possible) the conditions previously published by our group on ignition of propane-air mixtures.[6]

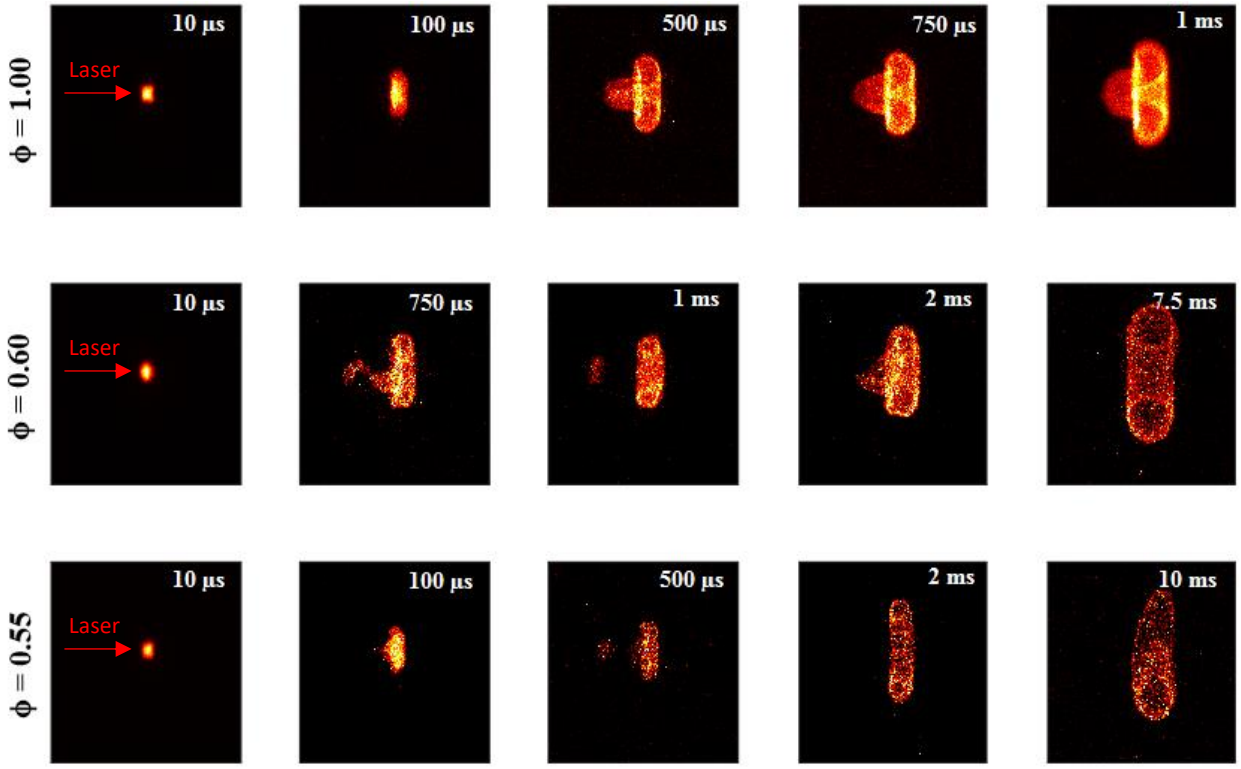

Figure 4: Flame propagation for the single pulse NIR plasma in methane-air mixtures at a variety of equivalence ratios. Indicated times are relative to laser energy deposition inside the chamber. Images have physical dimensions of 28 mm x 22 mm in the horizontal and vertical directions, respectively. Note the tendency of the third lobe to form and separate for the leaner cases.

Figure 5 details similar flame kernel evolution for single pulse NIR plasmas in hydrogen-air mixtures. Single pulse NIR combustion of hydrogen-air mixtures exhibits distinctly different kernels as compared to methane-air mixtures. Primarily, the timescale for complete combustion was much shorter. The hydrogen-air flame takes around 1 ms to fill the entire frame, while the methane-air flame takes longer than 2.5 ms. More rapid combustion can be expected based on higher predicted flame speeds associated with hydrogen.[25] This can also be seen in the pressure histories of Fig. 2. In terms of kernel shape, the main difference compared to methane is that near stoichiometric conditions we observe highly different flame speeds in the radial and longitudinal (beam propagation) directions. The images show that the kernel expands rapidly over the radial axis when compared with the longitudinal axis. The flame speed of the third lobe is significantly smaller than that of the adjacent toroid, and the result is an ovular shaped kernel and a third lobe that never fully develops. However, we hypothesize that it is possible that the third lobe attempts to form in this near stoichiometric scenario, but is accompanied by large rates of flame strain, resulting in quenching and rapid extinction of this third lobe. As the equivalence ratio decreases, we begin to see the third lobe become more pronounced, which may be due to more uniform flame speeds and reduced strain rate. By ϕ=0.65, we see the third lobe on occasion, at ϕ=0.4 we see it every time, and around ϕ=0.20 we see separation begin to occur. Below ϕ=0.20, we see separation of the third lobe, though there is still enough energy in the independent lobes to sustain combustion in localized regions. This is seen in the bottom right image where a section of the kernel has expanded above the frame and is overlaid with kernels still in the frame (ϕ=0.13, t=25 ms).

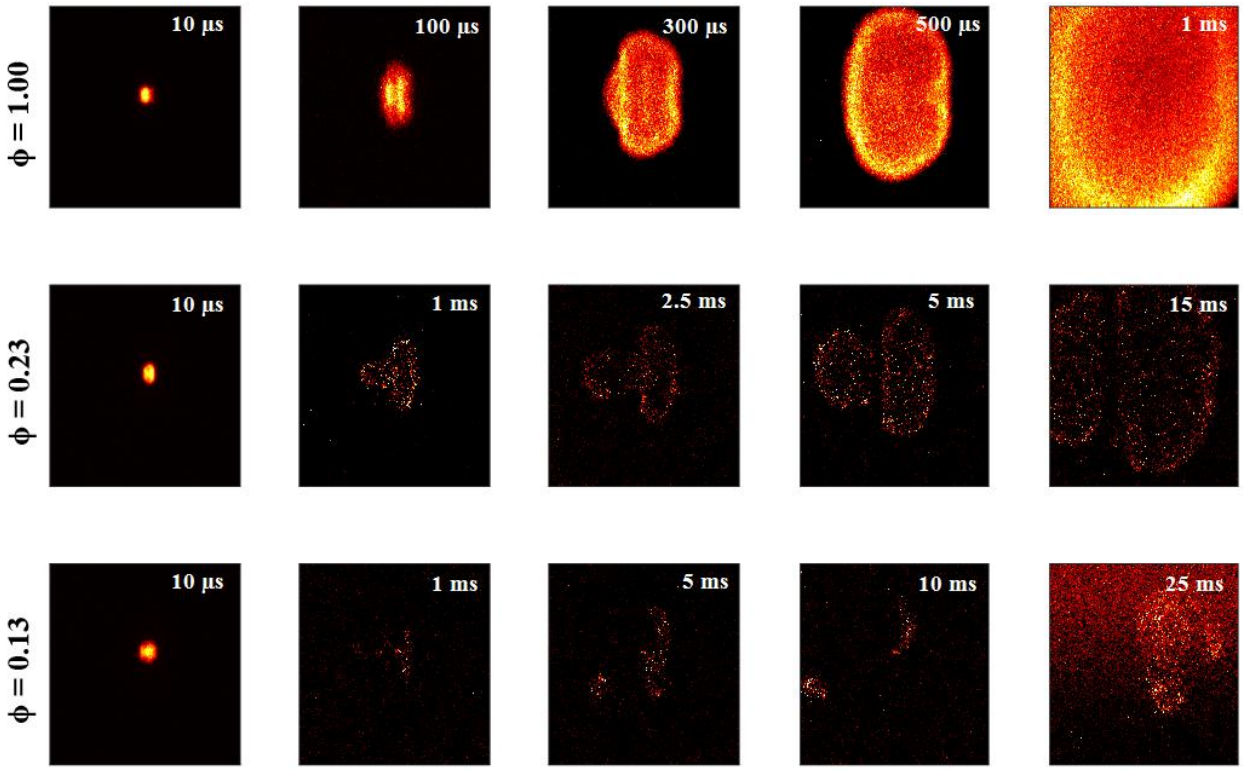

Figure 5: Flame propagation for the single pulse NIR plasma in hydrogen-air mixtures at a variety of equivalence ratios. Indicated times are relative to laser energy deposition inside the chamber. Images have physical dimensions of 28 mm x 22 mm in the horizontal and vertical directions, respectively. Note the ovular shape of the kernel as well as the segmentation that takes place for leaner mixtures, resulting in localized ignition events.

Using the same techniques presented above for the single pulse NIR plasma and kernel, we analyze the dual-pulse plasma for ignition in both methane-air and hydrogen-air mixtures. We see that in both fuel-air mixtures, for all equivalence ratios, the dual-pulse plasma kernel exhibits the characteristic shape of a preionization channel and a larger energy addition kernel over the range of tens of microseconds.[12] Fig. 6 shows methane-air ignition. For equivalence ratios in the range ϕ=1.0-0.70 the energy deposition profile suppresses the development of the third lobe.[6] For the stoichiometric case, the direction of plasma propagation (or the direction in which the third lobe would form if it did) is unpredictable. As mentioned earlier, each image represents a separate ignition event, so that each image should be evaluated individually rather than as a sequence. In eleven combustion events, we report that five of these kernels propagated towards the laser beam, while four propagated away (two were indeterminable). We attribute this to the axial overlap of the two beams, and believe that variability in propagation direction is indicative of good overlap (Δz=0), which leads to suppression of the third lobe. This is studied more rigorously in the offset investigation in Section C. Below ϕ=0.7, despite successful overlap, the third lobe is formed, but it takes a long time to develop (tens of ms), which may explain why this result was not reported on in the past for propane-air mixtures.[6] Around ϕ=0.55, we observe third lobe detachment, kernel segmenting and extinction, and localized kernels which then propagate towards a complete ignition event.

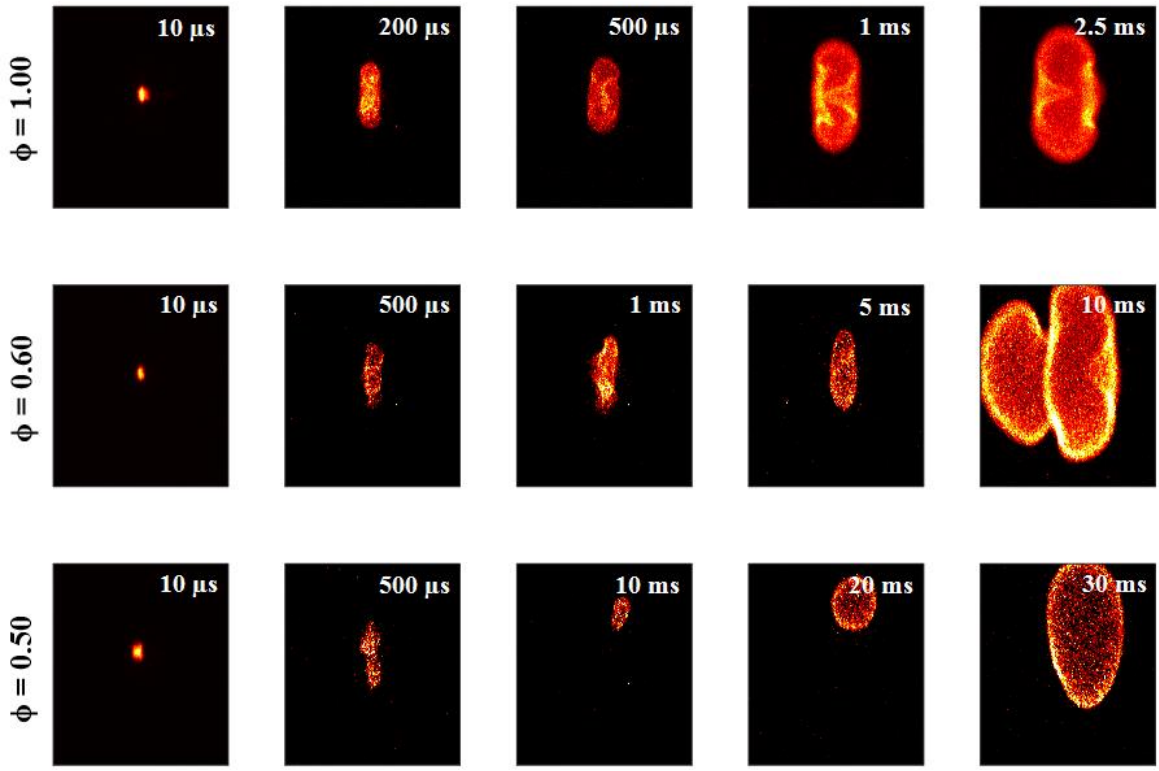

Figure 6: Flame propagation for the dual-pulse plasma in methane-air mixtures at a variety of equivalence ratios. Indicated times are relative to laser energy deposition inside the chamber. Images have physical dimensions of 28 mm x 22 mm in the horizontal and vertical directions, respectively. Note the non-existence of the third lobe for the stoichiometric case. Additionally note the timescale over which the third lobe is seen for the intermediate equivalence ratios and the localized combustion that occurs near the lean limit.

Much like the single pulse NIR plasma, kernel shapes for dual-pulse ignition of hydrogen-air mixtures were much different compared to those formed in methane air mixtures, likely due to fuel reactivity. Again, for all equivalence ratios, the dual-pulse plasma kernel exhibits a distinct preionization channel and energy addition kernel over the first few microseconds. For equivalence ratios in the range ϕ=1.0-0.5, the dual-pulse plasma kernel propagates with this characteristic cross shape all the way through the ignition process. Though this occurs for all equivalence ratios in this range, it is most visible for the ϕ=0.9 case. Below ϕ=0.5, the third lobe is formed, as a net central fluid flow is developed in the center of the toroid, forcing the third lobe in the direction of laser incidence. Around ϕ=0.2, we see segmenting and separation in the kernels, and near the limit we see localized pockets of ignition similar to those seen for single pulse ignition.

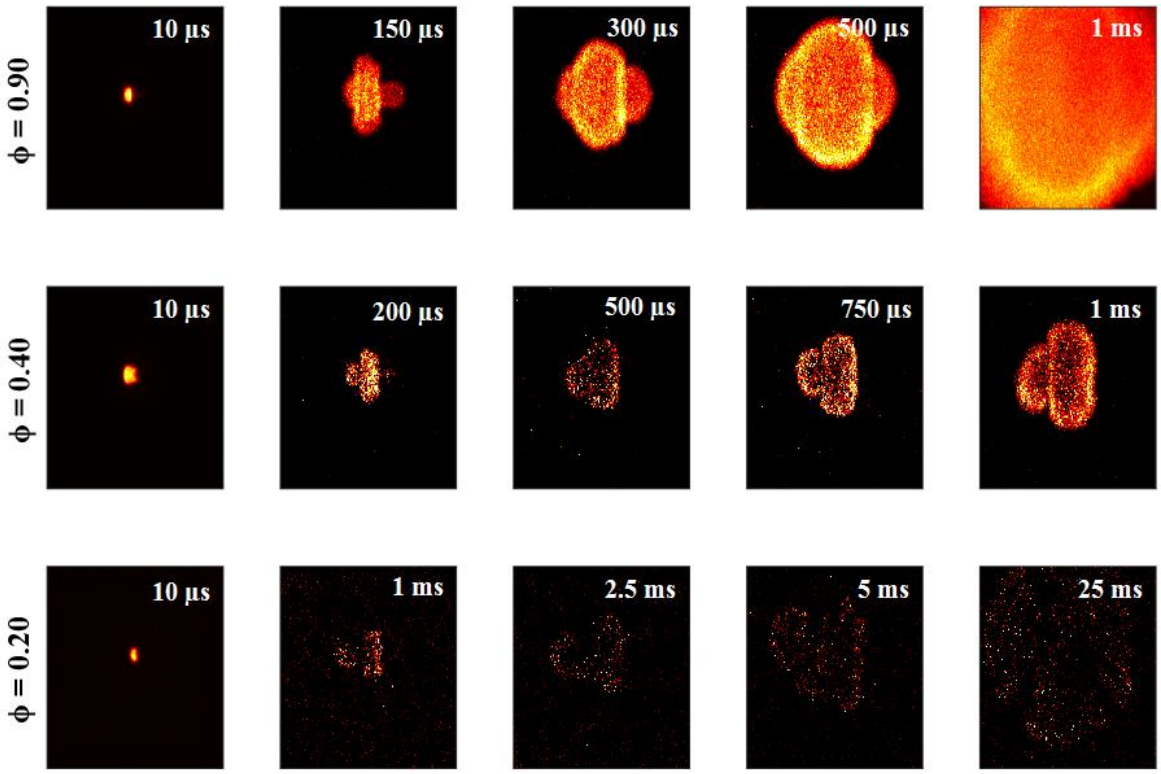

Figure 7: Flame propagation for the dual-pulse plasma in hydrogen-air mixtures at a variety of equivalence ratios. Indicated times are relative to laser energy deposition inside the chamber. Images have physical dimensions of 28 mm x 22 mm in the horizontal and vertical directions, respectively. Note the unique cross shaped kernel for the stoichiometric case.

C. Investigation of Axial Offset in Dual-Pulse Ignition

Previous work in our group has demonstrated that dual-pulse plasma kernel dynamics in propane-air mixtures are a strong function of the energy deposition profile, i.e. the focusing conditions and axial overlap of the two pulses.[6] The previous section demonstrated that third lobe formation can be inhibited near stoichiometric conditions for both methane-air and hydrogen-air mixtures. In order to better characterize this effect and the impacts of deviation from perfect overlap, a test space consisting of a series of axial offsets (Δz = -5.0, -2.0, -0.5, 0.0, +0.5, +2.0, +5.0 mm) and equivalence ratios (ϕ=0.50, 0.60, 0.80, 1.00) was developed. Example axial offsets are shown in Fig. 8 where a negative axial offset corresponds to the energy addition pulse (NIR) focusing upstream of the preionization pulse (UV) and vice versa. In practice, this is done by fixing the location of the UV beam, while moving the focus of the NIR beam via a translation stage on which the lens is mounted.[9]

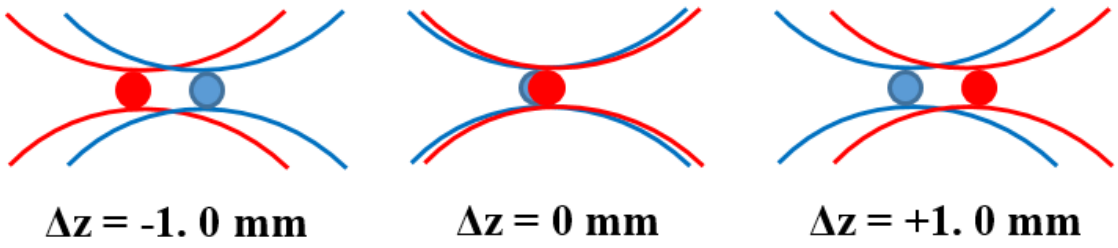

Figure 8: Example axial offsets where the red trace represents the focusing of the energy addition (NIR) beam, and the blue trace represents the focusing conditions of the preionization (UV) beam. The zero offset case is slightly shifted for visualization.

For each combination of axial offset and equivalence ratio, at least three combustion events were attempted, though for the zero offset case at least ten combustion events were averaged as described in Section A. The absolute limit to ignition was also determined as the minimum equivalence ratio for which at least one of the ignition attempts resulted in combustion of the fuel mixture. Experiments were performed in methane-air mixtures. Fig. 9 shows the effects of offset variability on kernel shapes, where each image is taken at a time of t=1 ms after laser energy deposition using an exposure value of Δt=500 µs. In these images, the laser beam enters from the left. Neither beam has sufficient energy to generate full breakdown (and ignition) independently, and therefore each flame kernel can be considered a dual-pulse flame kernel. Note that the lean scenario (shown in the top row of Fig. 9) varied with the offset in order to be able to obtain a successful ignition event. Within $\Delta z = \pm 0.5$ mm, this lean scenario corresponded to an equivalence ratio of ϕ=0.50, but outside this offset, the lean scenario corresponded to ϕ=0.525.

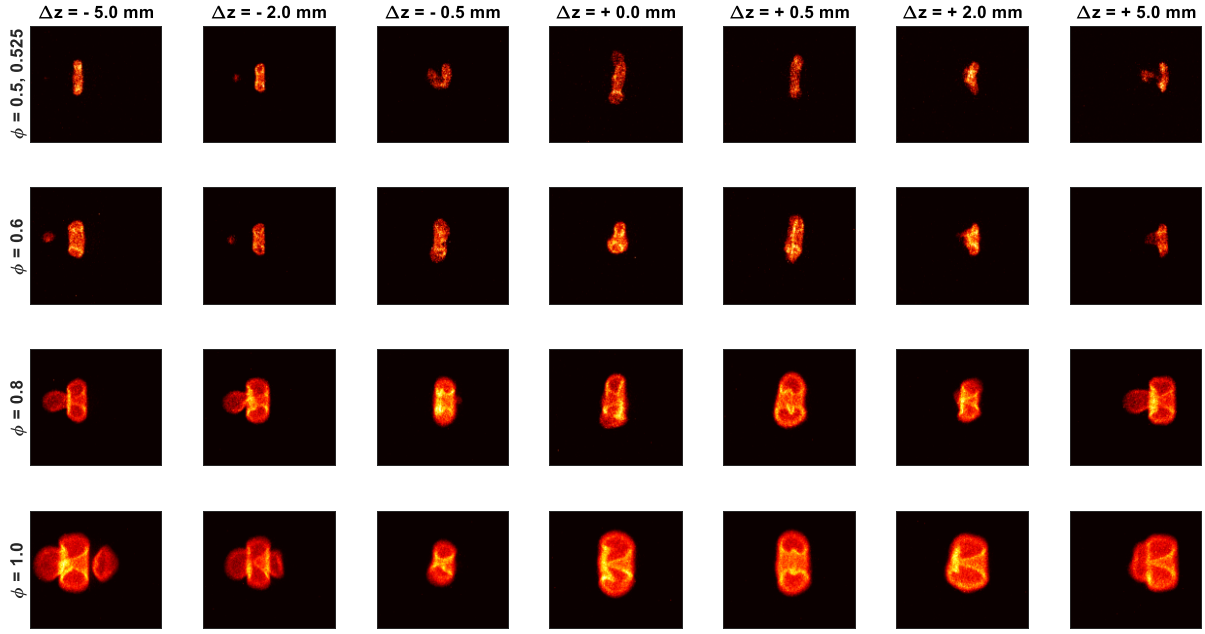

Figure 9: Flame kernel shapes from the dual-pulse plasma in methane-air mixtures at a variety of equivalence ratios and offset conditions. Each image is taken at a time of t=1 ms using an exposure of Δt=500 µs. Images have physical dimensions of 28 mm x 22 mm in the horizontal and vertical directions, respectively.

The cases for which the energy addition pulse is focused upstream of the preionization pulse tend to exhibit higher longitudinal flame speeds for the third lobe, resulting in much more common third lobe detachment than equal axial offsets that focus downstream of the preionization pulse. We hypothesize to this be to be due to the free electron densities along the longitudinal axis, and the corresponding MPI/EAI electron production proportions for each beam.[12] For the upstream case (negative axial offsets), the energy addition beam has not passed through an electron dense region when it reaches its focal point. Though some of the pulse energy gets absorbed by free electrons downstream of the focal point, the proportion of energy that reaches these free electrons is smaller, and the plasma tends to develop as if it were a single pulse plasma, where the energy addition pulse becomes responsible for both MPI and EAI. An interesting phenomenon is observed for the negative axial offset at the stoichiometric condition, where a "fourth lobe" is developed near the location of preionization focus. This suggests that in these conditions, sufficient energy deposition occurs downstream of the focal point in the preionization channel to develop another lobe. Much like the third lobe, this lobe is susceptible to separation from the main toroid, as is seen in the extreme offset case of Δz=-5.0 mm.

The cases where the energy addition pulse is downstream of the preionization pulse tend to have less flame stretching of the third lobe, and separation occurs less frequently. We hypothesize this to be due to better inverse bremsstrahlung absorption of the energy addition pulse, which in this case has to completely pass through the preionization channel before it reaches its focal point. This results in better absorption of the energy addition pulse, as it is responsible for a much smaller proportion of MPI and contributes mainly to EAI, developing kernel shapes that better suppress the third lobe. We also see in Fig. 9 that the overlap precision is difficult to discern by simply looking

at kernel shapes. As mentioned before, for the zero offset case, we see that the flame growth is unpredictable, sometimes occurring upstream and sometimes occurring downstream (seen in the first row of Fig. 6 and described in Section B). We see that within the range of $\Delta z \leq 0.5$ mm, this trend continues. Somewhere between 0.5 mm and 2 mm, this variability breaks down and the three lobe structure grows towards the laser for every ignition test.

In conjunction with imaging, pressure histories were collected so that efficiencies could be calculated. For each condition, three combustion events were attempted, and successful events were averaged. The resulting ignition efficiencies as a function of offset and equivalence ratio are shown in Fig. 10 (left). The zero offset case has increased ignition efficiency for nearly all equivalence ratios, though no observable trend exists for the other offsets at equivalence ratios far from the lean limit. Near the lean limit, the closer the axial offset to the zero offset case, the further the absolute ignition limit was extended. For the zero offset case, the absolute ignition limit was ϕ=0.48. For an axial offset of Δz=0.5 mm in either direction, the absolute ignition limit was found to be ϕ=0.50. Once the axial offset reached Δz=2.0 mm, the absolute ignition limit was ϕ=0.53. This matches the lean limit of single pulse ignition. Therefore, we conclude that in order to benefit from dual-pulse ignition lean limit extension, the axial offset between waists must be less than 2 mm, though the range of acceptable offsets is likely much smaller and further investigation is warranted.

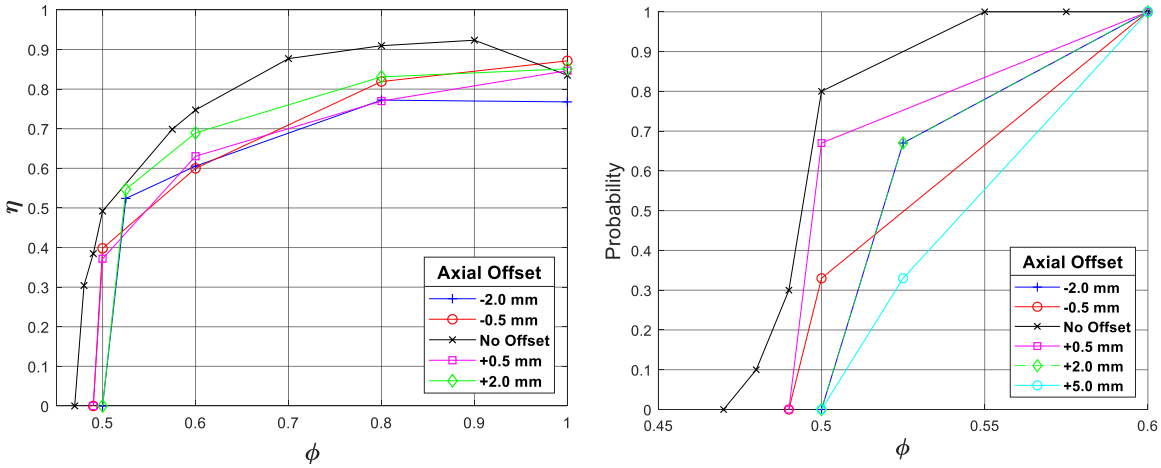

Figure 10: Combustion efficiency (left) and ignition probability (right) for a variety of axial offsets and equivalence ratios. Each point represents the average of at least three ignition attempts. Note the decreasing efficiency with increasing offset distance. Also note how increasing axial offset results in decreasing probability of ignition and how the -0.5 mm case has higher probability of ignition that the +0.5 mm case, attributed to better suppression of the third lobe seen in the OH* chemiluminescence images.

It is also informative to look at the probabilities of ignition as a function of offset. The measured probabilities of ignition are shown in Fig. 10 (right). The limited resolution step size in equivalence ratio inhibits our ability to draw thorough conclusions though we do note some important trends. We see that the probability of ignition increases with better overlap precision. Additionally, we notice an increase in probability for the downstream focusing condition when compared with the upstream condition at Δz=0.5 mm. We attribute this to the better suppression of third lobe as commented upon in the OH* chemiluminescence section of the offset investigation. Recall that this third lobe is known to transport heat and intermediate species away from the kernel, so suppression of it results in more stable combustion, therefore increasing the probability of ignition.

IV. Conclusions

We have demonstrated combustion characteristics of single pulse NIR and dual-pulse plasmas for both methane-air and hydrogen-air mixtures. We report higher efficiencies (particularly in methane-air mixtures) and slightly extended lean limits for dual-pulse plasmas when compared with single pulse plasmas. The lean limits for single pulse NIR plasmas are determined to be ϕ=0.12 for hydrogen and ϕ=0.53 for methane. Corresponding values for the dual-pulse plasma are ϕ=0.11 for hydrogen and ϕ=0.50 for methane, which matches the values reported for resonant dual-pulse plasma in previous work.[13] OH* chemiluminescence for single pulse NIR plasmas in methane-air mixtures

showed similar three lobe structures to those well established for propane-air mixtures, while hydrogen-air mixtures tended to have much more rapid radial growth when compared with longitudinal growth of the third lobe. For the dual-pulse plasma, the preionization channel was clearly seen, and had sufficient energy to dictate kernel shape for near stoichiometric conditions in hydrogen-air mixtures. Suppression of the third lobe occured in both mixtures near stoichiometric conditions, but the third lobe could be observed at extended delays for the leaner cases. Hydrogen-air mixtures ignited much more rapidly for both plasmas when compared with methane-air mixtures. An investigation into the axial offset between waists for the dual-pulse plasmas showed that it is preferable to focus the energy addition beam further downstream from the preionization pulse rather than upstream, if perfect overlap (Δz=0.0 mm) cannot be achieved. For downstream focusing, third lobe suppression is stronger and ignition probability is increased. For upstream focusing, the energy addition pulse acts more like a single pulse plasma, responsible for both MPI and EAI and forming a three lobe structure more frequently. At near stoichiometric conditions, upstream focusing can result in a four lobe structure with the fourth lobe centered near the preionization channel. This fourth lobe typically detaches from the main toroid much like the third lobe. We find that zero axial offset (Δz=0.0 mm) results in the most efficient and most probable ignition with the lowest lean limit. The benefit of lean limit extension completely ceases by an offset of 2 mm, while kernel flame propagation directions are highly variable in the region of ±0.5 mm.

V. References

1. Herdin, G., Klausner, J., Weinrotter, M., Graf, J., and Wimmer, A., "GE Jenbacher's Update on Laser Ignited Engines," ICEF-ASME 2006.

2. Bradley, D., Sheppard, C. G. W., Suardjaja, I. M., and Woolley, R., "Fundamentals of high-energy spark ignition with lasers," Combustion and Flame, vol. 138, Jul. 2004, pp. 55–77.

3. Dumitrache, C., Baumgardner, M., Boissiere, A., Maria, A., Roucis, J., Marchese, A. J., and Yalin, A., "A study of laser induced ignition of methane – air mixtures inside a Rapid Compression Machine," Proceedings of the Combustion Institute, vol. 36, 2017, pp. 3431–3439.

4. Kopecek, H., Maier, H., Reider, G., Winter, F., and Wintner, E., "Laser ignition of methane–air mixtures at high pressures," Experimental Thermal and Fluid Science, vol. 27, Apr. 2003, pp. 499–503.

5. Herdin, G., and Klausner, J., "Laser Ignition: A New Concept to Use and Increase the Potentials of Gas Engines," ICEF- ASME 2005.

6. Dumitrache, C., Vanosdol, R., Limbach, C. M., Azer, &, and Yalin, P., "Control of Early Flame Kernel Growth by Multi-Wavelength Laser Pulses for Enhanced Ignition," Scientific Reports, 2017.

7. Dumitrescu, C., Puzinauskas, P. and Yalin, A., "Fiber-Optic Spark Delivery for Gas-Phase Laser-Induced Breakdown Spectroscopy." Applied Spectroscopy 61, 2007, pp 1338-1343.

8. Yalin, A., Defoort, M., Wilson, B., and Galvanauskas, A., "Fiber Optic Delivery of Nanosecond Laser Pulses for Spark Formation in Gases." Laser Applications to Chemical, Security and Environmental Analysis, 2006, pp 1338-1343.

9. Tropina, A., Shneider, M., and Miles, R., "Modeling of Dual-Pulse Laser Ignition." 2017 AIAA Aerospace Sciences Meeting, AIAA SciTech Forum, 2017.

10. Tropina, A., Mahamud, R., Shneider, M., and Miles, R., "Mathematical Modeling of Dual-Pulse Laser Ignition in a Turbulent Flow." 2017 AIAA Aerospace Sciences Meeting, AIAA SciTech Forum, 2017.

11. Dumitrache, C., VanOsdol, R., Limbach, C., and Yalin, A., “Laser Ignition of Propane-Air Mixtures Using a Dual-Pulse Technique,” 55th AIAA Aerospace Sciences Meeting, AIAA Scitech Forum, (AIAA 2017-1976).

12. Dumitrache, C., Limbach, C., and Yalin, A., “Threshold Characteristics of Ultraviolet and Near Infrared Nanosecond Laser Induced Plasmas,” AIP Physics of Plasmas, 2018.

13. Butte C., Dumitrache C., and Yalin A., “Dual-Pulse Laser Ignition Using Oxygen REMPI Preionization,” 2019 AIAA Aerospace Sciences Meeting, AIAA Aviation Forum, 2019.

14. Butte C., Dumitrache C., and Yalin A., “Properties of Dual-Pulse Laser Plasmas and Ignition Characteristics in Propane-Air and Methane-Air Mixtures,” 2019 AIAA Aerospace Sciences Meeting, AIAA SciTech Forum, 2019.

15. Ballester, J., Hernandez, R., Sanz, A., Smolarz,A., Barroso, J., and Pina, A., “Chemiluminescence monitoring in premixed flames of natural gas and its blends with hydrogen.” Proc. Combust. Inst. 32, 2009, pp. 2983–2991.

16. He, L., Guo, Q., Gong, Y., Wang, F., and Yu G., “Investigation of OH* chemiluminescence and heat release in laminar methane—oxygen co-flow diffusion flames.” Combustion and Flame 201, 2019, pp. 12-22.

17. Kathrotia, T., Dreier, T., Riedel, U., and Shulz, C., “Strain rate and fuel composition dependence of chemiluminescent species profiles in non-premixed counterflow flames: comparison with model results.” Applied Physics B 107, 2012, pp. 561-569.

18. Morsy, M. H., and Chung, S. H., “Numerical simulation of front lobe formation in laser-induced spark ignition of CH_4/Air Mixtures.” Proc. Combust. Inst. 29, 2002, pp. 1613–1619.

19. Endo, T. et al., “An Experimental Study on the Ignition Ability of a Laser-Induced Gaseous Breakdown.” Combust. Flame 178, 2017.

20. Bradley, D., Sheppard, C., Suardjaja, I. M., and Woolley, R., “Fundamentals of High-Energy Spark Ignition with Lasers.” Combust. Flame 138, 2004, pp. 55–77.

21. Kojima, H., Takahashi, E. and Furutani, H., “Breakdown Plasma and Vortex Flow Control for Laser Ignition using a Combination of Nano- and Femto-second Lasers.” Opt. Express 22, 2014.

22. Beduneau, J., Bonggyu, K., Zimmer, L., and Ikeda, Y., “Measurements of Minimum Ignition Energy in Premixed Laminar Methane/Air Flow by using Laser Induced Sparks.” Combust. Flame 132, 2003, pp. 653–665.

23. Wermer, L., Hansson, J. and Im, S., “Dual-pulse Laser-Induced Spark Ignition and Flame Propagation of a Methane Diffusion Jet Flame.” Proc. Combust. Inst. 36, 2017, pp 4427–4434.

24. Dumitrache C., and Yalin A., “Numerical Modeling of the Hydrodynamics Induced by Dual-Pulse Plasma,” 2018 AIAA Aerospace Sciences Meeting, AIAA SciTech Forum, 2018.

25. Glassman, I., Yetter, R., and Glumac, N. *Combustion.* 2014.

AIAA SciTech Forum
11–15 & 19–21 January 2021, VIRTUAL EVENT
AIAA Scitech 2021 Forum

10.2514/6.2021-1788

Effects of the Laser Intensity Profile on Ignition of Hydrogen-Air Mixture

Sagar Pokharel[1] and Albina A. Tropina [2]
Department of Aerospace Engineering, Texas A&M University, College Station, TX 77840

Mikhail N. Shneider[3]
Department of Aerospace and Mechanical Engineering, Princeton University, Princeton, NJ 08544

We consider ignition of the lean-hydrogen-air mixture using a combination of ultraviolet and near-infrared laser pulses. A two-dimensional three-temperature plasma model coupled with Navier-Stokes equations was used for the numerical simulations. The dependence of the ignition kernel dynamics on laser defocusing is reported. The results showed that an offset in peak of gas temperature and radical species caused by defocusing effect affects the hot ignition spot location.

I. Introduction

In recent years plasma technology is studied extensively because of its potential to enhance combustion, reduce emissions and provide efficient ignition strategies, all of which are crucial for increased engine performance requirements [1]. For supersonic combustion such as in scramjet engines, studies using different variants of plasma have showed that it can enhance ignition, flame stabilization, and fuel/air mixing via chemical, thermal, and plasma induced aerodynamic effects [2]. Numerical modeling of non-equilibrium plasma [3] has shown that detonation engines can also benefit from its use by shortening the deflagration to detonation transition time and length.

Non-equilibrium plasma interacts with the fluid on different aspects, mainly chemical kinetics, transport properties, and thermal energy. So, laser induced plasma ignition systems can be used for wide range of ignition applications. Electrodes are absent in laser induced plasma ignition systems which eliminates the flame quenching effect and enhances the kernel growth [4]. Further advantages are, very high flexibility of the ignition location within the combustion chamber, and extension of flammability limits. But difficulties including high cost of a laser ignition system and accurate experimental measurement of important properties underline the importance of mathematical modeling and a deeper understanding of the coupling between plasma physics, combustion kinetics and hydrodynamics. Only with better understanding and control of the laser energy deposition, mature and more diverse applications of the technology is warranted.

Laser ignition mechanisms [5] strictly depend on the laser wavelength, repetition rate, the amount of energy deposited and laser focusing. At laser wavelengths, λ, below $250\ nm$, ignition can occur through photochemical mechanism without a significant gas ionization, when a chain initiation stage is replaced by the phodissociation of molecules, mainly molecular oxygen by a single photon-excitation. Other ignition mechanisms include thermal ionization, non-resonant, and resonant laser spark ignition. Laser breakdown mechanisms in different media are extensively studied in optics, leading to the development of high-sensitivity laser–induced breakdown spectroscopy (LIBS) [6]. One issue that inhibits the application of laser ignition is the minimum ignition energy, which is greater

[1] Graduate Student, Aerospace Engineering, AIAA Student Member
[2] Research Professor, Aerospace Engineering, AIAA Associate Fellow
[3] Senior Research Scholar, Mechanical and Aerospace Engineering, AIAA Associate Fellow

than the minimum ignition energy for conventional sparks [7,8]. The greater values of the minimum ignition energy for a single laser pulse ignition relate to the additional energy required for the laser optical breakdown to create initial seed electrons at the beam focus. Also, a significant amount of the deposited energy in that case is consumed by a propagating blast wave. A new concept of the laser energy deposition which uses two laser pulses to decouple the process of the initial ionization and energy addition is advantageous in this aspect. As such, this method can be used to control the electron temperature, electron number-density, size of the ignition kernel and post hydrodynamic behavior of the energy deposition kernel [4,9,10].

We consider here a dual-pulse laser energy addition using combination of the ultraviolet (UV) and near infrared (NIR) laser pulses. The first step is to create a preliminary ionization region using the ultra-violet laser pulse with a small amount of energy below breakdown by multiphoton and avalanche ionization mechanisms. The second step is a subsequent energy addition through joule heating using the near infrared laser pulse [11]. The dual-pulse laser scheme with combination of UV, $\lambda = 266$ nm, and NIR, $\lambda = 1064$ nm, laser pulses demonstrated an increase of combustion efficiency, flame speed enhancement and successful ignition of the lean fuel-air mixture below the flammability limits [12]. Furthermore, energy consumption and energy losses associated with the shockwave propagation are significantly lower for two successive laser pulses with a time interval compared with a single pulse with the same total incident energy.

During dual pulse operation when plasma is already present in the focal area, the remainder of the laser pulse is partially reflected causing different spatial distribution of laser intensity profile compared with the Gaussian profile. Gradient of density and pressure plays an important role in post hydrodynamics of the plasma kernel which in turn is dictated by the spatio-temporal shape of the laser intensity profile of the pulses [13]. The effect of non-uniform energy deposition can lead to the generation of large–scale coherent vortices and transition to turbulence [14]. So, the spatio-temporal modulation of the laser intensity is a major parameter in tailoring the dual-pulse laser concept to specific application needs. Recent developments in optical devices have substantially enhanced the capability to shape the laser pulses in both the temporal and spatial domains. But most of the numerical modeling for non-equilibrium plasma is done for the Gaussian beam in both spatial and temporal domain [15]. Goal of this work is to extend the study on effects of laser intensity shaping. One and two-dimensional mathematical model of dual-pulse laser ignition using a three-temperature plasma approach [10] was developed in [9,16] to understand a role of plasma driven gas dynamics, chemical kinetics and laser physics in controllable ignition and combustion of methane-air mixtures. Previous study of hydrogen-air ignition [17] with dual pulse concluded that with temporal shaping of the laser intensity, ignition of the mixture occurs at significantly low initial electron number density compared with the standard Gaussian profile. Current work further extends this study with inherent defocusing present in laser intensity profiles and mainly looks at corresponding effects on the ignition delay, flame kernel shape and hydrodynamics of the resulting flame kernel in hydrogen-air mixture.

II. Results and discussion

The multiscale and multi-physics process of the laser energy deposition comprises particle-wave interaction, chemical reactions, and fluid dynamics effect with time scales ranging from nanoseconds (plasma formation and decay) to microseconds (fluid dynamics). To include the non-equilibrium behavior of the formed laser plasma a three-temperature (3T) plasma model was used. The mathematical model combines two-dimensional Navier-Stokes equations with the three-temperature plasma model, which includes additional equations for the translational gas temperature, electron temperature, vibrational energy of nitrogen molecules and balance equations for twelve species of the hydrogen-air mixture, $H_2, O_2, N_2, H, O, OH, HO_2, H_2O, H_2O_2, O_2^+, N_2^+, e$. The model was briefly discussed and validated in our previous papers [9,16] and it is not shown here.

We consider the lean hydrogen-air mixture, $\Phi = 0.7$, ignition by two laser pulses with pulse width of 10 ns and $13\ ns$ for first and second pulse respectively. The temporal offset between the peak of the two pulses was also 10 ns. The maximum electron number density was $5 * 10^{23} \mathrm{m}^{-3}$ while the maximum laser intensity was $3.5 * 10^{14} \mathrm{W/m}^2$ The pre-ionizing pulse had wavelength of $\lambda = 266\ nm$ and the theoretical beam waist of $\omega_0 = 22.062\ \mu m$. Similarly, for the second pulse, $\lambda = 1064\ nm$ and $\omega_0 = 22.015\ \mu m$. The initial size of the ionization spot was $\Delta x = 6.65$ mm and $\Delta y = 1.60$ mm in x and y respectively. A laser beam with initial Gaussian radial profile would produce a maximum plasma density at the axis causing the laser beam to defocus due to the minimum refractive index on the axis [18]. To account for plasma defocusing effect we have included an additional part for evaluation of temporal changes of the laser intensity. Those temporal effects of laser-plasma interactions are captured by discretizing the laser pulses and using a beam propagation method to trace each pulse segment through the numerical domain (outside

of the hydrogen-air ignition solver). During the dual pulse operation when plasma is already present in the focal area, the remainder of the laser pulse is partially reflected causing different spatial distribution of laser intensity profile as shown in Fig.1. Here defocusing effect is seen at 25 ns when the second pulse had just passed its peak intensity point in time. The case without defocusing was formulated with the same profiles of intensity as with defocusing but the profiles with elongated tails due to defocusing were replaced by the profiles before the tails appear and the magnitude was scaled to make both the cases have same peak values at the same time period of the pulse. This means that the electron number density profiles were also different between these cases. The electron mole fraction is shown in Fig.2 for the case with and without defocusing. Clearly, with defocusing effect the electron number density profile has resulted into a formation of the tear drop shape. Finally, this result was coupled with the developed solver by feeding different profiles of intensity and electron number density during the pulse period.

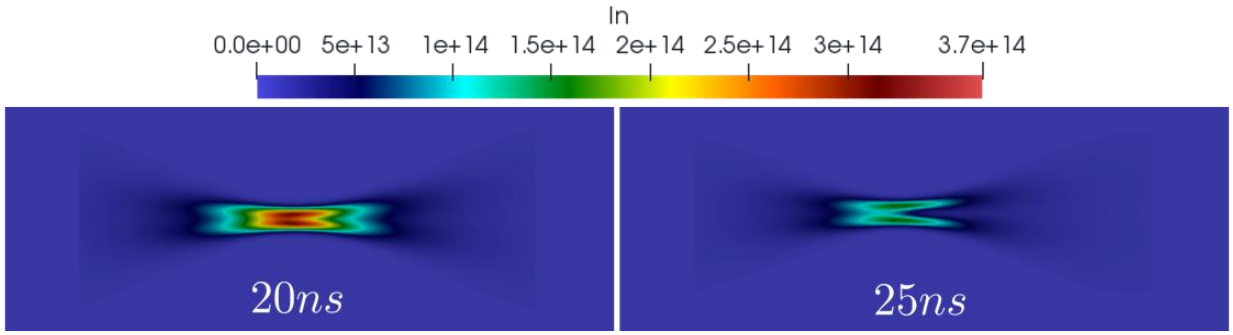

Fig 1: Defocusing effect as seen in the intensity profiles.

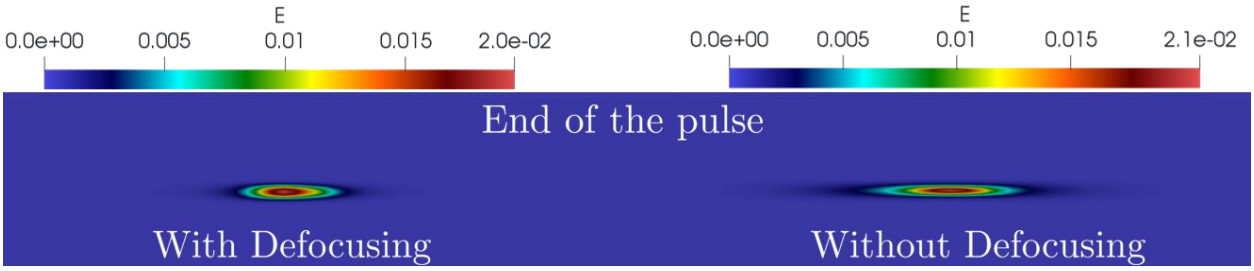

Fig 2: Electron mole fraction at the end of the second pulse.

The intensity field and electron number density peaks do not match spatially with defocusing case. While not considering defocusing the peaks match and thus for the same magnitude of the initial electron number density and intensity profile, the joule heating term which has strong dependence on those two parameters, becomes high. This affects the electron and gas temperature balance.

The temporal behavior of the electron temperature has also changed depending on the fuel. Compared with the case of the methane-air mixture in the hydrogen-air mixture we observed the increase of the electron energy loss in the processes of the momentum transfer in electron-neutral collisions ν_m and in electron-ion Coulomb collisions ν_c. Fig.3 shows the collision frequency, $\nu_s = \nu_m + \nu_c$, for the lean methane-air and hydrogen air-mixtures at the equivalence ratio $\Phi = 0.7$. The rate of heating due to the energy exchange between electrons and heavy particles is $Q_{ET} = \frac{3}{2}\delta_e(\nu_m + \nu_c)k_B(T_e - T)$ and it is proportional to ν_s. At other conditions being equal an increase of the frequency of the momentum transfer in electron-neutral collisions and in electron-ion Coulomb collisions results in the higher rate of heating in the hydrogen-air mixture, which leads to the faster local ignition at the point with the maximum electron number density.

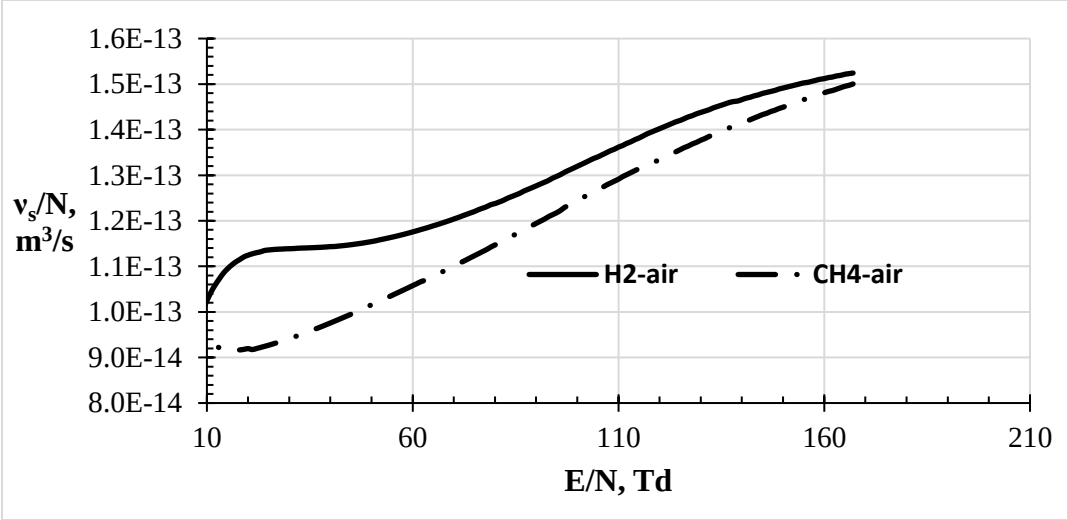

Fig 3: Collision frequency as a function of the reduced electric field.

Fig. 4 shows the energy deposition kernel for hydrogen gas with minor impurities as O_2, N_2 at 7.2e-5 s. When the energy deposition from of the second laser pulse is sufficiently offset from the first laser pulse, formation of the three-lobed energy deposition kernel after the blast wave for air is reported in [19]. Taking into account the defocusing effect, although the energy deposition peak is offset, the offset was not sufficient for the third lobe formation. So, a two-toroid kernel, like in the case of the Gaussian shaped laser intensity without defocusing is seen for both cases.

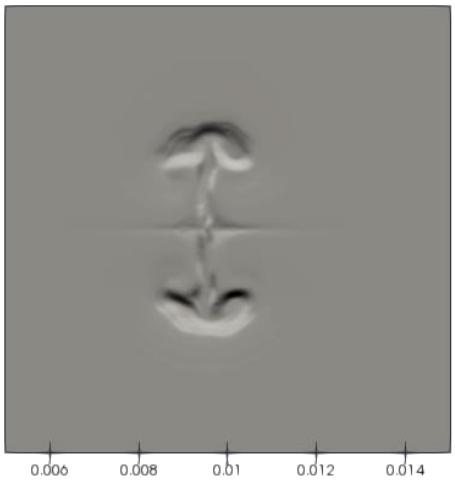

Fig 4: Numerical Schlieren for the dual pulse energy deposition at 7.2e-5 s

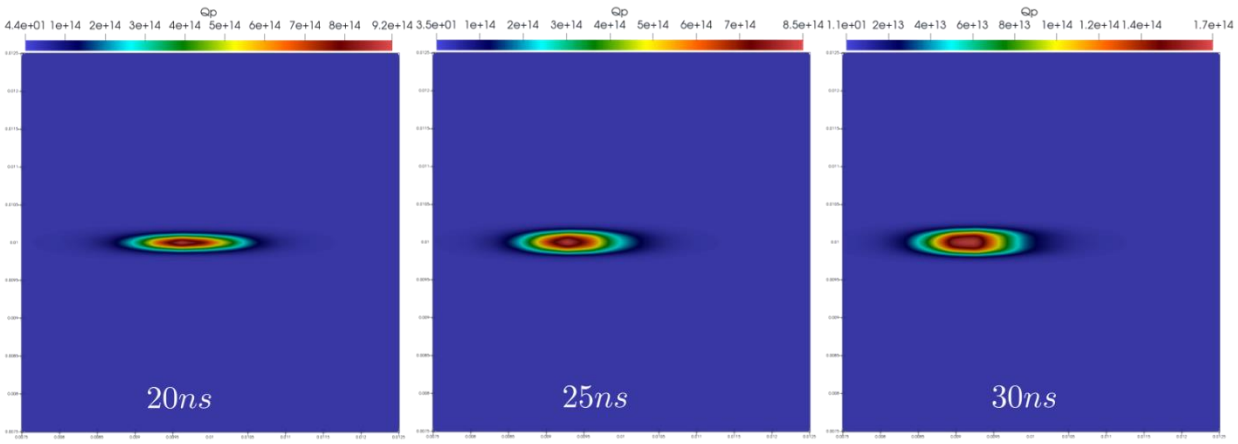

Fig 5: Temporal Evolution of the Joule heating term during the pulse

Fig.5 shows the progression of joule heating in the mixture which relates to the increase in electron energy. Due to defocusing, the energy deposition broadens in the direction perpendicular to the laser pulse propagation. While the joule heating is symmetrical for the case without defocusing it is contrastingly different for the case with defocusing. Asymmetrical joule heating results in the elongated tear drop temperature profile at the end of the pulse as shown in Fig.6. Despite the fact that we have the same symmetrical Gaussian profile for ions as an initial condition, the oxygen atoms distribution after the second laser pulse shown in Fig. 6 also changes with defocusing. These changes were attributed to the changes in the electron number density and electron temperature distributions (Fig.7) which are significantly different in the two cases. It is worth noting that the kinetic model did not include pathways for the O_3, NO formation, which could move the effects of defocusing further ahead in time.

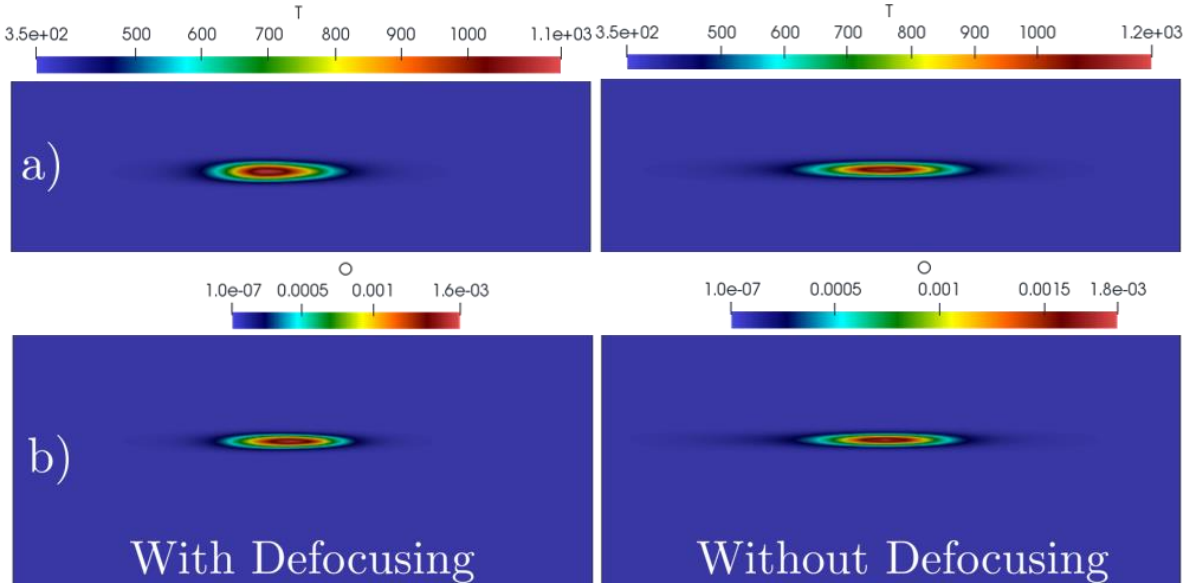

Fig 6: Temperature (a) and oxygen atom profiles (b) at the end of the second pulse.

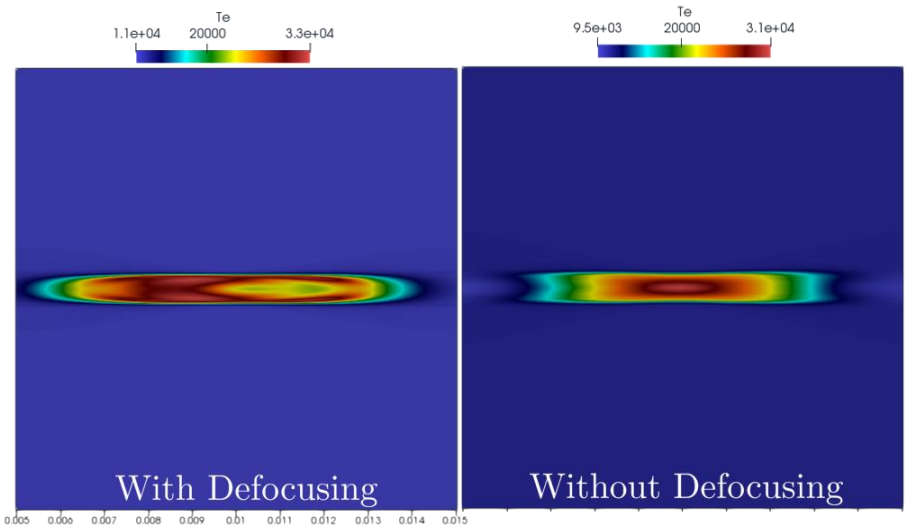

Fig 7: The Electron Temperature distribution at the end of the pulse

At the end of the pulse, defocusing causes offset between the peaks of the gas temperature and the O atoms concentration. Thus, the rate of decay of O atoms is not even in both the right and the left directions from the peak. It is seen in detail in Fig. 8, 9 which show axial profiles of radicals O, OH , and temperature at different moments for cases with no defocusing effect and for the case with defocusing, respectively. The decay of O is maximum where the temperature is highest initially and this leads to chain branching thereby producing other radicals like OH, H . But the case without defocusing (Fig.8) clearly shows that the peaks in O and temperature are coincident. Only when the gas temperature is sufficiently high, at the later time period, the concentration of O atoms increases again. Even at $t = 1.64e-6$ s the offset between peaks of O and temperature still exist for the case with defocusing of the laser intensity Fig.9. As a result, the initial ignition spot is shifted compared to the two cases. This can be observed in Fig.10, where the temperature and H_2O production are maximum at $x = 5$ mm for the case without defocusing and it is shifted left, closer to $x = 4$ mm when defocusing is considered. Here x is the axial coordinate along the center of the laser energy deposition such that $x = 5$ mm represents both radial and axial center of the plume.

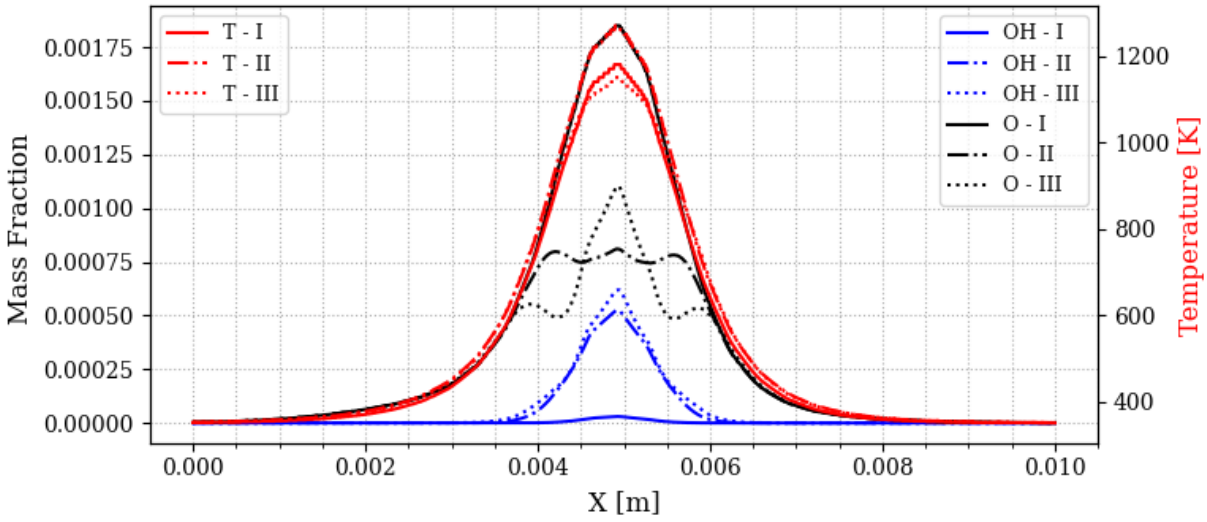

Fig 8: Temperature and mass fraction of species, no defocusing, I = 35e-9 s, II = 3.35e-7 s, III = 1.64e-6 s

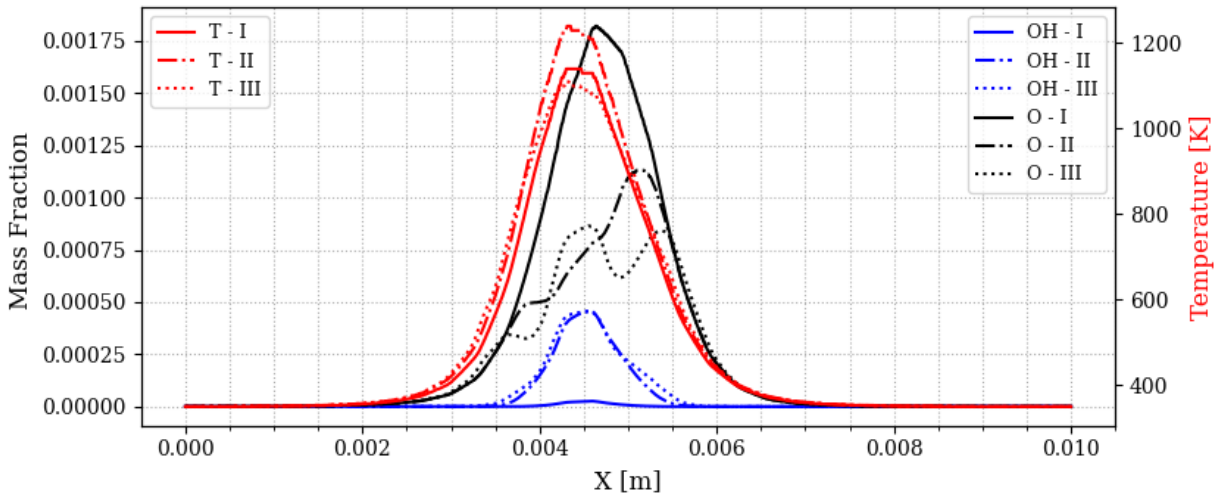

Fig 9: Temperature and mass fraction of species, with defocusing, I = 35e-9 s, II = 3.35e-7 s, III = 1.64e-6 s

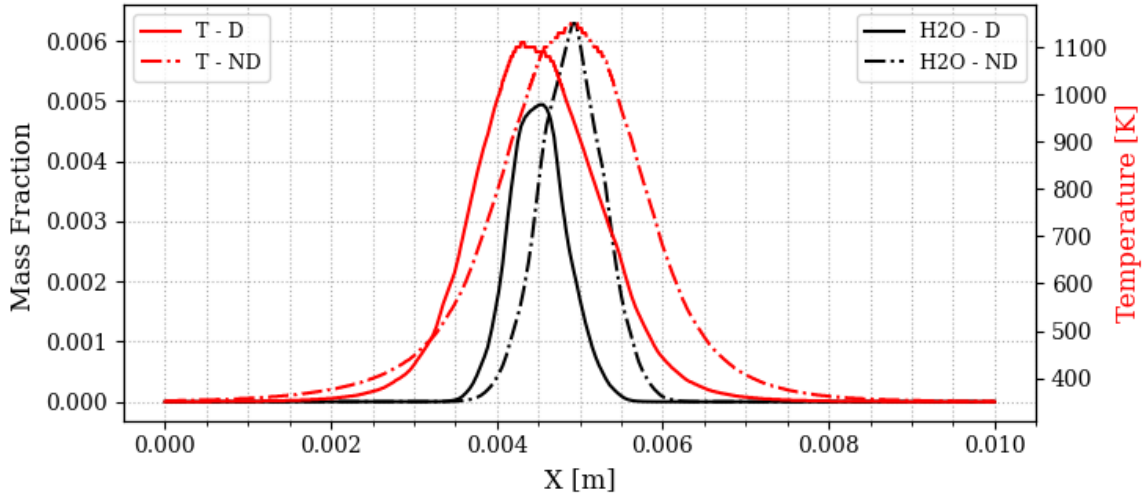

Fig. 10: Comparison of temperature and H2O for case with defocusing (D) and without defocusing (ND) at 1.64e-6 s.

Depending on the propagating direction of the second laser pulse, the offset in peaks of O and temperature profiles can flip. This suggests that the dual-pulse laser ignition system could be favorable for controllable ignition because the consumption of excited species changes with the variation of intensity profiles.

According to the simulation results the ignition delay time for the hydrogen-air mixture with $\Phi = 0.7$ was 65.7 μs. Addition of oxygen atoms at different proportions to the hydrogen-air mixture has shown similar values of the ignition delay time [2]. The relatively short ignition delay time compared to cases without plasma was attributed to the high initial electron number density $5 * 10^{23} m^{-3}$ and laser peak intensity $\sim 3.5 * 10^{14} W/m^2$ which results in the higher concentration of initial ionized species and high concentration of O atoms.

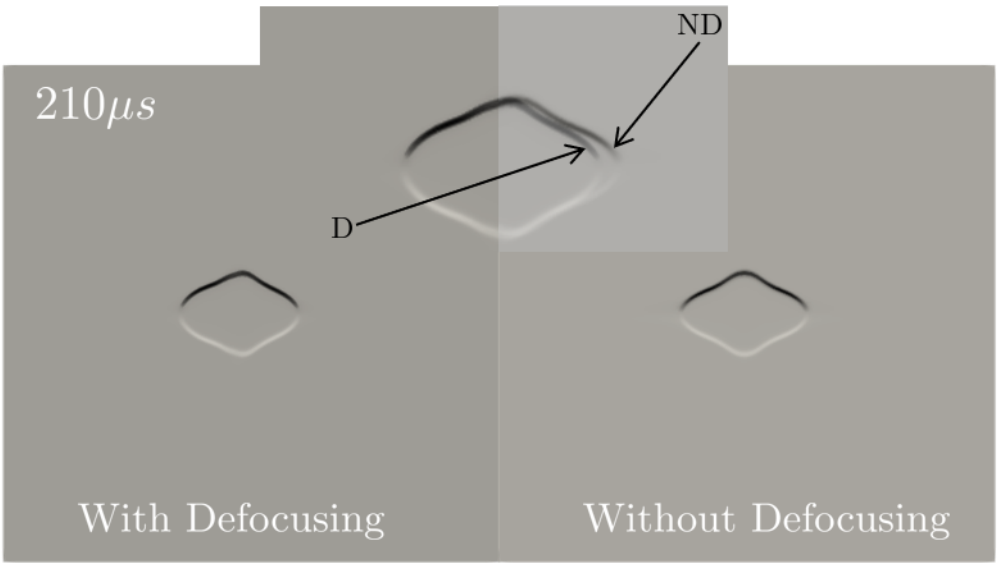

Fig 11: Comparison of Numerical Schlieren for case with (D) and without (ND) defocusing at 21.0e-5 s

Fig.11 shows the schlieren image for the hydrogen-air mixture with $\Phi = 0.7$ at 210 μs. Although the ignition kernel shapes look similar in both cases effect of defocusing slightly changes the oval shaped perfectly symmetrical ignition kernel to the asymmetrical oval shaped kernel. Before the velocity normal to the direction of the laser pulse propagation was established, ignition from the central hot spot propagated towards both directions in the x-axis. Thus, the oval shaped profile was observed rather than the two-toroid shape seen in Fig. 4. This result is in a good agreement with the experimental measurements of the OH chemiluminescence from [19] which showed similar shape of the ignition kernel in the lean hydrogen-air mixture with equivalence ratio $\Phi = 0.9$.

III. Conclusion

We considered dual pulse laser ignition of the lean hydrogen-air mixture. It was shown that the first pulse is beneficial for ionizing the mixture and generating excited species thus affecting the ignition kernel. Due to the variation of the intensity profiles, offset in peak of gas temperature and radical species occurs thereby affecting ignition due to both hydrodynamic and chemical kinetic effects. We suggested that a specific direction of the second laser pulse could be favored when there is a flow specified in one direction. This case warrants more study, for example, for the dual-pulse laser energy deposition for the initiation of detonation or for the deflagration to detonation transition because the velocity of the brunt gases is either larger than incoming or less the incoming reactants depending on the flame specification .

Acknowledgments

This work was supported by DOD-AFOSR award AWD1005727 and DOD-AFOSR award under Subcontract with Princeton University SUB0000242.

References

[1] Tropina, A. A., Shneider, M. N., and Miles, R. B. “Ignition by Short Duration, Nonequilibrium Plasma: Basic Concepts and Applications in Internal Combustion Engines.” *Combustion Science and Technology*, 2016. https://doi.org/10.1080/00102202.2015.1125347.

[2] Ju, Y., and Sun, W. Plasma Assisted Combustion: Dynamics and Chemistry. *Progress in Energy and Combustion Science*.
[3] Tropina, A., Mahamud, R., Yorn, D. W., and Miles, R. B. Deflagration to Detonation Transition Assisted by Equilibrium and Non-Equilibrium Plasma. 2019.
[4] Padhi, U. P., Singh, A. P., and Joarder, R. "Experimental and Numerical Investigations of Double Pulse Laser Energy Deposition in Air." *International Journal of Heat and Fluid Flow*, 2020. https://doi.org/10.1016/j.ijheatfluidflow.2020.108563.
[5] Ronney, P. D. "Laser versus Conventional Ignition of Flames." *Optical Engineering*, 1994. https://doi.org/10.1117/12.152237.
[6] Anabitarte, F., Cobo, A., and Lopez-Higuera, J. M. "Laser-Induced Breakdown Spectroscopy: Fundamentals, Applications, and Challenges." *ISRN Spectroscopy*, 2012. https://doi.org/10.5402/2012/285240.
[7] Brieschenk, S., O'Byrne, S., and Kleine, H. "Laser-Induced Plasma Ignition Studies in a Model Scramjet Engine." *Combustion and Flame*, 2013. https://doi.org/10.1016/j.combustflame.2012.08.011.
[8] Syage, J. A., Fournier, E. W., Rianda, R., and Cohen, R. B. "Dynamics of Flame Propagation Using Laser-Induced Spark Initiation: Ignition Energy Measurements." *Journal of Applied Physics*, 1988. https://doi.org/10.1063/1.341824.
[9] Tropina, A. A., Miles, R. B., and Shneider, M. N. "Mathematical Model of Dual-Pulse Laser Ignition." *Journal of Propulsion and Power*, 2017. https://doi.org/10.2514/1.b36687.
[10] Shneider, M. N., Zheltikov, A. M., and Miles, R. B. "Tailoring the Air Plasma with a Double Laser Pulse." *Physics of Plasmas*, Vol. 18, No. 6, 2011, p. 063509. https://doi.org/10.1063/1.3601764.
[11] Shneider, M. N., and Miles, R. B. "Laser Induced Avalanche Ionization in Gases or Gas Mixtures with Resonantly Enhanced Multiphoton Ionization or Femtosecond Laser Pulse Pre-Ionization." *Physics of Plasmas*, Vol. 19, No. 8, 2012, p. 083508. https://doi.org/10.1063/1.4747344.
[12] Dumitrache, C., VanOsdol, R., Limbach, C. M., and Yalin, A. Laser Ignition of Propane-Air Mixtures Using a Dual-Pulse Technique. 2017.
[13] Ghosh, S., and Mahesh, K. "Numerical Simulation of the Fluid Dynamic Effects of Laser Energy Deposition in Air." *Journal of Fluid Mechanics*, Vol. 605, 2008, pp. 329–354. https://doi.org/10.1017/S0022112008001468.
[14] Koroteeva, E., Znamenskaya, I., Orlov, D., and Sysoev, N. "Shock Wave Interaction with a Thermal Layer Produced by a Plasma Sheet Actuator." *Journal of Physics D: Applied Physics*, Vol. 50, No. 8, 2017, p. 085204. https://doi.org/10.1088/1361-6463/AA5874.
[15] Alberti, A., Munafò, A., Pantano, C., Freund, J. B., and Panesi, M. "Collinear Dual-Pulse Laser Optical Breakdown and Energy Deposition." *Journal of Physics D: Applied Physics*, Vol. 53, No. 20, 2020, p. 205202. https://doi.org/10.1088/1361-6463/AB7564.
[16] Mahamud, R., Tropina, A. A., Shneider, M. N., and Miles, R. B. "Dual-Pulse Laser Ignition Model." *Physics of Fluids*, 2018. https://doi.org/10.1063/1.5043295.
[17] Tropina, A., and Shneider, M. N. Modeling of Laser Ignition in Hydrogen-Air Mixture. 2020.
[18] Liu, C. S., and Tripathi, V. K. "Laser Frequency Upshift, Self-Defocusing, and Ring Formation in Tunnel Ionizing Gases and Plasmas." *Physics of Plasmas*, 2000. https://doi.org/10.1063/1.1313568.
[19] Dumitrache, C., and Yalin, A. P. "Gas Dynamics and Vorticity Generation in Laser-Induced Breakdown of Air." *Optics Express*, 2020. https://doi.org/10.1364/oe.385430.

Laser Physics Letters

Astro Ltd.

LETTER

Displacement of energy deposition during formation of nanosecond laser plasmas by self-defocusing

IOP Publishing | Astro Ltd Laser Physics Letters
Laser Phys. Lett. **18** (2021) 036001 (5pp) https://doi.org/10.1088/1612-202X/abd932

Letter

Displacement of energy deposition during formation of nanosecond laser plasmas by self-defocusing

Matthew R New-Tolley[1], Mikhail N Shneider[1] and Richard B Miles[1,2]

[1] Department of Mechanical and Aerospace Engineering, Princeton University, Princeton, NJ, 08540
[2] Department of Aerospace Engineering, Texas A&M University, College Station, TX 77843, United States of America

E-mail: m.newtolley@princeton.edu

Received 9 December 2020
Accepted for publication 24 December 2020
Published 28 January 2021

Abstract
The long-term hydrodynamics of laser generated plasma regions are dictated by the spatial distribution of the deposited laser energy. Using an integrated chemical-optical solver to track energy deposition from single and dual nanosecond laser pulses, we show that self-defocusing results in a biased growth of the plasma region towards the focusing lens. This displacement of energy deposition scales with the Rayleigh range and can be reduced by maximizing the beam divergence.

Keywords: self-defocusing, dual-pulse, nanosecond laser breakdown

(Some figures may appear in colour only in the online journal)

1. Introduction

Carefully tailored atmospheric laser plasmas can be harnessed for remote sensing [1], optical modulation [2], waveguiding [3], and lean ignition [4, 5]. The ability to control plasma parameters in two-pulse laser plasmas has been demonstrated in [6]. More recently, two-pulse laser plasmas have been used to suppress the formation of 'third lobe' structures (left lobe figure 1(a)) routinely observed following single pulse laser breakdown [7]. These structures arise from asymmetric deposition of laser energy about the beam waist [8, 9] which can be corrected in two pulse systems (figure 1(b)) by manually offsetting the beam waists of the first and second pulses [7]. Control of these large scale flow structures are critical for ignition applications where third lobe formation prevents proper ignition of lean fuel/air mixtures [7]. We use an integrated chemical-optical solver to characterize the displacement of peak energy deposition towards the focusing lens for a range of different focal conditions in single and dual pulse systems. The displacement of energy deposition by self-defocusing occurs at electron densities well below breakdown and, in systems with longer focal lengths, can prevent breakdown from occurring. Similarly, depending on the focal length of the system, self-defocusing will either perturb or dominate the Laser Assisted Breakdown wave (LABW) mechanism detailed by Raizer [10] and Phuoc [11].

2. Method

Axisymmetric laser beams are propagated through the numerical domain using the beam propagating method (BPM) with a Hankel transform as described in [12]. When perturbations in the refractive index throughout the domain are small, the scalar Helmholtz equation (1) can be solved to give the electric field E (full derivation given in [13] by Feit and Fleck):

$$\nabla_{\perp}^{2} E + \frac{\partial^{2} E}{\partial z^{2}} + \frac{\omega^{2}}{c^{2}} n^{2} E = 0, \tag{1}$$

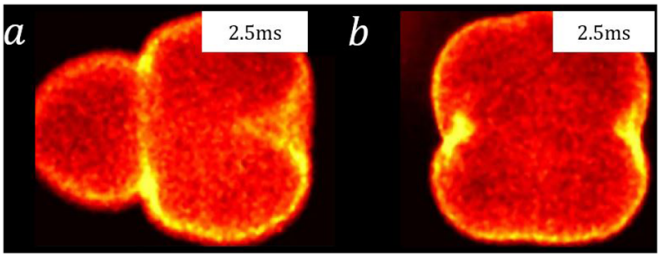

Figure 1. OH^* chemiluminescence images showing (a) the third lobe (left lobe) resulting from single pulse laser breakdown and (b) dual pulse suppression of the third lobe. Laser propagates from left to right. Adapted with permission from Springer Nature Customer Service Centre GmbH: Nature, Scientific Reports, [7] © (2017). CC BY 4.0.

here ω is the laser frequency, n is the refractive index and c is the speed of light. Once the electric field has been determined, the average laser intensity is calculated from:

$$I_L = \frac{cn\varepsilon_0}{2} |E|^2 \quad (\mathrm{W \cdot m^{-2}}), \tag{2}$$

where ε_0 is the vacuum permittivity. The local refractive index in equations (1) and (2) is updated each time-step from the local gas composition:

$$n \approx 1 + \frac{1}{2}\sum_i^2 \frac{n_i \alpha_i}{\varepsilon_0} - \frac{1}{2}\frac{\omega_p^2}{\omega^2 + \nu_m^2}, \tag{3}$$

where ν_m is the electron-neutral collision frequency, n_i is the number density of the ith species, α_i is the static molecular polarizability ($\alpha_{O_2} = 1.5812 \times 10^{-30}\, 4\pi\varepsilon_0\, (\mathrm{F \cdot m^2})$ and $\alpha_{N_2} = 1.7403 \times 10^{-30}\, 4\pi\varepsilon_0\ (\mathrm{F \cdot m^2})$), and ω_p is the local plasma frequency:

$$\omega_p = \sqrt{\frac{n_e e^2}{m_e \varepsilon_0}}\ (\mathrm{s^{-1}}), \tag{4}$$

where e and m_e are the charge and mass of an electron respectively and n_e is the electron density calculated using the plasma chemistry model outlined in the following section.

For the intensities investigated, the contribution of Kerr self-focusing to the refractive index were on the order of 10^{-10} and hence neglected.

2.1. Plasma chemistry

The electron density is calculated by discretizing (forward difference) [4, 6, 14]:

$$\frac{\partial n_e}{\partial t} = w_{mpi} n_i + \nu_{ai} n_e - \nu_d n_e - \nu_{rec} n_e - \nu_{att} n_e + B_g, \tag{5}$$

which accounts for electron production via multiphoton (mpi) and avalanche ionization (ai) as well as losses from diffusion (d), recombination (rec) and attachment (att). B_g is a background production term which is set so the rate goes to zero when the laser intensity is zero. The multiphoton ionization rate is given by:

$$w_{mpi} n_i = w_{O_2} n_{O_2} + w_{N_2} n_{N_2} \quad (\mathrm{m^{-3} \cdot s^{-1}}), \tag{6}$$

where w_i the probability of ionizing a molecule of the ith species. In SI units [8]

$$w_i = B\omega\eta^{\frac{3}{2}} \left(\frac{1}{4\varepsilon_0}\frac{\exp(1)e^2}{m_e\omega^2 cn}\frac{I_L}{I_i(J)}\right)^{\eta} (\mathrm{s^{-1}}), \tag{7}$$

where $B \approx 1$, η is the number of photons of frequency ω which must be simultaneously absorbed to generate free electrons, and I_i is the ionization energy of the ith species. Here, the gas is assumed to be a mixture of 80% nitrogen and 20% oxygen which have ionization energies of 15.6 and 12.2 eV respectively.

Avalanche ionization is modeled using:

$$\nu_{ai} \approx \frac{J_H}{n_e}\xi\left(\frac{0.2}{I_{O_2}} + \frac{0.8}{I_{N_2}}\right) (\mathrm{s^{-1}}), \tag{8}$$

where ξ is taken to be 0.75 and Joule heating (J_H) is [6]:

$$J_H = \frac{n_e e^2 \nu_m I_L}{c m_e \varepsilon_0 \left[\omega^2 + \nu_m{}^2\right]} (\mathrm{J \cdot s^{-1} \cdot m^{-3}}). \tag{9}$$

The electron-neutral collision frequency (ν_m) is given by $\nu_m = \gamma p\,(\mathrm{atm})\ (\mathrm{s^{-1}})$ at constant temperature [14]. The coefficient γ has been modified from 2.0×10^{12} $(\mathrm{s^{-1}})$ used in [14] to 2.7×10^{12} $(\mathrm{s^{-1}})$ to reflect data obtained from the plasma chemistry solver in Shneider *et al* [6]. In these simulations the pressure (in atm) is unity since fluid effects have been neglected. This is justified as significant energy deposition only occurs when the electron density nears the breakdown threshold (10^{21} $(\mathrm{m^{-3}})$). This naturally confines energy deposition to the latter parts of the IR pulses ensuring the timescale for energy deposition (10^{-9} (s)) remain negligible compared to the timescales of fluid motion (10^{-7} (s)).

The recombination rate is obtained from the two reactions:

$$N_2^+ + e \rightarrow N + N \text{ and } O_2^+ + e \rightarrow O + O \tag{10}$$

and give a combined recombination coefficient of:

$$\nu_{rec} = k_1 n_{N_2^+} + k_2 n_{O_2^+} (\mathrm{s^{-1}}), \tag{11}$$

where $k_1 = 3.18 \times 10^{-14}$ $(\mathrm{m^3 \cdot s^{-1}})$ and $k_2 = 22.27 \times 10^{-14}$ $(\mathrm{m^3 \cdot s^{-1}})$ [6]. For these simulations the electron temperature (T_e) was set to 2 eV as was assumed in [14] and in line with computational results in [6].

The diffusion rate is given by $\nu_d = \frac{D}{\Lambda^2}$ $(\mathrm{s^{-1}})$ where $\Lambda^2 = \frac{\omega_0^2}{2.4^2}$ [8]. When the electron density is low, diffusion is driven by free electrons. Once the plasma density increases positively charged ions slow the diffusion rate and the process transitions to ambipolar diffusion. This transition occurs when the Debye length becomes smaller than the beam waist:

$$\lambda_D = \sqrt{\frac{\varepsilon_0 k T_e}{n_e e^2}}\ (\mathrm{m}), \tag{12}$$

Table 1. Single pulse laser simulation parameters.

	$f_\# = 50$	$f_\# = 100$	$f_\# = 200$
R_R (mm)	2.84 ± 0.25	12.4 ± 1.09	51.8 ± 4.56
E_P (mJ)	49 ± 4	213 ± 19	889 ± 78

where k is the Boltzmann constant. The coefficient D has the form $D = \mu T_e(\text{eV})$. For free electron diffusion the electron mobility $\mu_e = 45p\,(\text{Torr})^{-1}$ $\left(\text{m}^2 \cdot \text{V}^{-1} \cdot \text{s}^{-1}\right)$ taken from [15] is approximated from experimental data which gives a free electron diffusion coefficient of $0.12\,(\text{m}^2 \cdot \text{s}^{-1})$. The ambipolar diffusion coefficient is calculated from the low field limit of the ion mobility $\mu_a = 0.21p^{-1}\,(\text{Torr})$ $\left(\text{m}^2 \cdot \text{V}^{-1} \cdot \text{s}^{-1}\right)$ in [16] hence $D_a = 5.5 \times 10^{-4}$ $\left(\text{m}^2 \cdot \text{s}^{-1}\right)$.

The attachment rate coefficient is [17]:

$$\nu_{att} = \nu_{a\text{N}_2} + \nu_{a\text{O}_2}\ (\text{s}^{-1}), \tag{13}$$

where $\nu_{a\text{O}_2} = 2.47 \times 10^{-43} n_{\text{O}_2}^2$ (s^{-1}) and $\nu_{a\text{N}_2} = 1.70 \times 10^{-43} n_{\text{O}_2} n_{\text{N}_2}$ (s^{-1}).

2.2. Initial conditions

The initial refractive index is calculated assuming an electron concentration of $n_e = 10^{14}$ $\left(\text{m}^{-3}\right)$ [4] in a gas with $p = 101\,325$ Pa and $T_0 = 293.15$ K. The mesh has 4000 radial nodes equispaced between 0 and 0.015 m and 601 nodes in the z direction which extend from $z = -f$ to $z = f$. Nodes along the z axis are heavily concentrated about the focal position ($z = 0$). The initial electric field of the laser pulse immediately following the focusing lens is:

$$E(r,-f,t) = \left[\frac{2I_{0v}}{\text{c}n\varepsilon_0}\exp\left(-\frac{(t-t_0)^2}{2\sigma_t^2}\right)\right]^{\frac{1}{2}} \times \exp\left(-\frac{r^2}{\omega_a^2} - i\frac{kr^2}{2f}\right)\left(\frac{\omega_a}{\omega_0}\right), \tag{14}$$

where ω_a and ω_0 are the beam widths at the lens and waist respectively, σ_t^2 is the temporal pulse width, f refers to the focal length, k is the wavevector and I_{0v} is the peak pulse intensity in time and space. This peak intensity is only realized during propagation through a vacuum. In air, plasmas will defocus the beam which lowers the peak intensity. The f-number of a system is defined as $f_\# = f/2\omega_a$ and is useful to characterize the beam divergence. Since the beam is assumed to be collimated before the focusing lens the $f_\#$ is related to the beam divergence half angle (θ) by $\theta = 1/2f_\#$. Single pulse breakdown is simulated with a 1064 nm beam with an initial width of $\omega_a = 4$ (mm) and duration (FWHM $= 2\sqrt{2ln2}\sigma_t$) of 13 ns. The pulses have a peak intensity of $I_{0v} = 234$ $(\text{GW}\,\text{cm}^{-2})$ and focal parameters detailed in table 1. The energy per pulse (E_p) changes with focal conditions (table 1) so that the peak intensity in each simulation is identical.

In the dual pulse simulations, a pre-ionizing UV (266 nm) beam is applied with an intensity peak of $I_{0v_{266}} = 39$ $(\text{GW} \cdot \text{cm}^{-2})$ which occurs 10 ns before the 1064 nm pulse ($I_{0v_{1064}} = 62$ $(\text{GW} \cdot \text{cm}^{-2})$) as shown by the normalized intensity profiles in figure 5.

Table 2. Dual pulse laser parameters for simulations 1 (*S*#1) and 2 (*S*#2).

	S#1	*S*#2
UV	$f_\# = 200$	$f_\# = 400$
	$R_R = 11.4 \pm 1.9$ mm	$R_R = 45.6 \pm 7.4$ mm
	$E_p = 6.7 \pm 1.1$ mJ	$E_p = 26.7 \pm 4.3$ mJ
IR	$f_\# = 50$	$f_\# = 100$
	$R_R = 2.8 \pm 0.5$ mm	$R_R = 11.4 \pm 1.9$ mm
	$E_p = 12.7 \pm 2.1$ mJ	$E_p = 51.8 \pm 8.4$ mJ

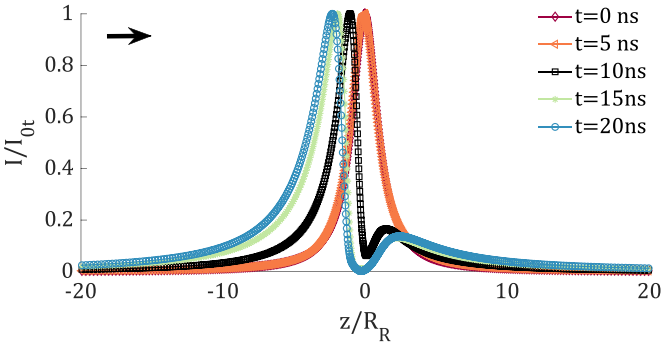

Figure 2. Sequence of axial intensity profiles normalized by the peak intensity at each time-step. Profiles were generated by simulations of a single pulse nanosecond laser with $f_\# = 50$.

The UV beam has an initial width of $\omega_a = 1$ (mm) with a FWHM of 10 ns. The IR pulse has $\omega_a = 4$ (mm) and a duration of 13 ns. In these simulations the beam waist and the focal length of the two laser systems are matched to mimic the experimental layout in [4]. This setup constrains the $f_\#$ of the UV pulse to be quadruple that of the IR pulse. Focal characteristics of the two dual pulse simulations are detailed in table 2.

3. Results

In all simulations, the production of electrons is initially symmetric about the focal position as shown by the normalized axial intensity profiles in figure 2 (0–5 ns). As the electron density increases, the defocusing becomes more pronounced resulting in a steeper decay of the profiles on the non-laser side (10–15 ns). Eventually, the beam is defocused before reaching the focal position which results in a displacement of the intensity peak toward the focusing lens (10–20 ns).

The changing intensity distribution is reflected in the local production of electrons and eventually results in a displacement of the location of peak energy deposition. The deposited energy is calculated from Joule heating and excess photon energy produced during multiphoton ionization. The evolution of the location of peak energy deposition for a 13 ns laser pulse under three different focal conditions is shown in figure 3. The displacements range over an order of magnitude from a maximum of -2.2 mm in the $f_\# = 50$ case to

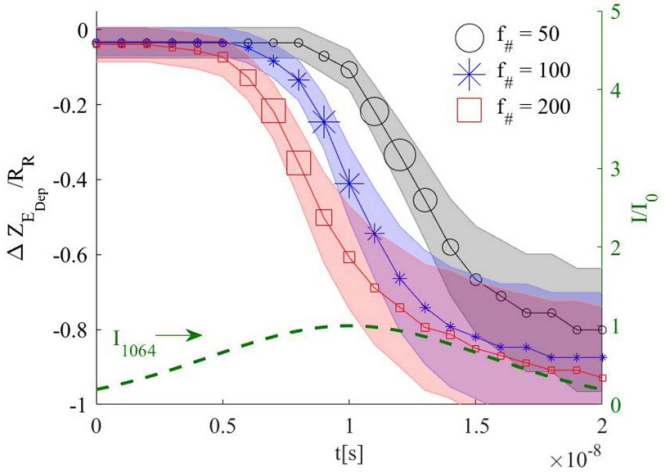

Figure 3. Location of the peak energy deposition (magnitude denoted by marker-size) for a 13 ns 1064 nm pulse with three different focusing conditions. Displacements are normalized by their respective Rayleigh ranges (table 1) and the normalized pulse intensity is shown for reference. The highlighted region indicates uncertainty which is dominated by the sensitivity of ω_0 (and thus R_R) to the radial mesh density (ω_0 is fit from simulation data at $t = 0$).

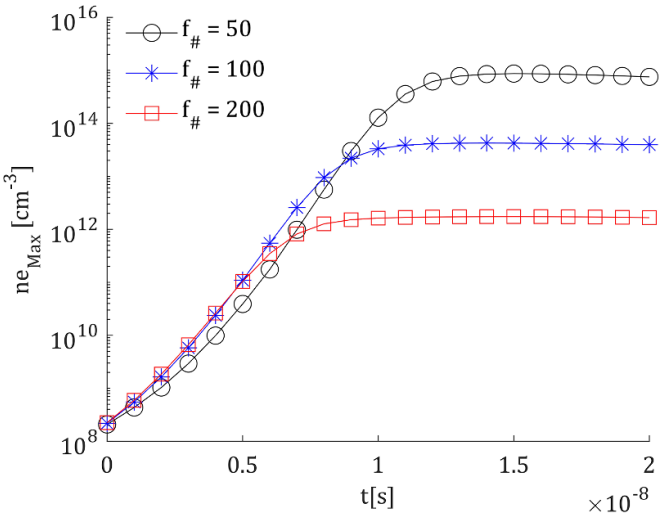

Figure 4. Evolution of peak electron density within the plasma (regardless of position).

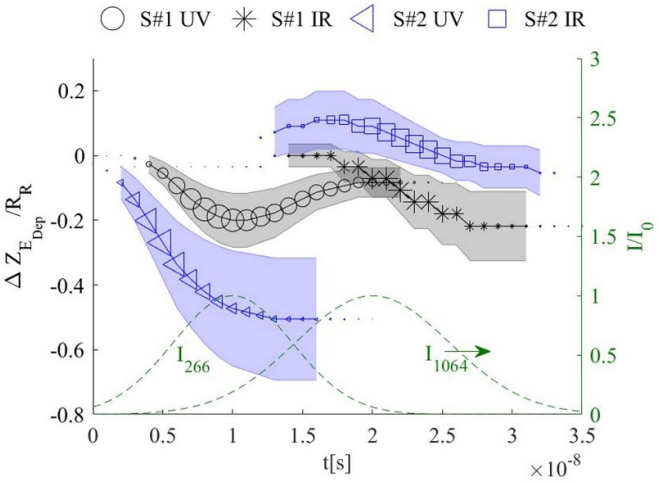

Figure 5. Location of peak energy deposition (magnitude denoted by marker-size) during a two-pulse laser breakdown sequence for two different focal configurations. Displacements are normalized by their respective Rayleigh ranges. Normalized temporal intensity profiles are shown for reference. The uncertainty, which is again dominated by the sensitivity of ω_0 to the radial mesh density, is displayed in regions where energy deposition is at least 10% of the maximum.

−48 mm for $f_\# = 200$. The normalized displacement profiles, however, are quite similar which suggests the displacement scales with Rayleigh range. The Rayleigh range is the distance along the axis where the laser intensity falls to half its peak value and hence is intrinsically linked to the scale of the plasma region. The identical temporal characteristics of the pulses in the simulations contribute to the similarity of the normalized displacement profiles.

As the $f_\#$ of the system increases, the plasma region lengthens ($R_R \approx \frac{4\lambda f_\#^2}{\pi}$), and laser radiation must propagate further through the strong radial refractive index gradients generated by the plasma. With longer propagation distances, smaller gradients of refractive index (lower axial electron densities) are required to defocus the beam. The effect of this trade-off can be observed in figure 4 where the maximum electron density of the plasma region decreases dramatically as the $f_\#$ of the system increases. Hence, self-defocusing would prevent breakdown in longer focal length systems.

For systems with a large $f_\#$, self-defocusing drives the growth of the plasma towards the focal lens even though local electron densities remain well below breakdown. This is in contrast to the Laser supported Breakdown Wave mechanism [10], where absorption of the laser light as it propagates through the plasma region following breakdown is used to explain the preferential growth of the plasma towards the focal lens. In small $f_\#$ systems, the plasma density is high enough that significant absorption will occur. This means that the defocusing and absorption mechanisms will occur in tandem.

These studies indicate that plasmas generated by single pulse lasers have an inherent asymmetry in their energy profile. The severity of asymmetry required for third lobe formation, however, is currently unknown so it is possible that there exists an $f_\#$ threshold below which the asymmetry of deposited energy does not result in 3rd lobe generation.

The location of the peak energy deposition from UV and IR lasers in a dual pulse system, normalized by their respective Rayleigh ranges, are illustrated in figure 5. The initial positive displacement of peak energy deposition by the IR lasers are a result of deflection by the plasma generated by the UV beam. This phenomena is also observed in figure 2 where a second peak arises as light from the beam wings is deflected by the plasma to a new focus behind its original position. The lower $f_\#$ of the IR pulse means that despite its longer wavelength making it more susceptible to refractive index changes (equation (3)), the location where it deposits energy remains relatively

constrained due to its smaller Rayleigh range (−0.62 mm displacement compared to −2.28 mm of the UV pulse in *S*#1).

The independence of the location of peak energy deposited by the UV pulse and the IR pulse through-out the simulation is important. It demonstrates that symmetric energy deposition about the beam waist can be obtained in a two pulse system by independently controlling the initial position of the beam waists.

4. Conclusion

As a laser generated plasma is formed it defocuses the beam which is generating it. This results in the displacement of the location of peak energy deposition towards the focusing lens. We show that this displacement is related to the $f_{\#}$ of the system, with lower $f_{\#}$ systems producing less displacement. This displacement causes the asymmetric energy deposition which can result in the formation of third lobe structures. While this asymmetry occurs in all single pulse systems, it can be suppressed in two pulse systems by offsetting the beam waists.

Acknowledgments

M N-T acknowledges support from a PPPL Program in Plasma Science and Technology Fellowship (PPST).

Funding information

This study was funded by Air Force Office of Scientific Research (AWD1005727).

Conflict of interest

The authors declare no conflict of interest.

References

[1] Gladkov S, Zheltikov A M, Koroteev N I, Rychev M and Fedotov A B 1989 Coherent anti-stokes Raman scattering by excited ions in a laser plasma *Sov. J. Quantum Electron.* **19** 923

[2] Yu L L, Zhao Y, Qian L-J, Chen M, Weng S-M, Sheng Z-M, Jaroszynski D, Mori W and Zhang J 2016 Plasma optical modulators for intense lasers *Nat. Commun.* **7** 11893

[3] Sprangle P, Esarey E, Krall J and Joyce G 1992 Propagation and guiding of intense laser pulses in plasmas *Phys. Rev. Lett.* **69** 2200

[4] Yalin A P, Wilvert N, Dumitrache C, Joshi S and Shneider M N 2014 Laser plasma formation assisted by ultraviolet pre-ionization *Phys. Plasmas* **21** 103511

[5] Mahamud R, Tropina A A, Shneider M N and Miles R B 2018 Dual-pulse laser ignition model *Phys. Fluids* **30** 106104

[6] Shneider M, Zheltikov A and Miles R 2011 Tailoring the air plasma with a double laser pulse *Phys. Plasmas* **18** 063509

[7] Dumitrache C, VanOsdol R, Limbach C M and Yalin A P 2017 Control of early flame kernel growth by multi-wavelength laser pulses for enhanced ignition *Sci. Rep.* **7** 1–8

[8] Raizer Y 1977 *Laser-Induced Discharge Phenomena* (New York: Consultants Bureau)

[9] Bradley D and Sheppard C, Suardjaja I and Woolley R 2004 Fundamentals of high-energy spark ignition with lasers *Combust. Flame* **138** 55–77

[10] Raizer Y P 1965 Heating of gas under the action of a powerful light pulse *Zh. Eksp. Teor. Fiz* **48** 1508–19 (http://www.jetp.ac.ru/cgi-bin/e/index/e/21/5/p1009?a=list)

[11] Phuoc T X 2006 Laser-induced spark ignition fundamental and applications *Opt. Lasers Eng.* **44** 351–97

[12] Guizar-Sicairos M and Gutiérrez-Vega J C 2004 Computation of quasi-discrete Hankel transforms of integer order for propagating optical wave fields *J. Opt. Soc. Am.* A **21** 53–58

[13] Feit M and Fleck J 1978 Light propagation in graded-index optical fibers *Appl. Opt.* **17** 3990–8

[14] Dumitrache C, Limbach C and Yalin A 2016 Threshold characteristics of ultraviolet and near infrared nanosecond laser induced plasmas *Phys. Plasmas* **23** 093515

[15] Raizer Y P and Allen J E 1997 *Gas Discharge Physics* vol 2 (Berlin: Springer)

[16] Macheret S O, Shneider M N and Miles R B 2002 Modeling of air plasma generation by repetitive high-voltage nanosecond pulses *IEEE Trans. Plasma Sci.* **30** 1301–14

[17] Kossyi I, Kostinsky A Y, Matveyev A and Silakov V 1992 Kinetic scheme of the non-equilibrium discharge in nitrogen–oxygen mixtures *Plasma Sources Sci. Technol.* **1** 207